



HAL
open science

Forming multiple C - C bonds upon electrocatalytic reduction of CO₂ by molecular transition metal macrocycles

Sĩ Thành Đồng

► **To cite this version:**

Sĩ Thành Đồng. Forming multiple C - C bonds upon electrocatalytic reduction of CO₂ by molecular transition metal macrocycles. Catalysis. Université Paris-Saclay, 2023. English. NNT : 2023UP-ASF004 . tel-03972287

HAL Id: tel-03972287

<https://theses.hal.science/tel-03972287>

Submitted on 3 Feb 2023

HAL is a multi-disciplinary open access archive for the deposit and dissemination of scientific research documents, whether they are published or not. The documents may come from teaching and research institutions in France or abroad, or from public or private research centers.

L'archive ouverte pluridisciplinaire **HAL**, est destinée au dépôt et à la diffusion de documents scientifiques de niveau recherche, publiés ou non, émanant des établissements d'enseignement et de recherche français ou étrangers, des laboratoires publics ou privés.

Forming multiple C – C bonds upon electrocatalytic reduction of CO₂ by molecular transition metal macrocycles

*Formation de multiples liaisons C - C au cours de la réduction
électrocatalytique du CO₂ par des macrocycles moléculaires de métaux de
transition*

Thèse de doctorat de l'Université Paris-Saclay

École doctorale n°571 : Sciences chimiques : molécules, matériaux, instrumentation et
biosystèmes (2MIB)
Spécialité de doctorat : Chimie
Graduate School : Chimie. Référent : Faculté des sciences d'Orsay

Thèse préparée au **Synchrotron SOLEIL**, sous la direction du Dr. **Benedikt LASSALLE-
KAISER**, Scientifique de ligne

Thèse soutenue à Paris-Saclay le 3 Janvier 2023, par

Si-Thanh DONG

Composition du Jury

Membres du jury avec voix délibérative

Elena SAVINOVA Professeur, Université de Strasbourg	Présidente
Jennifer PERON Maître de conférences, Université Paris Cité	Rapportrice & Examinatrice
Cyrille COSTENTIN Professeur, Université Grenoble Alpes	Rapporteur & Examineur
Pedro DE OLIVEIRA Professeur, Université Paris Saclay	Examineur
Audrey BONDUELLE Chef de projet, IFP Énergies nouvelles	Examinatrice

Titre : Formation de multiples liaisons C – C au cours de la réduction électrocatalytique du CO₂ par des macrocycles moléculaires de métaux de transition

Mots clés : Énergie renouvelable, réduction du CO₂, catalyse hétérogène, macrocycles moléculaires

Résumé : Les macrocycles moléculaires possèdent des sites actifs bien définis et sont des électrocatalyseurs prometteurs pour la réduction du dioxyde de carbone en produits chimiques à valeur ajoutée. Jusqu'à présent, la plupart de ces catalyseurs ne peuvent produire que des produits de type C₁. Nous avons étudié l'utilisation de la phtalocyanine de fer, une molécule disponible commercialement à base d'éléments abondants, pour générer des hydrocarbures légers lors de la réduction électrocatalytique du CO₂ dans des conditions aqueuses et à pH neutre. Une cellule spectroélectrochimique à écoulement imprimée en 3D a été développée en interne et connectée à un système de caractérisation des gaz en ligne. Lorsqu'un potentiel électrochimique est appliqué, des hydrocarbures linéaires saturés et insaturés de type C₁ à C₄ sont détectés. Des expériences de marquage isotopique ont montré sans ambiguïté que ces produits sont issus du CO₂. Des expériences de contrôle et une analyse par spectroscopie des rayons-X en conditions *operando* ont démontré l'intégrité structurale du catalyseur moléculaire pendant la catalyse et sa responsabilité dans la réaction. Une espèce terminale de type carbène terminal est proposée comme intermédiaire clé pour l'étape de formation de la liaison C – C sur la base d'expériences avec des substrats alternatifs. Nous avons ensuite exploré les paramètres d'électrocatalyse influençant les performances de la phtalocyanine de fer, notamment le débit et les concentrations de catalyseur, d'électrolyte et de support conducteur. Enfin, une série de phtalocyanines de différents métaux de transition, ainsi que de phtalocyanines de fer substituées et de porphyrines de fer ont été criblés pour leur capacité à former des produits avec des liaisons C – C lors de la réduction du CO₂.

Title : Forming multiple C – C bonds upon electrocatalytic reduction of CO₂ by molecular transition metal macrocycles

Keywords : Renewable energy, CO₂ reduction, heterogeneous catalysis, molecular macrocycles

Abstract : Molecular macrocycles have well-defined active sites and are promising electrocatalysts for reducing carbon dioxide into value-added chemicals. Up to now, most of these catalysts have produced only C₁ products. We investigate the use of iron phthalocyanine, a commercially available molecule based on earth-abundant elements, to generate light hydrocarbons upon electrocatalytic reduction of CO₂ in aqueous conditions and neutral pH. A 3D-printed spectro-electrochemical flow cell was developed and connected to an in-line gas characterization system. Under applied electrochemical potential, C₁ to C₄ saturated and unsaturated linear hydrocarbons are evolved. Isotopic labeling experiments unambiguously showed that these products stemmed from CO₂. Control experiments and *operando* X-ray spectroscopic analysis demonstrated the structural integrity of the molecular catalyst during catalysis and its involvement in the reaction. A terminal iron carbene species is proposed as the key intermediate for the C – C bond formation step based on experiments with alternative substrates. We then explored electrolysis parameters influencing iron phthalocyanine's performance, including flow rate, and concentrations of catalyst, electrolyte, and conductive support. Finally, a series of transition metal phthalocyanines, substituted iron phthalocyanine, and a series of iron porphyrins were screened for their ability to form products with C – C bonds upon CO₂ reduction.

RÉSUMÉ

La transition des combustibles fossiles vers les énergies propres est cruciale pour lutter contre le changement climatique. Cependant, la plupart des sources renouvelables sont intermittentes, par conséquent, le stockage de l'énergie est essentiel pour une utilisation à grande échelle d'énergies à faible émission de carbone. Inspirée de la photosynthèse naturelle, la réduction du CO₂ convertit ce gaz en carburants et en produits chimiques, stocke l'énergie dans des composés chimiques durables et transforme le CO₂ d'un déchet industriel en une opportunité économique.

L'électrocatalyse est une méthode prometteuse pour réduire le CO₂. Le cuivre est le catalyseur le plus largement utilisé pour cette application, mais la nature de son site actif rend difficile l'établissement d'une étude mécanistique détaillée. Les catalyseurs moléculaires ont généralement des sites actifs bien définis. Ainsi, réaliser la réduction de CO₂ avec cette famille de catalyseurs permet d'étudier le procédé de manière approfondie. Cependant, contrairement au cuivre, la plupart des catalyseurs moléculaires sont limités à des produits à un seul atome de carbone. Dans cette thèse, nous explorons l'utilisation de macrocycles moléculaires pour réduire le CO₂ en produits contenant plusieurs liaisons C – C.

Tout d'abord, une cellule électrochimique à écoulement microfluidique est développée pour effectuer une réduction séquentielle du CO₂ en produits hautement réduits. Cependant, la cellule ne pouvait pas fonctionner correctement pour deux raisons principales : la bulle de CO₂ piégée dans le canal microscopique et la nature flexible et perméable du polydiméthylsiloxane utilisé pour sa fabrication. Nous avons développé une cellule à écoulement millifluidique imprimée en 3D pour surmonter ces problèmes. La cellule maintient l'électrolyse pendant deux heures à l'aide d'une électrode sur laquelle un catalyseur de phtalocyanine de fer est déposé sous forme de film mince.

Lors de la réduction du CO₂ dans la cellule électrochimique à écoulement millifluidique imprimée en 3D avec un catalyseur de phtalocyanine de fer, des hydrocarbures possédant jusqu'à trois liaisons C - C sont détectés, tandis que le produit principal est le CO. En effectuant une électrolyse de contrôle et une chromatographie en phase gazeuse couplées à la spectrométrie de masse, nous avons confirmé que les atomes de carbone dans les hydrocarbures proviennent du CO₂. En utilisant la spectroscopie d'absorption des rayons X *operando*, nous avons montré que la phtalocyanine de fer conserve sa structure moléculaire tout au long du processus électrocatalytique. En réalisant une électrolyse avec du monoxyde de carbone ou du formaldéhyde, nous proposons un carbène terminal comme intermédiaire clé sur la voie des produits C₂₊. Ces données constituent un résultat nouveau, selon lequel les macrocycles de métaux de transition à site unique peuvent catalyser la formation de plusieurs liaisons carbone-carbone consécutives à partir du CO₂.

Nous avons optimisé les paramètres d'électrolyse en faisant varier le débit et les concentrations d'électrolyte, de catalyseur et de support carboné pour augmenter la sélectivité des produits C_{2+} . Bien que les résultats montrent des améliorations modestes, aucune percée significative n'est obtenue. Cependant, la corrélation entre la production élevée d'hydrogène et la production élevée d'hydrocarbures est observée. Enfin, nous étudions la formation de liaisons C – C à partir du CO_2 de macrocycles métalliques apparentés : les phtalocyanines métalliques, la phtalocyanine de fer substituée par différents groupes fonctionnels, et les porphyrines de fer et leurs dérivés. Nous avons constaté que le centre métallique joue un rôle essentiel dans la production des hydrocarbures, alors que les effets des ligands ne sont pas évidents.

Nous concluons la thèse en fournissant des perspectives futures sur les travaux et des commentaires généraux sur l'état du processus de transition énergétique pour faire face au changement climatique.

LIST OF PUBLICATIONS

An article titled "*Multiple C – C bond formation upon electrocatalytic reduction of CO₂ by an iron-based molecular macrocycle*", which contains data from Chapter 2 and Chapter 3, was published in the journal *Chemical Science*. <https://doi.org/10.1039/D2SC04729B>. An earlier version of this manuscript was uploaded to the ChemRxiv open platform. <https://doi.org/10.26434/chemrxiv-2021-j1h90>.

An article titled "*In situ/operando X-ray spectroscopy applied to electrocatalytic CO₂ reduction: Status and perspectives*" was published in the journal *Current Opinion in Colloid & Interface*. <https://doi.org/10.1016/j.cocis.2022.101635>.

An article titled "*In situ X-ray absorption spectroscopy in homogeneous conditions reveals interactions between CO₂ and a doubly and triply reduced iron(III) porphyrin, then leading to catalysis*" was published in the journal *ChemCatChem*. <https://doi.org/10.1002/cctc.202201298>

An article titled "*Degradation Mechanism of Metal-Organic Framework Drug Nanocarriers Studied by Solid-State Nuclear Magnetic Resonance and X-ray Absorption Near-Edge Structure Spectroscopy*" was published in the journal *Chemistry of Materials*. <https://doi.org/10.1021/acs.chemmater.2c01190>.

Copies of the above publications are available at the end of this thesis.

LIST OF AUTHORS' CONTRIBUTIONS

Dr. Benedikt LASSALLE-KAISER conceived the ideas of this thesis, advised on analyzing the data, and took part in performing X-ray absorption spectroscopy and gas chromatography-mass spectrometry experiments.

Ms. Anna MROSZCZAK, Ms. Chen XU, and Mr. Labeesan SRIMURUGATHAS took part in preparing samples, performing and analyzing electrocatalytic experiments, and assisting with X-ray absorption spectroscopy experiments.

Dr. Daniela MENDOZA took part in X-ray absorption spectroscopy experiments.

Ms. Chanjuan ZHANG and Dr. Zakaria HALIME assisted in performing nuclear magnetic resonance spectroscopy experiments.

Dr. Gary MOORE and Dr. Edgar Reyes CRUZ synthesized two iron-porphyrin-based catalysts and took part in analyzing the electrocatalytic experiments concerning the two catalysts.

Dr. Silvia DURAN and Dr. Cédric TARD took part in performing and analyzing cyclic voltammetry experiments.

Dr. Jean-Blaise BRUBACH and Ms. Chen XU took part in performing and analyzing infrared spectroscopy experiments.

Dr. Frédéric KANOUI and Dr. Yuanyuan LIAO advised on the finite element analysis.

Dr. Stephanie BLANCHANDIN and Ms. Karine CHAOUCHI assisted in gas chromatography-mass spectrometry experiments.

LIST OF ABBREVIATIONS AND ACRONYMS

CE	counter electrode	Pc	phthalocyanine
CNT	carbon nanotubes	PDMS	polydimethylsiloxane
CO ₂ RR	CO ₂ reduction reaction	PEEK	polyether ether ketone
CV	cyclic voltammetry	PEG	polyethylene glycol
DFT	density functional theory	PhOH	phenol
DMF	dimethylformamide	PP	protoporphyrin
DMSO	dimethyl sulfoxide	py	pyridine
EXAFS	Extended X-ray absorption fine structure	RE	reference electrode
FE	Faradaic efficiency	RHE	reversible hydrogen electrode
FeTPP	Iron tetraphenyl porphyrin	SAC	single-atom catalyst
FT	Fischer-Tropsch	SEM	scanning electron microscopy
GC	gas chromatograph	SHE	standard hydrogen electrode
GC-MS	gas chromatography-mass spectrometry	TEM	transmission electron microscopy
ICP-MS	inductively coupled plasma mass spectrometry	TOF	turnover frequency
MOF	metal-organic framework	TPP	tetraphenyl porphyrin
NHE	normal hydrogen electrode	WE	working electrode
NMR	nuclear magnetic resonance	XANES	X-ray absorption near edge structure
OCP	open circuit potential	XAS	X-ray absorption spectroscopy
P2VP	Poly(2-vinylpyridine)	XPS	X-ray photoelectron spectroscopy
P4VP	Poly(4-vinylpyridine)		

ACKNOWLEDGEMENT

First and foremost, I would like to express my heartfelt gratitude to my supervisor, Dr. Benedikt Lassalle-Kaiser. He did not only guide me through my scientific journey but also shared with me invaluable experience and lessons that I will hold dear in the future. He always believed in me, even when I had doubts about myself. Unlike many PhD students having a team of supervisors, he carried the responsibility of guiding a naïve early-career researcher all by himself. His job was made order-of-magnitude more challenging since the world was going through a once-in-a-lifetime pandemic at the beginning of my PhD, and yet he exceeded all my expectations. He went out of his way to ensure all my scientific and everyday needs were met, from sending me to the best conferences in the field to taking care of me when I caught Covid. I consider him my second family in France, someone I know I can count on in all circumstances. In the future, I will undoubtedly miss discussing politics, culture, and every other topic with him during our daily lunch. I could not have asked for a better person to guide me through this journey.

I have the distinct honor and privilege to have a group of excellent scientists on my jury: Dr. Jennifer Peron, Pr. Cyrille Costentin, Pr. Pedro de Oliveira, Pr. Elena Savinova, Dr. Audrey Bonduelle, and Dr. Stafford Sheehan. I sincerely thank them for taking the time to evaluate my work and attend my defense. The discussion we had was lively and insightful, and the questions and comments they posed significantly improved the quality of my thesis as well as opened new directions for future work.

I would like to express my sincere gratitude to all the collaborators I have worked with during my PhD. I thank Pr. Gary Moore and Dr. Edgar Reyes Cruz for providing the iron porphyrin samples and the exciting discussion that followed afterward. I thank Ms. Chanjuan Zhang and Dr. Zakaria Halime for helping me measure NMR samples in their laboratory. I am grateful to Dr. Jean-Blaise Brubach for his help in characterizing my samples using infrared spectroscopy. I thank Dr. Frédéric Kanoufi for the valuable advice regarding finite element analysis. I am grateful for the considerable support I received from the members of LUCIA and SAMBA beamlines, the microfluidics lab, and the chemistry lab in Synchrotron SOLEIL.

I want to thank all the colleagues and friends I have worked with during my time as a PhD student. To Dr. Daniela Mendoza, you were my mentor at the beginning of my PhD, and you are still a role-model researcher to me. Your pure love for science and chemistry is admirable. Our rants about all the stress during our PhDs indeed helped calm me down from time to time. To Dr. Yuanyuan Liao, I am thankful for your scientific advice, and I value all the experiences you shared with me. To Anna, Chen, and Labeesan, it was my great pleasure to work with you, I learned a lot from you, and your hard work has contributed significantly to my thesis. I appreciate all the members of the young researchers' group in SOLEIL for the opportunity to share our scientific

journey, as well as countless other activities.

I want to thank Dr. Cédric Tard, who was keeping track of my PhD as a member of my following committee. I enjoyed every discussion I had with him, and he always offered excellent guidance to improve the science I was doing. His advice about a scientific career certainly helped guide me through my scientific journey, which is undoubtedly less arduous because of him. I am also grateful to him and Dr. Silvia Duran for helping me with experiments in their laboratory.

I am grateful to Prof. Ally Aukauloo, Prof. Winfried Leibl, and Dr. Zakaria Halime, for allowing me the chance to participate in their groups' weekly bibliography meetings, especially Prof. Winfried Leibl for driving me to the meeting from time to time. The discussions certainly enhanced my scientific knowledge and transferable skills and better me as an early-career researcher. I also valued all the contributions made by the participants of the meetings.

I want to thank Dr. Jean Daillant, the director of SOLEIL, for allowing me the opportunity to do my PhD in Synchrotron SOLEIL. In addition, I would like to thank all the administrative employees at SOLEIL for their professionalism, which made my stay in France as a foreigner a much more welcoming experience.

I could not be the person I am today without my girlfriend, Mai Vuong. It was a unique experience for her and me to do our PhDs together, and we even managed to publish a paper together (mostly her work). She helped me scientifically, physically, and emotionally. She is there for me when I am unsure whether I can make it. She showed me my good side when I felt overwhelmed with negativity. I cherish every moment I was with her, from all of our vacation trips to all the times we complained about how hard it was to do a PhD. A scientist usually avoids using absolute statements, but I am undoubtedly sure that I am a better person because of her. I cannot overstate how lucky I am to be with her, and I look forward to our future together.

Finally, I dedicated everything I have achieved to my family. I always appreciate them, but being away in a foreign country makes me truly realize how much they mean to me. Back in Vietnam, I sometimes got annoyed by my mother caring a bit too much for me. And yet when I am not with her, I always look forward to answering her questions about the weather in France, whether I have enough sleep, or what I eat every day. Her constant updates about what is going on in our family make me feel like I am home despite being thousands of kilometers away. My brother always cheers me with silly memes in our group chat, and yet he goes out of his way to help whenever I need something from him. One of my greatest regrets is not being there to welcome his beloved daughter, my niece, into this world. My father, who I don't talk to very often, but I know how much he cares about me, and I can still feel his support deep down. I miss you all, and I cannot wait to see you again in person.

TABLE OF CONTENTS

Résumé	iii
List of publications	v
List of authors' contributions	vi
List of abbreviations and acronyms	vii
Acknowledgement.....	viii
Table of Contents	x
Chapter 1: Introduction	1
1.1 The big picture: Climate change, renewable energy, and energy storage solutions	2
1.1.1 Energy sources, greenhouse gas emissions, and climate change	2
1.1.2 Renewable energy sources to mitigate CO ₂ emissions	4
1.1.3 Artificial photosynthesis	5
1.1.4 CO ₂ reduction as energy storage and chemical-producing technology	6
1.2 Overview of CO ₂ reduction	7
1.2.1 History and basics of CO ₂ reduction	7
1.2.2 Products of CO ₂ reduction	8
1.2.3 CO ₂ reduction methods.....	9
1.3 Electrocatalytic reduction of CO ₂	12
1.3.1 Overview and basic concepts.....	12
1.3.2 Metal catalysts	14
1.3.3 Homogeneous molecular catalysts.....	16
1.3.4 Heterogeneous reduction of CO ₂ by molecular catalyst	24
1.3.5 Reduction of CO ₂ to C ₂₊ products by catalysts with well-defined active sites.....	34
1.3.6 Importance of <i>in situ</i> characterization and isotopic labeling.....	38
1.4 Thesis outline	39
1.5 Bibliography	42
Chapter 2: Fabrication and modeling of an electrochemical flow cell.....	57
2.1 Introduction.....	58
2.1.1 Cascade catalysis for CO ₂ reduction.....	58
2.1.2 Microfluidics and its application in electrochemical energy devices	59
2.1.3 Scope of the chapter	60
2.2 PDMS microfluidic flow cell.....	60
2.2.1 Fabrication	60
2.2.2 Electrochemistry performance.....	63
2.2.3 Evaluation and perspectives	64
2.3 3D-printed millifluidic flow cell.....	66
2.3.1 Design and fabrication.....	66
2.3.2 Flow characterization.....	67
2.3.3 Electrochemistry performance.....	68
2.4 Reactants and products concentration profiles	69
2.4.1 The geometry of the flow cell: 2D model and meshing	69
2.4.2 Multiphysics: Laminar flow and transport of diluted species	70
2.4.3 Concentration profile throughout the electrochemical cell	73
2.4.4 Concentration profile at specific locations.....	74
2.5 Millifluidic cell evaluation and perspective	74
2.6 Conclusion.....	75
2.7 Bibliography	76
Chapter 3: Forming C – C bonds with an iron phthalocyanine catalyst	79
3.1 Introduction.....	80

3.2	Products distributions based on applied potentials.....	80
3.2.1	Electrocatalysis and products identification.....	80
3.2.2	Origin of the products	83
3.2.3	Products quantifications	85
3.3	FePc catalyst characterization: stability and active site estimation	88
3.3.1	X-ray absorption spectroscopy	88
3.3.2	Infrared spectroscopy	89
3.3.3	Cyclic voltammetry and active site estimation.....	90
3.4	Control experiments with FePc and Fe ₃ O ₄ nanoparticles.....	92
3.4.1	<i>Ex situ</i> X-ray absorption spectroscopy	93
3.4.2	Electrolysis and product distribution	94
3.4.3	Operando X-ray absorption spectroscopy	96
3.4.4	Discussion.....	97
3.5	C – C bond formation mechanism.....	97
3.6	Conclusion.....	102
3.7	Chapter 3 annex	104
3.7.1	NMR characterization.....	104
3.7.2	Isotopic labeling experiments.....	104
3.7.3	Cyclic voltammetry and active site estimation.....	106
3.7.4	Infrared spectroscopy	108
3.8	Bibliography	109
Chapter 4: Optimizing electrolysis parameters of FePc and screening various catalysts..		113
4.1	Introduction.....	114
4.2	Influence of external factors on FePc	115
4.2.1	Flow rate.....	115
4.2.2	Electrolyte concentration and pH.....	118
4.2.3	FePc concentration.....	121
4.2.4	Conductive carbon support concentration.....	124
4.3	Metal phthalocyanines	126
4.3.1	Metal center effects	126
4.3.2	Ligand effects on FePc.....	129
4.4	Iron porphyrins and derivatives.....	134
4.5	Conclusion.....	138
4.6	Bibliography	140
Chapter 5: Conclusions and Perspectives		142
5.1	Chapter 1	142
5.2	Chapter 2	142
5.3	Chapter 3	143
5.4	Chapter 4	144
5.5	General discussion of the thesis.....	144
5.6	The big picture	145
Annex		148
6.1	Supplementary figure	149
6.2	Millifluidic cell assembly procedure.....	149
6.3	Ink and electrodes preparation procedure	152
6.4	Constant-potential electrolysis experimental setup.....	154
6.5	Gas chromatograph characterization	155
6.6	Faradaic efficiency calculation and electrode potential conversion	157
6.7	X-ray absorption spectroscopy experiments.....	158
6.8	Bibliography	158
6.9	Publications.....	159

1 CHAPTER 1: INTRODUCTION

1.1	The big picture: Climate change, renewable energy, and energy storage solutions	2
1.1.1	Energy sources, greenhouse gas emissions, and climate change	2
1.1.2	Renewable energy sources to mitigate CO ₂ emissions	4
1.1.3	Artificial photosynthesis	5
1.1.4	CO ₂ reduction as energy storage and chemical producing technology	6
1.2	Overview of CO ₂ reduction	7
1.2.1	History and basics of CO ₂ reduction	7
1.2.2	Products of CO ₂ reduction	8
1.2.3	CO ₂ reduction methods	9
1.3	Electrocatalytic reduction of CO ₂	12
1.3.1	Overview and basic concepts	12
1.3.2	Metal catalysts	14
1.3.3	Homogeneous molecular catalysts	16
1.3.4	Heterogeneous reduction of CO ₂ by molecular catalyst	24
1.3.5	Reduction of CO ₂ to C ₂₊ products by catalysts with well-defined active sites	34
1.3.6	Importance of in-situ characterization and isotopic labeling	38
1.4	Thesis outline	39
1.5	Bibliography	42

1.1 The big picture: Climate change, renewable energy, and energy storage solutions

1.1.1 Energy sources, greenhouse gas emissions, and climate change

Energy sources have been pivotal in all eras throughout human history. The discovery of fire transformed humanity and made biomass the world’s primary energy source until the Industrial Revolution in the 18th century. Since the Revolution, the world has relied heavily on fossil fuels to satisfy its energy demand. As shown in Figure 1-1, in 2021, the combination of oil, coal, and gas accounts for more than 80% of the world’s total energy consumption. Population boom and rising standard of living increase energy demand significantly (Figure 1-1). The rising trend is expected to continue, and total energy demand is projected to increase by 50% by 2050, with fossil fuels remaining the largest share of the energy mix.¹

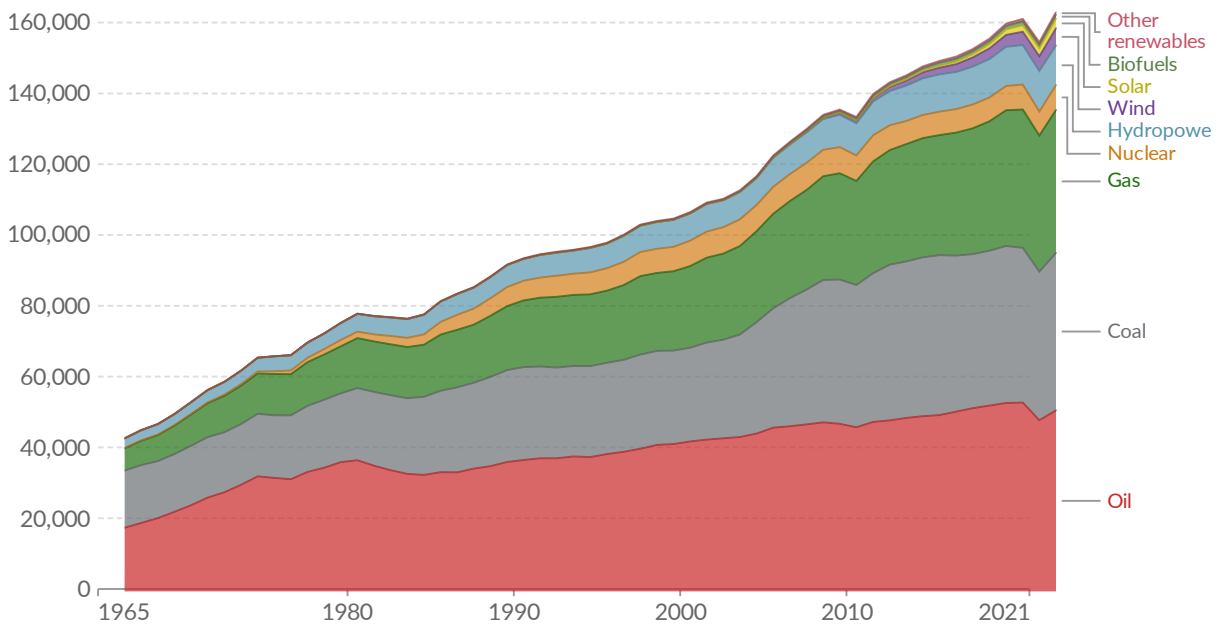


Figure 1-1. Energy consumption by sources, measured in TWh^{2,3}

The extensive combustion of fossil fuels since the Industrial Revolution has released millions of years’ worth of carbon dioxide into the atmosphere over a few hundred years.⁴ Consequently, CO₂ concentration in the air has risen dramatically in the last 200 years to approximately 400 ppm in 2022, the highest value in the previous 650 000 years.⁵ CO₂ is a greenhouse gas that can trap solar thermal energy in the atmosphere by the infrared absorption of sunlight reaching Earth. This effect results in a warmer planet compared to one without an atmosphere, thus keeping the temperature on Earth livable for humans and other species. However, as Arrhenius first mentioned in 1896,⁶ the release of an excessive amount of CO₂, a long-lasting greenhouse gas, in the atmosphere in such a short period would contribute significantly to the quick increase in the average temperature on Earth, as shown in Figure 1-2. It is a fact that this rise in temperature is the result of human activity.⁵

Chapter 1

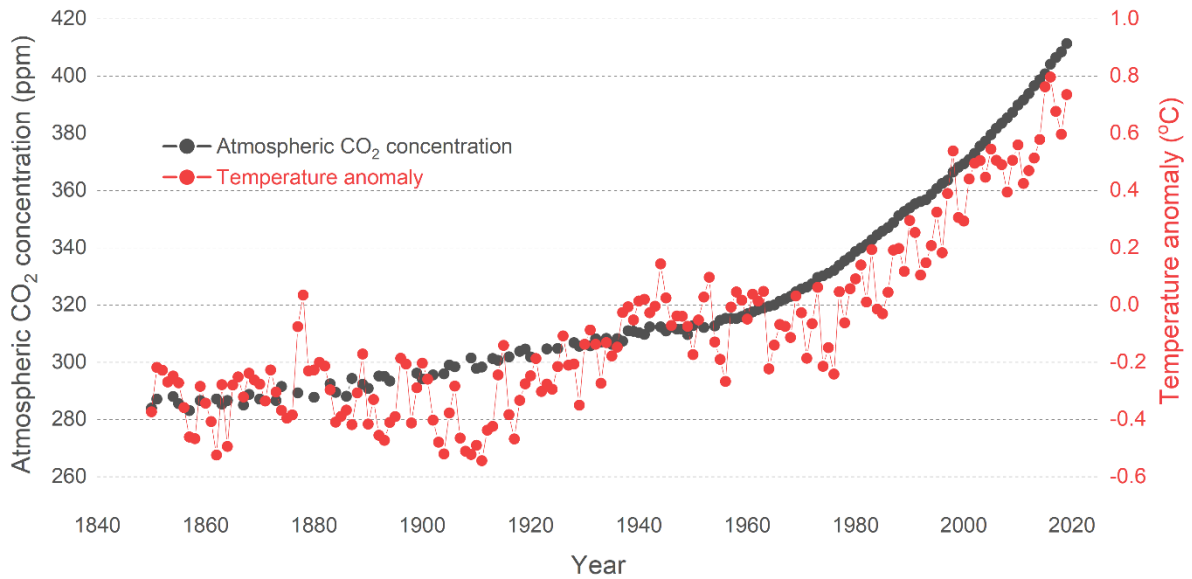


Figure 1-2. Evolution of atmospheric CO₂ concentration (NOAA)⁴ and temperature anomaly (Hadley Centre - HadCRUT4)⁷ from 1850 to 2020

The sudden change in climate has negatively affected humanity and, if left unchecked, will have catastrophic consequences for humans in particular and the whole biosphere of Earth in general. A higher frequency of extreme weather events, including drought, wildfire, heavy precipitation, and flood, has been attributed to human-induced climate change with high confidence.⁸ These weather events worsen the world's food and water security, disproportionately affecting vulnerable people in developing countries. Moreover, the rising temperature has contributed to the rising sea levels, mainly by melting ice caps at the two poles. The rising sea levels will disrupt the livelihoods of a large portion of the human population, as nearly 4 billion people live within 100 km of the coast.⁹ The consequences of climate change are cascaded and intertwined, so the more they happen and the higher the magnitude of their effects, the more complex the solutions will be.⁸ Therefore, it is in humanity's best interest to mitigate the impacts of climate change and ensure sustainable development in the shortest possible timeline.

While the impacts of climate change will be more pronounced in a relatively long-term timescale, the reliance on fossil fuels of the world economy has been the cause of short-term conflicts and instability in the past. The 1970s and early 1980s saw multiple events in the Middle East disrupting the oil supply, causing a recession and economic stagflation in Western countries and other parts of the world. In 2022, the Russian invasion of Ukraine interrupted the supply of oil and natural gas to the world, threatening a worldwide recession amid spiraling inflation and economic downturn. The impacts on European countries have been extreme, as Europe heavily relies on Russian gas for its industry and consumer uses. Therefore, the world's dependence on fossil fuels not only leads to the disastrous consequences of climate change but also gives authoritarian regimes a leveraging tool to achieve their purposes and cause instability in the world.

The 1970s oil crises sparked initial attempts to develop fuels saving technologies and alternative energy sources.¹⁰ Since then, awareness of fossil fuel reliance and climate change impacts has been slowly but steadily gaining traction among the public and political leaders. The first wide-ranging international effort to curb greenhouse gas emissions was the Kyoto protocol¹¹ in 1997, in which it made binding emission requirements for developed countries and encouraged the reduction of greenhouse gases where it is most cost-effective. In 2015, the Paris Agreement - the most significant effort to combat climate change to date - was adopted by 195 parties.¹² The agreement aims to keep the rise of global average temperature in the 21st century to well under 2°C, limiting the increase to 1.5°C compared to the pre-industrial period. The parties to the agreement are encouraged to establish independent road maps to reach the temperature targets while facilitating low-emission and climate-resilient development and adapting to the impact of global warming. The agreement calls for reducing the amount of CO₂ emission, increasing the percentage of renewable energy in the total energy sources, and increasing the energy efficiency to achieve greenhouse gas emission peaking.

1.1.2 Renewable energy sources to mitigate CO₂ emissions

In the past few decades, there have been tremendous research and development efforts for economical solutions to generating energy from sustainable sources, mainly solar and wind. The share of renewable energy generation has increased significantly in the last ten years, accounting for less than 1% of the total energy consumption in 2011 to 5% in 2021.² The price of electricity generated by solar and wind power has decreased dramatically in recent years, making them the cheapest sources of energy in certain places.¹³ As the renewable energy share in the total energy supply mix increases, the intermittency of renewable sources will become more pronounced. Since power generated by solar and wind varies depending on weather conditions, energy generated from other sources and storage devices needs to be modulated accordingly to meet immediate demand. Natural gas power plants are the favored method to accompany renewable energy, as their capacity can be quickly adjusted with high power and energy density.¹⁴ However, although natural gas burns cleaner than coal and oil, it still is a finite fossil fuel that emits greenhouse gases. And depending on the origin of the gas, relying on it for a short-term fossil-to-renewable transition period can still be problematic,¹⁴ with Germany's dependence on Russian natural gas serving as a cautionary tale. A net-zero emission scenario with renewable being the primary energy source must come with practical and economical means of storing extra energy to smooth out the intrinsic supply fluctuation.

Storing electrical energy is a difficult task. While batteries can store energy for relatively low-power applications, large-scale energy storage technology is limited. Currently, pump-storage hydroelectricity is the most widely-used technology, accounting for most grid energy storage. However, as it involves pumping a large volume of water between two reservoirs at different elevations, this technology is suitable for a limited

number of sites, making scaling up a challenge.¹⁵ Lithium-ion battery, propelled by the rise of electric vehicles, is a fast-growing technology for grid energy storage. While some pilot plants using the technology are operating, the requirement for limited minerals and the degradation of the battery renders the future of lithium-ion batteries in large-scale energy storage uncertain.¹⁶ Other technologies, including different types of batteries, compressed air, and flywheel, are in the early developing stages. Overall, large-scale energy storage is currently a diverse field without a dominant technology, thus calling for research and development efforts in varied directions.

1.1.3 Artificial photosynthesis

In nature, photosynthesis has been the energy storage solution of the biosphere since it started more than two billion years ago. Plants and other organisms use solar energy to convert atmospheric carbon dioxide and water into carbohydrates and oxygen through complex biochemical pathways, storing solar energy in chemical bonds of carbohydrates molecules. The stored energy is released in reverse when animals breathe in oxygen, consume the biomass directly or indirectly, and emit CO_2 and water, completing the natural carbon cycle (Figure 1-3 – left half). All biomass on Earth is produced via photosynthesis, directly or indirectly, and a portion of it is transformed into fossil fuels.¹⁷ However, relying on natural photosynthesis to store renewable energy and tackling humanity's problem of excess CO_2 is not a suitable approach. As the process is optimized by evolution for the survival of the photosynthetic organisms and not for storing energy, the solar-to-chemical efficiency of photosynthesis is only a few percent.¹⁸ Moreover, integrating natural photosynthesis to store energy within our current infrastructure is an improbable challenge.

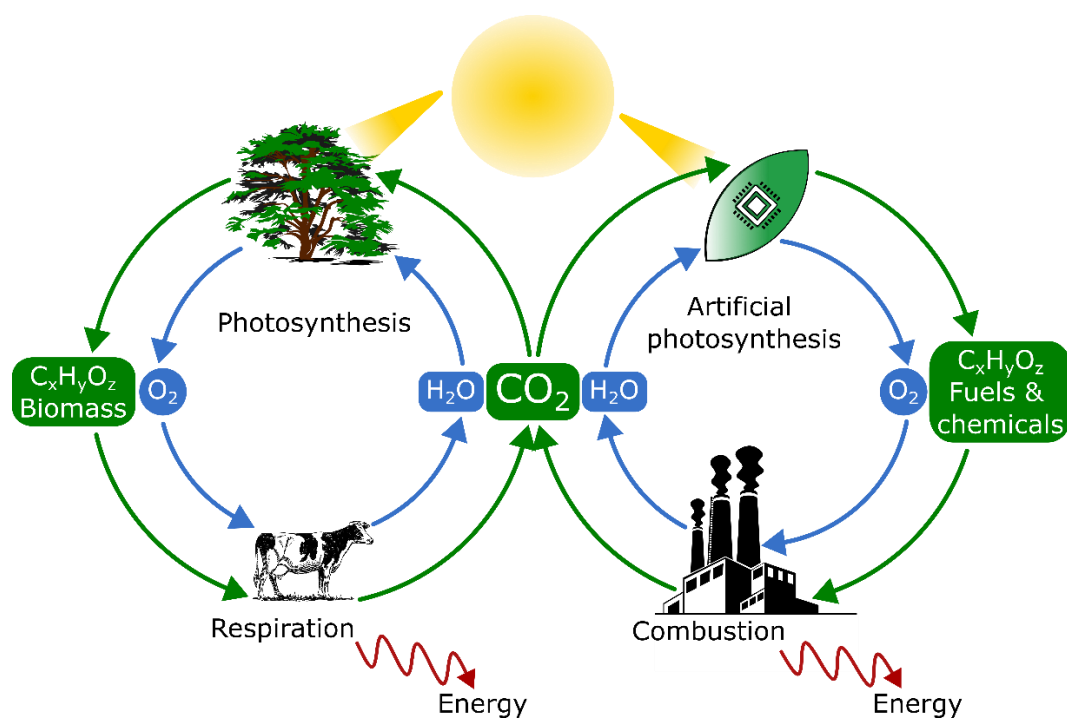


Figure 1-3. Simplified scheme of natural photosynthesis and artificial photosynthesis

While natural photosynthesis is not suitable to address the world's energy problem, an artificial version of photosynthesis is a promising energy storage solution. An ideal artificial photosynthesis device, the so-called artificial leaf, would harvest sunlight and use it to turn water and CO₂ into desired fuels and chemicals.¹⁸ A tandem system is another approach where the energy harvesting unit is decoupled with the chemicals production unit. In particular, a solar photovoltaic plant or a wind farm can produce electricity to power a plant, generating fuels and chemicals from CO₂ and water using electrochemistry.¹⁹ The generated products, either by artificial leaves or by a tandem system, store the renewable energy used to produce them. A reverse reaction can release the stored energy to account for renewable energy's intermittency or be used in other applications. This reverse process turns the chemical products back into CO₂ and water, completing the industrial carbon cycle without emitting net greenhouse gases into the atmosphere (Figure 1-3, right half).

The most straightforward product of artificial photosynthesis is hydrogen generated by splitting water. While the process does not consume CO₂, hydrogen production by water splitting using renewable energy does not emit CO₂ or other greenhouse gas. This type of hydrogen is named green hydrogen to differentiate it from hydrogen produced by natural gas sources that emit greenhouse gases. Green hydrogen can act as an energy carrier similar to fossil fuels, with its emission being water and oxygen instead of potent greenhouse gases. Therefore, green hydrogen has the potential to significantly facilitate the transition to a net-zero emission economy with its acting as an energy carrier and applications to other sectors, including transportation and materials and chemicals production.²⁰

1.1.4 CO₂ reduction as energy storage and chemical-producing technology

Another approach of artificial photosynthesis mimics the whole natural process: using renewable energy to reduce carbon dioxide and split water to produce fuels and chemicals and release oxygen (Figure 1-3, *right half*). Like green hydrogen, renewable energy is stored in the fuels and chemicals generated by this process. No net greenhouse gases are emitted to the atmosphere when the fuels are converted back to CO₂ and water to release the stored energy. But unlike green hydrogen, CO₂ reduction uses CO₂ as the carbon source, combining them with water to synthesize chemical products. Therefore, if the generated chemicals are used as feedstocks to produce long-lasting materials such as plastic or asphalt, the utilized carbon dioxide will be kept away from the atmosphere for an extended time without absorbing heat from sunlight and contributing to global warming. Using CO₂ as a carbon source is especially appealing as society is slowly moving away from extracting finite sources of fossil fuels. This process can potentially turn CO₂ from a waste product to a carbon source with excellent economic opportunities.

The CO₂ feedstock for CO₂ reduction can come from concentrated and atmospheric

sources. Concentrated CO₂ sources usually include flue gas of fossil fuels energy plants or steel and cement production plants, where CO₂ concentration is around 10%.²¹ Capturing CO₂ from concentrated sources requires less energy than CO₂ from the atmosphere, making reducing CO₂ from concentrated sources more economical than reducing CO₂ captured from the air. However, in the near term, the highest priority of the decarbonization process is to stop using carbon-intensive technologies and replace them with cleaner ones. As this process plays out, the importance of carbon capture, storage, and utilization to offset the emissions of carbon-intensive technologies that are challenging to replace will gradually grow.²² During this transition, the number of concentrated CO₂ sources will fall, leading to CO₂ captured from these sources becoming more limited, and CO₂ captured directly from air becoming more available. Moreover, even when a net-zero economy is achieved, the current CO₂ concentration in the atmosphere will continue to warm the planet above the pre-industrial level.²³ Therefore, in the long run, the CO₂ feedstock for CO₂ reduction would mainly come from the air, as CO₂ becomes the alternative carbon source to fossil fuels.

Overall, CO₂ reduction, under the context of artificial photosynthesis, would turn CO₂ from a waste product into an economic opportunity. The utilization of CO₂ incentivizes against releasing carbon dioxide into the atmosphere, getting humanity closer to a net-zero emission economy in the medium term. In the long run, CO₂ reduction can potentially expand the carbon sink to decrease the concentration of CO₂ in the atmosphere.

1.2 Overview of CO₂ reduction

1.2.1 History and basics of CO₂ reduction

Reports of electrochemical CO₂ reduction to formic acid on mercury and other inert electrodes dated back to 1870, and similar observations were reported consistently in the following decades.²⁴ Throughout this period, CO₂ reduction reports did not involve the applications of generating fuels and chemicals; hence there were no significant efforts to improve the reaction's performance or analyze its mechanism. Since the oil crisis in the late 1970s and early 1980s, CO₂ reduction has gained traction as an alternative way to synthesize fuels and chemicals.

Table 1-1 shows standard CO₂ reduction reaction (CO₂RR) products.²⁵ Although the reduction processes are generally facile in terms of thermodynamics, a significant activation barrier needs to be overcome to perform CO₂RR. Without a catalyst, most CO₂RRs go through the one-electron transfer step to create a bent radical anion (CO₂^{•-}) with high energy loss. The stability of CO₂ comes from it being the end product of exothermic reactions, making it a very inert molecule. In addition, the similarity of thermodynamic levels of different CO₂ reduction products causes making a particular product selectively a challenging task, especially with products requiring multiple

electrons transfer. Therefore, catalysts are essential for a selective CO₂RR with little to no waste energy. Typical catalysts for CO₂ reduction are based on transition metals in metallic form, molecular complex, or composite materials. Several sources can provide the energy needed to reduce CO₂, including electricity, heat, and light. Electrochemical and thermochemical reductions of CO₂ are currently the most advanced methods, while photochemical and other processes are at the early development stage.²⁶

Table 1-1. Standard CO₂ reduction processes and their thermodynamics potentials

Reduction process	E^0 vs SHE/V
$\text{CO}_2(\text{g}) + e^- \rightarrow \text{CO}_2^{\bullet-}(\text{g})$	-1.90 V
$\text{CO}_2(\text{g}) + 2\text{H}^+ + 2e^- \rightarrow \text{CO}(\text{g}) + \text{H}_2\text{O}(\text{l})$	-0.11 V
$\text{CO}_2(\text{g}) + 2\text{H}^+ + 2e^- \rightarrow \text{HCOOH}(\text{l})$	-0.25 V
$\text{CO}_2(\text{g}) + 4\text{H}^+ + 4e^- \rightarrow \text{HCHO}(\text{l}) + \text{H}_2\text{O}(\text{l})$	-0.07 V
$\text{CO}_2(\text{g}) + 6\text{H}^+ + 6e^- \rightarrow \text{CH}_3\text{OH}(\text{l}) + \text{H}_2\text{O}(\text{l})$	+0.02 V
$\text{CO}_2(\text{g}) + 8\text{H}^+ + 8e^- \rightarrow \text{CH}_4(\text{g}) + \text{H}_2\text{O}(\text{l})$	+0.17 V
$2\text{CO}_2(\text{g}) + 12\text{H}^+ + 12e^- \rightarrow \text{CH}_2\text{CH}_2(\text{g}) + 4\text{H}_2\text{O}(\text{l})$	+0.06 V
$2\text{CO}_2(\text{g}) + 12\text{H}^+ + 12e^- \rightarrow \text{CH}_3\text{CH}_2\text{OH}(\text{l}) + 3\text{H}_2\text{O}(\text{l})$	+0.08 V

1.2.2 Products of CO₂ reduction

The two most simple products of CO₂ reduction are CO and HCOOH. As they only require the transfer of two electrons, there are few intermediate steps and competitive reactions, making the problems of activation energy and selectivity less complicated to address. When more than two electrons are transferred to a CO₂ molecule, further reduced products are obtained, including formaldehyde, methanol, and methane. Transferring multiple electrons is generally complicated, making producing more reduced products less efficient than CO and HCOOH. The reduction of CO₂ can involve more than one molecule of CO₂, forming products with C – C bonds. This intricate process requires not only the generation of highly reduced intermediates but also the precise positioning of these intermediate species for the C – C coupling. As a result of their simplicity, under current economic conditions, the technology to reduce CO₂ to CO and HCOOH is closest to becoming market-ready.^{27,28} However, the market potential of formic acid is relatively small, and the toxicity and flammability of gaseous CO make its storage and transportation a logistical challenge.²⁸ In addition, these two C₁ molecules (molecules containing only one carbon atom) do not reflect the potential range of chemicals that can come from CO₂ reduction. Therefore, despite the intrinsic difficulties, producing long-chain carbon products from CO₂, especially in liquid form, is an appealing approach. For example, ethanol and n-propanol hold great market

potential, while ethylene can serve as a chemical feedstock to make plastic materials (Figure 1-4). Overall, simple C_1 products are closer to becoming economically viable, and C_{2+} products have high market potential but require substantial research and development efforts to compete with the current production methods.²⁶

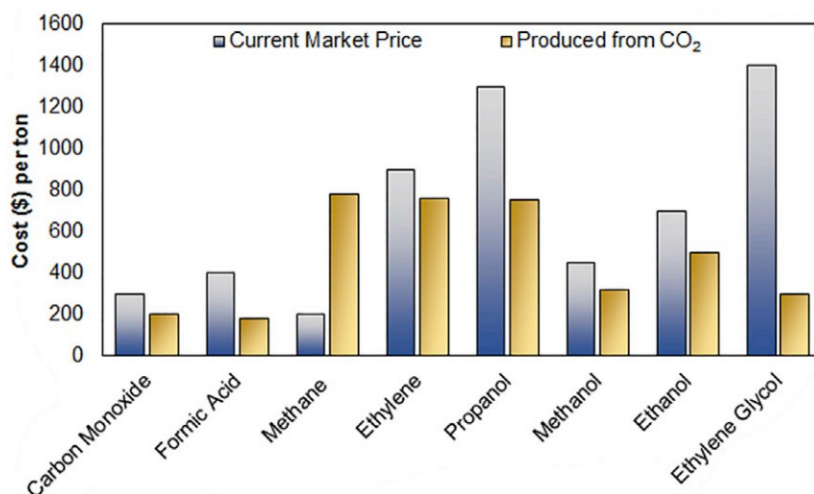


Figure 1-4. Comparison of cost of products between traditional and CO₂ reduction reproduced from reference²⁶

1.2.3 CO₂ reduction methods

CO₂ reduction is an endothermic process; therefore it needs an energy supply to occur. CO₂ reduction is categorized into several methods depending on the energy sources used. As discussed above, electrochemical and thermochemical are the two most mature ones, while photochemical reduction of CO₂ has also been extensively studied. Biochemical and chemical approaches can also be used to reduce CO₂, though their applications are more limited than other methods. Combinations of any two of these methods have also been studied.

Photochemical reduction of CO₂ using sunlight closely resembles the process of natural photosynthesis. Like the electrochemical method, CO₂ photoreduction can happen under homogeneous or heterogeneous conditions. Standard products of CO₂ reduction, including CO, HCOOH, and CH₄²⁹⁻³¹ have been generated using photocatalysis. Another approach to the photoreduction of CO₂ includes tandem devices, where photovoltaic solar cells are coupled to electrolysis systems. This device, often called an artificial leaf, combines the electricity produced by photovoltaic solar cells to carry out the electrochemical reduction of CO₂. Thus, it is more industrially ready than direct photoreduction. There are devices demonstrating CO₂ reduction and water-splitting processes using sunlight in real-world conditions.^{32,33} However, the field of photochemical CO₂ reduction has many intrinsic challenges to overcome. First, capturing sunlight and using it to drive the transfer of electrons and protons to CO₂ and water requires a system of intricate molecular machinery consisting of rare metals such as ruthenium or rhenium. While these systems can carry out the reaction in

Chapter 1

laboratory scale, scaling up a complex chemical system built around scarce materials is a challenging task. The intricate photochemical system is also often subject to premature degradation that is incompatible with industrial standards. Secondly, any system that uses sunlight as an energy source requires a large area to harvest sufficient energy due to the inherently low energy density of sunlight. However, unlike solar photovoltaic, a solar fuel plant needs a dedicated system to transfer and process the reactants and products, further complicating its implementation. Overall, despite the appealing aspects of the photochemical reduction of CO₂, the inherent challenges of the method limit its industrial application. Still, the insights gained from developing photochemical CO₂ reduction prove beneficial to develop catalysts for CO₂ reduction using other energy sources.

Reducing CO₂ using biological species, such as enzymes, is another approach toward CO₂ conversion. In nature, enzymatic reduction of CO₂ is a multi-step process employing three enzymes: formate hydrogenase, formate dehydrogenase, and alcohol dehydrogenase.³⁴ Artificial versions of biochemical CO₂ reduction include the works of Ai and co-workers,³⁵ and Lee and colleagues,³⁴ where they built a multi-enzyme system to reduce CO₂ to methanol. The biochemical reduction of CO₂ often involves intricate biochemistry processes, but the active species are often subject to rapid degradation, rendering them impractical for large-scale application. However, the chemistry of these complex biological processes can serve as inspiration to design and improve other catalysts utilizing different energy sources.^{36,37}

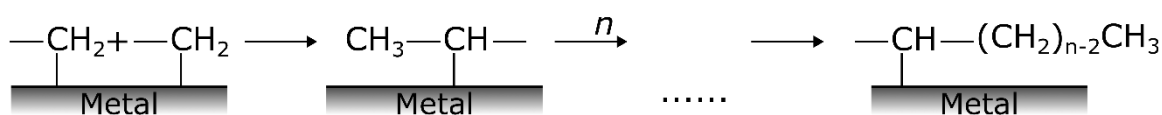
The cascade approach has been explored by combining electrochemical or photochemical with chemical synthesis. Skrystrup and colleagues used CO generated electrochemically from CO₂ to carry out carbonylation reactions on a Pd catalyst.³⁸ The same approach was reported by Aukauloo and co-workers, using photochemical instead of electrochemical methods to produce CO from CO₂.³⁹ However, these methods of CO₂ reduction are more suitable for small-scale applications than industrial-scale CO₂ utilization.⁴⁰ These small-scale applications demonstrate the versatility of the cascade catalysis approach for CO₂ reduction.

Thermochemistry is one of the major routes to reduce CO₂. Thermochemical reduction of CO₂ involves heating CO₂ at appropriate temperatures and pressure over catalysts to facilitate the conversion of CO₂. This process mainly yields CO, as the high-temperature requirement is unsuitable for producing more complicated products.⁴¹ Combination of thermochemistry and electrochemistry has been studied to make CO from CO₂ using molten carbonate or solid oxide electrolyzers.^{42,43} Concerning CO production, high-temperature solid oxide electrolysis has the highest technological readiness level.⁴² The Perseverance rover on Mars also employs this method to split CO₂ into CO and O₂, experimenting with providing breathable oxygen in the Martian atmosphere.⁴³

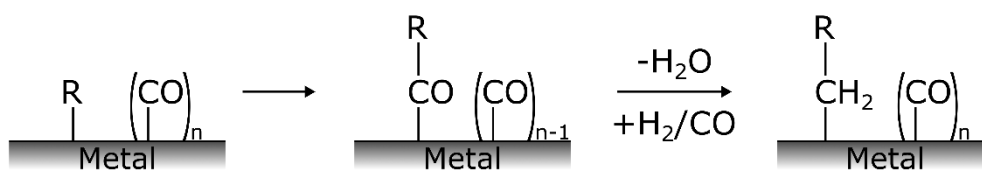
Fischer-Tropsch (FT) process is a notable thermochemical process that converts a

mixture of carbon monoxide and hydrogen, known as syngas, into hydrocarbons.⁴⁴ Developed in the late 1920s, it has recently gained considerable attention as a method to synthesize clean fuels and chemicals.⁴⁵ In particular, the scheme involves cascade catalysis, where CO₂ reduction and water splitting produce the syngas feedstock for the FT process.^{46,47} When the syngas mixture is heated at high temperature and pressure, typically 150 – 300°C, and several tens of atmosphere, CO and H₂ are converted to hydrocarbon in a process resembling chain growth polymerization, where the chain is initiated on metal catalysts. Common catalysts FT process include iron and cobalt, while ruthenium is an active catalyst but less widely used due to its scarcity.⁴⁵ The hydrocarbons resulting from the FT process follow the Flory–Schulz distribution, which favors shorter hydrocarbons than longer ones.⁴⁸ Three main polymerization schemes have been proposed regarding the formation of C – C bonds in FT synthesis: carbide, CO insertion, and hydroxycarbene mechanism (Figure 1-5). In the carbide mechanism, the hydrocarbons are formed by adsorbed M-CH₂ species reacting with each other. Figure 1-5B shows the propagation step in the CO insertion mechanism, where chains are grown by the insertion of carbon monoxide into the metal-alkyl bonds, followed by the reduction of the acyl group. The mechanism based on the formation of the hydroxycarbene species is shown in Figure 1-5C. The chemisorbed hydrogen hydrogenates the chemisorbed carbon monoxides to form hydroxycarbene. After eliminating water, a C – C bond is formed between the two hydroxymethylene groups.

A



B



C

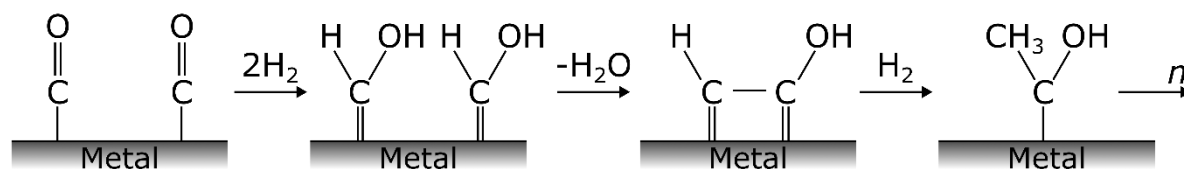


Figure 1-5. Chain growth pattern during the Fischer-Tropsch process of the carbide mechanism (A), CO insertion mechanism (B), and hydroxycarbene mechanism (C). R in panel B represents an H or alkyl group. Reproduced from reference⁴⁹

Electrochemical reduction at room temperature is another standard method to reduce CO₂. Under this condition, the CO formation rate is not as high as the high-

temperature electrolysis. However, the low temperature allows more intricate chemistry to occur. Consequently, high-value products such as ethylene or ethanol can be generated by room-temperature CO_2 electrolysis with specific catalysts. In the next section, the electrocatalytic reduction of CO_2 will be discussed in detail.

1.3 Electrocatalytic reduction of CO_2

1.3.1 Overview and basic concepts

The electrocatalytic reduction of CO_2 can be classified as homogeneous, where the catalysts and the reactants are in the same phase, or heterogeneous, where the components exist in different phases (Figure 1-6). Homogeneous catalysis electrochemical reduction of CO_2 involves both CO_2 and the catalyst dissolved in the working electrolyte, which can either be an organic solvent or water. In this approach, the catalyst acts as a shuttle to facilitate the electron transfer between the electrode and the substrate, lowering the activation barrier. On the other hand, heterogeneous electro-reduction of CO_2 involves solid catalysts immobilized on the electrode surface. The electrode material itself can be the catalyst for the reaction by providing a favorable surface for the substrate to bind, facilitating electron transfer, and lowering the activation barrier. Other immobilization strategies include physical bonding (drop-casting) or chemical bonding (covalent bonding) of the catalyst onto the surface of the electrode.

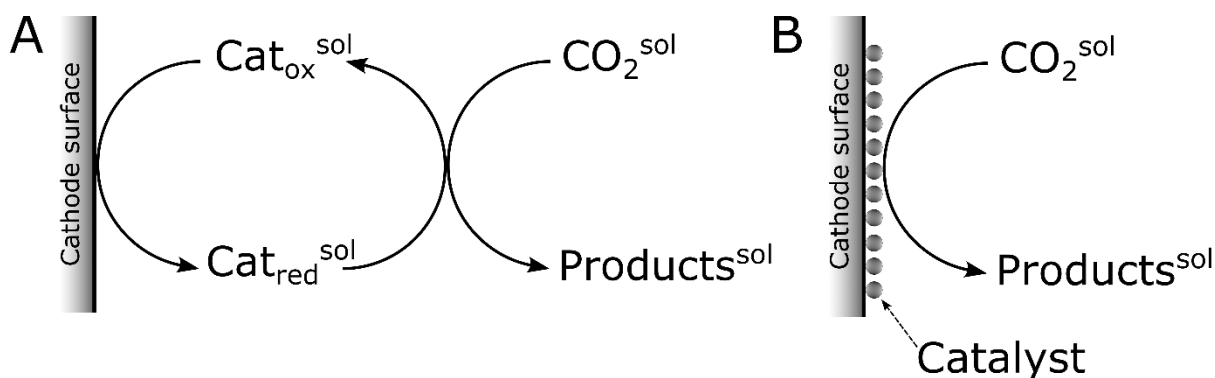


Figure 1-6. Homogeneous **(A)** and heterogeneous **(B)** electrocatalysis for the reduction of CO_2

In the homogeneous reduction of CO_2 , inert working electrodes (glassy carbon, platinum) are typically used in a static cell. The cell can contain one compartment (Figure 1-7A) or two compartments with a membrane or a frit separating the working and the counter sides (Figure 1-7B). A similar setup can be used with heterogeneous conditions. Under this configuration, diffusion is the primary mode of mass transport between the electrode surface, the catalysts, and the substrates. In addition, the available CO_2 is confined by the amount of CO_2 dissolved in the electrolyte. As a result, when catalysis is fast, the lack of supplied CO_2 or the slow rate of mass diffusion can be the limitation of the reaction. A flowing configuration can overcome these limits: electrolyte flow induces the convection mass transport mode, and CO_2 can be supplied

externally and flow into the cell where the reaction occurs (Figure 1-7C). To further increase the availability of CO_2 , a flowing setup with a gas diffusion electrode can be employed (Figure 1-7D). Gaseous CO_2 and liquid electrolytes are flown on opposite sides of a gas-permeable electrode, and CO_2 reduction happens at the interface of the gaseous CO_2 , the liquid electrolyte, and the solid catalyst. While a flowing configuration can be employed both heterogeneously and homogeneously, its primary use is for a heterogeneous system, as diffusion limit and CO_2 supply are more pronounced problems in fast and active heterogeneous catalysis.

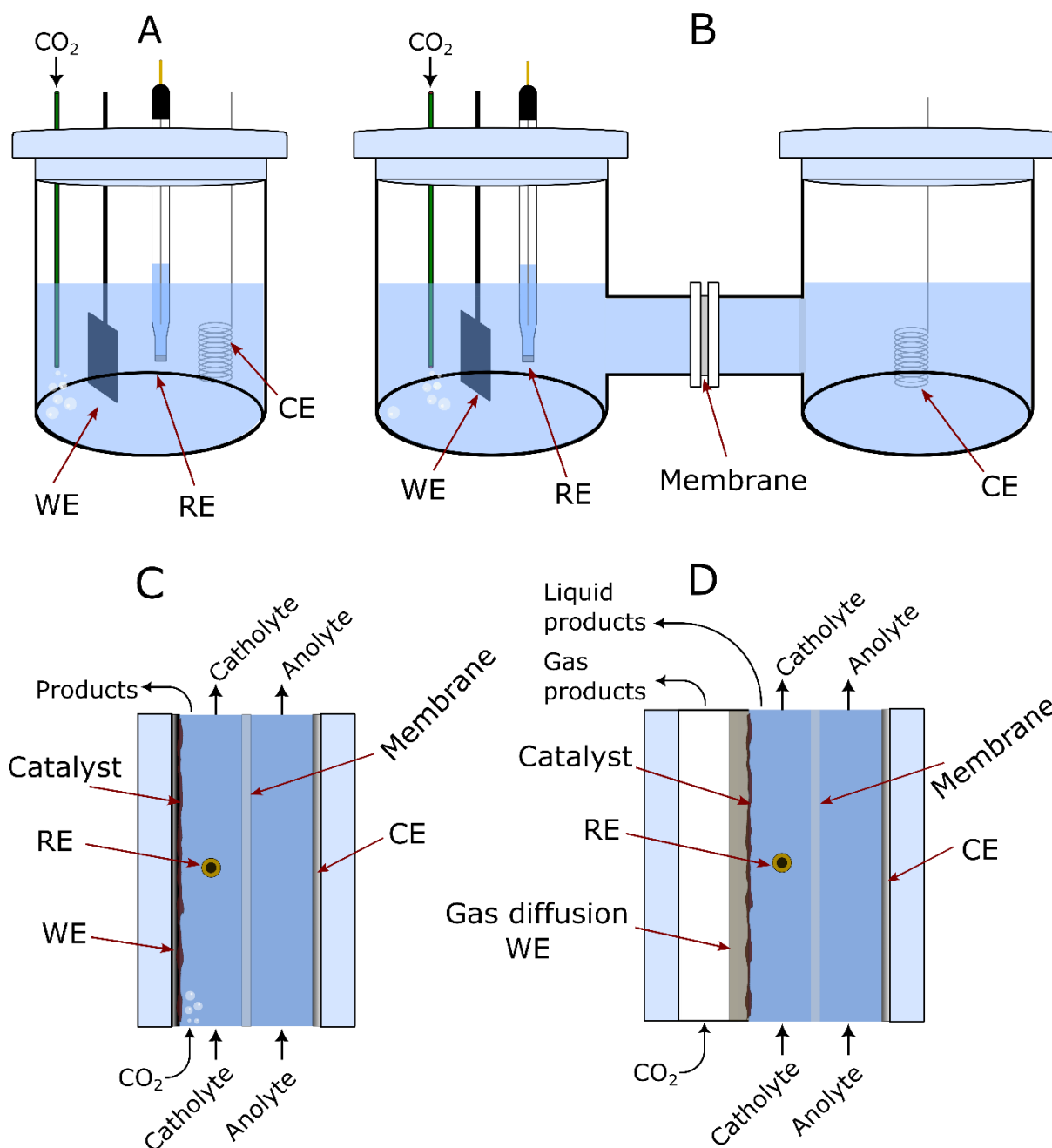


Figure 1-7. Types of electrochemical cells generally used for CO_2 reduction: **(A)** One-compartment static cell, **(B)** Two-compartment static cell, **(C)** Liquid flow cell, and **(D)** Flow cell with a gas-diffusion electrode. WE, CE, and RE stand for working electrode, counter electrode,

and reference electrode, respectively.

A benchmarking process is necessary to accurately characterize an electrocatalyst for CO₂ reduction and compare it with different species. Overpotential (η) and turnover frequency (TOF) are related parameters that reflect the intrinsic properties of a catalyst. Overpotential is defined as the difference between the thermodynamic potential of a CO₂ conversion process and the applied potential. The lower the overpotential, the more efficiently the catalyst lowers the activation barrier. TOF generally refers to the number of substrates reacting per active site per unit of time. The TOF represents the activity of a catalyst, so the higher the TOF, the faster one active site can convert reactants. Overpotential and TOF are usually linked together, and their relationship will be discussed in more detail in the following section. While the two parameters help assess a catalyst, they only represent a specific reaction at specific active sites. Therefore, non-selective catalysts with heterogeneous active sites are challenging to evaluate using only overpotential and TOF. Two critical global properties to evaluate an electrocatalytic system are its selectivity and current density. The selectivity of an electrocatalyst toward a product is represented by the Faradaic efficiency (FE), which is the ratio between the number of electrons involved in generating a product used and the number of total electrons passed through the system. Proton reduction to hydrogen is the most common competing side reaction in CO₂ reduction, causing the Faradaic efficiency to be less than unity. In addition, converting CO₂ to highly-reduced molecules with multiple electron transfers may result in a non-selective distribution with a wide range of products. While the TOF represents the intrinsic activity of a catalyst, the current density can be used to evaluate the global activity of an electrocatalysis system. While a highly-active catalyst is desirable, it usually comes with a stability tradeoff. Therefore, catalyst stability is critical in judging a catalyst and is a crucial factor in practical applications.

1.3.2 Metal catalysts

Pure metals are a common type of catalyst for CO₂ reduction. This type of catalyst is often employed under heterogeneous conditions with water-based electrolytes. As solid catalysts, the activity of metal catalysts follows Sabatier's principle:⁵⁰ to work effectively, the catalyst must adsorb the substrate neither too strongly nor too weakly. In other words, the binding energy between the metal and the key intermediates of the CO₂ reduction process (CO* and H*) plays an essential role in the activity of the catalyst. Transition metals generally possess the appropriate binding energy, and their selectivity is summarized in Figure 1-8.⁵¹ When the metals bind weakly with CO*, depending on the interaction with H*, they either favor the production CO (Ag, Au, Zn) or HCOOH (Sn, Pb, Hg). If the metals bind with too CO* strongly, the production of CO* from CO₂ can poison the catalyst, resulting in low CO₂-reducing activity, as in the case of Pt, Ni, or Pd. Cu is unique since it interacts with CO* and H* with intermediate binding energy. As a result, the intermediates can stay on the metal surface long enough to form products with multiple C – C bonds without poisoning the catalyst.

From the first work by Hori and co-workers in the 1980s^{52,53} where they observed C_{2+} molecules as products of CO_2 reduction on metallic copper, copper-based catalysts have been studied extensively.⁵⁴ Multiple C_{2+} species were identified as products of the electrochemical reduction of CO_2 , including ethylene and propylene as the majority species.⁵⁵ A variety of strategies were employed to improve the performance of Cu, including tuning the chemical composition of Cu to improve ethanol selectivity,⁵⁶ current density, overpotentials, and stability. While copper can produce C_{2+} products efficiently, silver and gold remain among the most active metal catalysts for CO production from CO_2 .⁵⁷ However, the limited supply and high cost of noble metals hinder gold and silver from becoming the catalysts of choice to produce CO on an industrial scale.

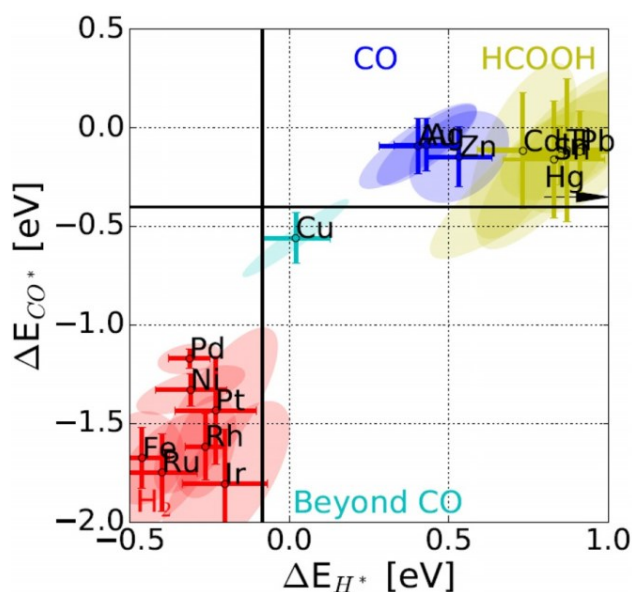


Figure 1-8. *CO and *H adsorption energy of different metals, reproduced from reference 51

Despite the excellent performance of metal catalysts, the exact mechanism of CO_2 reduction remains elusive. The concept of active sites in heterogeneous catalysis is not as straightforward as molecular catalysts,⁵⁸ so establishing a detailed mechanism for a reaction is an intricate task. The challenge of determining the reaction mechanism is exacerbated in the case of copper producing C_{2+} products, as the process involves multiple intermediates step. In particular, reducing CO_2 to C_{2+} molecules on copper is a dynamic process as it consists of restructuring copper during catalysis.⁵⁹⁻⁶¹ This evolution of the catalytically active sites renders constructing a comprehensive mechanistic model a complicated task. Therefore, detailed mechanisms derived from catalysts' well-defined active sites, such as molecular catalysts, could better the understanding of metal catalysts and inspire the rational design of efficient metal catalysts for CO_2 reduction.

1.3.3 Homogeneous molecular catalysts

1.3.3.1 Appeals for homogeneous molecular catalysts

Transition metal molecular complexes were one of the first known species to catalyze CO₂ reduction efficiently under homogeneous conditions.⁶² Unlike metals or composite materials, the structure of molecular catalysts can be accurately characterized, and their active sites are well-defined. The electrochemical responses of molecular catalysts under homogeneous conditions can be described precisely with advanced electrochemical methods.⁶³ Coupled with spectroscopy techniques to monitor the oxidation state, structure, and intermediate species, homogeneous molecular catalysts provide the ideal platform for the detailed study of CO₂ reduction mechanisms. Establishing structure-activity relations allows the rational design of catalysts with appropriate substituents to tune the catalytic performance.⁶⁴ Moreover, the well-defined metal active sites of molecules maximize the utilization of metal atoms since all metal atoms can be catalytically active during operation. In addition, some of the most active molecular catalysts are made of Earth-abundant, such as iron, carbon, and hydrogen, making large-scale implementation less challenging. Therefore, the study of molecules in solutions is valuable for the development of electrochemical CO₂ reduction catalysts.⁶⁵

Many molecular families, including pyridines,⁶⁶ cyclam,⁶⁷ porphyrin⁶⁵, and phthalocyanine (Pc)⁶⁸ can efficiently catalyze the CO₂ reduction reaction. However, porphyrin (Figure 1-9A) and phthalocyanine (Figure 1-9B) are the two macrocycles that stand out due to their exceptional performance.⁶⁸ Iron tetraphenyl porphyrin (FeTPP), where four phenyl rings are attached to the R positions indicated in Figure 1-9A, is one of the most efficient and extensively studied species. In the following section, FeTPP and its derivatives are discussed to demonstrate various aspects of homogeneous molecular catalysts for CO₂ reduction.

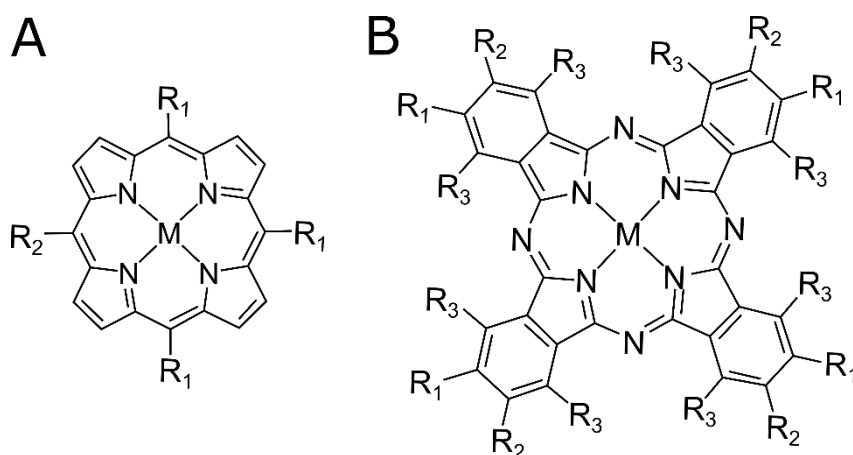


Figure 1-9. Structures of metal porphyrin (A) and metal phthalocyanine (B)

1.3.3.2 Catalyst benchmarking: overpotential, and turnover frequency calculation

By definition, the TOF at a specific overpotential can be calculated by performing electrolysis at the desired potential, quantifying the obtained products after a certain period, and determining the number of catalytically active sites. However, this meticulous process is prone to errors from secondary phenomena, including ohmic losses, substrate consumption, catalyst self-inhibition, and catalyst deactivation.⁶⁹ Savéant and colleagues have developed and proposed the foot-of-the-wave analysis based on non-destructive cyclic voltammetry (CV) to estimate the TOF of a catalyst.^{63,70} At a sufficiently low current and high scan rate, the analysis can avoid side phenomena, giving values close to those obtained from bulk electrolysis experiments.^{64,71} The rate constant of the reaction can be derived from the linear relation between the catalytic current i and the overpotential ($\eta = E - E_{cat}^0$):

$$\frac{i}{i_p^0} = \frac{2.24 \sqrt{\frac{RT}{F\nu}} k_{cat} C_{cat}^0}{1 + \exp\left[\frac{F}{RT}(E - E_{cat}^0)\right]}$$

where i is the catalytic current in the presence of CO₂, i_p^0 is the reduction peak current without CO₂, ν is the scan rate, C_{cat}^0 is the initial concentration of the reactants (CO₂), F is the Faraday constant, R is the gas constant, T is the absolute temperature, E is the applied potential, and E_{cat}^0 is the standard potential of the reversible reduction peak of the active form of the catalyst. From the rate constant, the maximum TOF_{max} can be calculated:

$$TOF_{max} = k_{cat} C_{cat}^0$$

The maximum TOF only depends on the rate constant and the initial concentration of CO₂. This value is reached when $\eta \geq E_{CO_2/CO}^0 - E_{cat}^0$. In the catalytic Tafel plot (logTOF vs. η - Figure 1-10A), this region is represented by the horizontal part, where logTOF equals logTOF_{max} and is independent of overpotential. The linear region of the plot can then be constructed following the equation:

$$\log TOF = \log TOF_{max} - \frac{F}{RT \ln 10} (E_{CO_2/CO}^0 - E_{cat}^0 - \eta)$$

The minimum logTOF₀ when η equals zero can be derived from this equation. From the catalytic Tafel plot, a catalyst can be assessed using two factors: the logTOF_{max} and effective overpotential at which the logTOF_{max} is achieved ($\eta' = E_{CO_2/CO}^0 - E_{cat}^0$). The higher logTOF_{max} and the lower η' , the more active and more efficient the catalyst is (Figure 1-10B).

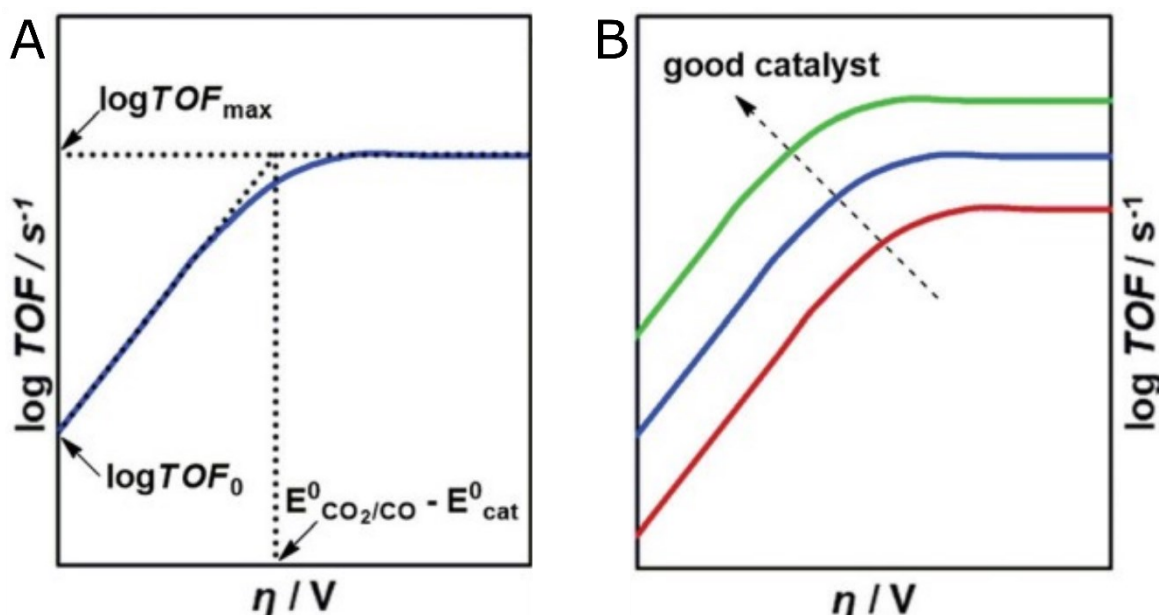


Figure 1-10. Catalytic Tafel plot with $\log TOF$ and overpotential η , reproduced from reference 71

1.3.3.3 CO_2 -to- CO performance and mechanism of FeTPP

Study on metal porphyrins for the electrochemical reduction of CO_2 date back to the late 70s,⁷² and Savéant and co-workers has contributed extensively to the understanding and development of FeTPP as a catalyst for CO_2RR . In their early study, the authors pointed out that in an aprotic solvent like dimethylformamide (DMF), the active species was the triply reduced $Fe(0)$ -TPP, as the catalytic wave coincided with the $Fe(I)$ - $Fe(0)$ wave in the cyclic voltammogram (Figure 1-11A and B).^{73,74} Proton source is a crucial factor in homogeneous CO_2 reduction by FeTPP, and weak Bronsted acids, including water, trifluoroethanol, and phenol (PhOH), significantly enhanced catalysis.^{74,75} Figure 1-11B demonstrates this phenomenon, where without CO_2 , the $Fe(II)$ species got reduced to $Fe(I)$ at -0.8 V vs. standard hydrogen electrode (SHE), and the $Fe(I)$ species subsequently got reduced to $Fe(0)$ at a more negative potential (-1.4 V vs. SHE). In the presence of CO_2 , and phenol as a proton source, a substantial increase in current and a change in the wave's shape were observed at the same position of the $Fe(I)/Fe(0)$ wave. The electrolysis experiment at -1.46 V vs. SHE ($\eta' = 0.74$ V) showed the product to be CO , with a $\log TOF_{max}$ of 2.75, and the Faradaic efficiency ranging from 100% to 94%, depending on the amount of PhOH.⁶⁴ Subsequent studies provided a detailed analysis of the CO_2 -to- CO reduction mechanism with FeTPP using cyclic voltammetry.^{63,76} By performing CV at various PhOH concentrations, the authors determined the reaction of CO_2 was first-order, while the reaction order with PhOH was first at low concentrations and second at high concentrations. Figure 1-11C illustrates the proposed catalytic cycle of CO_2 to CO with all intermediate steps. Upon the reduction of the initial $Fe(II)TPP$ to $Fe(0)TPP$, the $[Fe(0)-CO_2]^{2-}$ adduct is formed. The majority of this species exists in the form of $[Fe(I)-CO_2]^-$, as $Fe(I)$ is the dominant resonant structure, per DFT calculation. The nature of the reduced iron porphyrin is a matter of debate, as DeBeer and co-workers recently proposed that the second and

third electrons injected in $[\text{Fe}^{\text{III}}\text{TPP}]^+$ are localized on the porphyrin ring rather than on the metal.⁷⁷ Therefore, they formulated the two- and three-electron reduced species as $[\text{Fe}^{\text{II}}\text{TPP}\cdot]^-$ and $[\text{Fe}^{\text{II}}\text{TPP}\cdot\cdot]^{2-}$. A PhOH molecule forms a hydrogen bond with the bound CO_2 intermediate, and the C – O bond is broken upon a proton transfer of another PhOH molecule. This step involves a proton-coupled intermolecular electron transfer combined with the C – O bond cleavage. The C – O bond cleavage is the rate-determining step: at low acid concentrations, the reaction rate is second-order, and at higher concentrations of acid, this step becomes fast enough to change the reaction rate to first-order. A strong acid would not work because the proton reduction would be more favorable, and the strong acid can decoordinate the metal complex itself. The final step consists of a one-electron reduction of the $\text{Fe}(\text{II})\text{CO}$ species, releasing the bound CO molecule and returning two $\text{Fe}(\text{I})$ complexes, completing the catalytic cycle.

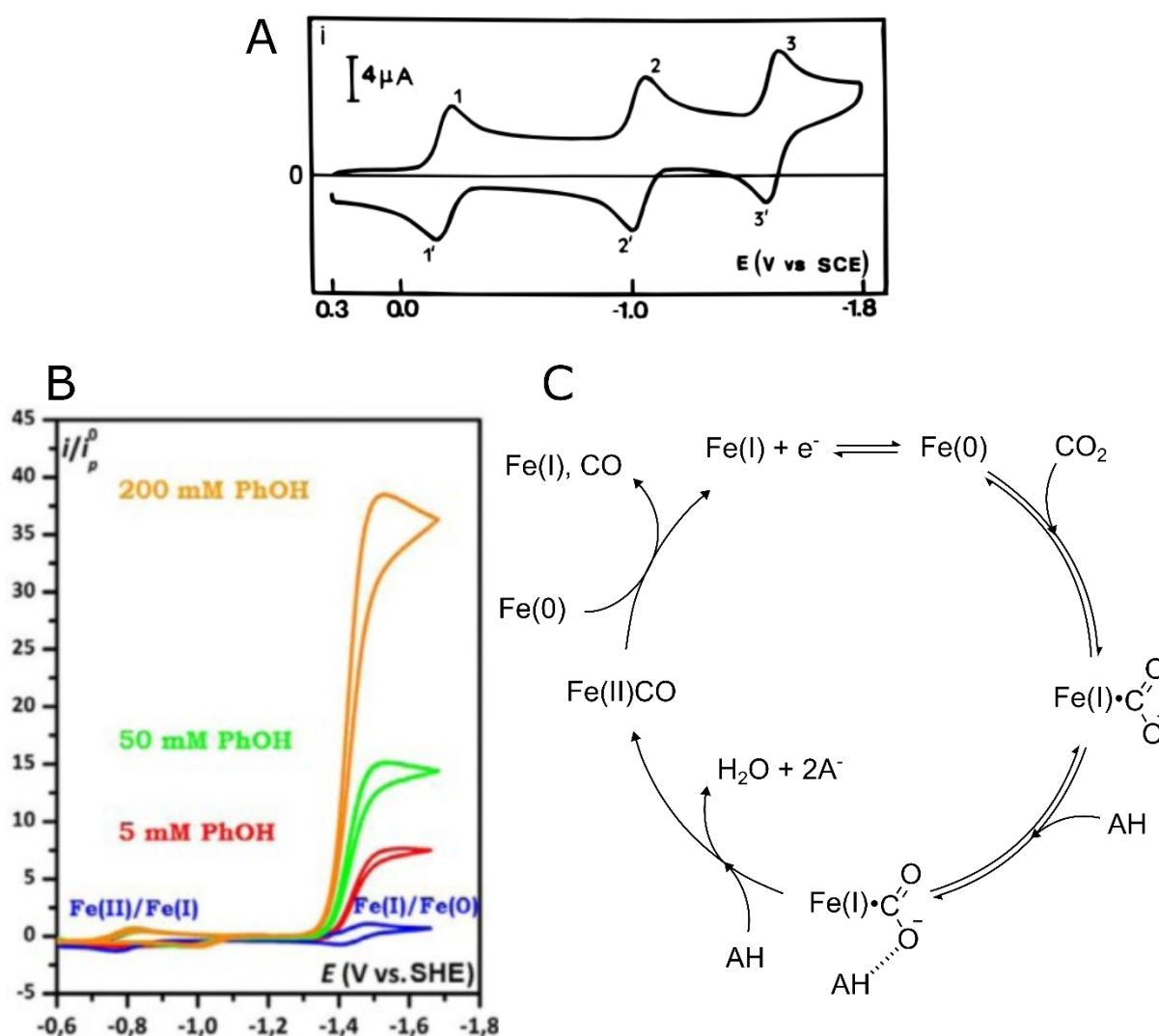


Figure 1-11. **(A)** Cyclic voltammogram of $\text{Fe}^{\text{III}}\text{TPP-Cl}$ (1 mM) in $\text{DMF} + 0.1\text{M NEt}_4\text{ClO}_4$ on a glassy carbon electrode under inert gas. **(B)** Cyclic voltammograms of FeTPP (1 mM) in $\text{DMF} + 0.1\text{M } n\text{-Bu}_4\text{NBF}_4$, in the absence (blue) and presence of 0.23M CO_2 and increasing amounts of PhOH (red 5 mM, green 50 mM, orange 200 mM) on a carbon electrode at 21°C . **(C)** Catalytic cycle of CO_2 -to- CO conversion. Reproduced from references 64 and 74

1.3.3.4 Influences of ligands on FeTPP: proton source

A significant appeal of molecular catalysts is the ability to precisely tune the metal active site's chemical environment. The beneficial effect of phenol addition to the organic electrolyte inspired the synthesis of a FeTPP-(OH)₈ species, where eight -OH groups were attached to the *ortho* positions of the four phenyl rings.⁷⁸ The -OH functional groups serve as the internal proton source for the CO₂-to-CO catalysis, delivering considerably higher local proton concentration than adding acid to the bulk electrolyte. The electrolysis in CO₂-saturated DMF/H₂O (2 M) showed over 90% Faradaic efficiency for CO with a current density of 0.31 mA/cm² at -1.16 V vs. normal hydrogen electrode (NHE). The FeTPP-(OH)₈ catalyst proved efficient and robust with the logTOF_{max} of 5.97 and an overpotential of 0.64 V while maintaining the selectivity with no observable degradation. Control experiments with FeTPP-(OCH₃)₈ and unmodified FeTPP with phenol addition were performed to further characterize the -OH substituents' contribution. FeTPP-(OCH₃)₈ showed a lower logTOF_{max} of 2.7 and a higher overpotential of 1.00 V compared to the -OH counterparts, emphasizing the importance of the -OH groups. Another study by Warren and a co-worker showed when there is only one -OH functional group, the activity of FeTPP-(OH) considerably decreases, with a logTOF_{max} of 2.1 and overpotential of 0.91 V.⁷⁹ Comparing the reaction rate of FeTPP-(OH)₈ with unmodified FeTPP with 4 M PhOH addition showed that the eight phenolic groups produced an equivalent of around 150 M PhOH in the bulk electrolyte.

Subsequent studies showed that the reduction mechanism on FeTPP-(OH)₈ differs from the unmodified FeTPP.^{80,81} In particular, the phenolic groups play two roles: a proton relay and an H-bond donor. The first adduct Fe(0)-CO₂ is stabilized by forming an H-bond with the -OH groups. Then the groups act as a proton relay in subsequent protonation and cleavage step. Unlike the mechanism of the unmodified FeTPP, the second electron transfer takes place before the C – O bond cleavage due to the strong stabilizing effect the -OH groups have on the intermediate adduct. Interestingly, external proton sources play an essential role in catalysis. When 3 M PhOH was used, the observed catalytic enhancement (logTOF_{max} = 3.8 and η' = 0.66 V) was more modest compared to when H₂O was used (logTOF_{max} = 5.97 and η' = 0.64 V). This implies competition happening between the phenolic functional groups and the PhOH molecules in the bulk electrolyte.

In addition to the through-space effects (H bond and proton donors), the electron-withdrawing nature of the -OH groups contributes to lowering the overpotential. This inductive effect was further explored by adding ten fluorine atoms to two opposite phenyl rings of FeTPP, keeping the -OH groups in the *ortho* positions of the two other rings (Figure 1-12B).⁸¹ Compared to FeTPP-(OH)₈, the addition of ten fluorine atoms decreases the overpotential (0.59 V vs. 0.64 V), but also reduces the logTOF_{max} (5.97 vs. 4.0). The inductive effect moves the standard potential to the positive direction, but it also lowers the electron density around the metal center, slowing down the electron

transfer process between CO₂ and the catalyst.

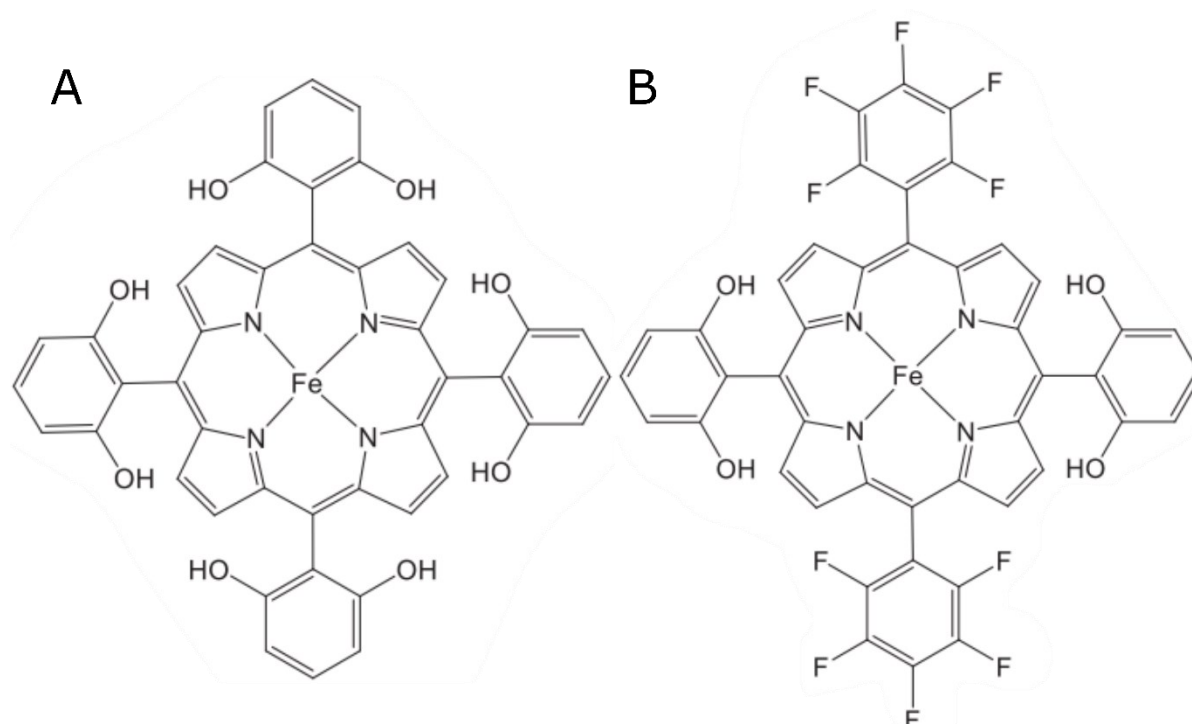


Figure 1-12. Structure of **(A)** FeTPP-(OH)₈, **(B)** FeTPP-(OH)₄F₁₀, reproduced from reference 82

1.3.3.5 Influences of ligands on FeTPP: second sphere interaction

The intermediates' stabilization effect can be exploited by designing functional groups capable of forming hydrogen bonds with metal-CO₂ adduct or with external proton sources. Attaching an amine group in the *ortho* position of the phenyl ring of a FeTPP molecule resulted in a higher log(TOF_{max}) (4.02) but also higher overpotential (0.76 V) compared to an unmodified FeTPP (log(TOF_{max}) = 3.01 and η' = 0.74 V).⁸³ However, when a -NH₂ group was placed in the *meta* position instead of *ortho*, its effect on both overpotential (0.82 V) and activity (logTOF_{max} = 3.4) was worse than its *ortho* counterpart, highlighting the importance of the functional groups positioning. Another study by Nocera and co-workers presented an FeTPP species modified with a more intricate guanidinium group to stabilize the adduct.⁸⁴ Although theoretical calculation showed a thermodynamically favored stabilization effect of the functional group, the catalytic activity was poorer (logTOF_{max} = 2.47 and η' = 0.77 V) compared to a simple amino function. The authors suggested that the dibenzofuran part did not provide an appropriate distance for the guanidinium to stabilize the intermediate.

A comprehensive study by Chang and co-workers underlined the impact of the positioning of functional groups.⁸⁵ They compared four versions of FeTPP derivatives bearing amide pendants at various positions of the metal center, as shown in Figure 1-13A. All candidates improve the catalytic activity, while there are only slight changes with the overpotential. The functional groups in the *ortho* position performed better than in the *para* position, and the amide groups at the more distanced place were

more active than the ones nearer to the phenyl rings of the FeTPP. Therefore, the best catalyst in the study was Fe-*ortho*-2-amide, with $\log\text{TOF}_{\text{max}}$ of 6.74 and overpotential of 0.80 V. In the same approach, Dey and co-workers synthesized FeTPP derivatives with four amide functional groups on the same side.⁸⁶ This catalyst had higher activity ($\log\text{TOF}_{\text{max}} = 5.71$) and lower overpotential (0.62 V) when performing catalysis in acetonitrile with 3 M PhOH. This result indicated that the number of functional groups could also influence the catalytic system.

Inspired by this approach, Aukauloo and colleagues employed a FeTPP derivative with four urea groups on the opposite sides of the porphyrin plane (FeTPP-Ur, Figure 1-13B), providing two points for hydrogen bond formation. This species considerably decreased the overpotential (0.43 V) while inducing a modest increase in the $\log(\text{TOF}_{\text{max}})$ (3.83). A control experiment was done with a FeTPP species containing amide groups, which serve as single-point hydrogen bond donors. A similar $\log(\text{TOF}_{\text{max}})$ (3.85) was obtained, but the overpotential (0.63 V) was higher than that of the urea species, underlying the crucial role of the multiple points hydrogen bond donors.

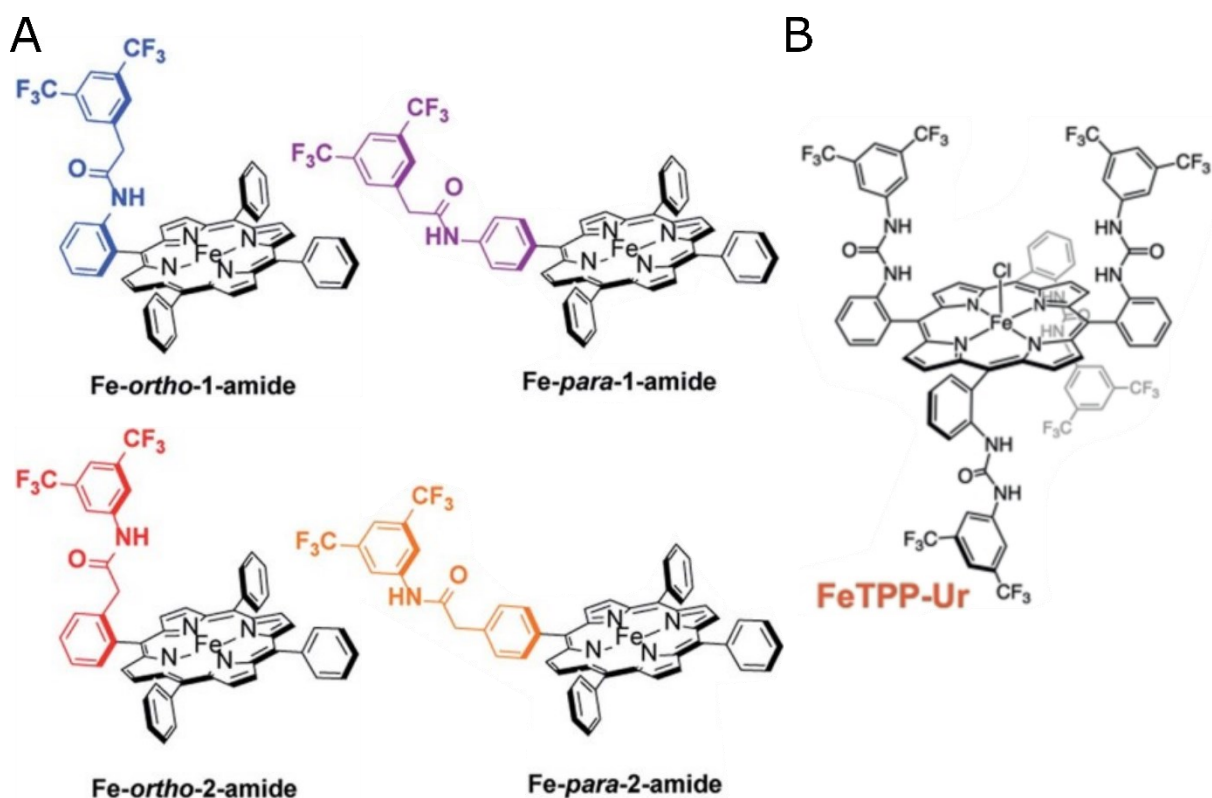


Figure 1-13. Structure of different modified FeTPP catalysts for hydrogen bond stabilization effect, reproduced from reference 85 (A) and reference 87 (B)

1.3.3.6 Influences of ligand on FeTPP: electrostatic interaction

Introducing charged functional groups to a FeTPP molecule can induce electrostatic interactions between the charged groups and the reaction intermediates. Regarding

this approach, Savéant and co-workers reported FeTPP derivatives grafted with four trimethylammonium groups.⁸⁸ In accordance with the result from FeTPP with hydrogen bond donors, the charged groups performed best in *ortho* positions, substantially lowering the overpotential (0.25 V) and increasing the catalytic activity of the catalyst ($\log\text{TOF}_{\text{max}} = 6$). Catalysis was still enhanced when the charged groups were in *para* positions (overpotential = 0.57, $\log\text{TOF}_{\text{max}} = 4.4$), though the effectiveness was lower than the *ortho* counterparts. Aukauloo and colleagues corroborated the positive effects of charged substituents. They found that a FeTPP species having four combined charged groups (methylimidazolium) and H-bond donor groups (amido) improved both the overpotential (0.37 V) and the $\log\text{TOF}_{\text{max}}$ (6.0).⁸⁹ The cationic functional groups also make the iron complex soluble in water, which can serve as an electrolyte and a proton source. In a water-based electrolyte, both iron porphyrin derivatives from the groups of Saveant⁸² and Aukauloo⁸⁹ resulted in high CO-selectivity (over 90%), low overpotential, and relatively good stability. However, incorporating negatively charged functional groups, such as sulfonate, increased the overpotential (0.74 V) and decreased the catalytic activity (3.6).⁸⁸ Another study using FeTPP with sulfonic acid groups confirmed this observation.⁸⁴ This result was attributed to the repelling interaction between the negatively charged function groups and reaction intermediates.

1.3.3.7 Bi-metallic complexes

While ligand modification is the typical strategy to tune the activity of a molecular catalyst, the nuclearity can also be modified to influence the catalysis. Inspired by the carbon monoxide dehydrogenase enzyme, Naruta and colleagues linked two FeTPP molecules using a phenyl linker, creating a dimer species with two metal centers facing each other (Figure 1-14). The Fe—Fe distance depends on whether the two monomers are connected via *ortho* or *meta* positions on the phenyl linker. The authors found that the *ortho* configuration, having a Fe—Fe distance of 3.2 to 4.0 Å, showed the best catalytic behaviors ($\log\text{TOF}_{\text{max}} = 4.3$, $\text{FE}_{\text{CO}} = 95\%$, and overpotential = 0.71 V).

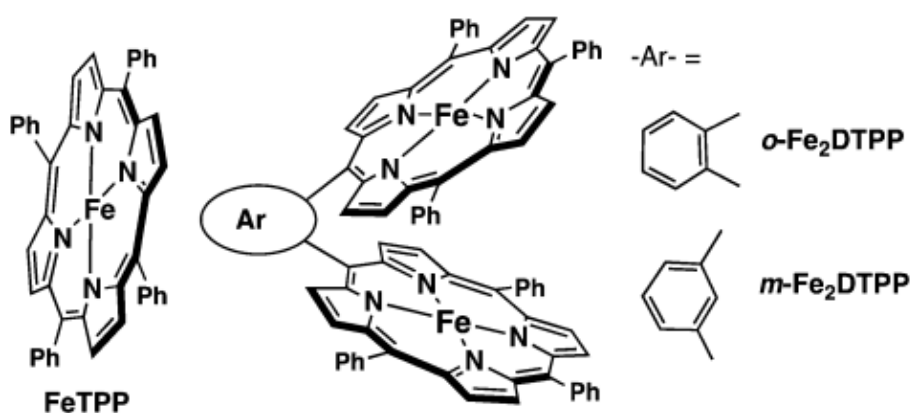


Figure 1-14. Structure of FeTPP dimer, reproduced from reference 90

1.3.3.8 Limitations of homogeneous molecular catalysts

As mentioned earlier, homogeneous molecular catalysts, having well-defined active sites and established electrochemical methods, are straightforward for studying the structure–reactivity relationships. This relationship allows the determination of detailed mechanisms, enabling precise chemical tuning around the active center. However, the current densities in most homogeneous systems are usually in the range of a few milliamperes per centimeter square, which is two orders of magnitude lower than the industry-relevant value.⁹¹ In addition, common molecular complexes, such as porphyrin and phthalocyanine, are generally only soluble in an organic solvent, complicating the scaling-up process. While water-soluble species may alleviate this problem, in a homogeneous system, only a minor amount of catalysts near the electrode surface is active - an inefficient use of catalysts. Moreover, despite the high selectivity, homogeneous molecular catalysts are mostly limited to producing CO and HCOOH.²⁵ Coupled with technical challenges like product separation, CO₂ conversion efficiency, and catalyst stability, homogeneous molecular catalysis is an unlikely candidate for industrial-scale CO₂ utilization solutions. Nonetheless, the fundamental insights gained from studying molecular species can play an essential role in better understanding and optimizing other catalytic systems.

1.3.4 Heterogeneous reduction of CO₂ by molecular catalyst

1.3.4.1 Appeals for heterogeneous molecular catalyst

The heterogenization of molecular macrocycles helped to increase the catalytic activity to meet the requirements of industrial applications.^{92–95} Like homogeneous conditions, porphyrin and phthalocyanine are the two most notable families of molecular catalysts under heterogeneous conditions. The heterogenization strategy includes physical adsorption by drop-casting a mixture of catalyst, support, and binder on the electrode surface; or chemical grafting of molecules directly on an electrode. Since the catalysts are immobilized on the surface of the electrode, catalyst diffusion is eliminated, minimizing the mass transport limitation. The immobilization of catalysts also removes the need for the separation of products and catalysts, simplifying the product collection step. As molecular catalysts are generally not soluble in water, an aqueous electrolyte can be used without the risk of catalysts leaching into the electrolyte. Compared to homogeneous conditions, heterogenization can lead to changes in the nature of active sites, where the behavior of molecules resembles a metal species.⁹⁶ Overall, the same catalyst under heterogeneous conditions can operate with a different activity, stability, and reaction mechanisms compared to under homogeneous conditions.⁹³

1.3.4.2 Influences of metal center on phthalocyanine species

The nature of the metal center in porphyrins and phthalocyanines plays a crucial role

in the performance of the catalysts, similar to metals and metal complexes in homogeneous conditions. For phthalocyanine, early research⁹⁷⁻⁹⁹ found that CoPc showed the highest current density at reducing CO₂, with CO being the primary product. Other minor products were observed under specific conditions, including oxalic acid and glycolic acid in quaternary ammonium electrolyte;⁹⁷ methanol at pH lower than 4.⁹⁸ NiPc, FePc, and CuPc were active in producing CO, but their current densities were lower than that of CoPc. These observations were corroborated and expanded by two comprehensive studies of metal center effects on phthalocyanine CO₂ reduction activity, using gas diffusion electrodes in 0.5 M KHCO₃.^{100,101} In particular, Furuya and co-workers found CoPc and NiPc to be highly selective at producing CO, reaching Faradaic efficiency of 100%. Other CO-selective catalysts included FePc and PdPc, with maximum CO Faradaic efficiency of 80% at -1.5 V vs. reversible hydrogen electrode (RHE). Phthalocyanines with metal centers from group IIIA and IVA, such as Al, Sn, Pb, and In, were selective to formic acid, with the best performance of 70% at -1.6 V vs. RHE. Methane was the main product from the reduction of CO₂ on CuPc, GaPc, and TiPc, with Faradaic efficiency ranging from 30% to 40%. The authors justified their findings using electron configurations of the metal center. Specifically, they argued that depending on the nature of the electrons in the HOMO and LUMO, the mode of CO binding could differ, resulting in different product distributions ranging from HCOOH to CO and CH₄.

In the group of CO-selective metal phthalocyanines, only CoPc can reach a high current density of 50 mA/cm² at around -1.3 V vs. SHE. To get the same current density with NiPc, a potential of -1.7 V vs. SHE must be applied. FePc can produce CO selectively at -1.2 V vs. SHE with a modest current density of 15 mA/cm², but the high CO faradaic efficiency quickly decreases at more negative potential.¹⁰¹ These findings suggest CoPc is the most active CO-producing catalyst, while NiPc and FePc are promising candidates if their overpotential and selectivity could be enhanced. Recently, Berlinguette, Robert, and co-workers demonstrated the potential of CoPc by reducing CO₂ to CO at an industrially relevant current density of 150 mA/cm² in a zero-gap membrane flow reactor operating in 1M KOH.⁹² In a microfluidic reactor with 0.5 M KHCO₃, the catalysts lasted for more than 100h while keeping the current density at 50 mA/cm² and CO selectivity at 80%.

Product H ₂							Product CO		Product CH ₄		Product HCOO ⁻		
22 Ti	23 V	24 Cr	25 Mn	26 Fe	27 Co	28 Ni	29 Cu	30 Zn	31 Ga	32 Ge	33 As		
40 Zr	41 Nb	42 Mo	43 Tc	44 Ru	45 Rh	46 Pd	47 Ag	48 Cd	49 In	50 Sn	51 Sb		
72 Hf	73 Ta	74 W	75 Re	76 Os	77 Ir	78 Pt	79 Au	80 Hg	81 Tl	82 Pb	83 Bi		

Figure 1-15. Products distribution from CO₂ reduction by different metal phthalocyanines, reproduced from reference 93

1.3.4.3 Influences of metal center on porphyrin species

For porphyrin macrocycles, the effects of metal centers on CO₂ reduction catalysis activity were reported in a comprehensive study by Sakata and co-workers.¹⁰² The reactions were carried out with the metal tetraphenyl porphyrins (TPPs) immobilized on gas diffusion electrodes in 0.5 M KHCO₃. A fixed current density of 100 mA/cm² was applied, and the catalysts were in a CO₂ atmosphere at 1 or 20 atm. Similar to phthalocyanines, at atmospheric pressure, CoTPP exhibits the highest selectivity for CO at 74.8% at -0.96 V vs. Ag/AgCl, followed by FeTPP at 42.4%. ZnTPP and CuTPP showed some activity for CO reduction, while HCOOH was also observed with CuTPP. Unlike NiPc, NiTPP hardly showed any activity for CO₂ reduction and mainly produced H₂. Other porphyrins, including MgTPP, MnTPP, and H₂TPP, showed no activity for CO₂ reduction.

A recent study looked at the influences of metal centers of different protoporphyrins (PPs) on CO₂ reduction to formate.¹⁰³ Protoporphyrins are a derivative of a general porphyrin macrocycle, having two vinyl, two propionic acids, and four methyl groups attached to the ring. Rh, In, and Sn protoporphyrins were the most active species in producing formate, while Cr, Mn, Co, and Fe yielded no formate. In-protoporphyrin had the best performance, with a Faradaic efficiency of 70% in a pH of 9.6 under an applied potential of -1.9 V vs. RHE. The authors showed a reverse correlation between formate production and hydrogen evolution reaction.

					No HCOO ⁻		Minor amounts of HCOO ⁻		Major amounts of HCOO ⁻		
22 Ti	23 V	24 Cr	25 Mn	26 Fe	27 Co	28 Ni	29 Cu	30 Zn	31 Ga	32 Ge	33 As
40 Zr	41 Nb	42 Mo	43 Tc	44 Ru	45 Rh	46 Pd	47 Ag	48 Cd	49 In	50 Sn	51 Sb
72 Hf	73 Ta	74 W	75 Re	76 Os	77 Ir	78 Pt	79 Au	80 Hg	81 Tl	82 Pb	83 Bi

Figure 1-16. Formate distribution from CO₂ reduction by various metal porphyrins, reproduced from reference 93

1.3.4.4 Metal-centered and ligand-centered reduction

The influences of the metal centers on CO₂ reduction activity and selectivity are somewhat consistent across porphyrin and phthalocyanine ligands, where Co and Fe species are most selective towards CO, and In and Sn are most selective towards HCOOH. Ni was one exception, as NiPc was more active at producing CO than NiTPP. A recent study by Wang and co-workers found a modified ZnTPP to be highly selective towards CO with 95% Faradaic efficiency at -1.7 V vs. RHE in DMF/H₂O electrolyte.¹⁰⁴ Interestingly, operando X-ray absorption spectroscopy showed no change in the oxidation state of Zn. From cyclic voltammetry and chemical reduction of ZnTPP, the authors demonstrated that CO₂ reduction was ligand-centered, but Zn's role was essential as there was little to no CO₂ reduction activity with metal-free porphyrin. Another study from McCrory also displayed no edge shift in the X-ray absorption near edge structure (XANES) result during catalysis, demonstrating that the rate-determining step during CO₂ to CO catalysis on a CoPc species did not involve changing the oxidation state of the metal center.¹⁰⁵ The findings suggest that both the ligands and the metal centers play essential roles in the functioning of the molecular catalyst.

1.3.4.5 Further-than-CO reduction

While Co-based macrocycles are very selective toward CO, recent studies showed that cobalt protoporphyrin and cobalt phthalocyanine could reduce CO₂ further than CO to make CH₄ or CH₃OH. In 2015, Koper et al. used a cobalt protoporphyrin catalyst to reduce CO₂, obtaining CO as the primary product, methane as a side product, and methanol in trace amounts.¹⁰⁶ The maximum selectivity for methane reached ca. 4% at high pressure (p = 10 atm) and low pH (pH = 1). In 2019, Wang and co-workers obtained more than 40% faradaic efficiency of methanol using cobalt phthalocyanine highly dispersed on carbon nanotubes (CNTs).¹⁰⁷ The authors attributed the high performance to the highly dispersed nature of the catalyst on suitable carbon nanotube supports. Similar observations of methanol produced from CO₂ using CoPc catalysts were reported, albeit with lower methanol selectivity.^{98,108} To form further reduced species with C – C bonds, Cu macrocycles proved the most effective. However, as discussed in more detail in section 1.3.6, the molecular nature of the utilized copper species was not preserved during catalysis. These results showed that depending on the metal center and the specific experimental conditions, metal phthalocyanines and porphyrins can catalyze the multi-electron reduction of CO₂ to highly reduced products.

1.3.4.6 Influences of ligand on porphyrins and phthalocyanines species

As in homogeneous conditions, ligands surrounding the molecular macrocycles can be precisely tuned to control the binding of intermediates to optimize reaction rate and selectivity. Two early studies by Kaneko and co-workers compared the effect electron donating groups (butoxy), and electron-withdrawing groups (cyano) have on the CO₂ reduction activity of CoPc. Under applied potential of -1.3 V vs. Ag/AgCl and in phosphate electrolyte with pH of 4.4, CoPc(BuO)₈ reduces CO₂ to CO with higher turnover frequency (306 s⁻¹ vs. 15 s⁻¹) and higher CO/H₂ ratio (4.34 vs. 0.69) compared to CoPc.¹⁰⁹ Under a similar electrolyte at -1.15 V vs. Ag/AgCl, CoPc(CN)₈ was also more selective at reducing CO₂ to CO without significantly impacting the turnover frequency.¹¹⁰ The authors suggested that the electron-donating BuO improves the electron density around the metal center, facilitating the binding of CO₂ and increasing activity and CO selectivity. Regarding the effect of the electron-withdrawing group, the authors argued that the rate-determining step was changed from the catalyst's second reduction to the desorption of CO from CoPc. Other recent studies also found increased activity and CO selectivity when electron-withdrawing groups, including CN¹¹¹ and F,¹¹² are attached to CoPc catalysts. The activity enhancement results from both electron-withdrawing and electron-donating groups did not give a clear trend of the effect of substituents. The conflicting observations suggest that other factors resulting from the functional groups' addition may play a non-negligible role in CO₂ reduction activity.

In 2019, Manthiram and co-workers reported a comprehensive study on the influences of different substituents (Figure 1-17A) on cobalt porphyrin activity of CO₂ to CO reduction.¹¹³ The authors used a low catalyst loading of 0.8 nmol/cm² to minimize aggregation and quantified the electron-withdrawing character based on Hammett parameters, and Mulliken charges. With cationic substituents, the log(TOF_{CO}) reversely correlated to the Hammett σ values of the functional groups (Figure 1-17B). The correlation indicates that the stronger the electron-donating character of the substituents, the higher the turnover frequency of the catalysts. The same effect was observed with neutral and anionic functional groups. However, the trendline drastically differed from cationic species (Figure 1-17B), with catalysts having a much lower log(TOF_{CO}) despite the strong electron-withdrawing character. This phenomenon suggests that the electrostatic effect of the substituents strongly affects the performance of the catalysts, which has been observed under homogeneous conditions.⁶⁹

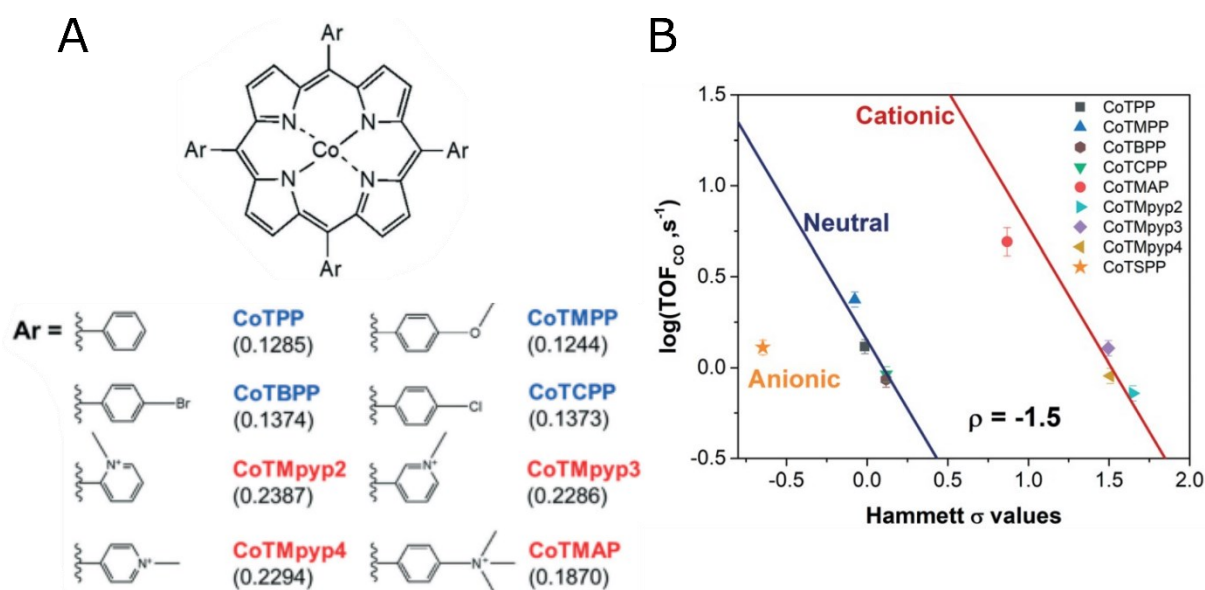


Figure 1-17. **(A)** Structures of cobalt porphyrin and its substituents **(B)** relation between Hammett values of substituents and the logarithm of the CO turnover frequency of substituted cobalt phthalocyanine (-1.02 V vs. RHE, 0.8 nmol/cm²), reproduced from reference 113

Besides induction and electrostatic effects, the steric effect of ligands of a molecular macrocycle can change how the catalyst interacts with the electrode surface. Officer and co-workers reported in 2019 that bulky alkoxy groups grafted on cobalt phthalocyanine reduce the aggregation of catalysts on the electrode surface, resulting in the increase of the TOF_{CO} compared to unmodified CoPc.¹¹⁴ Depending on the ligands, a molecular macrocycle can also serve as a precursor to creating highly dispersed metal catalysts. In 2012, Kenis et al. studied the CO_2 to CO catalytic activity of organometallic silver with different ligands.¹¹⁵ While no organometallic species perform better than the 70-nm-silver-nanoparticles, AgPc, Ag pyrazole, and Ag 3,5-diamino-1,2,4-triazole showed increased CO current density and selectivity. This improved performance happened at a much lower mass loading of nanoparticle silver, demonstrating a much more efficient use of the metal. Another study obtained active copper electrode materials via electrodeposition¹¹⁶ from a copper cyclam solution. When a fluorine-doped tin oxide electrode was subjected to multiple cyclic voltammetry cycles from -0.3 V to -2.0 V vs. Fc^+/Fc in a DMF/H₂O (97/3 v/v) containing 1.3 mM Cu(cyclam), a nanoparticle composite Cu materials with the organic ligand attached was deposited on the electrode. This functionalized electrode can produce HCOOH at 90% faradaic efficiency in a similar CO_2 -saturated DMF solution without the Cu(cyclam) complex, demonstrating a viable pathway for tuning the catalysis properties of metal catalysts using organic ligands.

1.3.4.7 Aggregation effects and TOF calculation

Similar to the homogeneous system, the turnover frequency of a catalyst represents its intrinsic activity, providing a reliable benchmark to compare different catalysts.⁷⁰ Typical cyclic voltammograms in heterogeneous molecular catalysts are not

electrochemically reversible, making foot-of-the-wave analysis unable to derive the TOF value. Therefore, performing electrolysis, quantifying the resulting products, and determining the number of active sites are necessary steps to accurately calculate the TOF of a heterogeneous catalyst. While the concept of active sites in heterogeneous catalysis is an intricate topic,⁵⁸ for heterogenized molecular complexes, a lower limit of the TOF can be estimated by considering all immobilized catalysts on the electrode to be active. The precise number of active sites is complicated to determine due to catalyst aggregation, which could result from external factors like loading, metal center, ligands, and electrode preparation.

The aggregation effect is more pronounced in the case of phthalocyanine and porphyrins, which are planar complexes with favorable $\pi - \pi$ stacking mode.¹¹⁷ Porosity, double layer capacitance measurement, and integrating catalytic redox peak from cycle voltammetry are standard techniques to estimate the number of active sites.¹¹⁸ However, porosity and electrochemically active area do not directly correlate to the catalytically active sites, and redox peak integration can induce uncertainty from baseline correction. In some cases, CV peaks of heterogenized species are not reliable.⁹³ One study demonstrated the effect of catalyst aggregation on the performance of CoPc on CO₂ reduction by varying the catalyst loading. When CoPc surface concentration increased from 10^{-11} to 10^{-7} mol/cm², aggregate can be seen from the scanning electron microscopy (SEM) images (Figure 1-18), and the turnover frequency increased three orders of magnitudes.¹¹⁹ Under aggregation-free conditions, the current density should be proportional to the catalyst loading, and the TOF should be constant at sufficiently high overpotential.¹²⁰ Therefore, to obtain accurate TOF of heterogenized molecular catalyst, the catalyst should be investigated at low concentration with all the influencing conditions adequately declared.¹²¹ In addition to using low catalyst loading, depositing the molecular species in a highly solubilizing solvent can better disperse the catalyst. In all cases, the lower bound TOF should be reported as the aggregate-free conditions are not the desired conditions to achieve high current density and selectivity.¹¹⁹

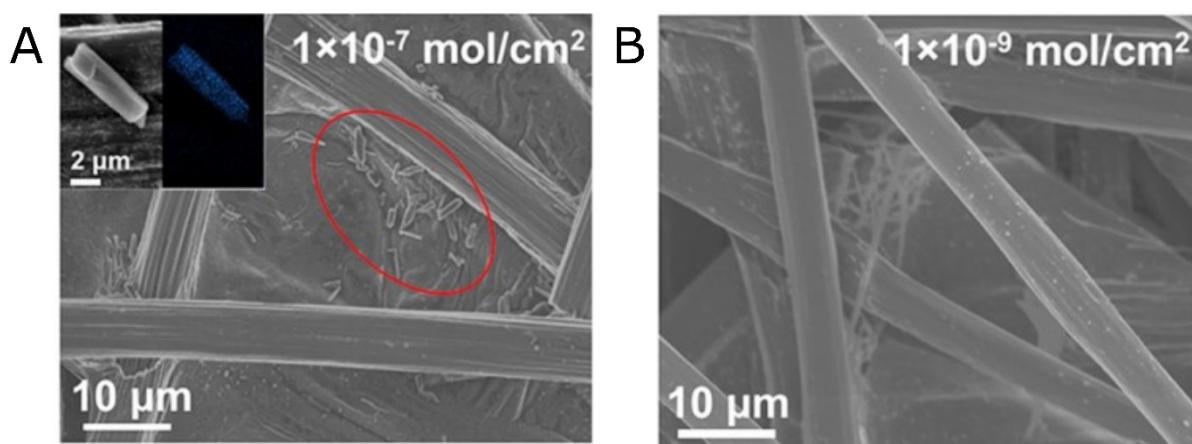


Figure 1-18. **(A)** SEM images of the CoPc-modified electrode (loading: 1×10^{-7} mol/cm²), on which crystals of CoPc are evident. The red oval highlights a region with many crystals. Inset:

High-magnification SEM image and the corresponding energy-dispersive X-ray spectroscopy mapping of Co. (B) SEM image of CoPc-modified electrode (loading: 1×10^{-9} mol/cm²) in which no crystals are evident. Reproduced from reference 119

1.3.4.8 Electrode support effects

The interaction between the electrode and the immobilized catalyst layer significantly influences their CO₂ reduction performance, a critical difference between heterogeneous and homogeneous catalysis. A wide range of factors affects the electrode-catalyst interaction: the nature of the electrode, the conductive support materials, the nature of the catalyst, and the immobilization method. Koper and co-workers conducted a systemic study assessing the impact of different carbon-based electrodes on CO₂-to-formate reduction using indium protoporphyrin (InPP).¹²² Out of the three studied materials, pyrolytic graphite substrate showed higher selectivity and reactivity than glassy carbon and boron-doped diamond, while the boron-doped diamond was the most stable. Since pyrolytic graphite has the highest electrochemically active area, it had less aggregation and was not saturated with InPP at high loading, unlike glassy carbon and boron-doped diamond. Although this study demonstrated the importance of electrode materials, the reasoning behind the observed activity difference was not clear.

The standard method of molecular catalyst immobilization is physical adsorption by drop-casting a mixture of molecular complex, conductive support, and binder onto the electrode surface. Commonly-used supports are carbon-based materials, including carbon nanotubes (CNTs), carbon black, and graphene, with CNTs generally outperforming the other materials. One study found that CoTPP displayed significantly higher current density (2.9 vs. 0.028 mA/cm²) and selectivity (91% vs. 28%) towards CO compared to the dissolved species.¹²³ When carbon black was used instead of CNTs, higher selectivity (97%) but lower current density (1.8 mA/cm²) were observed. Multiple studies corroborate the positive effect of CNTs towards CO₂ reduction with molecule macrocycles, including the increased formate current density with FeTPP,¹²⁴ increased CO current density with Co protoporphyrin¹²⁵ and CoPc, with CoPc/CNTs outperforming CoPc supported on reduced graphene oxide or carbon black.¹¹² The studies attributed the increased CO₂ reduction activity to the $\pi - \pi$ interaction between the macrocycles and the CNTs, since CNTs have the highest degree of sp² carbon in the studied species. Other beneficial factors include the high surface area and high electrical conductivity of CNTs.¹¹² In the studies of InPP,¹²² CoPP,¹²⁵ and CoPc,¹¹² the authors pointed out the influence of catalyst aggregation on the performance of the catalysts. This observation emphasizes the importance of decoupling the effects of increased dispersity and the intrinsic electronic interactions between the support and the catalyst. Besides physical adsorption, molecular complexes can be bonded to the electrode surface via covalent grafting to improve the catalytic performance and catalyst stability.¹²⁶

In addition to conductive carbon materials, polymer encapsulation is another strategy

to support catalysts on an electrode. Unlike conductive carbon materials, catalysts are typically chemically attached to the polymer support. Therefore, the support can influence the second-sphere interaction and the electronic structure of the active site, as well as control the local environment surrounding the catalysts. Poly(4-vinylpyridine) (P4VP) is a widely studied encapsulating agent for molecular macrocycles. An early study showed the CO₂-to-CO reaction was more selective and active when the CoPc catalyst was encapsulated by P4VP.¹²⁷ The authors attributed the enhancement effects of P4VP to the electron-donating nature of the axial pyridine ligand, the local proton source of the P4VP, and the increase in CO₂ local concentration. Later work by the same group of authors further optimized the reaction conditions: they found a pH of 4.4 to be best for CO production and a pH of 5 for optimal CO/H₂ selectivity.¹²⁸ The authors also found that Poly(2-vinylpyridine) (P2VP), a non-coordinating version of P4VP due to steric hindrance, performed worse than P4VP, suggesting the importance of the pyridine coordination effect. A more recent study provides a comprehensive assessment of the impact of polymer coordination on the CO₂ reduction performance of CoPc (Figure 1-19A).¹⁰⁵ The pyridine (py)-coordinated CoPc(py) and the non-coordinating polymer P2VP underperformed the coordinating polymer P4VP, indicating the combined effect of axial ligand and polymer backbone on the increased catalytic activity. When CoPc(py) was mixed with the non-coordinating P2VP, they obtained similar TOF_{CO} and FE_{CO}, suggesting that the combined effect was not synergistic.

Another study tested various polymers encapsulating InPP for formate production, including DDAB, P4VP, PEDOT/PSS, and Nafion (Figure 1-19B).¹²² Except for Nafion, all species enhanced the selectivity and current density compared to unmodified InPP. And while the P4VP species provided the highest formate selectivity, the current density was the lowest compared to the other three polymers. However, a control experiment with only P4VP showed a Faradaic efficiency of 20% for formate, which suggested the observed increase in activity may result from the independent catalysis on the polymer and the InPP.

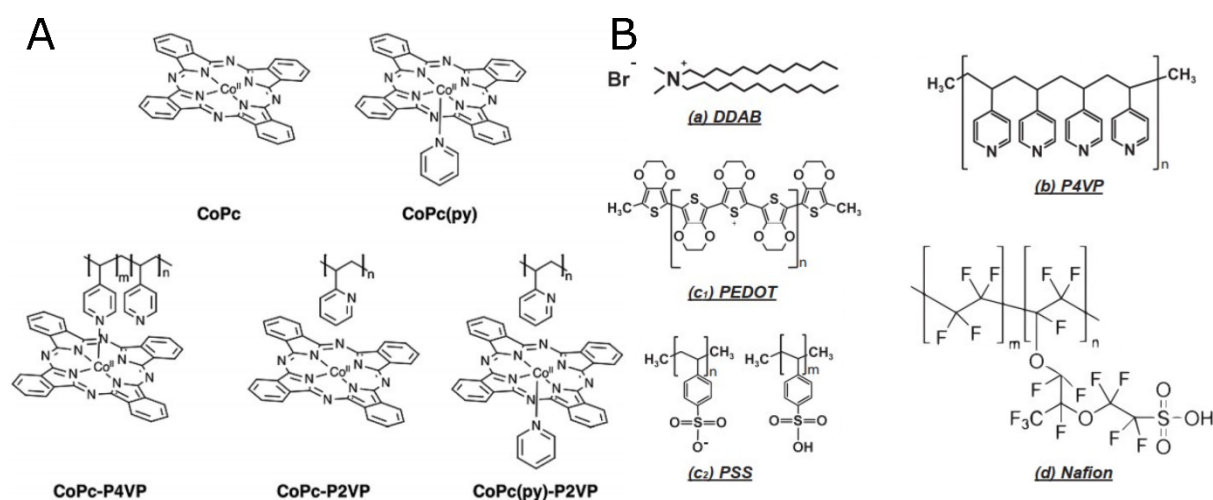


Figure 1-19. **(A)** Pyridine-based polymer encapsulation for CoPc - reproduced from reference¹⁰⁵

and **(B)** different types of polymer encapsulation for macrocycle catalyst – reproduced from reference 122

1.3.4.9 Co-catalytic systems

Heterogenized molecular complexes on catalytically active metal electrodes can work in tandem to increase the selectivity and activity of specific products. Grafting molecular ligands on metal electrodes can help stabilize and promote specific intermediates in the catalytic cycle. The highly selective nature of the molecular macrocycle can also be employed to reduce CO₂ to CO, which then gets further reduced on metal catalysts in a cascade manner. Concerning the first approach, metal-free tetra(4-aminophenyl) porphyrin ligand was electrochemically polymerized on gold substrates to enhance the catalysis of CO₂ to CO.¹²⁹ At -0.7 V vs. RHE, the modified electrode had significantly higher CO selectivity (95% vs. 25%) and current density (2.5 mA/cm² vs. 0.3 mA/cm²) compared to the unmodified gold substrate. Interestingly, when the ligand monomers were attached to the gold foil, no noticeable catalysis enhancement was observed, suggesting the importance of polymerization. The polymer layer thickness appears critical for the catalytic performance, with the optimal value at 60 nm. A similar strategy was used on gold nanoparticles with attached porphyrin ligands, and enhancement in CO production was also observed.¹³⁰ In addition to gold, porphyrin ligands can also tune the reduction of CO to C₂₊ products on copper.¹³¹ The porphyrin ligands, lying flat on the copper substrate by thiol linkers at the *ortho* position, increased the production of oxygenated species, with ethylene selectivity remaining unchanged. Interestingly, the ligand binding mode was crucial to the observed C₂₊ selectivity. When the thiol linkers were changed to the *para* position, the ligands were arranged perpendicular to the electrode, and C₂₊ products were diminished.

Regarding the approach of using metal complexes to produce CO selectively, Sargent and co-workers reported a tandem system of iron porphyrin sprayed on a copper-based gas diffusion electrode. The increase in local CO concentration near the copper sites steers the CO₂ reduction activity towards ethanol.¹³² Using a similar strategy, Buonsanti and colleagues found that a mixture of iron porphyrin and copper nanocubes adsorbed on a glassy carbon electrode produces more ethylene than the nanocubes alone.¹³³ The iron porphyrin species having the highest CO turnover frequency induces the most significant increase in ethylene generation on the copper catalyst, emphasizing the crucial role of the CO local concentration.

1.3.4.10 Limitations of heterogeneous molecular catalysts

Heterogeneous molecular catalysts generally reflect the benefits of the homogenous counterpart: having well-defined active sites, allowing for fine chemical tuning around the catalytic center. The determination of in-depth reaction mechanisms is, nonetheless, more complex. First, unlike in a homogeneous system, the cyclic voltammograms of adsorbed species often display broad, sometimes irreversible

peaks, making determining the exact oxidation states of the molecules challenging. The cyclic voltammetry response can also vary strongly depending on external factors such as the conductive carbon support, the catalyst concentration, or the solvent used for drop-casting. Furthermore, heterogeneous catalysis usually employs water-based electrolytes. While water is preferred in applied systems, it offers less control over the catalysis process since protons are typically available from the water reduction side reaction. Finally, evaluating the exact number of active sites in a heterogeneous catalysis system remains a question of debate.^{58,119} Therefore, a precise estimation of the turnover frequency is hard to achieve. In a homogeneous system, cyclic voltammetry usually exhibits well-defined and reversible waves, enabling the oxidation states of the investigated species to be determined precisely. Foot-of-the-wave analysis can make use of well-defined CV features to quickly and accurately estimate the turnover frequency. The use of organic solvents as electrolytes also offers control over the number of protons and the nature of their sources, allowing for complex analysis of a molecule's behaviors.

The heterogeneous nature means some issues related to the homogeneous system are not present, including inefficient catalyst use, water solubility, and product separation from catalysts. Heterogeneous molecular catalysts have also demonstrated industrially relevant current density and the ability to produce highly-reduced molecules like methanol and methane with modest selectivity. However, creating high-value products with C – C bonds and catalyst stability remain the two critical limitations. These two topics will be discussed in detail in the following section. Overall, heterogeneous molecular catalysts provide a bridge between fundamental study and more applied systems of metal and composite catalysts. Whether or not it applies to the industrial scale, the knowledge from studying heterogeneous molecular catalysts will be valuable for developing CO₂ utilization technologies.

1.3.5 Reduction of CO₂ to C₂₊ products by catalysts with well-defined active sites

As discussed earlier, in the scope of the CO₂ reduction reaction, C₂₊ products such as ethylene or ethanol hold special interests as they have both high value and a large market.²⁶ Forming C₂₊ products on catalysts with well-defined actives would provide a platform for a detailed mechanistic study of the process. Generating C₂₊ products primarily uses Cu-based species, but other transition metals catalysts,¹³⁴ or metal-free catalysts^{135,136}, can reduce CO₂ to C₂₊, albeit with much lower activity.

While most molecular catalysts for CO₂ reduction produce only C₁ products, there have been several reports of C – C bond formation from CO₂ using a molecular catalyst. In 2002, Fujishima and colleagues reported the presence of C₂H₄ and C₂H₆ after the electrochemical reduction of CO₂ with cobalt and copper phthalocyanine.¹³⁷ However, since the Faradaic efficiency of these highly reduced products was lower than 1%, they did not further characterize and study this aspect of their catalysts. The following

discussion focuses on examples of typical C₂+ products being formed with molecular catalysts and single-atom catalysts.

1.3.5.1 Oxalate

Oxalate is the least reduced product with a C – C bond from one electron CO₂ reduction. It can be formed by an un-catalyzed process involving two radical CO₂^{•-} anions on inert electrodes such as carbon, mercury,¹³⁸ lead, and thallium¹³⁹ with sufficiently negative potential. Transition metal complexes can also facilitate the formation of oxalate from CO₂ reduction. The first observation of oxalic and glycolic acid was reported by Tamaru and co-workers, who used CoPc and NiPc in a quaternary ammonium salt electrolyte.⁹⁷ Mononuclear complexes, including Ag and Pd-based,¹⁴⁰ Ni-based^{141,142}, and Fe-based¹⁴³ catalysts, have been reported to catalyze CO₂ to oxalate reaction in organic solvents. However, this pathway of reducing CO₂ to oxalate involves the formation of the radical CO₂^{•-} anion; hence the required reduction potential is very negative.

Another pathway includes multi-nuclear molecular complexes that form oxalate at a lower overpotential due to the synergistic effect of two or more binding sites in close proximity. Examples include polymerized rhenium complex,¹⁴⁴ bi, and tri-metal complex based on Co, Rh, Ir,^{145,146} and a binuclear ruthenium catalyst¹⁴⁷. One notable example consists of the work of Bouwman and co-workers,¹⁴⁸ where they used a di-nuclear copper complex as a catalyst to reduce CO₂ to oxalate with Faradaic efficiency of 96% at -0.03 V vs. NHE. Although the catalyst possesses two binding sites, the Cu—Cu distance is too far for the two sites to interact.

1.3.5.2 Ethylene

Copper-based molecular catalysts have been reported to reduce CO₂ to ethylene. In 2016, the groups of Brudvig and Wang¹⁴⁹ showed that CH₄ and C₂H₄ are generated on a carbon fiber electrode modified with Cu-porphyrin complex with a hydroxyl functional group. The total current density at -0.97 V vs. RHE is 7.5 mA/cm², with CH₄ and C₂H₄ faradaic efficiency of 25% and 17%, respectively. Control experiments with metal-free porphyrin ligand and Cu-porphyrin without hydroxyl functional group showed CO is the main product of CO₂ reduction. The experiments demonstrated the role of the Cu metal center and the -OH functional group in forming the C – C bond. The authors postulated the reactivity of the Cu center and the stabilizing effect of the -OH group facilitate the formation of the observed multi-carbon products, but a detailed mechanism was not provided. Finally, using X-ray photoelectron spectroscopy (XPS), transmission electron microscopy (TEM), and inductively coupled plasma mass spectrometry (ICP-MS), they showed the nature of the Cu molecular catalyst stayed unchanged before and after electrolysis.

Following the work of the groups of Brudvig and Wang, Yotsuhashi and co-workers¹⁵⁰

synthesized a crystalline copper phthalocyanine and studied its electrocatalytic activity for CO₂ reduction, as they argued that the distance between Cu atoms plays a vital role in forming C – C bond. Indeed, at -1.6 V vs. Ag/AgCl, they obtained 25% FE for C₂H₄ with a partial current density of 2.8 mA/cm². With a non-crystalline CuPc, CO was the main product of CO₂ reduction, demonstrating the role of the catalyst's crystallinity in forming the C – C bond. However, the selectivity for C₂H₄ was not maintained in electrolysis longer than 12h, indicating the poor stability of the crystal. Based on these findings, Nam and co-workers¹⁵¹ reported the activity of a di-nuclear copper complex with a Cu—Cu distance of 3.77Å for reducing CO₂ to C₁ products and C₂H₄. They demonstrate the dinuclear species yield maximum C₂H₄ at 42% Faradaic efficiency at -1.27 V vs. RHE, compared to 22% at -1.37 V vs. RHE with the mononuclear counterpart. However, they also show the effects of other parameters such as electrolyte salt and concentration, carbon support type, and electrode rotating speed affect the production of C₂H₄ at the same order of magnitude compared to monomer and dimer species.

Following the same theme, Liao et al. prepared a metal-organic framework (MOF) based on copper phthalocyanine ligands with CuO₄ node.¹⁵² The MOF exhibits a Faradaic efficiency of 50% at -1.2 V vs. RHE with a current density of 7.3 mA.cm⁻². They attribute the good selectivity to the synergistic effect between CuO₄ and CuPc, where the former has favor *CO adsorption energy to generate CO for C – C dimerization on the latter.

1.3.5.3 Ethanol and acetic acid

Although most C – C bond formations are reported on Cu-based molecular catalysts, there are a few examples of non-Cu molecular catalysts for CO₂ to C₂ products. In 2019, Roy, Schöfberger, and co-workers synthesized a fluorinated cobalt corrole molecular complex with a triphenylphosphine axial ligand and three polyethylene glycol (PEG) groups (Figure 1-20A) capable of reducing CO₂ to C₂H₅OH.¹⁵³ Using the cobalt-corrole-modified carbon paper in 0.1 M NaClO₄, CO₂ was reduced to ethanol with 48% Faradaic efficiency for five hours at -0.8 V vs. RHE. Other reduced products included methanol, formate, and acetate, with a small amount of formaldehyde and glyoxal. CO was not presented, leading the authors to propose a pathway of ethanol formation through formic acid and formaldehyde intermediates instead of the frequent CO pathway. The proposed pathway was partly demonstrated using formic acid, glyoxal, formaldehyde, and methanol as substrates, along with density functional theory (DFT) calculation. Ethanol was not generated in control experiments with similar cobalt corrole species without the polyethylene glycol substituents, demonstrating the PEG groups' crucial role in forming ethanol. Using a similar corrole ligand with a manganese metal center instead of cobalt (Figure 1-20B) as a catalyst for CO₂ reduction, the groups of Roy and Schöfberger were able to obtain acetic acid.¹⁵⁴ At -0.724 V vs. RHE, they observed 60% acetate with a specific current density of 0.570 mA.cm⁻² and a small amount of methanol. The proposed mechanism involved the binding of CO₂ and the subsequent

proton-coupled electron transfer step, converting it to an Mn-COOH species. The C – C bond formation step creates an intermediate oxalate species, which is converted to acetate by additional reduction, protonation, and dehydration steps.

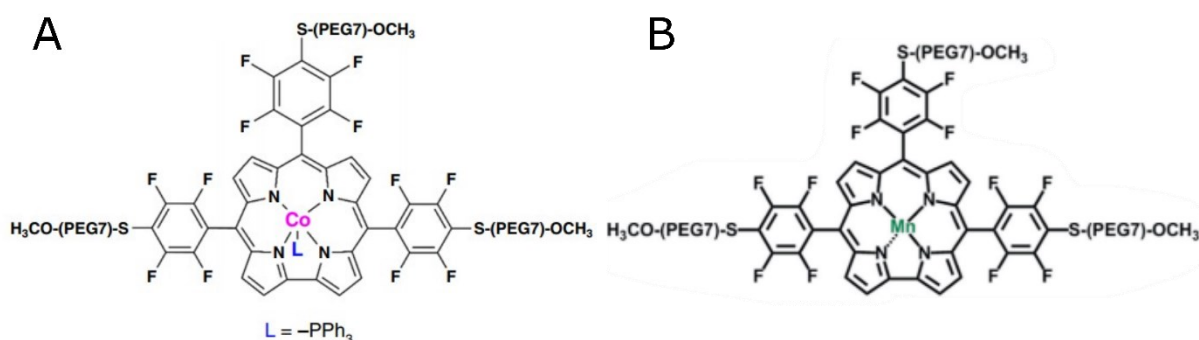


Figure 1-20. Structure of **(A)** cobalt-corrole and **(B)** manganese-corrole, reproduced from references 153 and 154

1.3.5.4 Single-atom catalysts

Since the work of Zhang and co-workers on CO oxidation using single-atom catalysts (SACs),¹⁵⁵ this family of catalysts has gained considerable interest in the field of CO₂ reduction due to their hybrid nature between molecular and materials catalysts. Similar to most molecular catalysts in single and separated active sites, the main product of CO₂ reduction on transition metals SACs is CO with high selectivity and current density,^{156–161} with a few works reporting higher reduced products. CH₃OH has been generated using Cu-based SACs,¹⁶² and CH₄ has been formed on Cu-doped CeO₂,¹⁶³ ZnN₄¹⁶⁴ and FeN₄¹⁶⁵ species. Indeed, DFT calculation showed SACs with porphyrin-like structures having different binding energy with radical species of CO and H than their metal counterparts, enabling reduction further than CO with MnN₄ and FeN₄, which is not favorable on purely metallic species.¹⁶⁶ Moreover, C₂₊ products, including ethanol,¹⁶⁷ acetone,¹⁶⁸ have been demonstrated as the result of the reduction of CO₂ on Cu-based SACs.

As most SACs are prepared by pyrolyzing a variety of starting materials, precisely controlling the material's structure is challenging.^{169–171} Extended X-ray absorption fine structure (EXAFS) spectroscopy and TEM are the most common techniques to characterize a SAC, mainly its coordination number and the nature of the neighboring species to the metal center. However, EXAFS will provide only the average coordination number, and different adjacent atoms can fit in one EXAFS model. At the same time, TEM images only represent specific spots and not the whole sample. Therefore, unlike molecular catalysts, whose structures are well characterized, SAC materials' exact nature is undetermined. The structure uncertainty makes both modeling and mechanism study a complicated task. In addition, similar to a molecular species, the structure of SACs is subject to changes during catalysis, making *in situ* characterization a necessity in studying the activity of SACs for CO₂ reduction.

1.3.5.5 Limitations of producing C_{2+} products from molecular and single-atom catalysts

Despite significant efforts, producing C_{2+} products from CO_2 using molecular species achieved limited success. The obtained current density and selectivity are often lower than their metal counterpart. More importantly, the structural integrity and the nature of the active species are a matter of debate. However, producing C_{2+} products from catalysts with well-defined active sites remains a great challenge and opportunity. Due to their well-defined structure and easy tunability, molecular catalysts provide a platform for the in-depth study of the mechanism of the CO_2 reduction catalysis process, both theoretically and experimentally. First, a detailed mechanistic cycle can be established by varying experimental parameters, i.e., substrates, electrolyte concentration, and proton sources. Based on the mechanism, spectroscopy techniques can reveal the local and electronic structures of intermediates. The rate-determining step can also be established from the catalytic cycle. Analyzing molecular catalysts will provide great insight into the development of other families of catalysts for CO_2 reduction

1.3.6 Importance of *in situ* characterization and isotopic labeling

While investigating the formation of the C – C bond from CO_2 using molecular catalysts, confirming the nature of the catalyst during its operation and identifying the origin of the obtained products are crucial. When investigating different copper complexes generating C_2H_4 from CO_2 , Wang and co-workers discovered that the catalysts transformed into copper nanoparticles under catalytic conditions.¹⁷² Using X-ray absorption spectroscopy, they obtained the signature signal of metallic copper from their molecular catalysts under applied reduction potential (Figure 1-21). The molecule-to-metal transformation was further corroborated by EXAFS fitting showing the coordination number and bond nature of a copper species and XPS and TEM signals. Interestingly, the CuPc and the previously reported Cu porphyrin¹⁴⁹ exhibited reversible nature, demonstrated by the similarities of X-ray absorption spectroscopy (XAS) and XPS spectra of the initial species and the species after applying an oxidative potential. This behavior was not observed on the Cu-based MOF and Cu(cyclam), where the application of oxidative potential did not reverse their structures. Using a similar operando XAS technique, Fontecave and co-workers showed similar reversible behavior of a Cu-N-C material¹⁷³ and an immobilized CuPc on carbon nanotubes¹⁷⁴.

These examples showed the importance of in-situ and operando characterization, as ex-situ analysis does not reveal the nature of the catalytically active species. However, in the work of Nam et al.,¹⁵¹ ex-situ characterization by XPS revealed changes in their copper-based catalyst before and after electrolysis, and XAS and TEM images confirmed metal nanoparticle formation. Due to the low amount of products generated by laboratory-scale reduction of CO_2 , it is crucial to verify the products' origin. The detected carbon products may arise from a non-catalytic reaction involving

the catalyst and/or other species in the system.

In 2014, Maverick et al. reported a binuclear copper complex reducing CO_2 to oxalate.¹⁷⁵ However, after further studies, Maverick, Beller and co-workers demonstrated that the previously reported oxalate resulted from ascorbate oxidation instead of CO_2 reduction.¹⁷⁶ Notably, when isotopic labeling using $^{13}\text{CO}_2$ was re-performed in a more controlled way, unlike the original study, the result showed only an unlabelled product. These discoveries resulted in the article's retraction. In addition, when studying water oxidation using cobalt porphyrin, which is also a common catalyst for CO_2 reduction, Sakai's group characterized the degradation of their catalyst.¹⁷⁷ Using electrospray ionization - mass spectrometry, they identified several degraded porphyrins with fewer carbon atoms on the ligand that could form molecules similar to the products of CO_2 reduction.

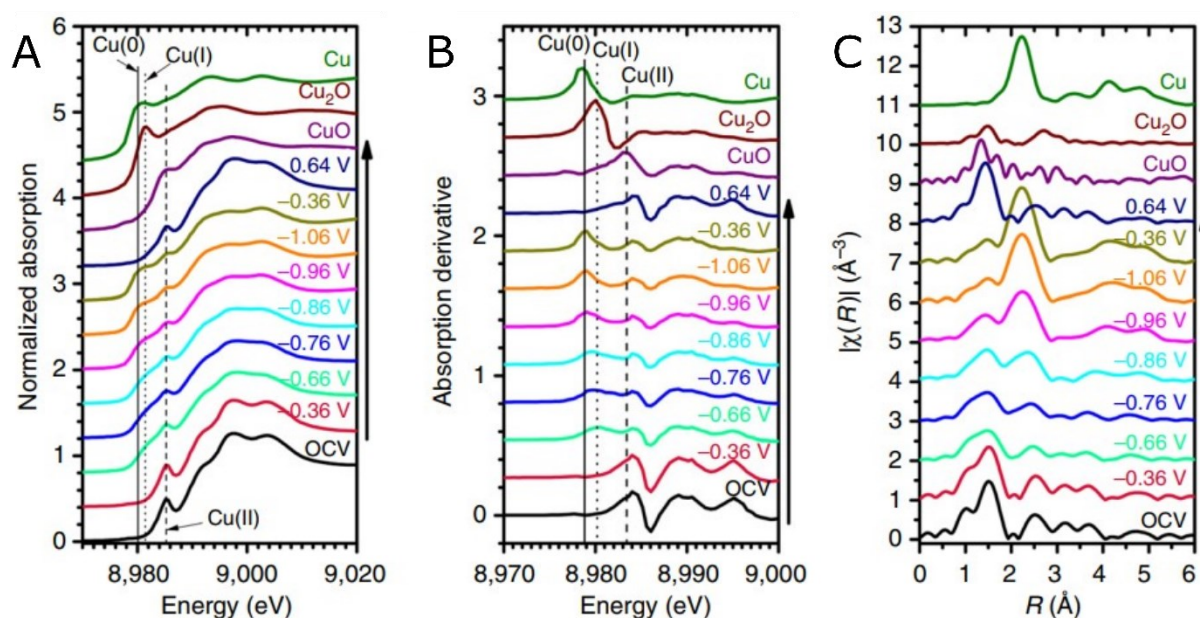


Figure 1-21. *In situ* XAS measurements of CuPc under resting and electrocatalytic reaction conditions. **(A)** Cu K-edge XANES spectra, **(B)** first-order derivatives of the XANES spectra, and **(C)** Fourier-transformed Cu K-edge EXAFS spectra for CuPc. Reproduced from reference 172

1.4 Thesis outline

This thesis aims to use molecular catalysts, namely molecular transition metal macrocycles, to carry out the electrochemical reduction of CO_2 beyond CO .

In chapter 2, we explore the cascade catalysis approach to achieve our aims by developing a series of microfluidic electrochemical flow cells. The idea would be for the first cell to reduce CO_2 to CO , which then travels to the subsequent cell to get further reduced. Upon encountering difficulties with the electrochemical performance of the microfluidic cell caused by bubbles generation, we fabricated a 3D-printed electrochemical flow cell with the channel in millimeter dimension. Laminar flow and the electrocatalytic performance of the cell were tested. We then used finite element

Chapter 1

analysis to build a model and calculate the concentration profiles of the products and reactants inside the flow channel of the cell during CO₂ electrolysis.

In chapter 3, we first tested the electrochemical reduction of CO₂ on an iron phthalocyanine catalyst using the 3D-printed millifluidic cell. Although our initial goal was the selective production of CO, upon detecting hydrocarbon products from the catalysis with just one reduction stage, we focused on the catalytic behavior of FePc further instead of building a sequential reduction system as the original aim. Therefore, we incorporate a gas chromatograph into the flow system to perform inline characterization of the gas products. The electrochemical cell was also modified to add a window for performing *operando* X-ray spectroelectrochemistry experiments. We then carried out a series of control experiments to confirm the origin of the detected carbon. Spectroscopic techniques (X-ray and infrared) were used to investigate the molecular nature of the FePc catalyst before, during, and after catalysis. A mechanism for the C – C bond formation step was proposed based on experiments with FePc, where CO₂ was replaced with other reactants, namely formaldehyde and CO.

In chapter 4, we first explored the influences of external parameters, namely the electrolyte flow rate and the concentrations of catalyst, electrolyte, and conductive carbon support, on the reduction of CO₂ on FePc. Then we studied the impact of substituent groups on FePc, as well as the effects of changing the metal center of the phthalocyanine ligands. Finally, we performed preliminary tests on iron porphyrin and its derivatives, focusing on their ability to produce C₂₊ products.

In the last chapter, we restate the novelty and impact of forming products with C – C bonds on a single-site catalyst. The summary of each chapter was provided, as well as future experiments and strategies to understand the CO₂-reducing activity of molecular macrocycles. We end the thesis by discussing the general role of CO₂ reduction and other electrochemical energy storage technologies in tackling climate change.

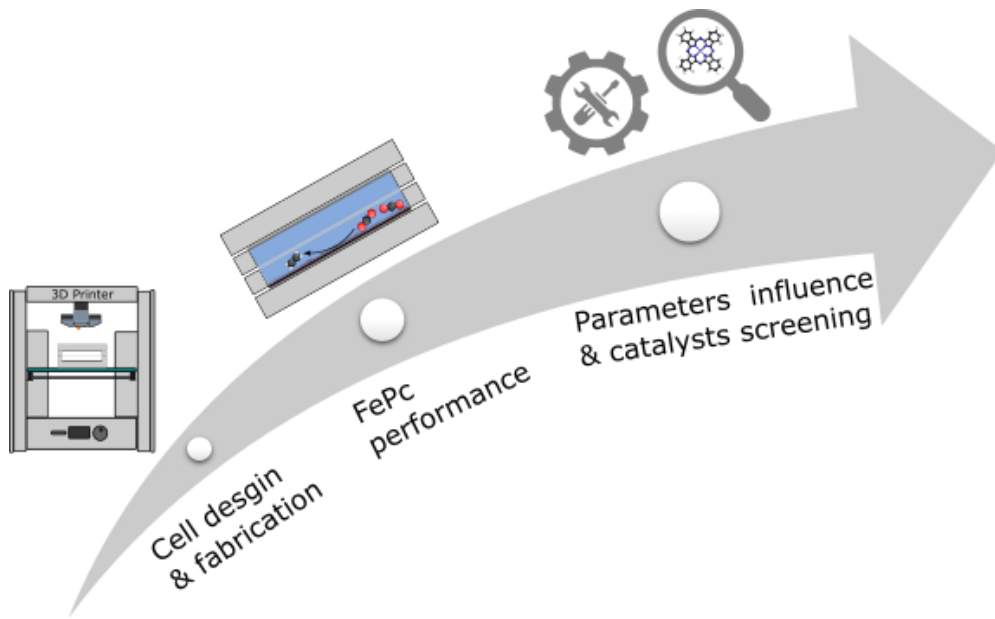


Figure 1-22. Thesis graphical outline

1.5 Bibliography

- (1) *International Energy Outlook - U.S. Energy Information Administration (EIA)*.
<https://www.eia.gov/outlooks/ieo/index.php> (accessed 2022-07-17).
- (2) Ritchie, H.; Roser, M.; Rosado, P. Energy. *Our World in Data* **2020**.
- (3) *Statistical Review of World Energy | Energy economics | Home*. BP global.
<https://www.bp.com/en/global/corporate/energy-economics/statistical-review-of-world-energy.html> (accessed 2022-07-16).
- (4) US Department of Commerce, N. NOAA/ESRL Global Monitoring Division - *THE NOAA ANNUAL GREENHOUSE GAS INDEX (AGGI)*.
<https://www.esrl.noaa.gov/gmd/aggi/aggi.html> (accessed 2019-08-07).
- (5) *Climate Change 2021: The Physical Science Basis. Contribution of Working Group I to the Sixth Assessment Report of the Intergovernmental Panel on Climate Change*; Masson-Delmotte, V., Zhai, P., Pirani, A., Connors, S. L., Péan, C., Berger, S., Caud, N., Chen, Y., Goldfarb, L., Gomis, M. I., Huang, M., Leitzell, K., Lonnoy, E., Matthews, J. B. R., Maycock, T. K., Waterfield, T., Yelekçi, Ö., Yu, R., Zhou, B., Eds.; Cambridge University Press, 2021.
<https://www.ipcc.ch/report/ar6/wg1/>.
- (6) Arrhenius, S. On the Influence of Carbonic Acid in the Air upon the Temperature of the Ground. *Philosophical Magazine and Journal of Science* **1896**, *41*, 303–315.
<https://doi.org/10.12987/9780300188479-028>.
- (7) Osborn, T. J.; Jones, P. D.; Lister, D. H.; Morice, C. P.; Simpson, I. R.; Winn, J. P.; Hogan, E.; Harris, I. C. Land Surface Air Temperature Variations Across the Globe Updated to 2019: The CRUTEM5 Data Set. *Geophys Res Atmos* **2021**, *126* (2).
<https://doi.org/10.1029/2019JD032352>.
- (8) *Climate Change 2022: Impacts, Adaptation and Vulnerability. Contribution of Working Group II to the Sixth Assessment Report of the Intergovernmental Panel on Climate Change*; Pörtner, H.-O., Roberts, D. C., Tignor, M. M. B., Poloczanska, E. S., Mintenbeck, K., Alegria, A., Craig, M., Langsdorf, S., Löschke, S., Möller, V., Okem, A., Rama, B., Eds.; 2022.
<https://www.ipcc.ch/report/ar6/wg2/>.
- (9) *The Ocean Conference, 5-9 June, 2017 - United Nations, New York*.
<https://www.un.org/en/conf/ocean/index.shtml> (accessed 2022-07-17).
- (10) Hassler, J.; Krusell, P.; Olovsson, C. Directed Technical Change as a Response to Natural Resource Scarcity. *Journal of Political Economy* **2021**, *129* (11), 3039–3072.
<https://doi.org/10.1086/715849>.
- (11) *Kyoto Protocol - Targets for the first commitment period*. <https://unfccc.int/process-and-meetings/the-kyoto-protocol/what-is-the-kyoto-protocol/kyoto-protocol-targets-for-the-first-commitment-period> (accessed 2022-07-17).
- (12) *The Paris Agreement | UNFCCC*. <https://unfccc.int/process-and-meetings/the-paris-agreement/the-paris-agreement> (accessed 2019-08-07).
- (13) *Why did renewables become so cheap so fast?*. Our World in Data. <https://ourworldindata.org/cheap-renewables-growth> (accessed 2022-07-18).

Chapter 1

- (14) Gürsan, C.; de Gooyert, V. The Systemic Impact of a Transition Fuel: Does Natural Gas Help or Hinder the Energy Transition? *Renewable and Sustainable Energy Reviews* **2021**, *138*, 110552. <https://doi.org/10.1016/j.rser.2020.110552>.
- (15) Pumped Hydro Energy Storage System: A Technological Review. *Renewable and Sustainable Energy Reviews* **2015**, *44*, 586–598. <https://doi.org/10.1016/j.rser.2014.12.040>.
- (16) Dunn, B.; Kamath, H.; Tarascon, J.-M. Electrical Energy Storage for the Grid: A Battery of Choices. *Science* **2011**, *334* (6058), 928–935. <https://doi.org/10.1126/science.1212741>.
- (17) Benson, A. A.; Bassham, J. A.; Calvin, M.; Goodale, T. C.; Haas, V. A.; Stepka, W. The Path of Carbon in Photosynthesis. V. Paper Chromatography and Radioautography of the Products. *J. Am. Chem. Soc.* **1950**, *72* (4), 1710–1718. <https://doi.org/10.1021/ja01160a080>.
- (18) Barber, J. Photosynthetic Energy Conversion: Natural and Artificial. *Chem. Soc. Rev.* **2009**, *38* (1), 185–196. <https://doi.org/10.1039/B802262N>.
- (19) Ardo, S.; Fernandez Rivas, D.; Modestino, M. A.; Schulze Greiving, V.; Abdi, F. F.; Alarcon Llado, E.; Artero, V.; Ayers, K.; Battaglia, C.; Becker, J.-P.; Bederak, D.; Berger, A.; Buda, F.; Chinello, E.; Dam, B.; Di Palma, V.; Edvinsson, T.; Fujii, K.; Gardeniers, H.; Geerlings, H.; H. Hashemi, S. M.; Haussener, S.; Houle, F.; Huskens, J.; James, B. D.; Konrad, K.; Kudo, A.; Kunturu, P. P.; Lohse, D.; Mei, B.; Miller, E. L.; Moore, G. F.; Muller, J.; Orchard, K. L.; Rosser, T. E.; Saadi, F. H.; Schüttauf, J.-W.; Seger, B.; Sheehan, S. W.; Smith, W. A.; Spurgeon, J.; Tang, M. H.; van de Krol, R.; Vesborg, P. C. K.; Westerik, P. Pathways to Electrochemical Solar-Hydrogen Technologies. *Energy Environ. Sci.* **2018**, *11* (10), 2768–2783. <https://doi.org/10.1039/C7EE03639F>.
- (20) Oliveira, A. M.; Beswick, R. R.; Yan, Y. A Green Hydrogen Economy for a Renewable Energy Society. *Current Opinion in Chemical Engineering* **2021**, *33*, 100701. <https://doi.org/10.1016/j.coche.2021.100701>.
- (21) Wattanaphan, P.; Sema, T.; Idem, R.; Liang, Z.; Tontiwachwuthikul, P. Effects of Flue Gas Composition on Carbon Steel (1020) Corrosion in MEA-Based CO₂ Capture Process. *International Journal of Greenhouse Gas Control* **2013**, *19*, 340–349. <https://doi.org/10.1016/j.ijggc.2013.08.021>.
- (22) Lau, H. C.; Ramakrishna, S.; Zhang, K.; Radhamani, A. V. The Role of Carbon Capture and Storage in the Energy Transition. *Energy Fuels* **2021**, *35* (9), 7364–7386. <https://doi.org/10.1021/acs.energyfuels.1c00032>.
- (23) Frölicher, T. L.; Winton, M.; Sarmiento, J. L. Continued Global Warming after CO₂ Emissions Stoppage. *Nature Clim Change* **2014**, *4* (1), 40–44. <https://doi.org/10.1038/nclimate2060>.
- (24) Teeter, T. E.; Van Rysselberghe, P. Reduction of Carbon Dioxide on Mercury Cathodes. *The Journal of Chemical Physics* **1954**, *22* (4), 759–760. <https://doi.org/10.1063/1.1740178>.
- (25) Francke, R.; Schille, B.; Roemelt, M. Homogeneously Catalyzed Electroreduction of Carbon Dioxide—Methods, Mechanisms, and Catalysts. *Chem. Rev.* **2018**, *118* (9), 4631–4701. <https://doi.org/10.1021/acs.chemrev.7b00459>.

Chapter 1

- (26) Bushuyev, O. S.; De Luna, P.; Dinh, C. T.; Tao, L.; Saur, G.; van de Lagemaat, J.; Kelley, S. O.; Sargent, E. H. What Should We Make with CO₂ and How Can We Make It? *Joule* **2018**, *2* (5), 825–832. <https://doi.org/10.1016/j.joule.2017.09.003>.
- (27) Shin, H.; Hansen, K. U.; Jiao, F. Techno-Economic Assessment of Low-Temperature Carbon Dioxide Electrolysis. *Nat Sustain* **2021**, *4* (10), 911–919. <https://doi.org/10.1038/s41893-021-00739-x>.
- (28) Jouny, M.; Luc, W.; Jiao, F. General Techno-Economic Analysis of CO₂ Electrolysis Systems. *Ind. Eng. Chem. Res.* **2018**, *57* (6), 2165–2177. <https://doi.org/10.1021/acs.iecr.7b03514>.
- (29) Rao, H.; Schmidt, L. C.; Bonin, J.; Robert, M. Visible-Light-Driven Methane Formation from CO₂ with a Molecular Iron Catalyst. *Nature* **2017**, *548* (7665), 74–77. <https://doi.org/10.1038/nature23016>.
- (30) Chang, X.; Wang, T.; Gong, J. CO₂ Photo-Reduction: Insights into CO₂ Activation and Reaction on Surfaces of Photocatalysts. *Energy & Environmental Science* **2016**, *9* (7), 2177–2196. <https://doi.org/10.1039/C6EE00383D>.
- (31) Liu, X.; Inagaki, S.; Gong, J. Heterogeneous Molecular Systems for Photocatalytic CO₂ Reduction with Water Oxidation. *Angewandte Chemie International Edition* **2016**, *55* (48), 14924–14950. <https://doi.org/10.1002/anie.201600395>.
- (32) Andrei, V.; Ucoski, G. M.; Pornrunroj, C.; Uswachoke, C.; Wang, Q.; Achilleos, D. S.; Kasap, H.; Sokol, K. P.; Jagt, R. A.; Lu, H.; Lawson, T.; Wagner, A.; Pike, S. D.; Wright, D. S.; Hoyer, R. L. Z.; MacManus-Driscoll, J. L.; Joyce, H. J.; Friend, R. H.; Reisner, E. Floating Perovskite-BiVO₄ Devices for Scalable Solar Fuel Production. *Nature* **2022**, *608* (7923), 518–522. <https://doi.org/10.1038/s41586-022-04978-6>.
- (33) Nishiyama, H.; Yamada, T.; Nakabayashi, M.; Maehara, Y.; Yamaguchi, M.; Kuromiya, Y.; Nagatsuma, Y.; Tokudome, H.; Akiyama, S.; Watanabe, T.; Narushima, R.; Okunaka, S.; Shibata, N.; Takata, T.; Hisatomi, T.; Domen, K. Photocatalytic Solar Hydrogen Production from Water on a 100-m² Scale. *Nature* **2021**, *598* (7880), 304–307. <https://doi.org/10.1038/s41586-021-03907-3>.
- (34) Singh, R. K.; Singh, R.; Sivakumar, D.; Kondaveeti, S.; Kim, T.; Li, J.; Sung, B. H.; Cho, B.-K.; Kim, D. R.; Kim, S. C.; Kalia, V. C.; Zhang, Y.-H. P. J.; Zhao, H.; Kang, Y. C.; Lee, J.-K. Insights into Cell-Free Conversion of CO₂ to Chemicals by a Multienzyme Cascade Reaction. *ACS Catal.* **2018**, *8* (12), 11085–11093. <https://doi.org/10.1021/acscatal.8b02646>.
- (35) Wang, X.; Li, Z.; Shi, J.; Wu, H.; Jiang, Z.; Zhang, W.; Song, X.; Ai, Q. Bioinspired Approach to Multienzyme Cascade System Construction for Efficient Carbon Dioxide Reduction. *ACS Catal.* **2014**, *4* (3), 962–972. <https://doi.org/10.1021/cs401096c>.
- (36) Yang, K. D.; Lee, C. W.; Jin, K.; Im, S. W.; Nam, K. T. Current Status and Bioinspired Perspective of Electrochemical Conversion of CO₂ to a Long-Chain Hydrocarbon. *J. Phys. Chem. Lett.* **2017**, *8* (2), 538–545. <https://doi.org/10.1021/acs.jpcllett.6b02748>.
- (37) Appel, A. M.; Bercaw, J. E.; Bocarsly, A. B.; Dobbek, H.; DuBois, D. L.; Dupuis, M.; Ferry, J. G.; Fujita, E.; Hille, R.; Kenis, P. J. A.; Kerfeld, C. A.; Morris, R. H.; Peden, C. H. F.; Portis, A. R.; Ragsdale, S. W.; Rauchfuss, T. B.; Reek, J. N. H.; Seefeldt, L. C.; Thauer, R. K.; Waldrop, G. L. Frontiers, Opportunities, and Challenges in Biochemical and Chemical Catalysis of CO₂ Fixation. *Chem. Rev.* **2013**, *113* (8), 6621–6658. <https://doi.org/10.1021/cr300463y>.

- (38) Jensen, M. T.; Rønne, M. H.; Ravn, A. K.; Juhl, R. W.; Nielsen, D. U.; Hu, X.-M.; Pedersen, S. U.; Daasbjerg, K.; Skrydstrup, T. Scalable Carbon Dioxide Electroreduction Coupled to Carbonylation Chemistry. *Nature Communications* **2017**, *8* (1). <https://doi.org/10.1038/s41467-017-00559-8>.
- (39) Gotico, P.; Del Vecchio, A.; Audisio, D.; Quaranta, A.; Halime, Z.; Leibl, W.; Aukauloo, A. Visible-Light-Driven Reduction of CO₂ to CO and Its Subsequent Valorization in Carbonylation Chemistry and ¹³C Isotope Labeling. *ChemPhotoChem* **2018**, *2* (8), 715–719. <https://doi.org/10.1002/cptc.201800012>.
- (40) Yaashikaa, P. R.; Senthil Kumar, P.; Varjani, S. J.; Saravanan, A. A Review on Photochemical, Biochemical and Electrochemical Transformation of CO₂ into Value-Added Products. *Journal of CO₂ Utilization* **2019**, *33*, 131–147. <https://doi.org/10.1016/j.jcou.2019.05.017>.
- (41) Wu, X.-Y.; Ghoniem, A. F. Mixed Ionic-Electronic Conducting (MIEC) Membranes for Thermochemical Reduction of CO₂: A Review. *Progress in Energy and Combustion Science* **2019**, *74*, 1–30. <https://doi.org/10.1016/j.pecs.2019.04.003>.
- (42) Küngas, R. Review—Electrochemical CO₂ Reduction for CO Production: Comparison of Low- and High-Temperature Electrolysis Technologies. *J. Electrochem. Soc.* **2020**, *167* (4), 044508. <https://doi.org/10.1149/1945-7111/ab7099>.
- (43) Hecht, M.; Hoffman, J.; Rapp, D.; McClean, J.; SooHoo, J.; Schaefer, R.; Aboobaker, A.; Mellstrom, J.; Hartvigsen, J.; Meyen, F.; Hinterman, E.; Voecks, G.; Liu, A.; Nasr, M.; Lewis, J.; Johnson, J.; Guernsey, C.; Swoboda, J.; Eckert, C.; Alcalde, C.; Poirier, M.; Khopkar, P.; Elangovan, S.; Madsen, M.; Smith, P.; Graves, C.; Sanders, G.; Araghi, K.; de la Torre Juarez, M.; Larsen, D.; Agui, J.; Burns, A.; Lackner, K.; Nielsen, R.; Pike, T.; Tata, B.; Wilson, K.; Brown, T.; Disarro, T.; Morris, R.; Schaefer, R.; Steinkraus, R.; Surampudi, R.; Werne, T.; Ponce, A. Mars Oxygen ISRU Experiment (MOXIE). *Space Sci Rev* **2021**, *217* (1), 9. <https://doi.org/10.1007/s11214-020-00782-8>.
- (44) Franz, F.; Hans, T. Process for the Production of Paraffin-Hydrocarbons with More than One Carbon Atom. US1746464A, February 11, 1930. <https://patents.google.com/patent/US2225487>.
- (45) Schulz, H. Short History and Present Trends of Fischer–Tropsch Synthesis. *Applied Catalysis A: General* **1999**, *186* (1), 3–12. [https://doi.org/10.1016/S0926-860X\(99\)00160-X](https://doi.org/10.1016/S0926-860X(99)00160-X).
- (46) Xie, C.; Chen, C.; Yu, Y.; Su, J.; Li, Y.; Somorjai, G. A.; Yang, P. Tandem Catalysis for CO₂ Hydrogenation to C₂–C₄ Hydrocarbons. *Nano Lett.* **2017**, *17* (6), 3798–3802. <https://doi.org/10.1021/acs.nanolett.7b01139>.
- (47) Sheehan, S. W. Systems and Methods for On-Site Liquid Alcohol Production from Carbon Dioxide. US20210147326A1, May 20, 2021. <https://patents.google.com/patent/WO2019010095A1/en>.
- (48) Henrici-Olivé, G.; Olivé, S. The Fischer-Tropsch Synthesis: Molecular Weight Distribution of Primary Products and Reaction Mechanism. *Angewandte Chemie International Edition in English* **1976**, *15* (3), 136–141. <https://doi.org/10.1002/anie.197601361>.
- (49) Mahmoudi, H.; Mahmoudi, M.; Doustdar, O.; Jahangiri, H.; Tsolakis, A.; Gu, S.; LechWyszynski, M. A Review of Fischer Tropsch Synthesis Process, Mechanism, Surface Chemistry and Catalyst Formulation. *Biofuels Engineering* **2017**, *2* (1), 11–31. <https://doi.org/10.1515/bfuel-2017-0002>.

Chapter 1

- (50) Fechete, I. Paul Sabatier – The Father of the Chemical Theory of Catalysis. *Comptes Rendus Chimie* **2016**, *19* (11), 1374–1381. <https://doi.org/10.1016/j.crci.2016.08.006>.
- (51) Bagger, A.; Ju, W.; Varela, A. S.; Strasser, P.; Rossmeisl, J. Electrochemical CO₂ Reduction: A Classification Problem. *ChemPhysChem* **2017**, *18* (22), 3266–3273. <https://doi.org/10.1002/cphc.201700736>.
- (52) Hori, Y.; Kikuchi, K.; Murata, A.; Suzuki, S. Production of Methane and Ethylene in Electrochemical Reduction of Carbon Dioxide at Copper Electrode in Aqueous Hydrogencarbonate Solution. *Chem. Lett.* **1986**, *15* (6), 897–898. <https://doi.org/10.1246/cl.1986.897>.
- (53) Hori, Y.; Kikuchi, K.; Suzuki, S. Production of CO and CH₄ in Electrochemical Reduction of CO₂ at Metal Electrodes in Aqueous Hydrogencarbonate Solution. *Chem. Lett.* **1985**, *14* (11), 1695–1698. <https://doi.org/10.1246/cl.1985.1695>.
- (54) Nitopi, S.; Bertheussen, E.; Scott, S. B.; Liu, X.; Engstfeld, A. K.; Horch, S.; Seger, B.; Stephens, I. E. L.; Chan, K.; Hahn, C.; Nørskov, J. K.; Jaramillo, T. F.; Chorkendorff, I. Progress and Perspectives of Electrochemical CO₂ Reduction on Copper in Aqueous Electrolyte. *Chemical Reviews* **2019**, *119* (12), 7610–7672. <https://doi.org/10.1021/acs.chemrev.8b00705>.
- (55) Kuhl, K. P.; Cave, E. R.; Abram, D. N.; Jaramillo, T. F. New Insights into the Electrochemical Reduction of Carbon Dioxide on Metallic Copper Surfaces. *Energy Environ. Sci.* **2012**, *5* (5), 7050–7059. <https://doi.org/10.1039/C2EE21234J>.
- (56) Xu, H.; Rebollar, D.; He, H.; Chong, L.; Liu, Y.; Liu, C.; Sun, C.-J.; Li, T.; Muntean, J. V.; Winans, R. E.; Liu, D.-J.; Xu, T. Highly Selective Electrocatalytic CO₂ Reduction to Ethanol by Metallic Clusters Dynamically Formed from Atomically Dispersed Copper. *Nature Energy* **2020**. <https://doi.org/10.1038/s41560-020-0666-x>.
- (57) Jones, J.-P.; Prakash, G. K. S.; Olah, G. A. Electrochemical CO₂ Reduction: Recent Advances and Current Trends. *Israel Journal of Chemistry* **2014**, *54* (10), 1451–1466. <https://doi.org/10.1002/ijch.201400081>.
- (58) Vogt, C.; Weckhuysen, B. M. The Concept of Active Site in Heterogeneous Catalysis. *Nat Rev Chem* **2022**, *6* (2), 89–111. <https://doi.org/10.1038/s41570-021-00340-y>.
- (59) Kim, Y.-G.; Baricuatro, J. H.; Soriaga, M. P. Surface Reconstruction of Polycrystalline Cu Electrodes in Aqueous KHCO₃ Electrolyte at Potentials in the Early Stages of CO₂ Reduction. *Electrocatalysis* **2018**, *9* (4), 526–530. <https://doi.org/10.1007/s12678-018-0469-z>.
- (60) Kim, Y.-G.; Javier, A.; Baricuatro, J. H.; Torelli, D.; Cummins, K. D.; Tsang, C. F.; Hemminger, J. C.; Soriaga, M. P. Surface Reconstruction of Pure-Cu Single-Crystal Electrodes under CO-Reduction Potentials in Alkaline Solutions: A Study by Seriatim ECSTM-DEMS. *Journal of Electroanalytical Chemistry* **2016**, *780*, 290–295. <https://doi.org/10.1016/j.jelechem.2016.09.029>.
- (61) Popović, S.; Smiljanić, M.; Jovanović, P.; Vavra, J.; Buonsanti, R.; Hodnik, N. Stability and Degradation Mechanisms of Copper-Based Catalysts for Electrochemical CO₂ Reduction. *Angewandte Chemie* **2020**, *132* (35), 14844–14854. <https://doi.org/10.1002/ange.202000617>.
- (62) Hawecker, J.; Lehn, J.-M.; Ziessel, R. Electrocatalytic Reduction of Carbon Dioxide Mediated by Re(Bipy)(CO)₃Cl (Bipy = 2,2'-Bipyridine). *J. Chem. Soc., Chem. Commun.* **1984**, No. 6, 328–330. <https://doi.org/10.1039/C39840000328>.

Chapter 1

- (63) Costentin, C.; Drouet, S.; Robert, M.; Savéant, J.-M. Turnover Numbers, Turnover Frequencies, and Overpotential in Molecular Catalysis of Electrochemical Reactions. Cyclic Voltammetry and Preparative-Scale Electrolysis. *J. Am. Chem. Soc.* **2012**, *134* (27), 11235–11242. <https://doi.org/10.1021/ja303560c>.
- (64) Bonin, J.; Maurin, A.; Robert, M. Molecular Catalysis of the Electrochemical and Photochemical Reduction of CO₂ with Fe and Co Metal Based Complexes. Recent Advances. *Coordination Chemistry Reviews* **2017**, *334*, 184–198. <https://doi.org/10.1016/j.ccr.2016.09.005>.
- (65) Costentin, C.; Robert, M.; Savéant, J.-M. Current Issues in Molecular Catalysis Illustrated by Iron Porphyrins as Catalysts of the CO₂-to-CO Electrochemical Conversion. *Acc. Chem. Res.* **2015**, *48* (12), 2996–3006. <https://doi.org/10.1021/acs.accounts.5b00262>.
- (66) Zhang, S.; Fan, Q.; Xia, R.; Meyer, T. J. CO₂ Reduction: From Homogeneous to Heterogeneous Electrocatalysis. *Acc. Chem. Res.* **2020**, *53* (1), 255–264. <https://doi.org/10.1021/acs.accounts.9b00496>.
- (67) Beley, M.; Collin, J.-P.; Ruppert, R.; Sauvage, J.-P. Nickel(II)-Cyclam: An Extremely Selective Electrocatalyst for Reduction of CO₂ in Water. *J. Chem. Soc., Chem. Commun.* **1984**, No. 19, 1315–1316. <https://doi.org/10.1039/C39840001315>.
- (68) Manbeck, G. F.; Fujita, E. A Review of Iron and Cobalt Porphyrins, Phthalocyanines and Related Complexes for Electrochemical and Photochemical Reduction of Carbon Dioxide. *J. Porphyrins Phthalocyanines* **2015**, *19* (01–03), 45–64. <https://doi.org/10.1142/S1088424615300013>.
- (69) Costentin, C.; Robert, M.; Savéant, J.-M. Catalysis of the Electrochemical Reduction of Carbon Dioxide. *Chemical Society Reviews* **2013**, *42* (6), 2423–2436. <https://doi.org/10.1039/C2CS35360A>.
- (70) Costentin, C.; Passard, G.; Savéant, J.-M. Benchmarking of Homogeneous Electrocatalysts: Overpotential, Turnover Frequency, Limiting Turnover Number. *J. Am. Chem. Soc.* **2015**, *137* (16), 5461–5467. <https://doi.org/10.1021/jacs.5b00914>.
- (71) Gotico, P.; Halime, Z.; Aukauloo, A. Recent Advances in Metalloporphyrin-Based Catalyst Design towards Carbon Dioxide Reduction: From Bio-Inspired Second Coordination Sphere Modifications to Hierarchical Architectures. *Dalton Trans.* **2020**, *49* (8), 2381–2396. <https://doi.org/10.1039/C9DT04709C>.
- (72) Takahashi, K.; Hiratsuka, K.; Sasaki, H.; Toshima, S. Electrocatalytic Behavior of Metal Porphyrins in the Reduction of Carbon Dioxide. *Chem. Lett.* **1979**, *8* (4), 305–308. <https://doi.org/10.1246/cl.1979.305>.
- (73) Hammouche, M.; Lexa, D.; Savéant, J. M.; Momenteau, M. Catalysis of the Electrochemical Reduction of Carbon Dioxide by Iron(“0”) Porphyrins. *Journal of Electroanalytical Chemistry and Interfacial Electrochemistry* **1988**, *249* (1), 347–351. [https://doi.org/10.1016/0022-0728\(88\)80372-3](https://doi.org/10.1016/0022-0728(88)80372-3).
- (74) Bhugun, I.; Lexa, D.; Savéant, J.-M. Catalysis of the Electrochemical Reduction of Carbon Dioxide by Iron(0) Porphyrins: Synergistic Effect of Weak Brönsted Acids. *J. Am. Chem. Soc.* **1996**, *118* (7), 1769–1776. <https://doi.org/10.1021/ja9534462>.
- (75) Bhugun, I.; Lexa, D.; Saveant, J.-M. Ultraefficient Selective Homogeneous Catalysis of the Electrochemical Reduction of Carbon Dioxide by an Iron(0) Porphyrin Associated with a

Chapter 1

- Weak Broensted Acid Cocatalyst. *J. Am. Chem. Soc.* **1994**, 116 (11), 5015–5016.
<https://doi.org/10.1021/ja00090a068>.
- (76) Costentin, C.; Drouet, S.; Passard, G.; Robert, M.; Savéant, J.-M. Proton-Coupled Electron Transfer Cleavage of Heavy-Atom Bonds in Electrocatalytic Processes. Cleavage of a C–O Bond in the Catalyzed Electrochemical Reduction of CO₂. *J. Am. Chem. Soc.* **2013**, 135 (24), 9023–9031. <https://doi.org/10.1021/ja4030148>.
- (77) Römelt, C.; Song, J.; Tarrago, M.; Rees, J. A.; van Gastel, M.; Weyhermüller, T.; DeBeer, S.; Bill, E.; Neese, F.; Ye, S. Electronic Structure of a Formal Iron(0) Porphyrin Complex Relevant to CO₂ Reduction. *Inorg. Chem.* **2017**, 56 (8), 4745–4750.
<https://doi.org/10.1021/acs.inorgchem.7b00401>.
- (78) Costentin, C.; Drouet, S.; Robert, M.; Savéant, J.-M. A Local Proton Source Enhances CO₂ Electroreduction to CO by a Molecular Fe Catalyst. *Science* **2012**, 338 (6103), 90–94.
<https://doi.org/10.1126/science.1224581>.
- (79) Sinha, S.; Warren, J. J. Unexpected Solvent Effect in Electrocatalytic CO₂ to CO Conversion Revealed Using Asymmetric Metalloporphyrins. *Inorg. Chem.* **2018**, 57 (20), 12650–12656. <https://doi.org/10.1021/acs.inorgchem.8b01814>.
- (80) Costentin, C.; Passard, G.; Robert, M.; Savéant, J.-M. Pendant Acid–Base Groups in Molecular Catalysts: H-Bond Promoters or Proton Relays? Mechanisms of the Conversion of CO₂ to CO by Electrogenerated Iron(0)Porphyrins Bearing Prepositioned Phenol Functionalities. *J. Am. Chem. Soc.* **2014**, 136 (33), 11821–11829.
<https://doi.org/10.1021/ja506193v>.
- (81) Costentin, C.; Passard, G.; Robert, M.; Savéant, J.-M. Ultraefficient Homogeneous Catalyst for the CO₂-to-CO Electrochemical Conversion. *Proceedings of the National Academy of Sciences* **2014**, 111 (42), 14990–14994. <https://doi.org/10.1073/pnas.1416697111>.
- (82) Costentin, C.; Robert, M.; Savéant, J.-M.; Tatin, A. Efficient and Selective Molecular Catalyst for the CO₂-to-CO Electrochemical Conversion in Water. *Proceedings of the National Academy of Sciences* **2015**, 112 (22), 6882–6886.
<https://doi.org/10.1073/pnas.1507063112>.
- (83) Liu, G.; Fan, Y.-J.; Zhang, J.-L. Construction of Secondary Coordination Sphere Boosts Electrochemical CO₂ Reduction of Iron Porphyrins. *J. Porphyrins Phthalocyanines* **2020**, 24 (01n03), 465–472. <https://doi.org/10.1142/S1088424619501608>.
- (84) Margarit, C. G.; Schnedermann, C.; Asimow, N. G.; Nocera, D. G. Carbon Dioxide Reduction by Iron Hangman Porphyrins. *Organometallics* **2019**, 38 (6), 1219–1223.
<https://doi.org/10.1021/acs.organomet.8b00334>.
- (85) M. Nichols, E.; S. Derrick, J.; K. Nistanaki, S.; T. Smith, P.; J. Chang, C. Positional Effects of Second-Sphere Amide Pendants on Electrochemical CO₂ Reduction Catalyzed by Iron Porphyrins. *Chemical Science* **2018**, 9 (11), 2952–2960.
<https://doi.org/10.1039/C7SC04682K>.
- (86) Sen, P.; Mondal, B.; Saha, D.; Rana, A.; Dey, A. Role of 2nd Sphere H-Bonding Residues in Tuning the Kinetics of CO₂ Reduction to CO by Iron Porphyrin Complexes. *Dalton Transactions* **2019**, 48 (18), 5965–5977. <https://doi.org/10.1039/C8DT03850C>.
- (87) Gotico, P.; Boitrel, B.; Guillot, R.; Sircoglou, M.; Quaranta, A.; Halime, Z.; Leibl, W.; Aukauloo, A. Second-Sphere Biomimetic Multipoint Hydrogen-Bonding Patterns to Boost CO₂

Chapter 1

- Reduction of Iron Porphyrins. *Angewandte Chemie International Edition* **2019**, *58* (14), 4504–4509. <https://doi.org/10.1002/anie.201814339>.
- (88) Azcarate, I.; Costentin, C.; Robert, M.; Savéant, J.-M. Through-Space Charge Interaction Substituent Effects in Molecular Catalysis Leading to the Design of the Most Efficient Catalyst of CO₂-to-CO Electrochemical Conversion. *J. Am. Chem. Soc.* **2016**, *138* (51), 16639–16644. <https://doi.org/10.1021/jacs.6b07014>.
- (89) Khadhraoui, A.; Gotico, P.; Boitrel, B.; Leibl, W.; Halime, Z.; Aukauloo, A. Local Ionic Liquid Environment at a Modified Iron Porphyrin Catalyst Enhances the Electrocatalytic Performance of CO₂ to CO Reduction in Water. *Chem. Commun.* **2018**, *54* (82), 11630–11633. <https://doi.org/10.1039/C8CC06475J>.
- (90) A. Mohamed, E.; N. Zahran, Z.; Naruta, Y. Efficient Electrocatalytic CO₂ Reduction with a Molecular Cofacial Iron Porphyrin Dimer. *Chemical Communications* **2015**, *51* (95), 16900–16903. <https://doi.org/10.1039/C5CC04273A>.
- (91) Shin, H.; Hansen, K. U.; Jiao, F. Techno-Economic Assessment of Low-Temperature Carbon Dioxide Electrolysis. *Nat Sustain* **2021**, *4* (10), 911–919. <https://doi.org/10.1038/s41893-021-00739-x>.
- (92) Ren, S.; Joulié, D.; Salvatore, D.; Torbensen, K.; Wang, M.; Robert, M.; Berlinguette, C. P. Molecular Electrocatalysts Can Mediate Fast, Selective CO₂ Reduction in a Flow Cell. *Science* **2019**, *365* (6451), 367–369. <https://doi.org/10.1126/science.aax4608>.
- (93) Corbin, N.; Zeng, J.; Williams, K.; Manthiram, K. Heterogeneous Molecular Catalysts for Electrocatalytic CO₂ Reduction. *Nano Res.* **2019**, *12* (9), 2093–2125. <https://doi.org/10.1007/s12274-019-2403-y>.
- (94) Wang, M.; Torbensen, K.; Salvatore, D.; Ren, S.; Joulié, D.; Dumoulin, F.; Mendoza, D.; Lassalle-Kaiser, B.; Işci, U.; Berlinguette, C. P.; Robert, M. CO₂ Electrochemical Catalytic Reduction with a Highly Active Cobalt Phthalocyanine. *Nature Communications* **2019**, *10* (1), 1–8. <https://doi.org/10.1038/s41467-019-11542-w>.
- (95) Zhang, X.; Wang, Y.; Gu, M.; Wang, M.; Zhang, Z.; Pan, W.; Jiang, Z.; Zheng, H.; Lucero, M.; Wang, H.; Sterbinsky, G. E.; Ma, Q.; Wang, Y.-G.; Feng, Z.; Li, J.; Dai, H.; Liang, Y. Molecular Engineering of Dispersed Nickel Phthalocyanines on Carbon Nanotubes for Selective CO₂ Reduction. *Nat Energy* **2020**, *5* (9), 684–692. <https://doi.org/10.1038/s41560-020-0667-9>.
- (96) Kaminsky, C. J.; Weng, S.; Wright, J.; Surendranath, Y. Adsorbed Cobalt Porphyrins Act like Metal Surfaces in Electrocatalysis. *Nat Catal* **2022**, *5* (5), 430–442. <https://doi.org/10.1038/s41929-022-00791-6>.
- (97) Meshitsuka, S.; Ichikawa, M.; Tamaru, K. Electrocatalysis by Metal Phthalocyanines in the Reduction of Carbon Dioxide. *J. Chem. Soc., Chem. Commun.* **1974**, No. 5, 158. <https://doi.org/10.1039/c39740000158>.
- (98) Kapusta, S.; Hackerman, N. Carbon Dioxide Reduction at a Metal Phthalocyanine Catalyzed Carbon Electrode. *J. Electrochem. Soc.* **1984**, *131* (7), 1511. <https://doi.org/10.1149/1.2115882>.
- (99) Tanabe, H.; Ohno, K. Electrocatalysis of Metal Phthalocyanine Thin Film Prepared by the Plasma-Assisted Deposition on a Glassy Carbon in the Reduction of Carbon Dioxide. *Electrochimica Acta* **1987**, *32* (7), 1121–1124. [https://doi.org/10.1016/0013-4686\(87\)90042-9](https://doi.org/10.1016/0013-4686(87)90042-9).

Chapter 1

- (100) Furuya, N.; Koide, S. Electroreduction of Carbon Dioxide by Metal Phthalocyanines. *Electrochimica Acta* **1991**, 36 (8), 1309–1313. [https://doi.org/10.1016/0013-4686\(91\)80010-6](https://doi.org/10.1016/0013-4686(91)80010-6).
- (101) Furuya, N.; Matsui, K. Electroreduction of Carbon Dioxide on Gas-Diffusion Electrodes Modified by Metal Phthalocyanines. *Journal of Electroanalytical Chemistry and Interfacial Electrochemistry* **1989**, 271 (1), 181–191. [https://doi.org/10.1016/0022-0728\(89\)80074-9](https://doi.org/10.1016/0022-0728(89)80074-9).
- (102) Sonoyama, N.; Kirii, M.; Sakata, T. Electrochemical Reduction of CO₂ at Metal-Porphyrin Supported Gas Diffusion Electrodes under High Pressure CO₂. *Electrochemistry Communications* **1999**, 1 (6), 213–216. [https://doi.org/10.1016/S1388-2481\(99\)00041-7](https://doi.org/10.1016/S1388-2481(99)00041-7).
- (103) Birdja, Y. Y.; Shen, J.; Koper, M. T. M. Influence of the Metal Center of Metalloprotoporphyrins on the Electrocatalytic CO₂ Reduction to Formic Acid. *Catalysis Today* **2017**, 288, 37–47. <https://doi.org/10.1016/j.cattod.2017.02.046>.
- (104) Wu, Y.; Jiang, J.; Weng, Z.; Wang, M.; Broere, D. L. J.; Zhong, Y.; Brudvig, G. W.; Feng, Z.; Wang, H. Electroreduction of CO₂ Catalyzed by a Heterogenized Zn–Porphyrin Complex with a Redox-Innocent Metal Center. *ACS Cent. Sci.* **2017**, 3 (8), 847–852. <https://doi.org/10.1021/acscentsci.7b00160>.
- (105) Kramer, W. W.; McCrory, C. C. L. Polymer Coordination Promotes Selective CO₂ Reduction by Cobalt Phthalocyanine. *Chemical Science* **2016**, 7 (4), 2506–2515. <https://doi.org/10.1039/C5SC04015A>.
- (106) Shen, J.; Kortlever, R.; Kas, R.; Birdja, Y. Y.; Diaz-Morales, O.; Kwon, Y.; Ledezma-Yanez, I.; Schouten, K. J. P.; Mul, G.; Koper, M. T. M. Electrocatalytic Reduction of Carbon Dioxide to Carbon Monoxide and Methane at an Immobilized Cobalt Protoporphyrin. *Nat Commun* **2015**, 6 (1), 8177. <https://doi.org/10.1038/ncomms9177>.
- (107) Wu, Y.; Jiang, Z.; Lu, X.; Liang, Y.; Wang, H. Domino Electroreduction of CO₂ to Methanol on a Molecular Catalyst. *Nature* **2019**, 575 (7784), 639–642. <https://doi.org/10.1038/s41586-019-1760-8>.
- (108) Boutin, E.; Wang, M.; Lin, J. C.; Mesnage, M.; Mendoza, D.; Lassalle-Kaiser, B.; Hahn, C.; Jaramillo, T. F.; Robert, M. Aqueous Electrochemical Reduction of Carbon Dioxide and Carbon Monoxide into Methanol with Cobalt Phthalocyanine. *Angewandte Chemie International Edition* **2019**, 58 (45), 16172–16176. <https://doi.org/10.1002/anie.201909257>.
- (109) Abe, T.; Taguchi, F.; Yoshida, T.; Tokita, S.; Schnurpfeil, G.; Wöhrle, D.; Kaneko, M. Electrocatalytic CO₂ Reduction by Cobalt Octabutoxyphthalocyanine Coated on Graphite Electrode. *Journal of Molecular Catalysis A: Chemical* **1996**, 112 (1), 55–61. [https://doi.org/10.1016/1381-1169\(96\)00242-7](https://doi.org/10.1016/1381-1169(96)00242-7).
- (110) Abe, T.; Imaya, H.; Yoshida, T.; Tokita, S.; Schlettwein, D.; Wöhrle, D.; Kaneko, M. Electrochemical CO₂ Reduction Catalysed by Cobalt Octacyanophthalocyanine and Its Mechanism. *J. Porphyrins Phthalocyanines* **1997**, 01 (04), 315–321. [https://doi.org/10.1002/\(SICI\)1099-1409\(199710\)1:4<315::AID-JPP35>3.0.CO;2-V](https://doi.org/10.1002/(SICI)1099-1409(199710)1:4<315::AID-JPP35>3.0.CO;2-V).
- (111) Morlanés, N.; Takanabe, K.; Rodionov, V. Simultaneous Reduction of CO₂ and Splitting of H₂O by a Single Immobilized Cobalt Phthalocyanine Electrocatalyst. *ACS Catal.* **2016**, 6 (5), 3092–3095. <https://doi.org/10.1021/acscatal.6b00543>.

Chapter 1

- (112) Zhang, X.; Wu, Z.; Zhang, X.; Li, L.; Li, Y.; Xu, H.; Li, X.; Yu, X.; Zhang, Z.; Liang, Y.; Wang, H. Highly Selective and Active CO₂ Reduction Electrocatalysts Based on Cobalt Phthalocyanine/Carbon Nanotube Hybrid Structures. *Nat Commun* **2017**, *8* (1), 14675. <https://doi.org/10.1038/ncomms14675>.
- (113) Zhu, M.; Yang, D.-T.; Ye, R.; Zeng, J.; Corbin, N.; Manthiram, K. Inductive and Electrostatic Effects on Cobalt Porphyrins for Heterogeneous Electrocatalytic Carbon Dioxide Reduction. *Catal. Sci. Technol.* **2019**, *9* (4), 974–980. <https://doi.org/10.1039/C9CY00102F>.
- (114) Choi, J.; Wagner, P.; Gambhir, S.; Jalili, R.; MacFarlane, D. R.; Wallace, G. G.; Officer, D. L. Steric Modification of a Cobalt Phthalocyanine/Graphene Catalyst To Give Enhanced and Stable Electrochemical CO₂ Reduction to CO. *ACS Energy Lett.* **2019**, *4* (3), 666–672. <https://doi.org/10.1021/acseenergylett.8b02355>.
- (115) Tornow, C. E.; Thorson, M. R.; Ma, S.; Gewirth, A. A.; Kenis, P. J. A. Nitrogen-Based Catalysts for the Electrochemical Reduction of CO₂ to CO. *J. Am. Chem. Soc.* **2012**, *134* (48), 19520–19523. <https://doi.org/10.1021/ja308217w>.
- (116) Tran Ngoc Huan; Andreiadis, E. S.; Heidkamp, J.; Simon, P.; Derat, E.; Cobo, S.; Royal, G.; Bergmann, A.; Strasser, P.; Dau, H.; Artero, V.; Fontecave, M. From Molecular Copper Complexes to Composite Electrocatalytic Materials for Selective Reduction of CO₂ to Formic Acid. *J. Mater. Chem. A* **2015**, *3* (7), 3901–3907. <https://doi.org/10.1039/C4TA07022D>.
- (117) Mizuguchi, J. π - π Interactions of Magnesium Phthalocyanine as Evaluated by Energy Partition Analysis. *J. Phys. Chem. A* **2001**, *105* (47), 10719–10722. <https://doi.org/10.1021/jp011169h>.
- (118) Duran, S.; Elmaalouf, M.; Odziomek, M.; Piquemal, J.; Faustini, M.; Giraud, M.; Peron, J.; Tard, C. Electrochemical Active Surface Area Determination of Iridium-Based Mixed Oxides by Mercury Underpotential Deposition. *ChemElectroChem* **2021**, *8* (18), 3519–3524. <https://doi.org/10.1002/celec.202100649>.
- (119) Zhu, M.; Ye, R.; Jin, K.; Lazouski, N.; Manthiram, K. Elucidating the Reactivity and Mechanism of CO₂ Electroreduction at Highly Dispersed Cobalt Phthalocyanine. *ACS Energy Letters* **2018**, *3* (6), 1381–1386. <https://doi.org/10.1021/acseenergylett.8b00519>.
- (120) Boulatov, R.; Collman, J. P.; Shiryayeva, I. M.; Sunderland, C. J. Functional Analogues of the Dioxygen Reduction Site in Cytochrome Oxidase: Mechanistic Aspects and Possible Effects of CuB. *J. Am. Chem. Soc.* **2002**, *124* (40), 11923–11935. <https://doi.org/10.1021/ja026179q>.
- (121) Kozuch, S.; Martin, J. M. L. "Turning Over" Definitions in Catalytic Cycles. *ACS Catal.* **2012**, *2* (12), 2787–2794. <https://doi.org/10.1021/cs3005264>.
- (122) Birdja, Y. Y.; Vos, R. E.; Wezendonk, T. A.; Jiang, L.; Kapteijn, F.; Koper, M. T. M. Effects of Substrate and Polymer Encapsulation on CO₂ Electroreduction by Immobilized Iridium(III) Protoporphyrin. *ACS Catal.* **2018**, *8* (5), 4420–4428. <https://doi.org/10.1021/acscatal.7b03386>.
- (123) Hu, X.-M.; Rønne, M. H.; Pedersen, S. U.; Skrydstrup, T.; Daasbjerg, K. Enhanced Catalytic Activity of Cobalt Porphyrin in CO₂ Electroreduction upon Immobilization on Carbon Materials. *Angewandte Chemie International Edition* **2017**, *56* (23), 6468–6472. <https://doi.org/10.1002/anie.201701104>.

Chapter 1

- (124) Zhao, H.-Z.; Chang, Y.-Y.; Liu, C. Electrodes Modified with Iron Porphyrin and Carbon Nanotubes: Application to CO₂ Reduction and Mechanism of Synergistic Electrocatalysis. *J Solid State Electrochem* **2013**, *17* (6), 1657–1664. <https://doi.org/10.1007/s10008-013-2027-1>.
- (125) Zhu, M.; Chen, J.; Huang, L.; Ye, R.; Xu, J.; Han, Y.-F. Covalently Grafting Cobalt Porphyrin onto Carbon Nanotubes for Efficient CO₂ Electroreduction. *Angewandte Chemie International Edition* **2019**, *58* (20), 6595–6599. <https://doi.org/10.1002/anie.201900499>.
- (126) Aga, H.; Aramata, A.; Hisaeda, Y. The Electroreduction of Carbon Dioxide by Macrocyclic Cobalt Complexes Chemically Modified on a Glassy Carbon Electrode. *Journal of Electroanalytical Chemistry* **1997**, *437* (1), 111–118. [https://doi.org/10.1016/S0022-0728\(97\)00386-0](https://doi.org/10.1016/S0022-0728(97)00386-0).
- (127) Yoshida, T.; Kamato, K.; Tsukamoto, M.; Iida, T.; Schlettwein, D.; Wöhrle, D.; Kaneko, M. Selective Electrocatalysis for CO₂ Reduction in the Aqueous Phase Using Cobalt Phthalocyanine/Poly-4-Vinylpyridine Modified Electrodes. *Journal of Electroanalytical Chemistry* **1995**, *385* (2), 209–225. [https://doi.org/10.1016/0022-0728\(94\)03762-R](https://doi.org/10.1016/0022-0728(94)03762-R).
- (128) Abe, T.; Yoshida, T.; Tokita, S.; Taguchi, F.; Imai, H.; Kaneko, M. Factors Affecting Selective Electrocatalytic CO₂ Reduction with Cobalt Phthalocyanine Incorporated in a Polyvinylpyridine Membrane Coated on a Graphite Electrode. *Journal of Electroanalytical Chemistry* **1996**, *412* (1), 125–132. [https://doi.org/10.1016/0022-0728\(96\)04631-1](https://doi.org/10.1016/0022-0728(96)04631-1).
- (129) Cai, X.; Liu, H.; Wei, X.; Yin, Z.; Chu, J.; Tang, M.; Zhuang, L.; Deng, H. Molecularly Defined Interface Created by Porous Polymeric Networks on Gold Surface for Concerted and Selective CO₂ Reduction. *ACS Sustainable Chem. Eng.* **2018**, *6* (12), 17277–17283. <https://doi.org/10.1021/acssuschemeng.8b04691>.
- (130) Cao, Z.; Zacate, S. B.; Sun, X.; Liu, J.; Hale, E. M.; Carson, W. P.; Tyndall, S. B.; Xu, J.; Liu, X.; Liu, X.; Song, C.; Luo, J.; Cheng, M.-J.; Wen, X.; Liu, W. Tuning Gold Nanoparticles with Chelating Ligands for Highly Efficient Electrocatalytic CO₂ Reduction. *Angewandte Chemie* **2018**, *130* (39), 12857–12861. <https://doi.org/10.1002/ange.201805696>.
- (131) Gong, M.; Cao, Z.; Liu, W.; Nichols, E. M.; Smith, P. T.; Derrick, J. S.; Liu, Y.-S.; Liu, J.; Wen, X.; Chang, C. J. Supramolecular Porphyrin Cages Assembled at Molecular–Materials Interfaces for Electrocatalytic CO Reduction. *ACS Cent. Sci.* **2017**, *3* (9), 1032–1040. <https://doi.org/10.1021/acscentsci.7b00316>.
- (132) Li, F.; Li, Y. C.; Wang, Z.; Li, J.; Nam, D.-H.; Lum, Y.; Luo, M.; Wang, X.; Ozden, A.; Hung, S.-F.; Chen, B.; Wang, Y.; Wicks, J.; Xu, Y.; Li, Y.; Gabardo, C. M.; Dinh, C.-T.; Wang, Y.; Zhuang, T.-T.; Sinton, D.; Sargent, E. H. Cooperative CO₂-to-Ethanol Conversion via Enriched Intermediates at Molecule–Metal Catalyst Interfaces. *Nat Catal* **2020**, *3* (1), 75–82. <https://doi.org/10.1038/s41929-019-0383-7>.
- (133) Wang, M.; Nikolaou, V.; Loiudice, A.; D. Sharp, I.; Llobet, A.; Buonsanti, R. Tandem Electrocatalytic CO₂ Reduction with Fe-Porphyrins and Cu Nanocubes Enhances Ethylene Production. *Chemical Science* **2022**. <https://doi.org/10.1039/D2SC04794B>.
- (134) Kudo, A.; Nakagawa, S.; Tsuneta, A.; Sakata, T. Electrochemical Reduction of High Pressure CO₂ on Ni Electrodes. <https://iopscience.iop.org/article/10.1149/1.2221599>.

Chapter 1

- (135) Liu, Y.; Fan, X.; Nayak, A.; Wang, Y.; Shan, B.; Quan, X.; Meyer, T. J. Steering CO₂ Electroreduction toward Ethanol Production by a Surface-Bound Ru Polypyridyl Carbene Catalyst on N-Doped Porous Carbon. *Proceedings of the National Academy of Sciences* **2019**, 116 (52), 26353–26358. <https://doi.org/10.1073/pnas.1907740116>.
- (136) Wu, J.; Ma, S.; Sun, J.; Gold, J. I.; Tiwary, C.; Kim, B.; Zhu, L.; Chopra, N.; Odeh, I. N.; Vajtai, R.; Yu, A. Z.; Luo, R.; Lou, J.; Ding, G.; Kenis, P. J. A.; Ajayan, P. M. A Metal-Free Electrocatalyst for Carbon Dioxide Reduction to Multi-Carbon Hydrocarbons and Oxygenates. *Nat Commun* **2016**, 7 (1), 13869. <https://doi.org/10.1038/ncomms13869>.
- (137) Magdesieva, T. V.; Yamamoto, T.; Tryk, D. A.; Fujishima, A. Electrochemical Reduction of CO₂ with Transition Metal Phthalocyanine and Porphyrin Complexes Supported on Activated Carbon Fibers. *J. Electrochem. Soc.* **2002**, 149 (6), D89. <https://doi.org/10.1149/1.1475690>.
- (138) Eggins, B. R.; Brown, E. M.; McNeill, E. A.; Grimshaw, J. Carbon Dioxide Fixation by Electrochemical Reduction in Water to Oxalate and Glyoxylate. *Tetrahedron Letters* **1988**, 29 (8), 945–948. [https://doi.org/10.1016/S0040-4039\(00\)82489-2](https://doi.org/10.1016/S0040-4039(00)82489-2).
- (139) Ikeda, S.; Takagi, T.; Ito, K. Selective Formation of Formic Acid, Oxalic Acid, and Carbon Monoxide by Electrochemical Reduction of Carbon Dioxide. *BCSJ* **1987**, 60 (7), 2517–2522. <https://doi.org/10.1246/bcsj.60.2517>.
- (140) Y. Becker, J.; Vainas, B.; Levin, R. E. (née; Orenstein, L. K. Electrocatalytic Reduction of CO₂ to Oxalate by Ag II and Pd II Porphyrins. *Journal of the Chemical Society, Chemical Communications* **1985**, 0 (21), 1471–1472. <https://doi.org/10.1039/C39850001471>.
- (141) Rudolph, M.; Dautz, S.; Jäger, E.-G. Macrocyclic [N42-] Coordinated Nickel Complexes as Catalysts for the Formation of Oxalate by Electrochemical Reduction of Carbon Dioxide. *J. Am. Chem. Soc.* **2000**, 122 (44), 10821–10830. <https://doi.org/10.1021/ja001254n>.
- (142) Udugala-Ganeheneghe, M. Y.; Dissanayake, N. M.; Liu, Y.; Bond, A. M.; Zhang, J. Electrochemistry of Nickel(II) and Copper(II) N,N'-Ethylenebis(Acetylacetoniminato) Complexes and Their Electrocatalytic Activity for Reduction of Carbon Dioxide and Carboxylic Acid Protons. *Transition Met Chem* **2014**, 39 (7), 819–830. <https://doi.org/10.1007/s11243-014-9864-3>.
- (143) Pun, S.-N.; Chung, W.-H.; Lam, K.-M.; Guo, P.; Chan, P.-H.; Wong, K.-Y.; Che, C.-M.; Chen, T.-Y.; Peng, S.-M. Iron(I) Complexes of 2,9-Bis(2-Hydroxyphenyl)-1,10-Phenanthroline (H₂Dophen) as Electrocatalysts for Carbon Dioxide Reduction. X-Ray Crystal Structures of [Fe(Dophen)Cl]₂ · 2HCON(CH₃)₂ and [Fe(Dophen)(N-Melm)₂]ClO₄ (N-Melm = 1-Methylimidazole). *Journal of the Chemical Society, Dalton Transactions* **2002**, 0 (4), 575–583. <https://doi.org/10.1039/B108472K>.
- (144) O'Toole, T. R.; Sullivan, B. P.; Bruce, M. R.-M.; Margerum, L. D.; Murray, R. W.; Meyer, T. J. Electrocatalytic Reduction of CO₂ by a Complex of Rhenium in Thin Polymeric Films. *Journal of Electroanalytical Chemistry and Interfacial Electrochemistry* **1989**, 259 (1), 217–239. [https://doi.org/10.1016/0022-0728\(89\)80049-X](https://doi.org/10.1016/0022-0728(89)80049-X).
- (145) Kushi, Y.; Nagao, H.; Nishioka, T.; Isobe, K.; Tanaka, K. Oxalate Formation in Electrochemical CO₂ Reduction Catalyzed by Rhodium-Sulfur Cluster. *Chem. Lett.* **1994**, 23 (11), 2175–2178. <https://doi.org/10.1246/cl.1994.2175>.

- (146) Tanaka, K.; Kushi, Y.; Tsuge, K.; Toyohara, K.; Nishioka, T.; Isobe, K. Catalytic Generation of Oxalate through a Coupling Reaction of Two CO₂ Molecules Activated on [(Ir(η^5 -C₅Me₅)₂(Ir(η^4 -C₅Me₅)CH₂CN)(μ -3-S)₂]. *Inorg. Chem.* **1998**, 37 (1), 120–126. <https://doi.org/10.1021/ic9702328>.
- (147) Ali, M. M.; Sato, H.; Mizukawa, T.; Tsuge, K.; Haga, M.; Tanaka, K. Selective Formation of HCO₂⁻ and C₂O₄²⁻ in Electrochemical Reduction of CO₂ Catalyzed by Mono- and Di-Nuclear Ruthenium Complexes. *Chem. Commun.* **1998**, No. 2, 249–250. <https://doi.org/10.1039/A707363A>.
- (148) Angamuthu, R.; Byers, P.; Lutz, M.; Spek, A. L.; Bouwman, E. Electrocatalytic CO₂ Conversion to Oxalate by a Copper Complex. *Science* **2010**, 327 (5963), 313–315. <https://doi.org/10.1126/science.1177981>.
- (149) Weng, Z.; Jiang, J.; Wu, Y.; Wu, Z.; Guo, X.; Materna, K. L.; Liu, W.; Batista, V. S.; Brudvig, G. W.; Wang, H. Electrochemical CO₂ Reduction to Hydrocarbons on a Heterogeneous Molecular Cu Catalyst in Aqueous Solution. *J. Am. Chem. Soc.* **2016**, 138 (26), 8076–8079. <https://doi.org/10.1021/jacs.6b04746>.
- (150) Kusama, S.; Saito, T.; Hashiba, H.; Sakai, A.; Yotsuhashi, S. Crystalline Copper(II) Phthalocyanine Catalysts for Electrochemical Reduction of Carbon Dioxide in Aqueous Media. *ACS Catal.* **2017**, 7 (12), 8382–8385. <https://doi.org/10.1021/acscatal.7b02220>.
- (151) Balamurugan, M.; Jeong, H.; Choutipalli, V. S. K.; Hong, J. S.; Seo, H.; Saravanan, N.; Jang, J. H.; Lee, K.; Lee, Y. H.; Im, S. W.; Subramanian, V.; Kim, S. H.; Nam, K. T. Electrocatalytic Reduction of CO₂ to Ethylene by Molecular Cu-Complex Immobilized on Graphitized Mesoporous Carbon. *Small* **2020**, 16 (25), 2000955. <https://doi.org/10.1002/sml.202000955>.
- (152) Qiu, X.-F.; Zhu, H.-L.; Huang, J.-R.; Liao, P.-Q.; Chen, X.-M. Highly Selective CO₂ Electroreduction to C₂H₄ Using a Metal–Organic Framework with Dual Active Sites. *J. Am. Chem. Soc.* **2021**, 143 (19), 7242–7246. <https://doi.org/10.1021/jacs.1c01466>.
- (153) Gonglach, S.; Paul, S.; Haas, M.; Pillwein, F.; Sreejith, S. S.; Barman, S.; De, R.; Müllegger, S.; Gerschel, P.; Apfel, U.-P.; Coskun, H.; Aljabour, A.; Stadler, P.; Schöfberger, W.; Roy, S. Molecular Cobalt Corrole Complex for the Heterogeneous Electrocatalytic Reduction of Carbon Dioxide. *Nat Commun* **2019**, 10 (1), 3864. <https://doi.org/10.1038/s41467-019-11868-5>.
- (154) De, R.; Gonglach, S.; Paul, S.; Haas, M.; Sreejith, S. S.; Gerschel, P.; Apfel, U.-P.; Vuong, T. H.; Rabeah, J.; Roy, S.; Schöfberger, W. Electrocatalytic Reduction of CO₂ to Acetic Acid by a Molecular Manganese Corrole Complex. *Angewandte Chemie International Edition* **2020**, 59 (26), 10527–10534. <https://doi.org/10.1002/anie.202000601>.
- (155) Qiao, B.; Wang, A.; Yang, X.; Allard, L. F.; Jiang, Z.; Cui, Y.; Liu, J.; Li, J.; Zhang, T. Single-Atom Catalysis of CO Oxidation Using Pt₁/FeO_x. *Nature Chem* **2011**, 3 (8), 634–641. <https://doi.org/10.1038/nchem.1095>.
- (156) Cheng, Q.; Mao, K.; Ma, L.; Yang, L.; Zou, L.; Zou, Z.; Hu, Z.; Yang, H. Encapsulation of Iron Nitride by Fe–N–C Shell Enabling Highly Efficient Electroreduction of CO₂ to CO. *ACS Energy Lett.* **2018**, 3 (5), 1205–1211. <https://doi.org/10.1021/acsenergylett.8b00474>.
- (157) Pan, Y.; Lin, R.; Chen, Y.; Liu, S.; Zhu, W.; Cao, X.; Chen, W.; Wu, K.; Cheong, W.-C.; Wang, Y.; Zheng, L.; Luo, J.; Lin, Y.; Liu, Y.; Liu, C.; Li, J.; Lu, Q.; Chen, X.; Wang, D.; Peng, Q.;

Chapter 1

- Chen, C.; Li, Y. Design of Single-Atom Co–N₅ Catalytic Site: A Robust Electrocatalyst for CO₂ Reduction with Nearly 100% CO Selectivity and Remarkable Stability. *J. Am. Chem. Soc.* **2018**, *140* (12), 4218–4221. <https://doi.org/10.1021/jacs.8b00814>.
- (158) Li, X.; Bi, W.; Chen, M.; Sun, Y.; Ju, H.; Yan, W.; Zhu, J.; Wu, X.; Chu, W.; Wu, C.; Xie, Y. Exclusive Ni–N₄ Sites Realize Near-Unity CO Selectivity for Electrochemical CO₂ Reduction. *J. Am. Chem. Soc.* **2017**, *139* (42), 14889–14892. <https://doi.org/10.1021/jacs.7b09074>.
- (159) Zheng, W.; Yang, J.; Chen, H.; Hou, Y.; Wang, Q.; Gu, M.; He, F.; Xia, Y.; Xia, Z.; Li, Z.; Yang, B.; Lei, L.; Yuan, C.; He, Q.; Qiu, M.; Feng, X. Atomically Defined Undercoordinated Active Sites for Highly Efficient CO₂ Electroreduction. *Advanced Functional Materials* **2020**, *30* (4), 1907658. <https://doi.org/10.1002/adfm.201907658>.
- (160) Yang, F.; Song, P.; Liu, X.; Mei, B.; Xing, W.; Jiang, Z.; Gu, L.; Xu, W. Highly Efficient CO₂ Electroreduction on ZnN₄-Based Single-Atom Catalyst. *Angewandte Chemie International Edition* **2018**, *57* (38), 12303–12307. <https://doi.org/10.1002/anie.201805871>.
- (161) He, Q.; Lee, J. H.; Liu, D.; Liu, Y.; Lin, Z.; Xie, Z.; Hwang, S.; Kattel, S.; Song, L.; Chen, J. G. Accelerating CO₂ Electroreduction to CO Over Pd Single-Atom Catalyst. *Advanced Functional Materials* **2020**, *30* (17), 2000407. <https://doi.org/10.1002/adfm.202000407>.
- (162) Yang, H.; Wu, Y.; Li, G.; Lin, Q.; Hu, Q.; Zhang, Q.; Liu, J.; He, C. Scalable Production of Efficient Single-Atom Copper Decorated Carbon Membranes for CO₂ Electroreduction to Methanol. *J. Am. Chem. Soc.* **2019**, *141* (32), 12717–12723. <https://doi.org/10.1021/jacs.9b04907>.
- (163) Wang, Y.; Chen, Z.; Han, P.; Du, Y.; Gu, Z.; Xu, X.; Zheng, G. Single-Atomic Cu with Multiple Oxygen Vacancies on Ceria for Electrocatalytic CO₂ Reduction to CH₄. *ACS Catal.* **2018**, *8* (8), 7113–7119. <https://doi.org/10.1021/acscatal.8b01014>.
- (164) Han, L.; Song, S.; Liu, M.; Yao, S.; Liang, Z.; Cheng, H.; Ren, Z.; Liu, W.; Lin, R.; Qi, G.; Liu, X.; Wu, Q.; Luo, J.; Xin, H. L. Stable and Efficient Single-Atom Zn Catalyst for CO₂ Reduction to CH₄. *J. Am. Chem. Soc.* **2020**, *142* (29), 12563–12567. <https://doi.org/10.1021/jacs.9b12111>.
- (165) Ju, W.; Bagger, A.; Wang, X.; Tsai, Y.; Luo, F.; Möller, T.; Wang, H.; Rossmeisl, J.; Varela, A. S.; Strasser, P. Unraveling Mechanistic Reaction Pathways of the Electrochemical CO₂ Reduction on Fe–N–C Single-Site Catalysts. *ACS Energy Lett.* **2019**, *4* (7), 1663–1671. <https://doi.org/10.1021/acsenergylett.9b01049>.
- (166) Bagger, A.; Ju, W.; Varela, A. S.; Strasser, P.; Rossmeisl, J. Single Site Porphyrine-like Structures Advantages over Metals for Selective Electrochemical CO₂ Reduction. *Catalysis Today* **2017**, *288*, 74–78. <https://doi.org/10.1016/j.cattod.2017.02.028>.
- (167) Jiao, Y.; Zheng, Y.; Chen, P.; Jaroniec, M.; Qiao, S.-Z. Molecular Scaffolding Strategy with Synergistic Active Centers To Facilitate Electrocatalytic CO₂ Reduction to Hydrocarbon/Alcohol. *J. Am. Chem. Soc.* **2017**, *139* (49), 18093–18100. <https://doi.org/10.1021/jacs.7b10817>.
- (168) Zhao, K.; Nie, X.; Wang, H.; Chen, S.; Quan, X.; Yu, H.; Choi, W.; Zhang, G.; Kim, B.; Chen, J. G. Selective Electroreduction of CO₂ to Acetone by Single Copper Atoms Anchored on N-Doped Porous Carbon. *Nat Commun* **2020**, *11* (1), 2455. <https://doi.org/10.1038/s41467-020-16381-8>.

Chapter 1

- (169) Fei, H.; Dong, J.; Feng, Y.; Allen, C. S.; Wan, C.; Voloskiy, B.; Li, M.; Zhao, Z.; Wang, Y.; Sun, H.; An, P.; Chen, W.; Guo, Z.; Lee, C.; Chen, D.; Shakir, I.; Liu, M.; Hu, T.; Li, Y.; Kirkland, A. I.; Duan, X.; Huang, Y. General Synthesis and Definitive Structural Identification of MN_4C_4 Single-Atom Catalysts with Tunable Electrocatalytic Activities. *Nat Catal* **2018**, *1* (1), 63–72. <https://doi.org/10.1038/s41929-017-0008-y>.
- (170) Yang, H.; Shang, L.; Zhang, Q.; Shi, R.; Waterhouse, G. I. N.; Gu, L.; Zhang, T. A Universal Ligand Mediated Method for Large Scale Synthesis of Transition Metal Single Atom Catalysts. *Nat Commun* **2019**, *10* (1), 4585. <https://doi.org/10.1038/s41467-019-12510-0>.
- (171) Xiao, M.; Zhu, J.; Ma, L.; Jin, Z.; Ge, J.; Deng, X.; Hou, Y.; He, Q.; Li, J.; Jia, Q.; Mukerjee, S.; Yang, R.; Jiang, Z.; Su, D.; Liu, C.; Xing, W. Microporous Framework Induced Synthesis of Single-Atom Dispersed Fe-N-C Acidic ORR Catalyst and Its in Situ Reduced Fe-N₄ Active Site Identification Revealed by X-Ray Absorption Spectroscopy. *ACS Catal.* **2018**, *8* (4), 2824–2832. <https://doi.org/10.1021/acscatal.8b00138>.
- (172) Weng, Z.; Wu, Y.; Wang, M.; Jiang, J.; Yang, K.; Huo, S.; Wang, X.-F.; Ma, Q.; Brudvig, G. W.; Batista, V. S.; Liang, Y.; Feng, Z.; Wang, H. Active Sites of Copper-Complex Catalytic Materials for Electrochemical Carbon Dioxide Reduction. *Nat Commun* **2018**, *9* (1), 415. <https://doi.org/10.1038/s41467-018-02819-7>.
- (173) Karapinar, D.; Huan, N. T.; Ranjbar Sahraie, N.; Li, J.; Wakerley, D.; Touati, N.; Zanna, S.; Taverna, D.; Galvão Tizei, L. H.; Zitolo, A.; Jaouen, F.; Mougél, V.; Fontecave, M. Electroreduction of CO₂ on Single-Site Copper-Nitrogen-Doped Carbon Material: Selective Formation of Ethanol and Reversible Restructuration of the Metal Sites. *Angewandte Chemie International Edition* **2019**, *58* (42), 15098–15103. <https://doi.org/10.1002/anie.201907994>.
- (174) Karapinar, D.; Zitolo, A.; Huan, T. N.; Zanna, S.; Taverna, D.; Galvão Tizei, L. H.; Giaume, D.; Marcus, P.; Mougél, V.; Fontecave, M. Carbon-Nanotube-Supported Copper Polyphthalocyanine for Efficient and Selective Electrocatalytic CO₂ Reduction to CO. *ChemSusChem* **2020**, *13* (1), 173–179. <https://doi.org/10.1002/cssc.201902859>.
- (175) Pokharel, U. R.; Fronczek, F. R.; Maverick, A. W. RETRACTED ARTICLE: Reduction of Carbon Dioxide to Oxalate by a Binuclear Copper Complex. *Nat Commun* **2014**, *5* (1), 5883. <https://doi.org/10.1038/ncomms6883>.
- (176) Khamespanah, F.; Marx, M.; Crochet, D. B.; Pokharel, U. R.; Fronczek, F. R.; Maverick, A. W.; Beller, M. Oxalate Production via Oxidation of Ascorbate Rather than Reduction of Carbon Dioxide. *Nat Commun* **2021**, *12* (1), 1997. <https://doi.org/10.1038/s41467-021-21817-w>.
- (177) Nakazono, T.; Parent, A. R.; Sakai, K. Cobalt Porphyrins as Homogeneous Catalysts for Water Oxidation. *Chem. Commun.* **2013**, *49* (56), 6325–6327. <https://doi.org/10.1039/C3CC43031F>.

2 CHAPTER 2: FABRICATION AND MODELING OF AN ELECTROCHEMICAL FLOW CELL

2.1	Introduction.....	58
2.1.1	Cascade catalysis for CO ₂ reduction.....	58
2.1.2	Microfluidics and its application in electrochemical energy devices	59
2.1.3	Scope of the chapter	60
2.2	PDMS microfluidic flow cell	60
2.2.1	Fabrication	60
2.2.2	Electrochemistry performance.....	63
2.2.3	Evaluation and perspectives	64
2.3	3D-printed millifluidic flow cell	66
2.3.1	Design and fabrication.....	66
2.3.2	Flow characterization.....	67
2.3.3	Electrochemistry performance.....	68
2.4	Reactants and products concentration profiles.....	69
2.4.1	The geometry of the flow cell: 2D model and meshing	69
2.4.2	Multiphysics: Laminar flow and transport of diluted species.....	70
2.4.3	Concentration profile throughout the electrochemical cell	73
2.4.4	Concentration profile at specific locations	74
2.5	Millifluidic cell evaluation and perspective.....	74
2.6	Conclusion	75
2.7	Bibliography	76

2.1 Introduction

2.1.1 Cascade catalysis for CO₂ reduction

Cascade catalysis is an appealing approach toward CO₂ reduction. As discussed in chapter 1, reducing CO₂ often involves multiple electron transfer steps, with various pathways the reaction could follow, especially when high-value products with C – C bonds are concerned. The complexity of the reaction can result in a non-selective process that yields many side products along with the desired one, lowering the overall efficiency. The cascade catalysis approach separates a complex reaction into a series of simpler processes.¹ Cascade catalysis is common in nature. One example includes the Calvin cycle, where carbon dioxide is reduced to glucose in a stepwise fashion.² When the reaction steps happen sequentially, the number of undesirable pathways the reaction can follow is minimized, resulting in higher selectivity for the desired products. Moreover, in a sequential system, each step can be tuned independently, leading to a more efficient reaction since all intermediate processes happen under the optimized conditions.

Many studies have applied cascade catalysis to the field of CO₂ reduction. Two common strategies involve utilizing a system of reactors to carry out a series of reactions and tuning the catalyst to incorporate different active species responsible for different reaction steps. Concerning the former approach, Xiang and co-workers calculated that a two-step conversion from CO₂ to C₂H₆O would result in higher solar-to-fuel efficiency than a one-step conversion.³ The role of cascade catalysis was highlighted, as each reactor could have a specific catalyst and potential optimized to convert CO₂ to CO and CO to C₂H₆O. Spurgeon and colleagues studied the reduction of CO₂ to ethanol in a series of two flow reactors.⁴ The first reactor consisted of a silver cathode to generate CO. The resulting CO was transferred to the second reactor, which was converted to ethanol on an oxide-derived copper catalyst. The sequential system yielded ethanol with an average faradaic efficiency of 11% at an average applied potential of -0.52 V vs. RHE. Although this result was not inherently better than a direct conversion of CO₂, the study demonstrated the sequential concept and proposed a better reactor design to improve the CO conversion. A similar approach was reported by Ager and co-workers, where two plates of silver and copper form an electrochemical flow cell cathode.⁵ The tandem electrode exhibited a higher CO conversion rate with increased oxygenated products having C – C bonds.

Upon reducing CO₂ to CO, chemical conversion of CO to high-value products is an alternative strategy instead of electrochemical reduction.⁶ Skrystrup and colleagues developed a CO₂ reduction system consisting of a two-chamber glass cell connected via a glass bridge. The first chamber electro-reduced CO₂ to CO with FeTPP catalyst in TBABF₄/DMF electrolyte. The next chamber contained a Pd catalyst and other reagents to perform carbonylation reactions with CO. The amount of synthesized organic species correlated with the amount of CO generated in a linear relationship. They also

demonstrated that the same strategy worked with atmospheric CO₂ using a three-chamber cell, with the additional cell containing CO₂ binder to capture CO₂ from the atmosphere. Aukauloo and co-workers employed a similar approach to valorize CO via carbonylation reaction on a Pd catalyst.⁷ The same two-chamber glass cell was used, but the electroreduction was replaced by the photoreduction of CO₂ using ruthenium-based photosensitizer and rhenium-based catalyst with DMF and water (9:1) as solvent and proton donor, respectively.

The catalyst-tuning approach was partly discussed in the co-catalytic systems in Chapter 1 with the work of Sargent and co-workers, where they functionalized a copper surface with iron porphyrin to increase the local concentration of CO.⁸ The group of Ager also patterned a gold and silver electrode with copper sites for cascade CO₂ reduction.⁹ In both cases, the high local concentration of CO steers copper's catalytic activity toward oxygenate products, agreeing with the above observation made by Ager's group. Tandem catalyst design is not limited to the electrochemical reduction of CO₂. Yang and co-workers designed a nanostructured core-shell catalyst, CeO₂-Pt@mSiO₂-Co, to convert CO₂ to C₂ – C₄ hydrocarbon via thermochemical reduction.¹⁰ The Pt/CeO₂ part carried out the reverse water-gas shift reaction, converting a mixture of CO₂ and H₂ to CO. The product mixture was the feedstock for the Fischer – Tropsch process happening on the Co-SiO₂ site to form the hydrocarbon products. Under optimum temperature and pressure, the process had a 60% selectivity toward the hydrocarbon products. Likewise, Lee and co-workers used a system of three different enzymes to perform a stepwise conversion of CO₂ to methanol via formate and formaldehyde.¹¹

2.1.2 Microfluidics and its application in electrochemical energy devices

Microfluidics deals with manipulating fluids in systems with at least one dimension from tens to hundreds of micrometers. In a microscopic channel, the role of viscosity dominates that of inertia, resulting in laminar flow, a notable characteristic of a microfluidic device. In a laminar flow, fluids move in parallel layers without any turbulence and eddies; thus the diffusion of molecules between the layers is the only mode of mass transport.¹²

Since microfluidic devices offer greater control in fluid handling due to laminar flow, manipulating reaction intermediates and implementing multi-step synthesis using these devices can be advantageous compared to a batch system.¹³ In electrochemical energy systems, the microscopic dimension of the fluid channel means the electrode distance is similar to the diffusion layer's thickness, potentially leading to better energy efficiency and improved power density. Moreover, the limited mixing action in laminar flow enables the design of membraneless electrochemical devices, where their flow separates the catholyte without needing a membrane.¹⁴

Fuel cells are the most notable energy conversion device currently being developed

under microfluidic conditions; flow batteries and electrolyzers are other examples.¹⁴ Microfluidic fuel cells have been demonstrated to have high power density and shorter refueling times.^{15,16} Hydrogen bromide flow battery also showed improved performance under microfluidic conditions.¹⁷ Membraneless water splitting electrolyzer developed by Modestino and co-workers showed promising performance and excellent product separation at the device's output.¹⁸ Microfluidic CO₂ electrolyzers often employ a gas diffusion electrode, where a thin layer (1 – 3 μm) of flowing electrolyte separates the anode and the cathode.¹⁹ Kenis and colleagues developed a microfluidic CO₂ reactor using a gas-diffusion electrode to reduce CO₂ to HCOOH.²⁰ The versatility of the microfluidic reactor allows for rapid investigation of catalysts under different operating conditions. Although these devices function in microscopic dimensions, their uses in large-scale applications are possible by areal scaling or parallelization.¹⁴

2.1.3 Scope of the chapter

In this chapter, we present the development of a polydimethylsiloxane (PDMS) microfluidic reactor aiming to carry out CO₂ reduction sequentially. The performance of the cell was evaluated using cobalt phthalocyanine as a catalyst. We then discussed the limitations of the cell design and envisioned a different microfluidics design to address some of the problems encountered.

Subsequently, we fabricated a millifluidic electrochemical flow cell by 3D printing. The cell can perform an *operando* spectro-electrochemical experiment to study CO₂-reducing catalysts using X-ray absorption spectroscopy. A mixing test demonstrated the dimensions of the millifluidic cell can still induce a laminar flow in its channel. An iron phthalocyanine catalyst was used to assess the CO₂-reducing behavior in the cell. The distribution of products inside the flow channels was calculated using finite element analysis. Finally, we discussed the advantages and drawbacks of the cell and provided some perspectives to improve the design.

2.2 PDMS microfluidic flow cell

A microfluidic PDMS flow cell was designed and fabricated to investigate the prospect of CO₂ reduction by membrane-free electrolysis based on laminar flow separation. The PDMS material was chosen since it is the standard material for building microfluidic devices. The flow cell would serve as a reactor in a sequential system to reduce CO₂ to high-value products.

2.2.1 Fabrication

A PDMS microfluidics electrochemical flow cell was made following the design scheme shown in Figure 2-1A. The process started with fabricating a mold for the PDMS casting. A 250 μm thick SU-8 negative photoresist was spin-coated onto a 3-inch

diameter, 360 μm thick, (111) silicon wafer. The photoresist layer thickness defined the thickness of the microfluidic channel, which in turn defined the distance between the working and the counter electrodes. Afterward, the coated wafer was loaded into the Kloe Dilase 250 laser writer lithography machine, which shined a laser onto the photoresist according to a pre-designed pattern. Finally, the wafer was washed with the SU-8 photoresist developing solution. Since a negative photoresist was used, the photoresist parts not shined on by the laser would be dissolved after the developing step. The final structure of the mold on the silicon wafer is illustrated in Figure 2-1B. It consists of the main microfluidic channel, two circles for the input and output holes, and two support blocks for the placement of the counter electrode.

The counter electrode of the cell was made by attaching a 10 x 10 x 0.3 mm glassy carbon SIGRADUR® plate (HTW) to a piece of copper tape. A copper wire was soldered to the copper tape, and the assembly was glued to a 3D-printed support plate made with Veroclear® plastic to increase the mechanical strength of the glassy carbon plate. The electrode assembly was then placed on the mold indicated by the transparent black square in Figure 2-1B, in which the two support blocks ensured that the surface of the glassy carbon plate lay flat with the channel. A mixture of PDMS and curing agent (10/1 weight ratio, respectively) from Sylgard was mixed, and bubbles were removed by putting the mixture in a vacuum chamber. The silicon wafer mold was placed into a petri dish, and the bubble-free PDMS was slowly poured onto the mold until the thickness of the PDMS was approximately 5 mm. The container was loaded into a vacuum chamber to evacuate the bubbles formed in the pouring process. When the PDMS was bubble-free again, the dish was placed inside an oven at 73°C for at least one hour. The excess was cut when the PDMS was fully cured, forming a 2.5 x 3 cm rectangular PDMS chip. Three holes were punched to accept 1/16 inch outer diameter, 0.2 mm inner diameter Teflon tubing. Two holes at the ends of the channel are for the inlet and outlet of the working solution, while the hole indicated by the grey circle in Figure 2-1B is for reference electrode connection.

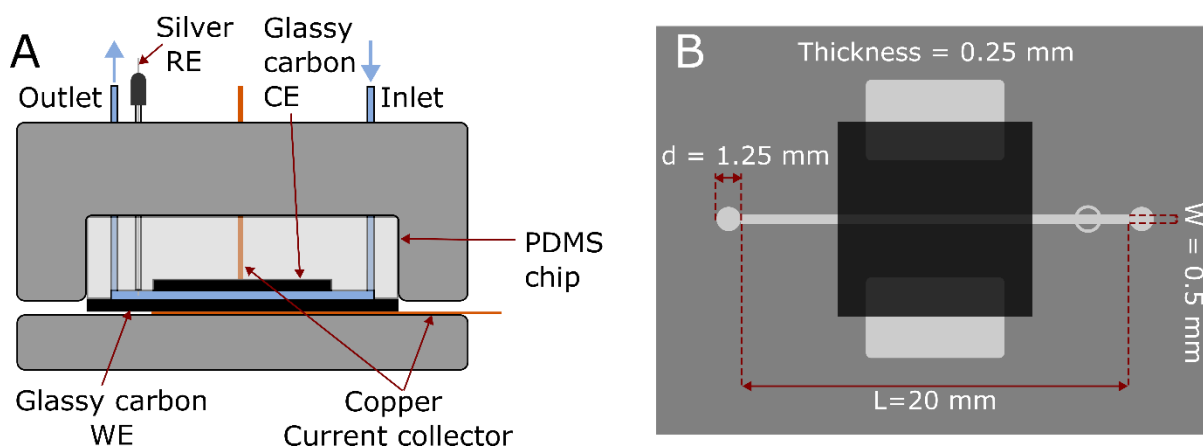


Figure 2-1. **(A)** Simplified scheme of the PDMS microfluidics electrochemical flow cell (not to scale); **(B)** Photoresist mold for the PDMS casting of the electrochemical flow cell ($L = 20\text{ mm}$, $W = 0.50\text{ mm}$, $Z = 0.25\text{ mm}$, $d = 1.25\text{ mm}$, the transparent black square represents the

Chapter 2

placement of counter electrode assembly, the circle represents the hole for the reference electrode), the scheme is scaled 300% for clarity.

A 25 x 10 x 0.3 mm glassy carbon SIGRADUR® plate was used as the working electrode. The plate was masked with a 25- μ m-thick Kapton tape with a 2 x 4 mm² rectangle opening (Figure 2-2A). The mask made the electro-active area of the working electrode five times smaller than the counter electrode. The electrical connector was made by sticking a piece of copper tape on the other side of the glassy carbon plate. The reference electrode was prepared by inserting a 0.3 mm diameter silver wire (99.99%, Goodfellow) into a short section of a 1/16 inch outer diameter, 0.5 mm inner diameter PTFE tubing. The silver wire was adjusted so that one end was flush with the tubing while the other was glued to the tubing with Torr Seal epoxy, leaving about 2 cm protruding outside the tubing.

The actual photographs of the PDMS cell are shown in Figure 2-2B-D. The working electrode was placed under the PDMS chip to assemble the cell, so the channel was covered entirely, as shown in Figure 2-2D. Then the chip and the working electrode were placed inside a 3D-printed holder, also made of Veroclear®, consisting of a bottom and a top cover (Figure 2-2E). The two parts were held together by six M3 nuts and bolts, which pressed the PDMS chip tightly against the working electrode, creating a leak-free seal between the channel and the working. After that, the input, output, and reference electrode tubing were connected to the chip using 1/16 inch outer diameter and 0.2 mm inner diameter Teflon tubing (Figure 2-2E).

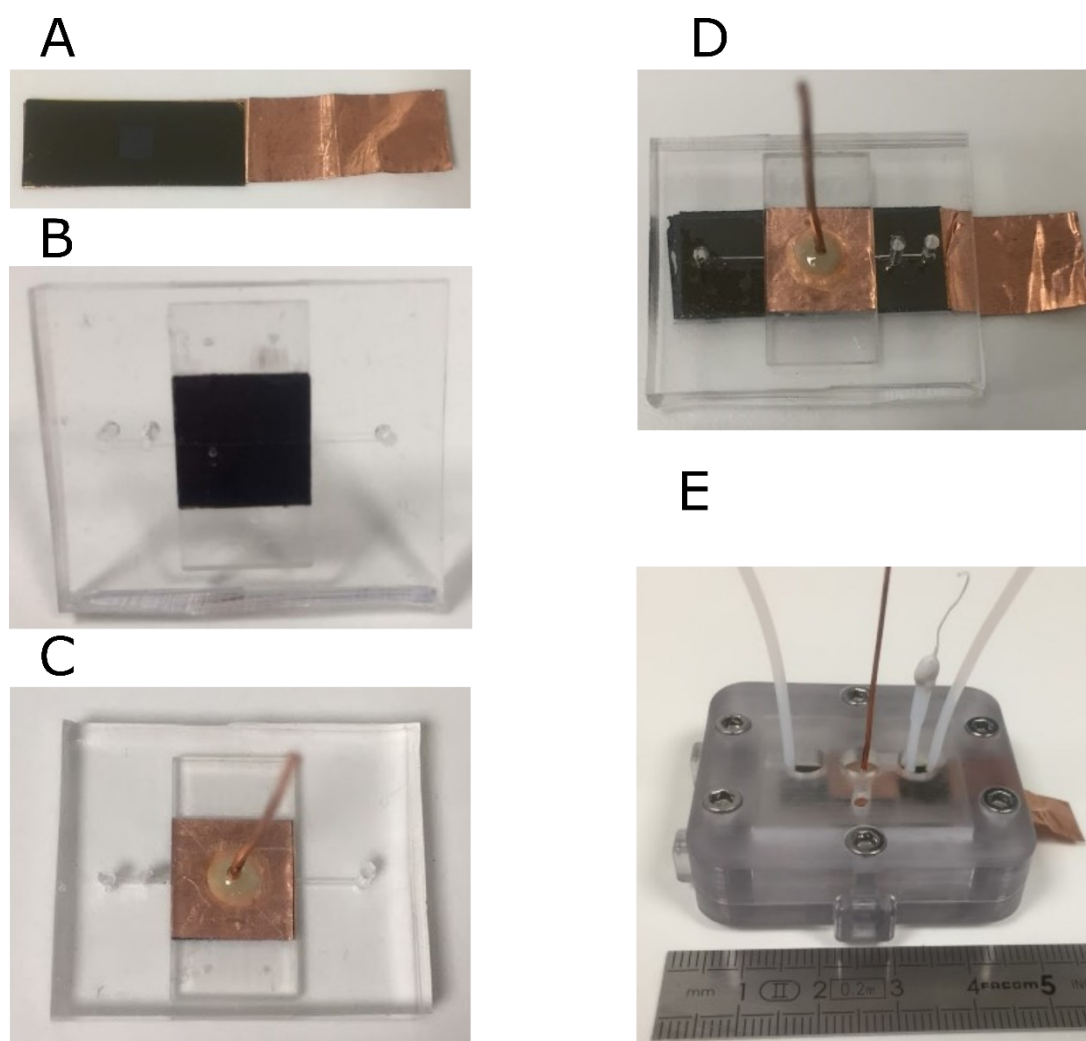


Figure 2-2. **(A)** Glassy carbon working electrode with a Kapton mask; **(B)** bottom view of PDMS chip; **(C)** top view of PDMS chip; **(D)** PDMS chip on top of GC working electrode; and **(E)** PDMS chip fully assembled inside the 3D-printed holder

2.2.2 Electrochemistry performance

Cyclic voltammetry and chronoamperometry were performed with the PDMS cell using the flow system described in the annex. The electrolyte flow rate was kept at $15 \mu\text{L}/\text{min}$, and the catalyst used was cobalt phthalocyanine (CoPc) with a loading of $15 \text{ nmol}/\text{cm}^2$. Figure 2-3A shows the cyclic voltammograms of two CoPc-modified electrodes under an Ar and CO_2 environment and a CoPc-free modified electrode under a CO_2 -saturated electrolyte. Without the presence of the catalyst, no electrochemical activity was observed, as illustrated by the black curves in Figure 2-3A. When cyclic voltammetry was performed with a CoPc-modified electrode under Ar, a wave at highly negative potential appeared, corresponding to water reduction. A broad reduction wave was also visible around -0.9 V , which might indicate oxygen reduction activity. With a CO_2 -saturated electrolyte, the CoPc-modified electrode exhibited an increase in current in the last wave of the cyclic voltammogram at less negative potential. This current rise might indicate that the catalyst was reducing CO_2 , and the reduction partially

suppressed the water reduction activity. The broad peak near the -0.9 V point was still visible, signifying that oxygen was still present in the system.

Figure 2-3B shows the electrolysis current profiles of three electrodes in similar conditions to the cyclic voltammetry experiments. The trend of these curves was analogous to the cyclic voltammetry results, where a CoPc-modified electrode exhibited the highest activity in CO_2 -saturated electrolyte. Without the presence of CoPc or CO_2 , little to no electrochemical activity was observed. The noise level in experiments involving CO_2 was significantly higher than in experiments under Ar. Whenever CO_2 -saturated electrolyte was used, the bubbles formed in the pumping process tended to disturb the electrochemical technique when they passed by the electrode's surface, causing the observed noise. This effect intensified in the case of electrolysis, where a high amount of gas products was formed. These gases formed at the surface of the electrode in a constraint channel in a much more considerable amount compared to a cyclic voltammetry experiment, in combination with their low solubility in aqueous media, contributing significantly to the noise in these curves. These gas bubbles also interrupted the laminar flow inside the microfluidic chip, causing the catholyte and the anolyte to mix in the middle of the cell, resulting in unstable electrolysis. Nevertheless, the cyclic voltammograms and the electrolysis curves showed that the PDMS microfluidic cell can perform electrochemistry experiments and that CoPc was responsible for the CO_2 reduction catalytic activity.

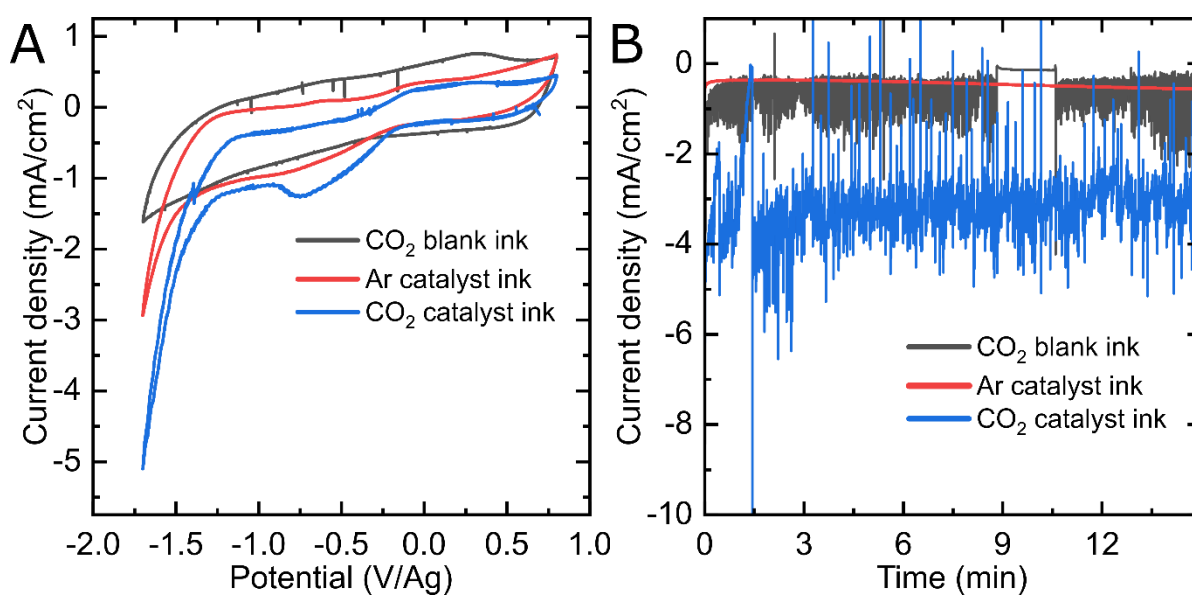


Figure 2-3. **(A)** Cyclic voltammograms and **(B)** electrolysis curves of electrodes modified with CoPc-free ink in CO_2 environment (black), CoPc ink in Ar (red), and CO_2 environment (blue). The electrolyte is 0.1 M KCl, the applied potential is -1.6 V vs. pseudo-Ag, and the flow rate is 15 $\mu\text{L}/\text{min}$.

2.2.3 Evaluation and perspectives

Despite these initial electrochemistry results, using a PDMS chip as an electrochemical

cell for electrocatalysis applications presented several drawbacks. First, the laminar separation of the catholyte and anolyte between the working and counter electrodes was not constantly achieved due to the gas bubbles generated from CO_2 and water reduction. In addition, using a pseudo reference electrode made converting the applied potential to an absolute potential scale a challenging task, given the changing chemical composition of the electrolyte. Finally, PDMS is a soft and permeable material. Therefore, gas products could escape the chip, and the geometry of the channel was changed when the chip was pressed tightly against the working electrode. The permeability of PDMS might also be responsible for oxygen contaminating the electrolyte; hence the oxygen reduction activity observed in cyclic voltammetry experiments. Due to these reasons, a sequential system to reduce CO_2 to high-value products has not been built. A different design for an electrochemical flow cell is necessary to address these problems.

Inspired by the work of Jensen and co-workers,²¹ we fabricated a microfluidic cell where the gasket itself acts as the flow channel. A fluorinated ethylene propylene gasket (127 μm thickness) with a 15 x 5 mm^2 rectangular cutout was sandwiched between two glassy carbon plates (25 x 10 x 0.3 mm^3), as shown in Figure 2-4. The inlet and outlet holes were etched through the glassy carbon plate by applying an oxidative potential of 4V in a 1 M KOH solution. The plate was masked with a piece of Kapton tape (25 μm thickness), leaving the locations of the two holes exposed to the electrolyte solution. The reference electrode was a silver wire glued to a cutout on the side of a polyether ether ketone (PEEK) tubing. The silver wire was flush with the end of the tube, ensuring constant contact between the reference electrode and the electrolyte. This microfluidic electrochemical cell was not made of PDMS; hence the geometry of the channel is well-defined, and the gas permeability is limited. However, a reliable seal between the gasket and the electrodes was not always achieved. Consequently, the cell was prone to leakage, and electrochemistry was not tested. Overall, this microfluidic cell is still in an early stage of development, and more optimization is necessary.

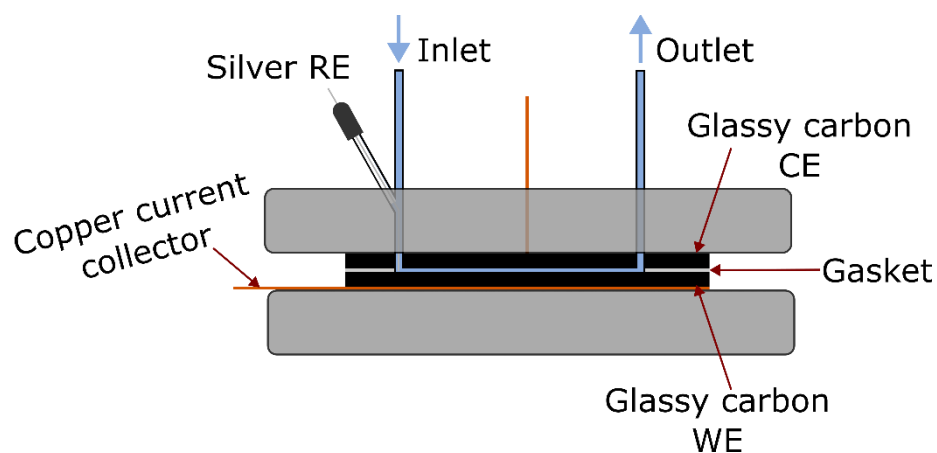


Figure 2-4. Scheme of the gasket microfluidics electrochemical flow cell (not to scale)

2.3 3D-printed millifluidic flow cell

2.3.1 Design and fabrication

The electrochemical cell design was inspired by the work of Ager and co-workers.⁵ The two flow plates shown in Figure 2-5A were the main components where the reactions occurred. The two pieces had similar designs and thicknesses (2.5 mm), except the cathodic one had an additional part with a hole on its side to mount the reference electrode. The compartments in both pieces had the dimensions of 15 x 5 x 2.5 mm³. The two covers held the two flow plates and other cell components (Figure 2-5B). The bottom cover contained a window for spectro-electrochemical experiments. This window had a 45-degree taper to avoid interfering with the beam when it hit the working electrode at an angle (Figure 2-5C). The top cover had a smaller window for accessing the counter electrode when the cell was fully assembled. The slots and holes in the two covers were for mounting the cell and electrical connection, respectively. The plates and the covers had eight holes, with four inner holes for the bolts and four outer ones for alignment during the assembly.

The flow plates and covers were 3D printed using the Objet30 Pro Polyjet 3D printer (Stratasys), with VeroClear printing materials and SUP706 support materials. After printing, the cell was cleaned and sonicated in a diluted solution of NaOH (~2%) to remove the support material. The inlet and outlet of the cell were made by gluing PEEK tubings (ID 0.75 mm, OD 1/16 inch) to the designated hole with Torr-seal epoxy, with the end of the tubes being flush with the flow channel. The reference electrode was held in place with a 3D-printed piece, an O-ring, and two bolts. The assembly of the electrochemical cell is shown in Figure 1. The four layers were pressed tightly together by four M3 bolts. Two silicone gaskets helped create the seals between the electrodes and the flow plates. A 212 Nafion membrane was sealed against the two flow plates using two other silicon gaskets that separated the catholyte and the anolyte. The annex of the thesis contains more details regarding the cell assembly procedure.

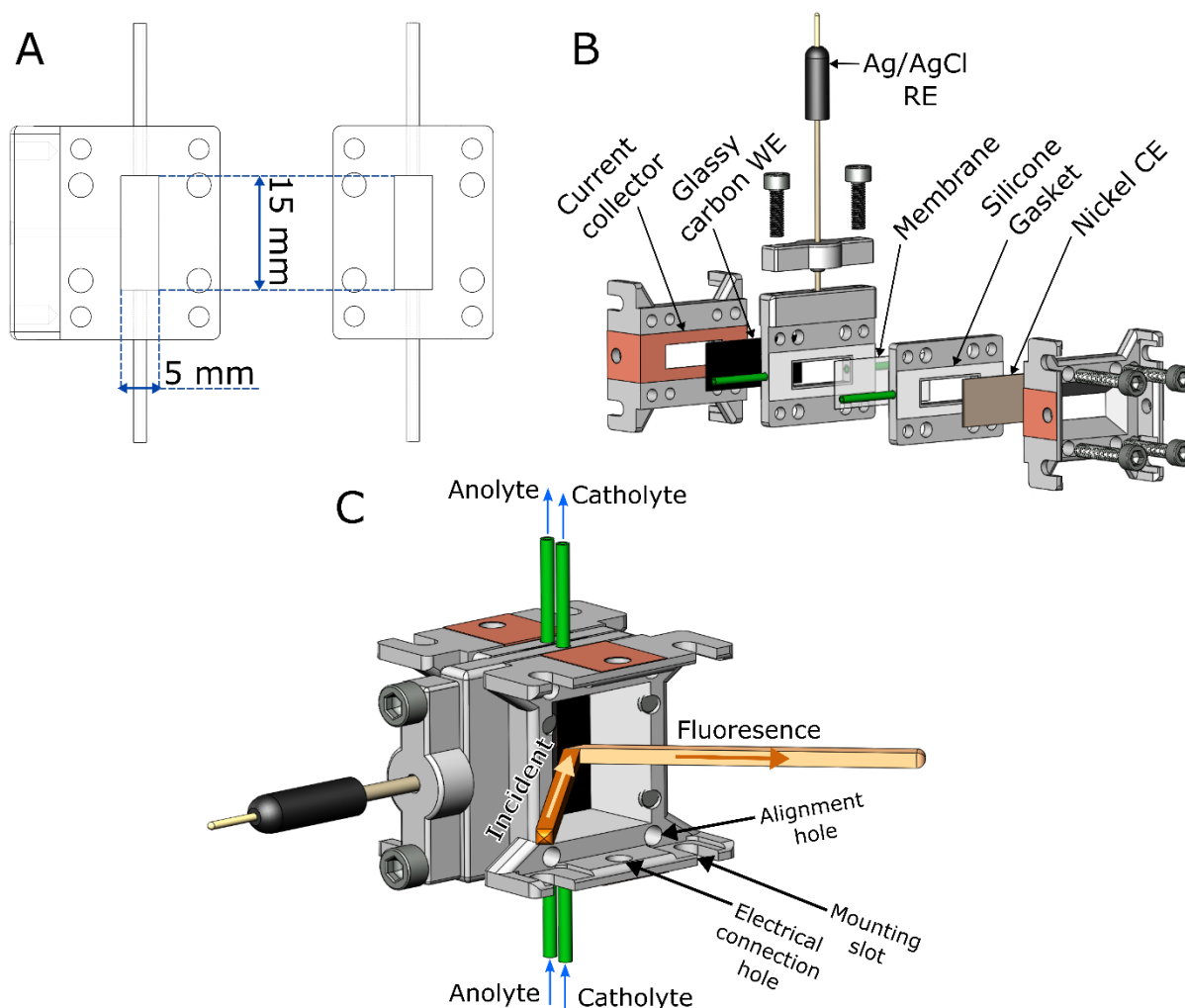


Figure 2-5. **(A)** Dimensions of the cathode and anode flow plates **(B)** Exploded view of the cell, with WE, CE, and RE standing for working electrode, counter electrode, and reference electrode, respectively. **(C)** View the fully assembled cell and beam bath from synchrotron radiation.

2.3.2 Flow characterization

The Reynold number predicts whether a flow system is in the laminar or turbulent flow region. At a Reynold number lower than 2000, the fluid flow stays in the laminar region, where fluid particles stay in parallel lines, with diffusion as the only mass transport mode.²² When the Reynold number is large, turbulent flow dominates, where the flow pattern is chaotic, and both convection and diffusion mass transport modes occur. As discussed above, if the flow pattern in the electrochemical cell is laminar, membrane-less electrolysis can be carried out. The Reynolds number associated with our electrochemical flow cell when the total aqueous electrolyte flow rate at 2 mL/min is calculated as follows:

$$Re = \frac{\rho u L}{\mu} = \frac{997 \frac{\text{kg}}{\text{m}^3} \times 8.90 \times 10^{-4} \text{Pa} \cdot \text{s} \times 5.1 \times 10^{-3} \text{m}}{1.27 \times 10^{-3} \text{m/s}} \approx 2.6$$

where ρ (kg/m^3) is the density of the fluid, μ ($\text{kg}/(\text{m} \cdot \text{s})$) is the dynamic viscosity of the

fluid, L (m) is the characteristic linear dimension, and u (m/s) is the flow speed of a fluid particle. In a rectangular channel, the characteristic linear dimension is represented by the hydraulic diameter $D_H = \frac{4A}{P}$, where A is the cross-section of the flow and P is the perimeter of the wetted area. The flow speed is calculated by dividing the flow rate by the cross-section of the flow channel. Since the electrolyte is a diluted salt solution, the density and dynamic viscosity of the electrolyte solution can be considered similar to water. As laminar flow occurs at $Re < 2000$, the Reynold number in the electrochemical cell system indicates that the flow is strictly in the laminar regime.

A mixing test was performed to verify the laminar flow result. The cell was assembled as previously described, except without a membrane between the plates. Solutions of water and green food coloring dye were flown at the same rate (1 mL/min) through the cathodic and anodic plates using a peristaltic pump. As shown in Figure 2-6, there was little to no solution mixing after flowing through the cell. This result indicated that the laminar flow condition is achieved in the cell.

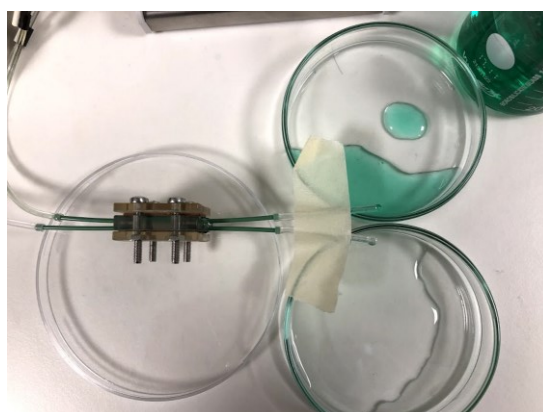


Figure 2-6. Laminar flow mixing test

Although the preliminary mixing test shows the solutions were well separated, membrane-less electrolysis was more complicated. Firstly, the flow rate of the two channels in the peristaltic pump tended to deviate slightly, resulting in mixing as the flow rate in the two flow plates was not the same. More importantly, the reduction of CO_2 (and water) on the cathode side and water oxidation on the anode side generated a significant amount of bubbles. These bubbles could disrupt the cell's laminar flow, causing mixing to occur. Therefore, a membrane was still necessary for a standard electrochemical experiment.

2.3.3 Electrochemistry performance

Figure 2-7 shows the cyclic voltammograms and electrolysis curves of two FePc-modified electrodes under an Ar and CO_2 environment and a FePc-free modified electrode under a CO_2 -saturated electrolyte. Unlike in the PDMS microfluidic cell, the electrolysis experiments in the 3D-printed flow cell could last at least two hours with a

lower noise level. The larger dimensions of the flow channel allowed the bubbles generated during electrolysis to be evacuated faster. Consequently, fewer bubbles interfered with the reference electrode, reducing the noise experienced. The Nafion membrane also prevented the crossing over of the catholyte and the anolyte, as the laminar flow was not achieved. The electrochemistry experiments using the 3D-printed cell and the resulting products will be discussed in more detail in the following chapters.

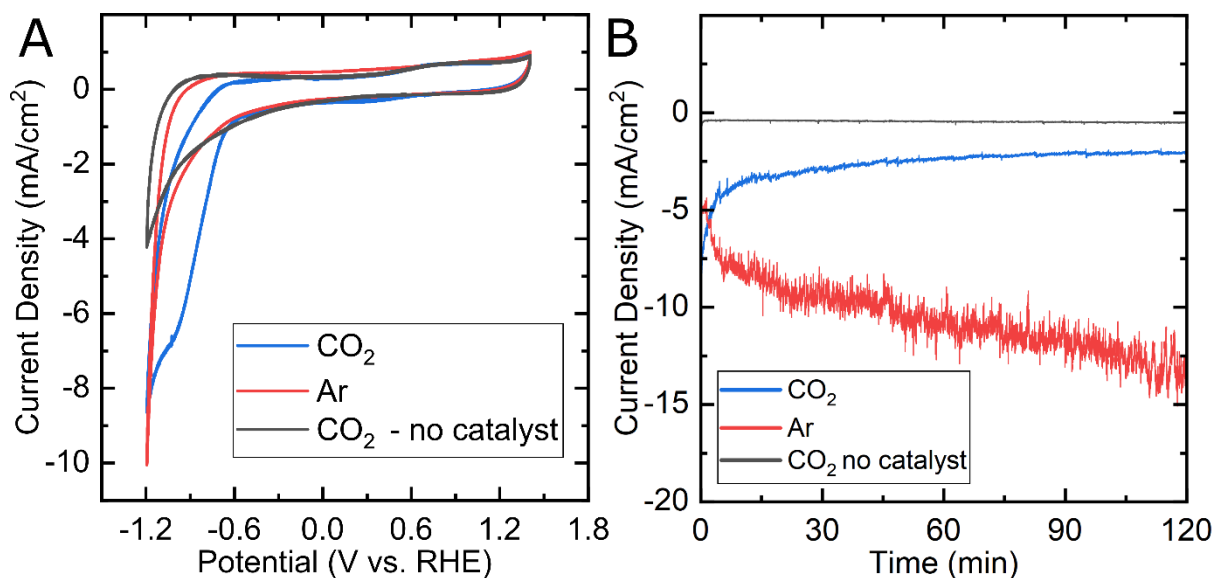


Figure 2-7. **(A)** Cyclic voltammograms and **(B)** electrolysis curves of electrodes modified with FePc-free ink in CO₂ environment (black), FePc ink in Ar (red), and CO₂ environment (blue). The electrolyte is 0.1 M KHCO₃, the applied potential is -1.1 V vs. RHE (-1.7 V vs. Ag/AgCl), and the flow rate is 1 mL/min.

2.4 Reactants and products concentration profiles

To characterize the distribution of the reactant and products during the electrolysis experiment described above, we performed a finite element analysis of the fluid flow inside the cell.

2.4.1 The geometry of the flow cell: 2D model and meshing

A two-dimensional model of our electrochemical flow cell was built with the COMSOL software version 5.2. The model consisted of the working electrode half of the cell, shown in Figure 2-8A. Figure 2-8B overlays the model on a picture of the actual electrochemical cell. Table 2-1 summarizes the geometric parameters of the model. The distance from the working electrode to the Nafion membrane included the thickness of the flow channel and the thickness of the two silicone gaskets between the electrode and the cell and between the membrane and the cell. The width of the channel was not used to build the model, but it was used to derive the active area of the electrode, which will be described in more detail in the following section. The model was meshed automatically using Physics-control meshed sequence with *Finer*

element size. The model after meshing is shown in Figure 2-8C.

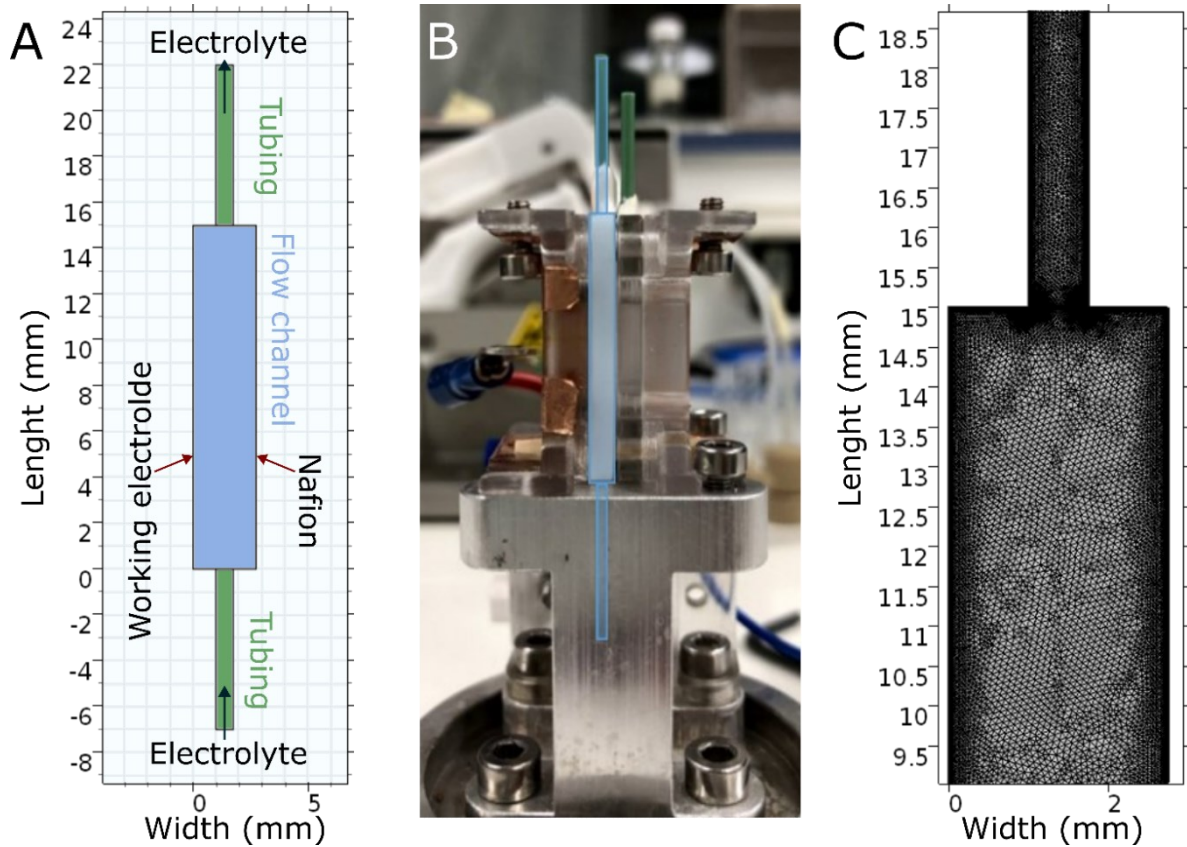


Figure 2-8. 2D model of the electrochemical flow cell built in COMSOL 5.2 (A); Overlay of the model geometry on an actual picture of the electrochemical flow cell (B); a zoom in the model after meshing (C)

Table 2-1. Dimension parameters for modeling the electrochemical flow cell

Parameters	Value	Unit
Tubing radius	0.375	mm
Tubing length	7	mm
Flow channel width	5	mm
Flow channel length	15	mm
Flow channel thickness	2.5	mm
Gasket thickness	0.127	mm

2.4.2 Multiphysics: Laminar flow and transport of diluted species

We based the simulation of our electrochemical flow cell on the model established by Gatrell *et al.*²³ and Ager *et al.*⁵

Chapter 2

As the Reynold number indicates the flow stayed in the laminar region, the laminar flow physics module was used to simulate the flow of electrolytes in our cell. This physics module uses the Navier-Stokes and the continuity equations to model the behavior of the fluid. The Inlet boundary condition was applied to the bottom boundary of the bottom tubing. Normal inflow velocity mode was used, and the velocity of the fluid was calculated by dividing the flow rate by the cross-section area of the tubing. The outlet boundary condition was applied to the top boundary of the top tubing, with outlet pressure equal to zero, and the suppress backflow option was enabled. No slip boundary condition was applied to all other boundaries. Initial values of velocity and pressure across all domains were set to zero. Under the above-mentioned conditions, the Navier-Stokes and the continuity equations are as follows:

$$\rho(u \cdot \nabla) = \nabla \cdot [-\rho I + \mu(\nabla u + (\nabla u)^T)] + F$$
$$\rho \nabla \cdot (u) = 0$$

where ρ , u , μ , and T are the density (kg/m^3), the velocity (m/s), the viscosity ($\text{Pa}\cdot\text{s}$), and the temperature (K) of the fluid, respectively. F is the external forces and ∇ is the divergence operator.

The transport of dilute species physics module was used to calculate the consumption rate of CO_2 and the generation rate of CO . Two modes of mass transport were considered: diffusion and convection. The mass balance equation is the governing equation of this physics module:

$$\nabla \cdot (-D_i \nabla c_i) + u \cdot \nabla c_i = R_i$$

where for species i , D is the diffusion coefficient (m^2/s), c is the concentration (mol/m^3), u is the velocity (m/s), R is the reaction rate ($\text{mol}/(\text{m}^3\cdot\text{s})$), and ∇ is the divergence operator.

The velocity field resulting from the laminar flow physics calculation was used in the model inputs. A flux boundary condition was applied at the working electrode, with one flux accounting for CO_2 and the other accounting for CO . The equation describes the flux as follows:

$$N_i = -D_i \nabla c_i + u c_i$$

where for species i , N is the flux ($\text{mol}/\text{m}^2\cdot\text{s}$), D is the diffusion coefficient (m^2/s), c is the concentration (mol/m^3), u is the velocity (m/s), and ∇ is the divergence operator.

The flux of CO_2 ($\text{mol}/(\text{m}^2\cdot\text{s})$) was calculated based on the current density resulting from electrolysis at -1.1 V vs. RHE in CO_2 and the faradaic efficiencies of all carbon-containing species as follows:

$$Flux = -\frac{j \times FE}{F}$$

Chapter 2

$$= -\frac{j}{F} \times \left(\frac{FE_{CO}}{2} + \frac{FE_{CH_4}}{8} + \frac{FE_{C_2H_6}}{7} + \frac{FE_{C_3H_6}}{6} + \frac{FE_{C_3H_8}}{20/3} + \frac{FE_{C_2H_4}}{6} + \frac{FE_{C_4H_{10}}}{6.5} \right)$$

where j (A/m²) is the electrolysis current density at -1.1V vs. RHE in CO₂, F is the Faraday constant (C/mol), and FE is the Faradaic efficiencies of the corresponding products. The Faradaic efficiencies were divided by the number of electrons needed to be injected into one molecule of CO₂ to reduce it to the corresponding species.

Similarly, the flux of CO (mol/(m².s)) was calculated based on the electrolysis current density at -1.1 V vs. RHE in CO₂ and the faradaic efficiencies of CO:

$$Flux = -\frac{j \times FE_{CO}}{F}$$

where j (A/m²) is the electrolysis current density at -1.1 V vs. RHE in CO₂, F is the Faraday constant (C/mol), and FE_{CO} is the Faradaic efficiency of CO. The current density and the Faradaic efficiency were obtained from electrolysis experiments that will be discussed in more detail in the next chapter.

Like the inlet and outlet boundary conditions, inflow and outflow boundary conditions were applied to the bottom-most and top-most boundaries of the tubing, respectively. The concentration of the inflow was set to be the saturated concentration of CO₂ at 25°C (33.4 mM). No flux boundary condition was applied to all other boundaries. Initial values of CO₂ concentration in all domains were set to 33.4 mM, and that of CO was to be zero. Table 2-2 summarizes the parameters used in the two physics modules.

Table 2-2. Physics parameters used for laminar flow and transport of diluted species physics

Parameters		Value	Unit	Reference
CO ₂ diffusion coefficient at 25°C		1.92 x 10 ⁻⁹	m ² /s	Ager <i>et al.</i> ⁵
CO diffusion coefficient at 25°C		2.03 x 10 ⁻⁹	m ² /s	Ager <i>et al.</i> ⁵
CO ₂ saturated concentration in water at 25°C		33.4	mM	Ager <i>et al.</i> ⁵
Current density at -1.1 V vs. RHE		2.52	mA/cm ²	Experimental
Faradaic efficiencies at -1.1 V vs. RHE	CO	23.25	%	Experimental
	CH ₄	3.81		
	C ₂ H ₆	0.22		
	C ₃ H ₆	0.21		
	C ₃ H ₈	0.11		
	C ₂ H ₄	0.1		

	C ₄ H ₁₀	0.11		
Water viscosity at 25°C		8.90 x 10 ⁻⁴	Pa/s	COMSOL
Water density at 25°C		997	kg/m ³	COMSOL

2.4.3 Concentration profile throughout the electrochemical cell

The concentration profiles of CO₂ and CO in the electrochemical cell are illustrated in Figure 2-9, which shows the conversion of CO₂ to CO only took place close to the electrode surface, and the majority of CO₂ passing through the cell was not consumed. This agrees with the gas chromatograph result, as the amount of CO₂ after 2-hour electrolysis at -1.1 V vs. RHE stayed relatively unchanged. However, since the electrolyte flow near the corners of the cell was significantly slower, one can observe the decrease of CO₂ and buildup of CO in these regions, which can exceed the saturated concentration of CO in an aqueous solution.

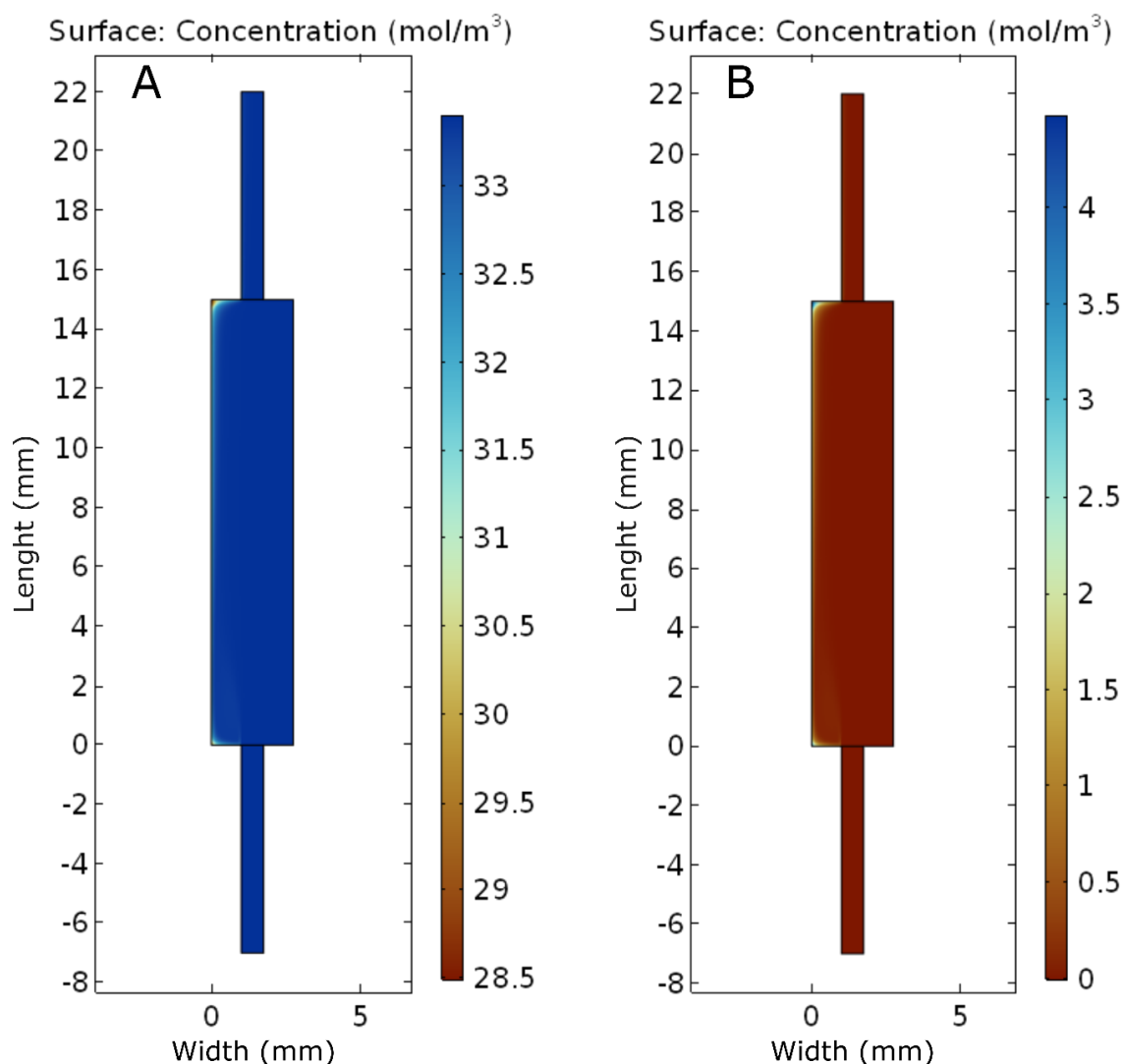


Figure 2-9. Concentration profile (in mmol/L) in the electrochemical cell of CO₂ (A) and CO (B) when a constant potential of -1.1 V vs. RHE is applied. The color graph shows the concentrations.

2.4.4 Concentration profile at specific locations

To better characterize the concentration profile in Figure 2-9, the concentrations of CO₂ and CO at the entrance ($y = 0$), in the middle ($y = 7.5$ mm), and at the end ($y = 15$ mm) were plotted as a function of distance from the electrode surface in Figure 2-10. The results show significant consumption of CO₂ in the corner of both the entrance and the end, resulting in the increased concentration of CO in these positions above the saturated concentration of CO in an aqueous solution (1 mM). These concentration patterns were disrupted at 1 mm from the electrode since the electrolyte entered and exited the tubing at this position. In the middle of the electrode, which represented most of the electrode surface area, the decrease of CO₂ concentration and CO concentration was less pronounced than in the corners. However, in the close vicinity of the electrode (less than 20 μm), CO still existed in a supersaturated state (*ca.* 1.5 mM).

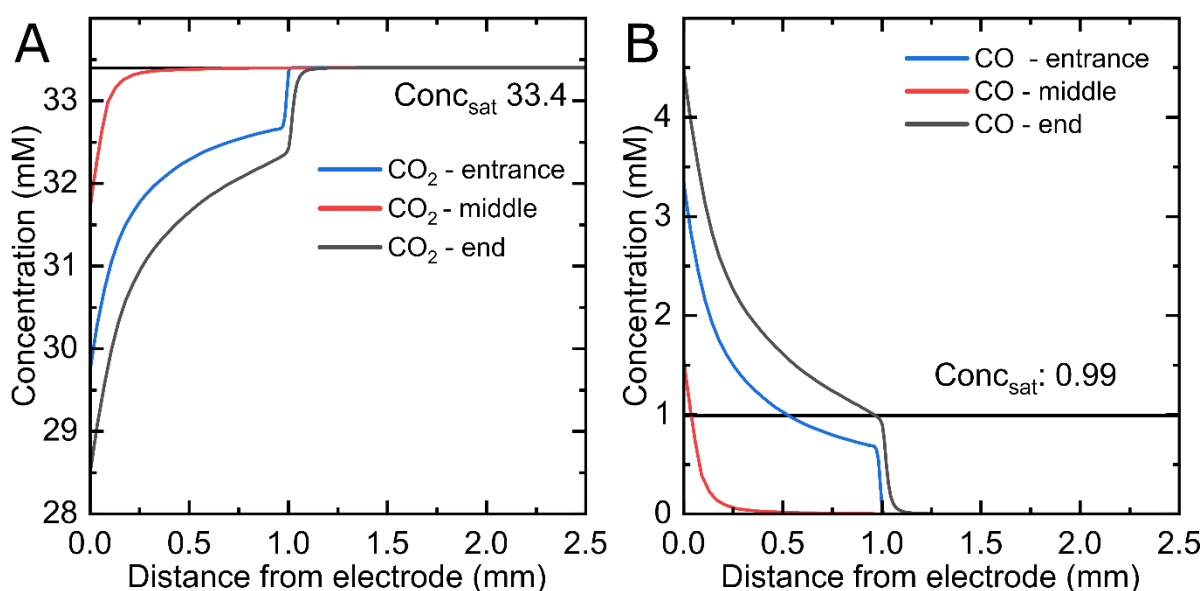


Figure 2-10. Concentration profile as a function of distance from the electrode at the entrance ($y = 0$), in the middle ($y = 7.5$ mm), and at the end ($y = 15$ mm) of the electrochemical cell of CO₂ (a) and CO (b) when a constant potential of -1.1 V vs. RHE is applied.

2.5 Millifluidic cell evaluation and perspective

Although the laminar flow inside the cell was not achieved, overall, the 3D-printed millifluidic flow cell was a reliable device for lab-scale electrochemical experiments. The 3D-printing fabrication method enabled quick changes to be made, making modifying the cell to adapt to specific needs (e.g., *operando* spectro-electrochemistry) a more straightforward task. Moreover, the versatile design allowed different electrode and membrane materials to be used.

However, several aspects of the cell are subject to improvement. First, the cell was made of a plastic material only compatible with water-based electrolytes in mild

conditions. Therefore, experiments in harsh conditions, such as at high temperatures and pressure or with organic solvents as the electrolyte, were out of the cell's capability. Another drawback of the cell was the liquid connections with a PEEK tubing glued to the 3D-printed flow plates. These connections could degrade and form cracks over repeated use of the cell, which was prone to leakage. Finally, while 3D printing could produce a cell quickly, it often results in the pieces having rough surfaces, making sealing and cleaning the cell a complicated task. In fact, a cell with incorporated flat-bottom fittings liquid connection was fabricated to avoid the glue joint, but the rough surface prevented the connectors from forming a good seal. A cell fabricated with PEEK or Teflon, with dedicated liquid connection ports built into the flow plates, would address the mentioned drawbacks. PEEK or Teflon are robust materials that can withstand experiments in demanding conditions. And a smooth surface finish with precise built-in liquid connections can be achieved from the machining process required to fabricate this thermoplastic.

2.6 Conclusion

In this chapter, we presented the design and fabrication of a PDMS microfluidic cell to carry out membraneless electrolysis and to build a system for the cascade reduction of CO₂. Using a CoPc catalyst, we demonstrated that CO₂ was reduced to CO in the cell. However, the PDMS cell behaved poorly in terms of electrochemistry, as the small dimensions of the cell prevented the gas bubbles from the products and the reactant from being evacuated quickly, leading to unstable electrochemistry. Moreover, while PDMS is the standard material for microfluidic devices, it was unsuitable for this electrochemical application due to its inherent flexibility and gas permeability. We then proposed a different design for the microfluidic cell without using PDMS. Although the bubble problem proved complicated, reducing CO₂ in a thin channel is still an attractive idea, as it allows CO₂ to be consumed completely, which is challenging to achieve in a cell employing a gas diffusion electrode due to the high CO₂ flux.

In parallel, we presented the development of a 3D-printed millifluidic electrochemical flow cell capable of performing *operando* X-ray absorption spectroscopy. The laminar flow conditions were achieved in the cell, but gas bubbles in a CO₂-reducing experiment caused the turbulent flow to occur in the cell's flow channels. Therefore, a membrane was necessary for the performance of the cell. With a membrane employed, CO₂ electrolysis using an FePc catalyst could last at least two hours with a lower noise level than the PDMS cell. The concentration profiles of the reduced products were characterized using finite element analysis based on laminar flow and transport of diluted species physics. The calculation showed CO concentration existed in a supersaturated concentration near the electrode surface, but the CO₂ conversion rate was poor. Finally, an improved version of the cell was proposed.

2.7 Bibliography

- (1) Kroutil, W.; Rueping, M. Introduction to ACS Catalysis Virtual Special Issue on Cascade Catalysis. *ACS Catal.* **2014**, *4* (6), 2086–2087. <https://doi.org/10.1021/cs500622h>.
- (2) Benson, A. A.; Bassham, J. A.; Calvin, M.; Goodale, T. C.; Haas, V. A.; Stepka, W. The Path of Carbon in Photosynthesis. V. Paper Chromatography and Radioautography of the Products. *J. Am. Chem. Soc.* **1950**, *72* (4), 1710–1718. <https://doi.org/10.1021/ja01160a080>.
- (3) Zhou, X.; Xiang, C. Comparative Analysis of Solar-to-Fuel Conversion Efficiency: A Direct, One-Step Electrochemical CO₂ Reduction Reactor versus a Two-Step, Cascade Electrochemical CO₂ Reduction Reactor. *ACS Energy Letters* **2018**, *3* (8), 1892–1897. <https://doi.org/10.1021/acsenergylett.8b01077>.
- (4) Theaker, N.; Strain, J. M.; Kumar, B.; Brian, J. P.; Kumari, S.; Spurgeon, J. M. Heterogeneously Catalyzed Two-Step Cascade Electrochemical Reduction of CO₂ to Ethanol. *Electrochimica Acta* **2018**, *274*, 1–8. <https://doi.org/10.1016/j.electacta.2018.04.072>.
- (5) Gurudayal; Perone, D.; Malani, S.; Lum, Y.; Haussener, S.; Ager, J. W. Sequential Cascade Electrocatalytic Conversion of Carbon Dioxide to C–C Coupled Products. *ACS Appl. Energy Mater.* **2019**, *2* (6), 4551–4559. <https://doi.org/10.1021/acsaem.9b00791>.
- (6) Nielsen, D. U.; Hu, X.-M.; Daasbjerg, K.; Skrydstrup, T. Chemically and Electrochemically Catalysed Conversion of CO₂ to CO with Follow-up Utilization to Value-Added Chemicals. *Nature Catalysis* **2018**, *1* (4), 244–254. <https://doi.org/10.1038/s41929-018-0051-3>.
- (7) Gotico, P.; Del Vecchio, A.; Audisio, D.; Quaranta, A.; Halime, Z.; Leibl, W.; Aukauloo, A. Visible-Light-Driven Reduction of CO₂ to CO and Its Subsequent Valorization in Carbonylation Chemistry and ¹³C Isotope Labeling. *ChemPhotoChem* **2018**, *2* (8), 715–719. <https://doi.org/10.1002/cptc.201800012>.
- (8) Li, F.; Li, Y. C.; Wang, Z.; Li, J.; Nam, D.-H.; Lum, Y.; Luo, M.; Wang, X.; Ozden, A.; Hung, S.-F.; Chen, B.; Wang, Y.; Wicks, J.; Xu, Y.; Li, Y.; Gabardo, C. M.; Dinh, C.-T.; Wang, Y.; Zhuang, T.-T.; Sinton, D.; Sargent, E. H. Cooperative CO₂-to-Ethanol Conversion via Enriched Intermediates at Molecule–Metal Catalyst Interfaces. *Nat Catal* **2020**, *3* (1), 75–82. <https://doi.org/10.1038/s41929-019-0383-7>.
- (9) Lum, Y.; Ager, J. W. Sequential Catalysis Controls Selectivity in Electrochemical CO₂ Reduction on Cu. *Energy Environ. Sci.* **2018**, *11* (10), 2935–2944. <https://doi.org/10.1039/C8EE01501E>.
- (10) Xie, C.; Chen, C.; Yu, Y.; Su, J.; Li, Y.; Somorjai, G. A.; Yang, P. Tandem Catalysis for CO₂ Hydrogenation to C₂–C₄ Hydrocarbons. *Nano Lett.* **2017**, *17* (6), 3798–3802. <https://doi.org/10.1021/acs.nanolett.7b01139>.
- (11) Singh, R. K.; Singh, R.; Sivakumar, D.; Kondaveeti, S.; Kim, T.; Li, J.; Sung, B. H.; Cho, B.-K.; Kim, D. R.; Kim, S. C.; Kalia, V. C.; Zhang, Y.-H. P. J.; Zhao, H.; Kang, Y. C.; Lee, J.-K. Insights into Cell-Free Conversion of CO₂ to Chemicals by a Multienzyme Cascade Reaction. *ACS Catal.* **2018**, *8* (12), 11085–11093. <https://doi.org/10.1021/acscatal.8b02646>.
- (12) Whitesides, G. M. The Origins and the Future of Microfluidics. *Nature* **2006**, *442* (7101), 368–373. <https://doi.org/10.1038/nature05058>.
- (13) Wegner, J.; Ceylan, S.; Kirschning, A. Ten Key Issues in Modern Flow Chemistry. *Chemical Communications* **2011**, *47* (16), 4583. <https://doi.org/10.1039/c0cc05060a>.

Chapter 2

- (14) Modestino, M. A.; Fernandez Rivas, D.; Hashemi, S. M. H.; Gardeniers, J. G. E.; Psaltis, D. The Potential for Microfluidics in Electrochemical Energy Systems. *Energy & Environmental Science* **2016**, 9 (11), 3381–3391. <https://doi.org/10.1039/C6EE01884J>.
- (15) Safdar, M.; Jänis, J.; Sánchez, S. Microfluidic Fuel Cells for Energy Generation. *Lab on a Chip* **2016**, 16 (15), 2754–2758. <https://doi.org/10.1039/C6LC90070D>.
- (16) Goulet, M.-A.; Kjeang, E. Co-Laminar Flow Cells for Electrochemical Energy Conversion. *Journal of Power Sources* **2014**, 260, 186–196. <https://doi.org/10.1016/j.jpowsour.2014.03.009>.
- (17) Braff, W. A.; Bazant, M. Z.; Buie, C. R. Membrane-Less Hydrogen Bromine Flow Battery. *Nature Communications* **2013**, 4 (1). <https://doi.org/10.1038/ncomms3346>.
- (18) H. Hashemi, S. M.; Modestino, M. A.; Psaltis, D. A Membrane-Less Electrolyzer for Hydrogen Production across the PH Scale. *Energy & Environmental Science* **2015**, 8 (7), 2003–2009. <https://doi.org/10.1039/C5EE00083A>.
- (19) Lees, E. W.; Mowbray, B. A. W.; Parlane, F. G. L.; Berlinguette, C. P. Gas Diffusion Electrodes and Membranes for CO₂ Reduction Electrolysers. *Nat Rev Mater* **2022**, 7 (1), 55–64. <https://doi.org/10.1038/s41578-021-00356-2>.
- (20) Whipple, D. T.; Finke, E. C.; Kenis, P. J. A. Microfluidic Reactor for the Electrochemical Reduction of Carbon Dioxide: The Effect of PH. *Electrochem. Solid-State Lett.* **2010**, 13 (9), B109. <https://doi.org/10.1149/1.3456590>.
- (21) Mo, Y.; Lu, Z.; Rughoobur, G.; Patil, P.; Gershenfeld, N.; Akinwande, A. I.; Buchwald, S. L.; Jensen, K. F. Microfluidic Electrochemistry for Single-Electron Transfer Redox-Neutral Reactions. *Science* **2020**, 368 (6497), 1352–1357. <https://doi.org/10.1126/science.aba3823>.
- (22) Reynolds' Number - an overview | ScienceDirect Topics. <https://www.sciencedirect.com/topics/engineering/reynolds-number> (accessed 2022-10-10).
- (23) Gupta, N.; Gattrell, M.; MacDougall, B. Calculation for the Cathode Surface Concentrations in the Electrochemical Reduction of CO₂ in KHCO₃ Solutions. *J Appl Electrochem* **2006**, 36 (2), 161–172. <https://doi.org/10.1007/s10800-005-9058-y>.

Chapter 2

3 CHAPTER 3: FORMING C – C BONDS WITH AN IRON PHTHALOCYANINE CATALYST

3.1	Introduction.....	80
3.2	Products distributions based on applied potentials.....	80
3.2.1	Electrocatalysis and products identification.....	80
3.2.2	Origin of the products	83
3.2.3	Products quantifications	85
3.3	FePc catalyst characterization: stability and active site estimation	88
3.3.1	X-ray absorption spectroscopy	88
3.3.2	Infrared spectroscopy	89
3.3.3	Cyclic voltammetry and active site estimation.....	90
3.4	Control experiments with FePc and Fe ₃ O ₄ nanoparticles.....	92
3.4.1	<i>Ex situ</i> X-ray absorption spectroscopy	93
3.4.2	Electrolysis and product distribution	94
3.4.3	Operando X-ray absorption spectroscopy	96
3.4.4	Discussion	97
3.5	C – C bond formation mechanism.....	97
3.6	Conclusion.....	102
3.7	Chapter 3 annex	104
3.7.1	NMR characterization.....	104
3.7.2	Isotopic labeling experiments.....	104
3.7.3	Cyclic voltammetry and active site estimation.....	106
3.7.4	Infrared spectroscopy	108
3.8	Bibliography	109

3.1 Introduction

As discussed in Chapter 1, molecular macrocycles are promising electrocatalysts for reducing carbon dioxide to value-added chemicals. Amongst them, transition metal phthalocyanines and porphyrins are the most noticeable since they exhibit high catalytic activity. However, most of these catalysts produced CO as the main product, with a few studies reporting the formation of further reduced C₁ products such as methanol^{1,2} and methane.³ In the phthalocyanine family, only CuPc has produced species containing C – C bonds with faradaic efficiencies greater than 1%.⁴ However, the molecular nature of the catalyst was not preserved during catalysis, and the C – C bond formation likely happened on copper metal nanoparticles.^{5,6} Ethylene and ethane were reported to form upon the reduction of CO₂ on a CoPc catalyst. Still, their selectivity was less than 1%, and no characterization of the catalyst after the catalysis experiment was performed.⁷ In this chapter, we report that iron phthalocyanine (Figure 3-1) could produce light hydrocarbons upon electrocatalytic reduction of CO₂ in aqueous conditions and neutral pH. Using the 3D-printed millifluidic electrochemical flow cell described in the previous chapter, C₁ to C₄ saturated and unsaturated linear hydrocarbons were evolved under suitable applied electrochemical potential. Isotopic labeling experiments unambiguously showed that these products stem from CO₂. Cyclic voltammetry was employed to estimate the number of active catalytic sites. Control experiments and *operando* X-ray spectroscopic analysis demonstrated that the molecular catalyst remained intact during catalysis and was responsible for the reaction. Based on experiments with alternate substrates, a mechanism is proposed for the C – C bond formation step.

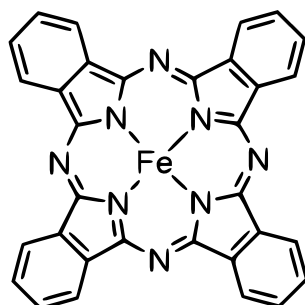


Figure 3-1. Iron phthalocyanine structure

3.2 Products distributions based on applied potentials

3.2.1 Electrocatalysis and products identification

Using the electrochemical cell previously reported in Chapter 2, we performed electrocatalytic experiments using FePc-modified electrodes with the catalyst loading of 80 nmol/cm². The electrolysis potentials ranged from -0.7 V vs. RHE (-1.3 V vs. Ag/AgCl) to -1.1 V vs. RHE (-1.7 V vs. Ag/AgCl). The lower limit of -1.1 V was the most negative potential at which the current was stable enough for extended electrolysis,

while the upper potential limit of -0.7 V is the least negative potential at which there are significant products of CO_2 reduction. The chapter and the thesis annex contain more details about the experiments.

Figure 3-2A shows three chronoamperometric curves of constant potential electrolysis under Ar or CO_2 for two hours. After poisoning an FePc-modified electrode at -1.1 V vs. RHE under a CO_2 atmosphere for two hours, the main products obtained are CO and H_2 , as shown in the chromatograms of Module A (Figure 3-2C, D). In module B, peaks corresponding to ethylene (C_2H_4), ethane (C_2H_6), propene (C_3H_6), propane (C_3H_8), and n-butane (C_4H_{10}) stand out (Figure 3-2B). Other peaks corresponding to unsaturated C_4 and n-pentane and unsaturated C_5 products can also be observed, albeit with a lower intensity. Methane (CH_4) is also presented in module A (Figure 3-2C). The catholyte was analyzed by ^1H nuclear magnetic resonance (NMR) spectroscopy to check for liquid products, but none was detected (Figure 3-3).

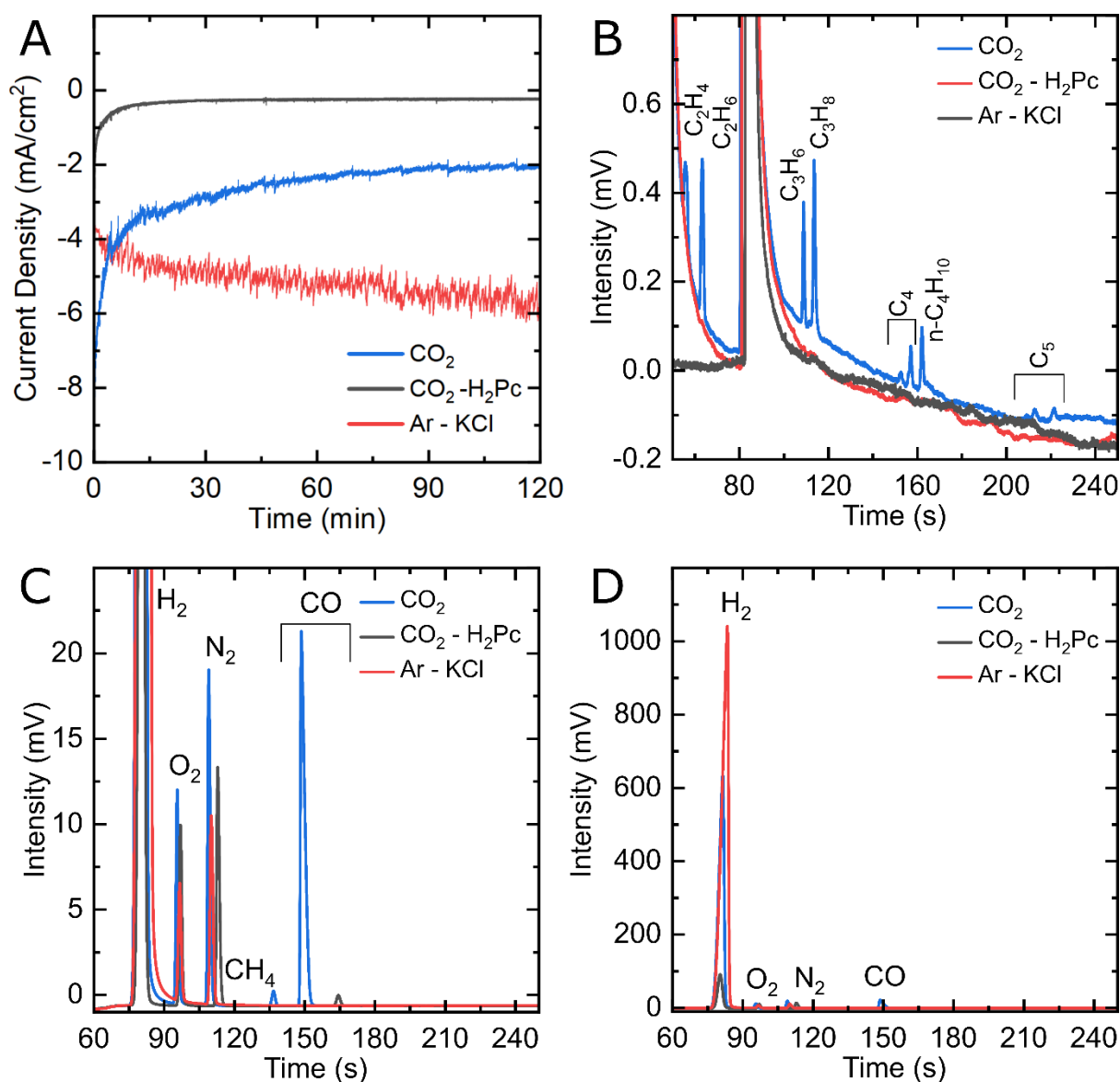


Figure 3-2. **(A)** Chronoamperometric curves, **(B)** Module B gas chromatograms, **(C)** Module A

Chapter 3

gas chromatograms – zoomed, and **(D)** Module A gas chromatogram of FePc-modified electrodes under Ar in 0.1 M KCl (red) and CO₂ in 0.1 M KHCO₃ (blue) and an H₂Pc modified electrode under CO₂ in KHCO₃ (black). Chronoamperometric experiments are performed at -1.1 V vs. RHE for two hours, after which a gas chromatograph (GC) samples their resulting gaseous products.

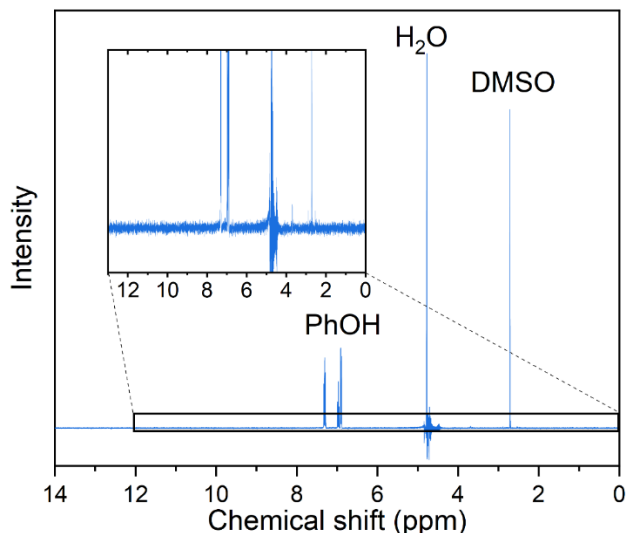


Figure 3-3. ¹H NMR spectrum of catholyte after 2-hour electrolysis in CO₂ saturated electrolyte at -1.1 V vs. RHE with FePc catalyst. The signal from PhOH and dimethyl sulfoxide (DMSO) are from internal references of the sample.

Control experiments were performed to ensure that FePc catalyzed the reduction of CO₂ into the products observed. When a FePc-modified electrode was set under catalytic conditions (-1.7 V vs. Ag/AgCl) in an Ar-saturated KHCO₃ electrolyte, hydrogen was the main product detected after two hours of electrolysis, with a trace amount of CO and hydrocarbons, as shown in Figure 3-4. The observed carbon products can be attributed to the small amount of CO₂ in equilibrium with the KHCO₃ electrolyte. In fact, a similar FePc-modified electrode, at the same potential, under a CO₂-free environment (Ar-saturated KCl electrolyte), produces only H₂ (Figure 3-2B, C, and D). The current density observed is higher than under CO₂, indicating a high activity of FePc towards hydrogen evolution in a CO₂-free environment at a high overpotential. When an H₂Pc-modified electrode was poised at -1.1 V in a CO₂-saturated KHCO₃ electrolyte, a twenty-fold decrease in current density was observed compared to an FePc-modified electrode, indicating negligible catalytic activity without the Fe center. In agreement with the low catalytic activity, the main product detected was H₂, with a minuscule amount of CO (Figure 3-2C). These results strongly indicate CO₂ as the source of the carbon products observed and underline the essential role of the metal center in the catalytic process.

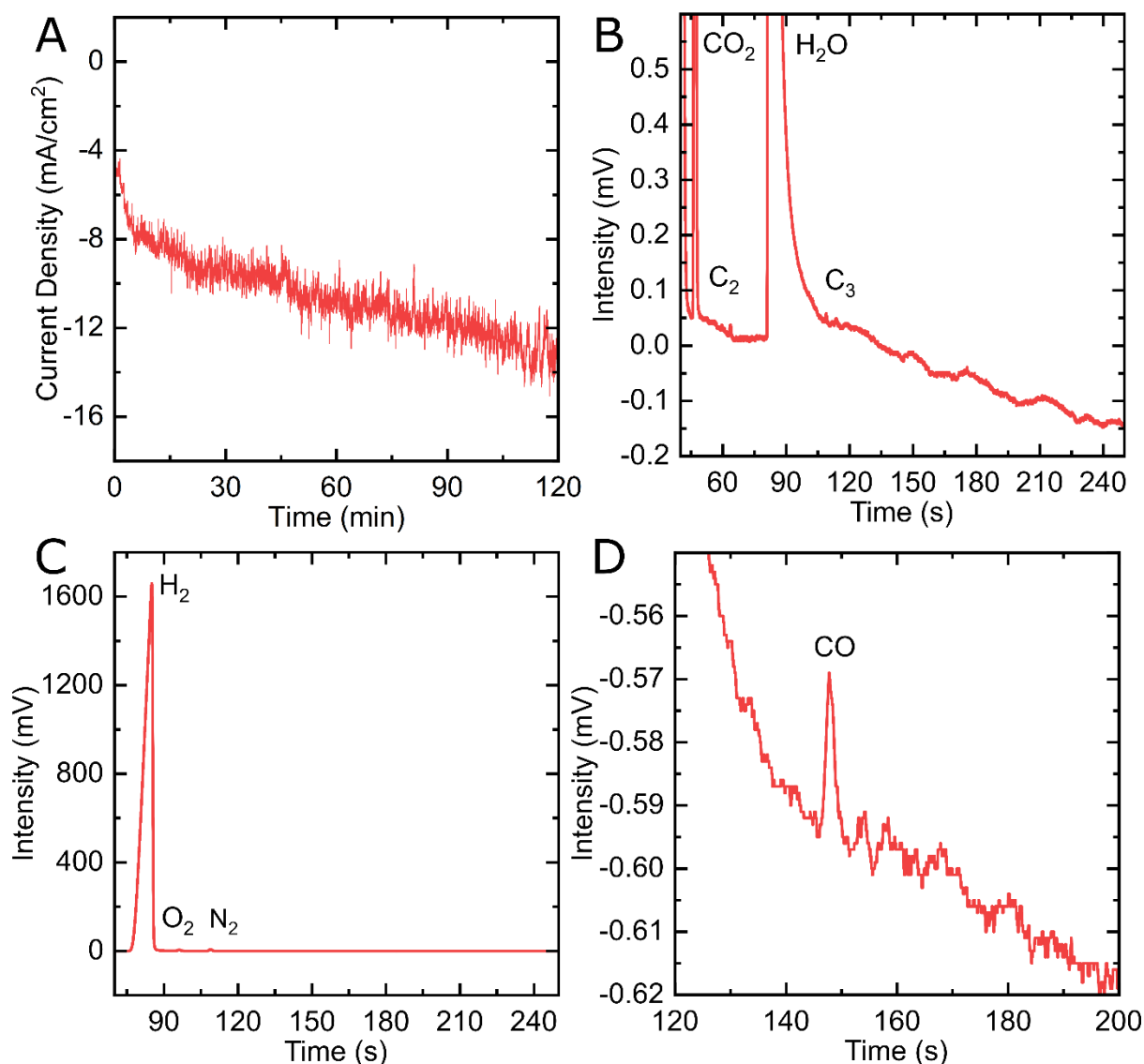


Figure 3-4. **(A)** Chronoamperometric curves, **(B)** Module B gas chromatograms, **(C)** Module A gas chromatograms – zoomed, and **(D)** Module A gas chromatogram of FePc-modified electrodes under Ar in 0.1 M KHCO_3 . Chronoamperometric experiments are performed at -1.7 V vs. Ag/AgCl for two hours, after which a GC samples the resulting gaseous products.

3.2.2 Origin of the products

To confirm the origin of the carbon atoms in the C_{2+} products observed in the chromatograms, we performed isotopic labeling experiments using $^{13}\text{CO}_2$. The GC was coupled with a mass spectrometer to perform gas chromatography-mass spectrometry (GC-MS) analysis of the products, with details in the annex of the chapter.

The major fragment of ^{12}CO in a mass spectrum is at $m/z = 28$, overlapping with major fragments of ethane and ethylene. Since the dominant product of the electrochemical reduction of CO_2 in our system was CO and the amount of C_2 products detected was orders of magnitude lower, the signal from the CO fragment overwhelmed the signals of other species in the region. Although the gas chromatograph could separate CO

and C_{2+} products somewhat effectively, the difference in signal-to-noise ratio made detecting mass signals of C_{2+} and some C_3 products with masses in the vicinity of $m/z = 28$ impossible with our setup. Similarly, the major fragment of $^{12}CO_2$ and $^{13}CO_2$ at m/z equal 44 and 45, respectively. These signals overlapped with some fragments of the C_3 and C_4 products detected. The catholyte was saturated with CO_2 , resulting in a high background signal around C_3 and C_4 products' main fragments near m/z of 44 and 45, making detecting these fragments challenging. Finally, the m/z value of 16 could come from the minor fragment of CO_2 and the mono-oxygen peak from the residual dioxygen, overlapping with the major signal of CH_4 . Therefore, the signal of CH_4 is also undetectable with the current setup due to signal interference with more dominating species. The peaks that were not subjects of background interference are $m/z = 41$ ($^{12}C_3H_5$), $m/z = 56$ ($^{12}C_4H_8$), and $m/z = 60$ ($^{13}C_4H_8$), which are shown in Figure 3-5. The detail of the GC-MS procedure is shown in section 3.7.2, along with the reference mass spectra of the concerning species.

Figure 3-5A and B show the GC-MS chromatograms corresponding to the retention time of C_4 products (190-240 s). We focused on the C_4H_8 signal because it had the highest intensity of all C_4 products without overlapping the signal of CO_2 or CO . The $m/z = 56$ mass, which corresponds to a C_4H_8 species containing four ^{12}C atoms, showed a peak when $^{12}CO_2$ was used as the reactant while not appearing in the presence of $^{13}CO_2$. The opposite behavior was observed with the $m/z = 60$ mass, corresponding to a C_4H_8 species with four ^{13}C atoms. The GC-MS chromatogram of the $m/z = 41$ mass at the region of the retention time of C_3 and C_4 products is shown in Figure 3-5C. The $m/z = 41$ mass, which corresponds to a $^{12}C_3H_5$ fragment (originating from both C_3 and C_4 products), showed two distinguishable peaks when $^{12}CO_2$ was used, which disappeared with $^{13}CO_2$. The first peak represented the signal of C_3 products since it was in the region of 130 – 170 s, which corresponds to the elution time of the C_3 species. Similarly, the second peak appeared in the retention time region from 190 to 240 s, corresponding to the elution time of the C_4 products. This observation agreed with the result of other C_4 fragments shown in Figure 3-5A and B. Overall, the isotopic labeling experiments demonstrated that the carbon atoms in the observed hydrocarbons come from CO_2 molecules. Although no signals of CH_4 and C_2 were obtained, the result of C_3 and C_4 products, which were present in lower concentrations, showed that the same behaviors are expected with all carbon products.

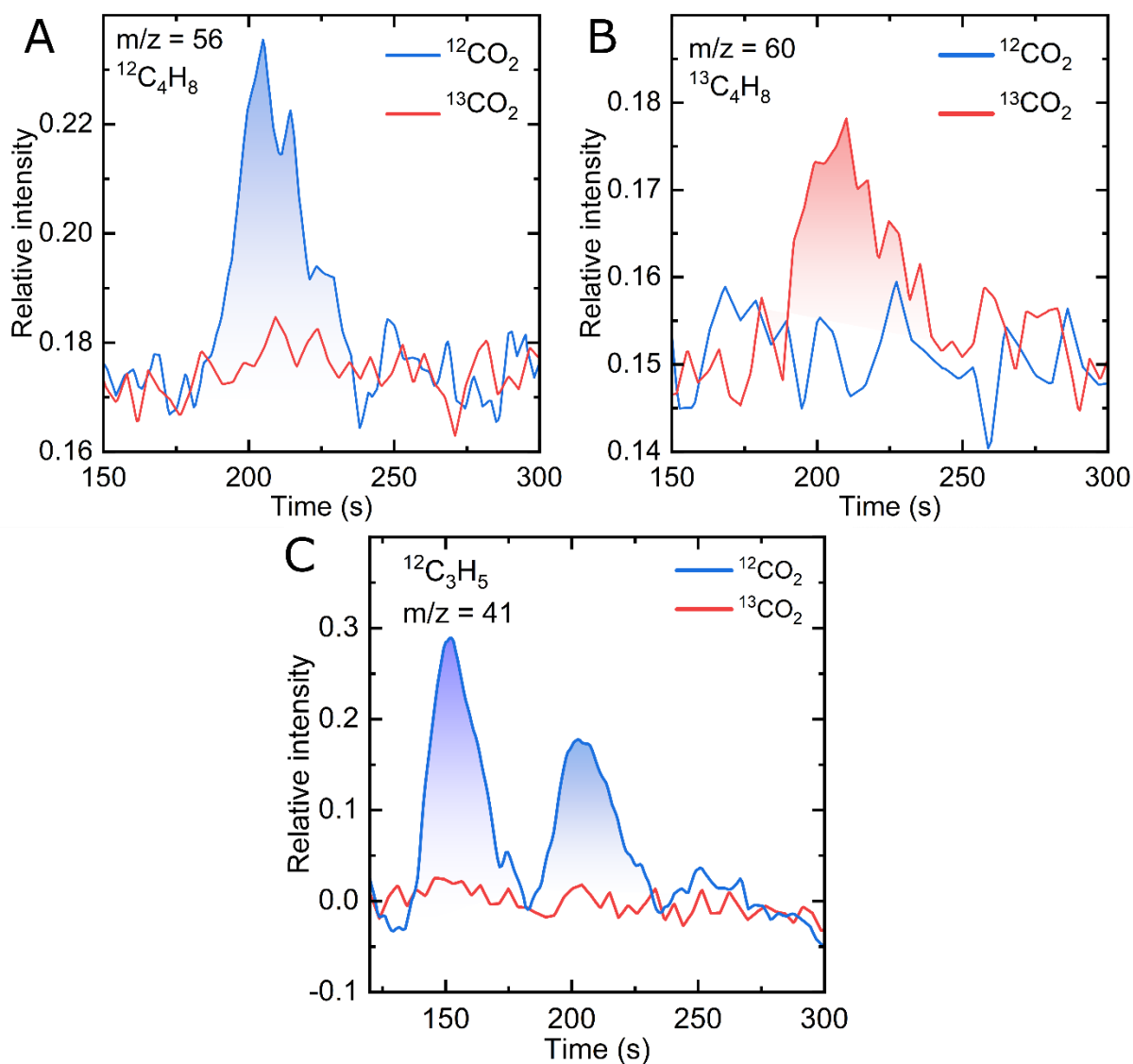


Figure 3-5. GC-MS chromatograms for mass $m/z = 56$ of $^{12}\text{C}_4\text{H}_8$ (**A**), mass $m/z = 60$ of $^{13}\text{C}_4\text{H}_8$ (**B**) at the retention time of C_4 products, and (**C**) mass $m/z = 41$ of $^{12}\text{C}_3\text{H}_5$ at the retention time of C_3 and C_4 products. Chronoamperometric experiments are performed on FePc-modified electrodes at -1.1 V vs. RHE for two hours, after which the GC-MS samples the resulting gaseous products.

3.2.3 Products quantifications

Figure 3-6 shows the electrolysis curves of FePc-modified electrodes with the catalyst loading of 80 nmol/cm^2 at applied potentials of -0.7 to -1.1 V vs. RHE. As expected, the current density decreased with less negative potentials. Figure 3-7 shows product distribution in terms of amount and faradaic efficiency (FE) for each product obtained after a 2-hours electrocatalytic experiment under CO_2 at different potentials. Between -0.7 V and -0.8 V, CO and H_2 were the only products reliably observed, with CO being the majority product (FE > 85%). When the potential turned more negative, the selectivity of CO decreased, and hydrogen gradually became the main product, with FE equaling 65 % at -1.1 V. This increase in hydrogen came from the fact that with

more negative potentials, the amount of CO stayed relatively constant, while H₂ amount increased, as shown in Figure 3-7A. A noticeable amount of hydrocarbons could be observed starting from -0.9 V, methane being the major species. At -1.1 V, the selectivity of CH₄ reached 4%, and ethylene, ethane, propene, propane, and n-butane were produced with faradaic efficiencies of 0.1 – 0.25% each. The total faradaic efficiency of hydrocarbon reached 5%, with C₂₊ products accounting for around 1%. It should be noted that the amount of ethylene was underestimated because of the high background generated by CO₂ in the chromatograph column. While the amount of CH₄ and C₂₊ products increased with more negative potential, their selectivity was generally constant from -1.0 V. This suggested the peak of hydrocarbons generation lies around the -1.0 V and -1.1 V vs. RHE, as more negative potential would mostly drive hydrogen evolution. Despite the low amounts of products generated, their distribution was reproducible, as shown by the replicates performed on three different electrodes.

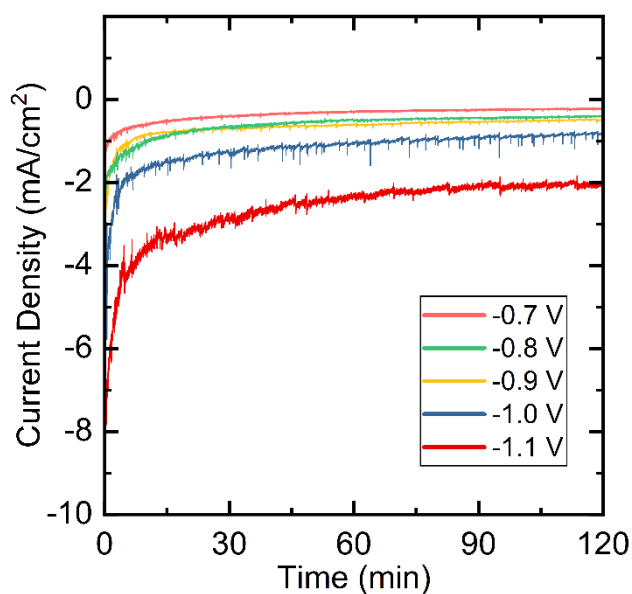


Figure 3-6. Chronoamperometric curves of FePc-modified electrodes under CO₂ in 0.1 M KHCO₃ performed at different potentials for two hours.

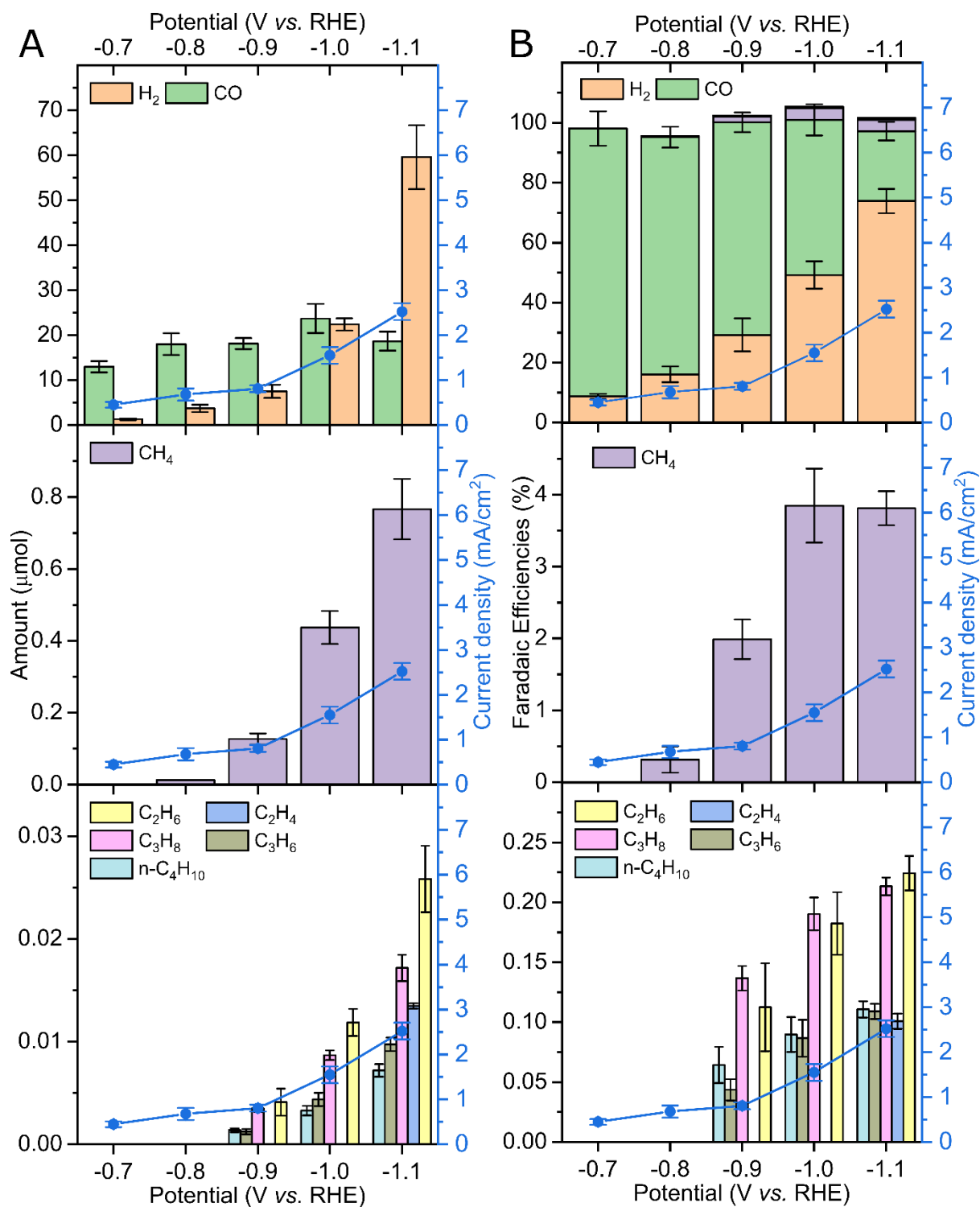


Figure 3-7. Product distribution observed with FePc-modified electrodes as amount (**A**) and faradaic efficiencies (**B**) as a function of applied potential. The total current densities at 60 minutes are plotted as a blue dot for each potential. The amount of ethylene (C_2H_4) is underestimated due to the high background generated by CO_2 in the chromatograph column.

3.3 FePc catalyst characterization: stability and active site estimation

3.3.1 X-ray absorption spectroscopy

To determine the nature of the catalyst under operating conditions and check its integrity, we performed *in situ* X-ray absorption spectroscopy (XAS) experiments at the iron K-edge in the same electrochemical cell described in Chapter 2. Figure 3-8 shows the X-ray absorption near-edge structure (XANES) spectra of the FePc-modified electrode under open circuit potential (OCP) and catalytic conditions in a CO₂ atmosphere. The spectrum of the electrode under resting state presented the same features as the pure, starting compound, showing the chemical robustness of the FePc catalyst after drop-casting and in the presence of an electrolyte. When poisoning the electrode at a potential of -1.1 V (at which C₂₊ products are observed), the spectrum showed a shift to lower energies (-2.7 eV at half-edge jump) while keeping the features that are characteristic of phthalocyanines,⁸ *i.e.*, two pre-edge peaks at 7114 eV and 7118 eV. A XANES spectrum was also recorded *in situ* after performing electrocatalytic experiments under a CO₂ atmosphere, and it was remarkably similar to the one collected on the starting electrode. The comparison between the spectra collected under *in situ* conditions and those of reference compounds (metallic iron, Fe₃O₄) ruled out the presence of metallic iron or iron oxide nanoparticles that the decomposition of the molecular catalyst would produce. Linear combination fitting of the *operando* spectrum using Fe, Fe₂O₃, and Fe₃O₄ as standards yielded a poor fit with FePc content to be 100%, suggesting FePc was the only species existing under catalytic conditions. Figure 3-8B shows the raw spectra without normalization. The spectrum of the FePc-modified electrode under oxidative potential after an electrolysis experiment experienced a decrease of 10% in intensity compared to the electrode under open circuit potential. The decline showed that the majority of the catalyst layer was robust enough to resist the mechanical erosion induced by the flowing electrolyte. Altogether, these spectroscopic data collected under *in situ* conditions clearly demonstrated the molecular nature and the stability of the catalyst throughout the experiment.

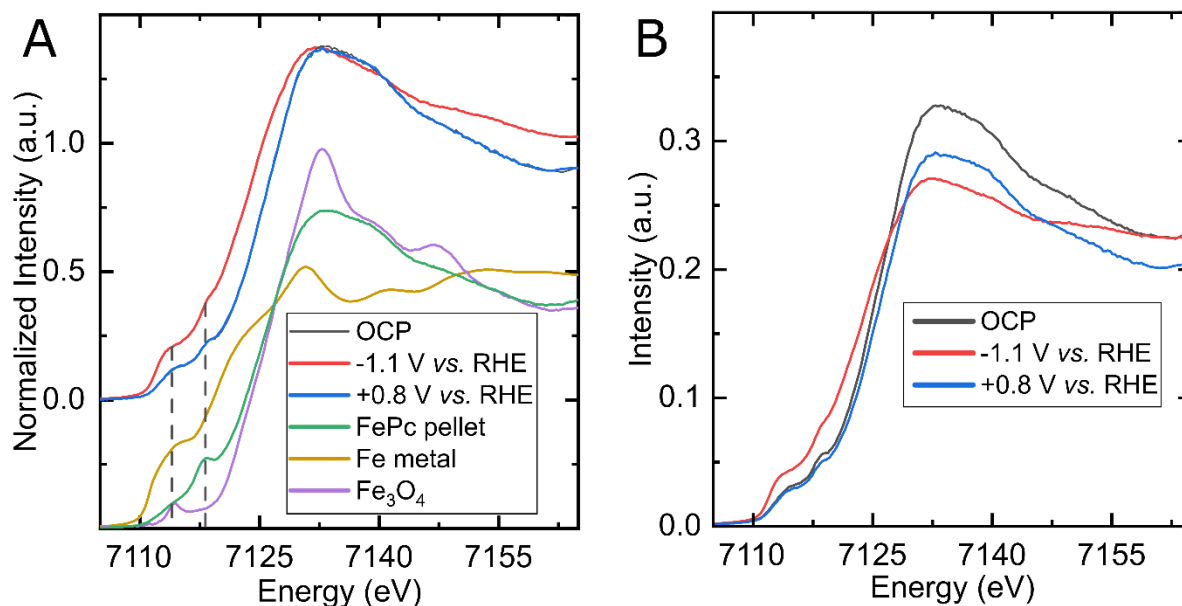


Figure 3-8. **(A)** Normalized X-ray absorption spectra collected on an FePc-modified electrode under different conditions and reference samples. The spectra at the top correspond to an FePc-modified electrode under a CO_2 atmosphere poised at OCP (black), at -1.1 V vs. RHE (red), and going back at $+0.8$ V vs. RHE (blue). The spectra at the bottom correspond to ex-situ reference spectra collected on a pellet of FePc (green), on a metallic sheet of iron (gold), and on a pellet of Fe_3O_4 (purple). The two dashed lines indicate the pre-edge features of FePc at 7114 eV and 7118 eV. **(B)** Corresponding raw X-ray absorption spectra collected on the FePc-modified electrode shown in panel A.

3.3.2 Infrared spectroscopy

Infrared spectra were recorded on the FePc catalyst powder and FePc-modified electrodes before and after electrolysis at -1.1 V vs. RHE (Figure 3-9). We could observe from the spectra the characteristic vibrational peaks of the phthalocyanine ligand in a typical metal phthalocyanine species: stretching modes of C=C, C–N=C, isoindole, and pyrrole groups from 1800 to 1330 cm^{-1} ; as well as scissoring modes of C–H and isoindole groups from 1330 cm^{-1} to 800 cm^{-1} .^{9,10} The peaks in the stretching region of pure FePc powder were more well-defined since the powder was not affected by the presence of carbon black and Nafion as in the electrodes. However, the IR spectra recorded with modified electrodes before and after electrolysis were identical, agreeing with the XAS results about the high stability of the catalyst during electrolysis.

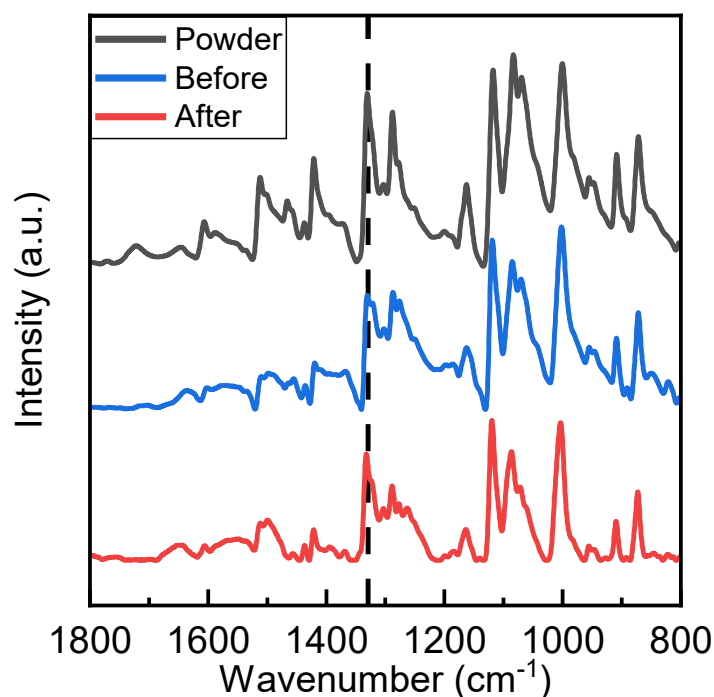


Figure 3-9. Infrared spectra of the FePc catalyst powder (black) and FePc-modified electrodes before (blue) and after (red) a 2-hours electrolysis at -1.1 V vs. RHE.

3.3.3 Cyclic voltammetry and active site estimation

Figure 3-10A shows the cyclic voltammograms (CVs) of an FePc-modified and catalyst-free modified electrode under CO₂ and Ar. Under CO₂, no catalytic activity was observed in the CV without the presence of FePc. On the contrary, the presence of FePc under Ar facilitated hydrogen evolution at a highly negative potential, starting from -1.1 V vs. RHE. When both CO₂ and FePc were presented, a current increase started around -0.6 V, forming a catalytic wave. The rise in current indicated the reduction of CO₂, as the onset potential was less negative than the potential needed for the hydrogen evolution reaction. Overall, the CVs corroborated the result obtained from electrolysis and product characterization, where an FePc-modified electrode exhibited a high CO selectivity at low overpotential, and low selectivity at high overpotential. However, the heterogenization of FePc on a large electrode and the use of a flow cell prevented its redox feature from being observed, as there were no visible redox peaks in the CVs.

We prepared a modified circular working electrode to obtain the redox peaks of FePc and performed cyclic voltammetry in a heart-shaped glass cell in Ar-saturated H₂SO₄ 0.05 M. When the redox feature is reliably observed, we can integrate a peak to obtain the amount of charge transferred in the reaction. We can deduce the fraction of the electrochemically active species by comparing the measured charge versus the theoretical charge needed to reduce or oxidize all the catalysts on the electrode surface. The chapter annex contains more details about the experimental setup. In Figure 3-10B, a reversible wave could be observed at 0.75 V vs. RHE. The oxidation

peak was stable after ten cycles of cyclic voltammetry, and the reversible wave was observed with three independent experiments (Figure 3-24), indicating the repeatability of the feature. This feature represented a one-electron redox process that happened on FePc, as shown in a previous study with immobilized FePc in acidic conditions.¹¹ A reduction peak appeared in the range of 0.2 to 0.4 V in the first cycle, but it was not visible in subsequent repetitions, indicating that it was not an intrinsic feature of the catalyst layer (Figure 3-10B). As observed earlier, when an electrode was modified with a FePc-free ink, its CV exhibited a broad peak with no reversible feature (Figure 3-10C). The lack of the reversible feature without FePc indicates that the observed reversible wave in Figure 3-10B comes from FePc. Comparing the charge obtained by the peak versus the charge needed to reduce Fe(II) to Fe(I), the percentage of the active catalyst in the drop cast layer is $7.8 \pm 0.8\%$.

Although the percentage of active sites was relatively low, some cautions should be made when interpreting this result. First, the experimental conditions of the cyclic voltammetry experiments in a glass cell with visible redox features were different from the conditions of standard electrolysis in the flow cell. Moreover, the accuracy of the active sites deduced from CV peaks integration was a question of debate due to the uncertainty in baseline correction,¹² and the unreliability of the peaks themselves.¹³ Furthermore, the XAS spectrum during catalysis significantly changed compared to the spectra obtained before and after electrolysis. Given that the loss of the material was limited, the change in 8% of the catalyst would unlikely lead to the observed change. Overall, the percentage of the active sites determined electrochemically could serve as a lower limit value, but it might not reflect the most accurate percentage of the active catalyst.

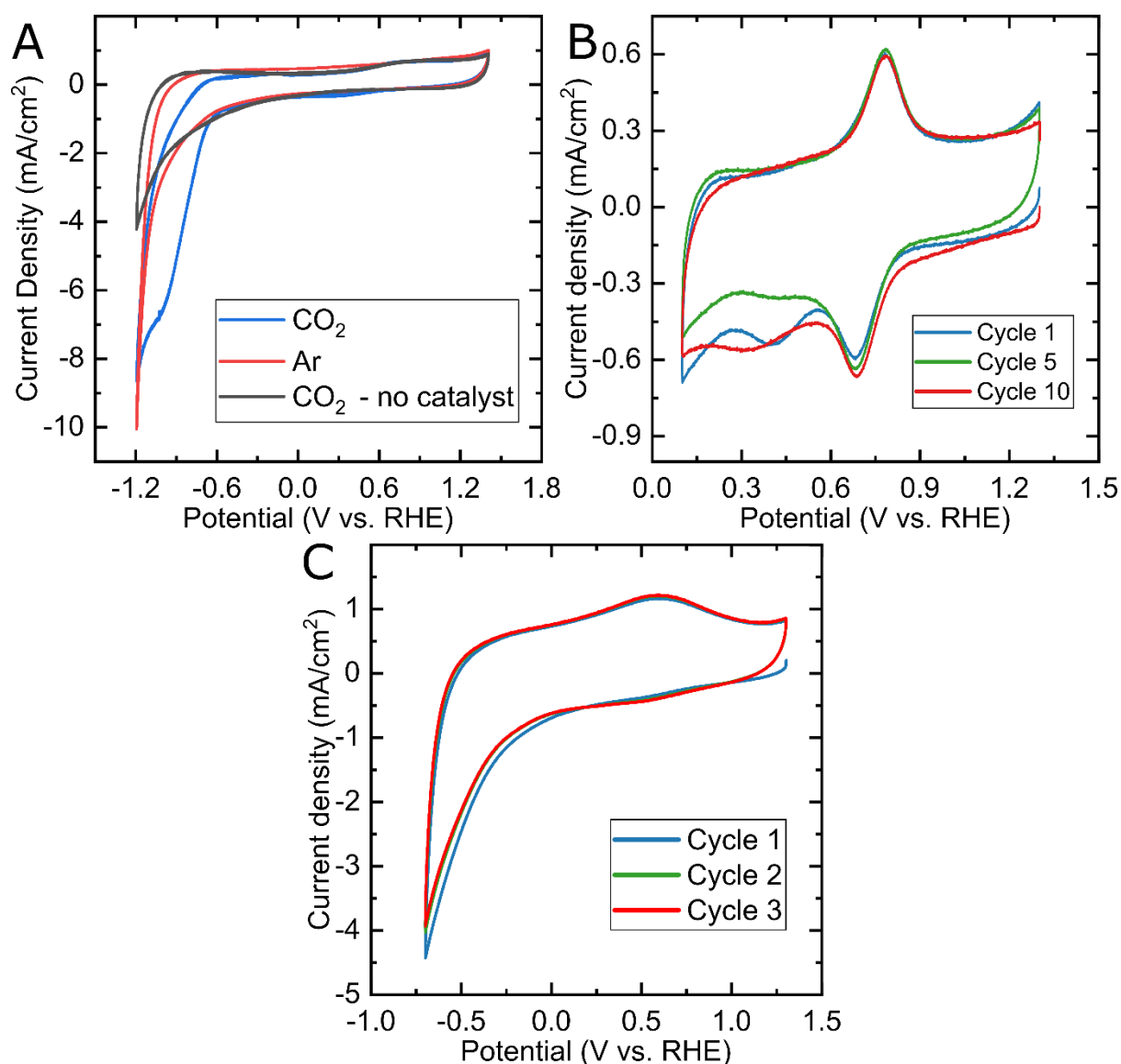


Figure 3-10. **(A)** Cyclic voltammograms of an FePc-modified electrode under Ar (red) and CO₂ (blue) and of a catalyst-free modified electrode under CO₂ (black) in 0.1 M KHCO₃ in the electrochemical flow cell without flowing; Multiple cyclic voltammograms of FePc-modified electrode **(B)** and catalyst-free electrode **(C)** under Ar in 0.05 M H₂SO₄ in a glass static cell

3.4 Control experiments with FePc and Fe₃O₄ nanoparticles

In the previous section, *operando* X-ray absorption spectroscopy was used to demonstrate the nature of the FePc catalyst during its operation. The spectrum during catalysis did not resemble that of iron or iron oxide species, and the spectra before and after electrolysis closely overlapped, proving the molecular nature of FePc. However, since not all of the catalysts were active, a small portion of the catalyst could degrade and form an iron-based material that might be responsible for the formation of products with C – C bonds. These iron materials could exist in a small quantity below the detection limit of X-ray absorption spectroscopy. To test this hypothesis, we experimented with 5-nm Fe₃O₄ nanoparticles (Sigma-Aldrich) as a catalyst for CO₂

reduction. The nanoparticles are stabilized by modified polyethylene glycol (PEG) ligands covalently bonded to the particle by a hydroxamic acid on the end of the PEG chain. The PEG concentration is less than 1 % in weight. First, we examined the characteristic features of electrodes containing a mixture of Fe_3O_4 nanoparticles and FePc using *ex situ* XAS. We then studied the catalytic behavior of solely the particles as well as mixtures of the nanoparticles and FePc. Finally, we performed *operando* X-ray absorption spectroscopy with an electrode having a mix of FePc and Fe_3O_4 . In all cases, we kept the total surface concentration of iron to 80 nmol/cm^2 , similar to the amount of iron on a standard FePc-modified electrode described in the previous section. The drop casting procedure was identical to the FePc casting process, except the solution of Fe_3O_4 suspension was added after adding FePc to the ink mixture. The electrolysis was carried out in a KHCO_3 0.1 M electrolyte with a flow rate of 1 mL/min.

3.4.1 *Ex situ* X-ray absorption spectroscopy

Figure 3-11 shows the XAS spectra collected on the $\text{Fe}_3\text{O}_4/\text{FePc}$ electrodes, as well as reference spectra collected with only FePc on an electrode and Fe_3O_4 powder. The Fe_3O_4 sample possessed a characteristic pre-edge peak at 7114 eV, which is visible in all samples containing Fe_3O_4 . Interestingly, the XAS spectrum of the electrode where Fe_3O_4 contributed only 5% of the iron content (black curve) showed a strong signal of Fe_3O_4 , while the two characteristic pre-edge peaks of FePc at 7114 and 7118 eV (purple curve) were hardly visible. When the theoretical iron content of Fe_3O_4 nanoparticles accounted for 50%, its signal (red curve) closely matches that of the 100% Fe_3O_4 sample (blue curve).

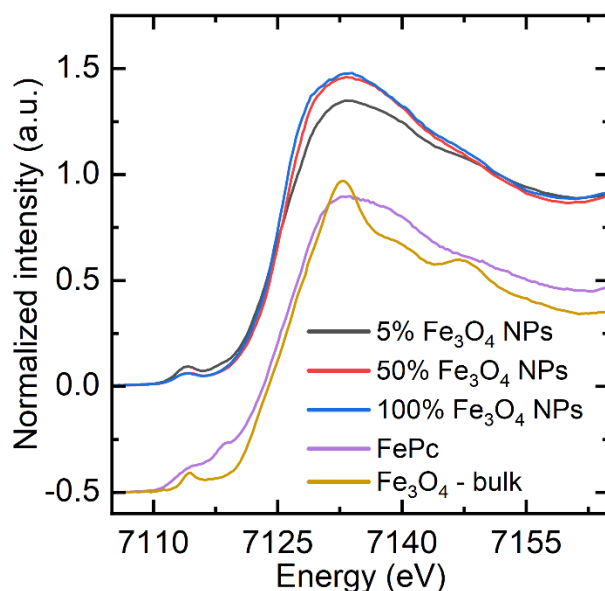


Figure 3-11. X-ray absorption spectra collected on an $\text{FePc}/\text{Fe}_3\text{O}_4$ -modified electrode with various Fe_3O_4 content and reference samples.

We performed linear combination fitting with two electrodes containing mixtures of FePc and Fe_3O_4 to quantify each species' actual contribution to the obtained iron

spectra. Using the spectra from the two electrodes containing FePc only and Fe₃O₄ nanoparticles only as references, the electrode supposedly with 5% of iron content coming from Fe₃O₄ yielded 22.1% Fe₃O₄ and 77.9% FePc (Figure 3-12A). Similarly, the electrode where FePc and Fe₃O₄ supposedly have equal iron content actually showed 81.4% Fe₃O₄ and 18.6% FePc, with a better fitting result (Figure 3-12B). Although the fit with the 5% nominal concentration of Fe₃O₄ was poor, both fit results indicated that the Fe₃O₄ content in each sample was higher than the calculated values. The significant deviation between the calculated concentrations and the observed concentrations meant the drop-casting process was poorly controlled. Subsequently, we will refer to the electrodes containing mixtures of FePc and Fe₃O₄ with their concentrations derived from XAS instead of their calculated iron concentrations. Despite the substantial difference between the theoretical and the actual Fe concentration, the XAS result demonstrated that considerable changes would be observed if a small fraction of Fe₃O₄ was presented on the measured electrodes.

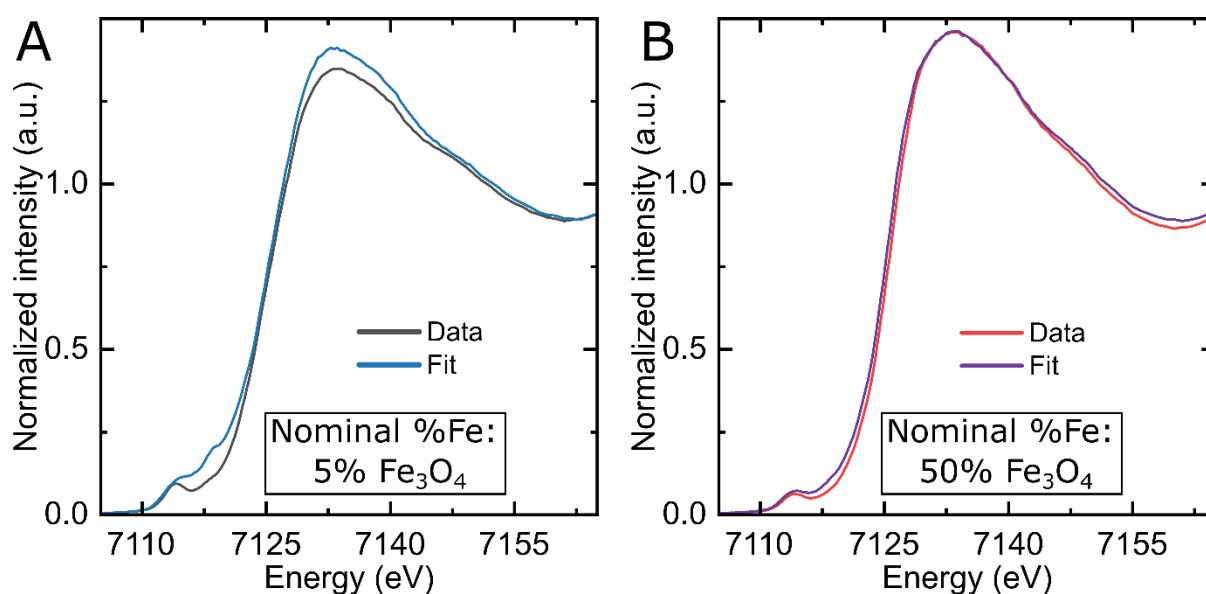


Figure 3-12. Linear combination fitting of spectra recorded on the electrode with 5% of the nominal iron content coming from Fe₃O₄ (**A**) and electrode with FePc and Fe₃O₄, each contributing 50% of the nominal iron content (**B**).

3.4.2 Electrolysis and product distribution

Figure 3-13A shows the electrolysis curves of electrodes modified with a mixture of FePc and Fe₃O₄ nanoparticles. We examined two electrodes with only Fe₃O₄ nanoparticles and only FePc, as well as one electrode containing a mixture of FePc and Fe₃O₄, with 5% of the iron contents theoretically contributed by Fe₃O₄. This number was actually 22.1%, based on the result of XAS linear combination fitting; thus, we referred to the corrected number in our analysis.

Concerning the electrochemistry performance, the highest current density obtained was the electrode having 22.1% of the Fe content from Fe₃O₄. The sample with 100% Fe₃O₄ appeared unstable as its electrolysis curve was trending downward. Since the

nanoparticles did not adhere well to the glassy carbon surface, mechanical erosion of the drop-casted layer may lead to the observed instability. This phenomenon will be discussed in more detail in the following section.

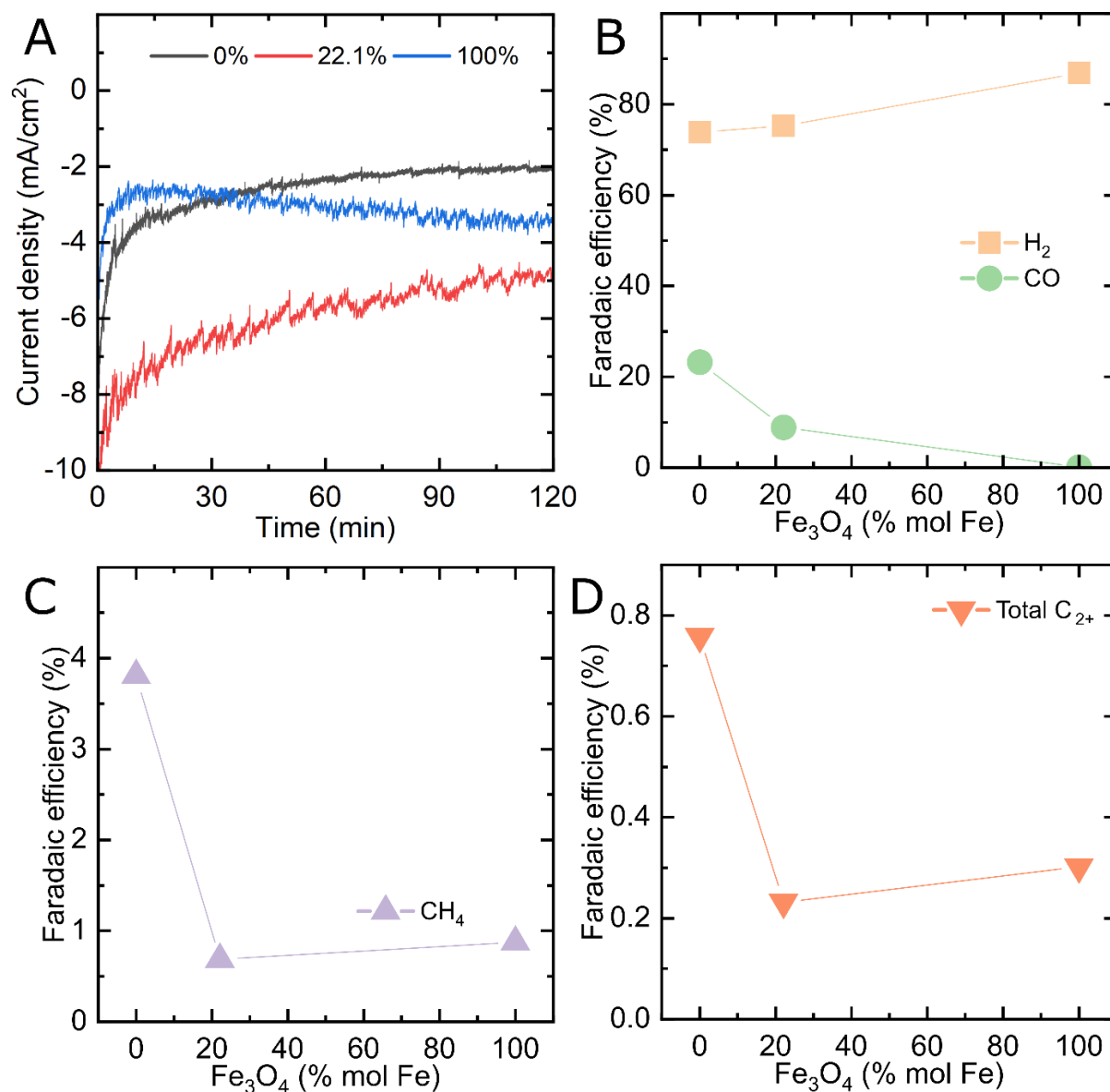


Figure 3-13. **(A)** Electrolysis curves of Fe₃O₄/FePc electrodes at -1.1 V vs. RHE under CO₂ in 0.1 M KHCO₃ performed for a mixture of FePc/Fe₃O₄ nanoparticles for two hours. **(B-D)** Product distribution observed with Fe₃O₄/FePc electrodes as faradaic efficiencies after the corresponding electrolysis -1.1 V vs. RHE as a function of the iron content of the Fe₃O₄ nanoparticles. The percentages indicate the iron content (in mole) contributed by the Fe₃O₄ nanoparticles out of the total iron content (80 nmol/cm²) of FePc and Fe₃O₄. The amount of ethylene (C₂H₄) is underestimated due to the high background generated by CO₂ in the chromatograph column.

Figure 3-13B, C, and D show the faradaic efficiencies (FE) of CO and H₂, CH₄, and C₂₊ products, respectively, after 2-hour electrolysis experiments at -1.1 V vs. RHE, with electrodes having different amounts of Fe₃O₄ and FePc. The presence of Fe₃O₄ hindered the CO₂-to-CO reduction activity, as the electrode containing only FePc produced CO most selectively, with a FE of around 20%. Hydrogen was the dominating

product on the electrode having no FePc, with CO accounting for less than 1% of the faradaic efficiency. This poor result is expected, as metallic iron or iron oxide are not known to be a good catalyst for CO₂-to-CO reduction.

CH₄ and C₂₊ products were observed after catalysis at -1.1 V vs. RHE on electrodes containing only Fe₃O₄ and a mixture of FePc and Fe₃O₄. The faradaic efficiencies of individual C₂₊ products are shown in Figure 3-14. The production of these hydrocarbons was likely the result of the PEG stabilizing ligands degradation, as the breaking of PEG chains yields various carbon-containing products.¹⁴ Therefore, the generation of hydrocarbons on Fe₃O₄ nanoparticles was not the result of CO₂ reduction.

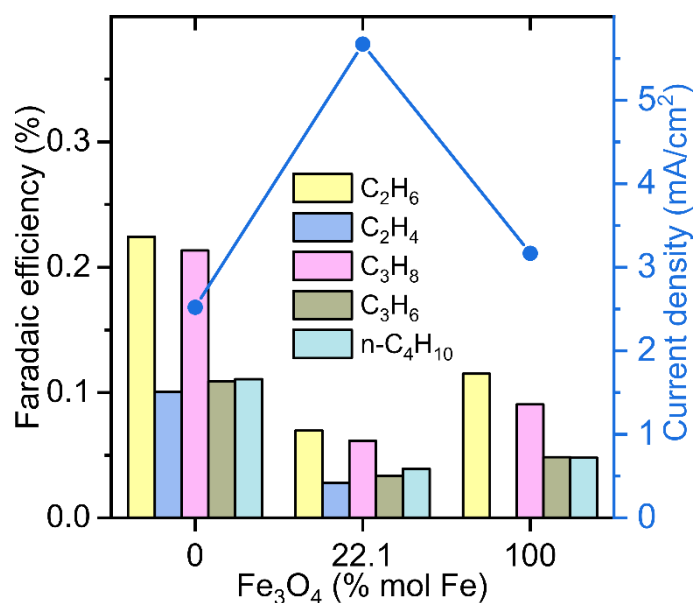


Figure 3-14. C₂₊ product distribution observed with Fe₃O₄/FePc electrodes as faradaic efficiencies after 2-hour electrolysis at -1.1 V vs. RHE. The total current densities at 60 minutes are plotted as a blue dot for each Fe percentage. The amount of ethylene (C₂H₄) is underestimated due to the high background generated by CO₂ in the chromatograph column.

3.4.3 Operando X-ray absorption spectroscopy

Figure 3-15 compares the spectra obtained with a 22.1% Fe₃O₄ iron sample before and after 2-hour electrolysis at -1.1 V vs. RHE. The normalized data in Figure 3-15A demonstrated that the overall shape of the spectra before and after electrolysis remained similar, albeit with a lower signal-to-noise ratio and other minor differences. These changes were likely due to the consequences of the loss of the materials, as shown in the raw spectra in Figure 3-15B. The signal intensity decreased by 95%, indicating a significant amount of materials loss, much more than what was observed with an FePc-modified electrode, as discussed in the previous section. Indeed, visible damage to the catalyst layer could be seen after electrolysis, with some black particles recovered in the catholyte bottle after the experiment finished. This result indicates that the presence of Fe₃O₄ nanoparticles decreased the adhesion between the glassy

carbon surface and the catalyst layer, and nanoparticles are more likely to be removed by the electrolyte flow.

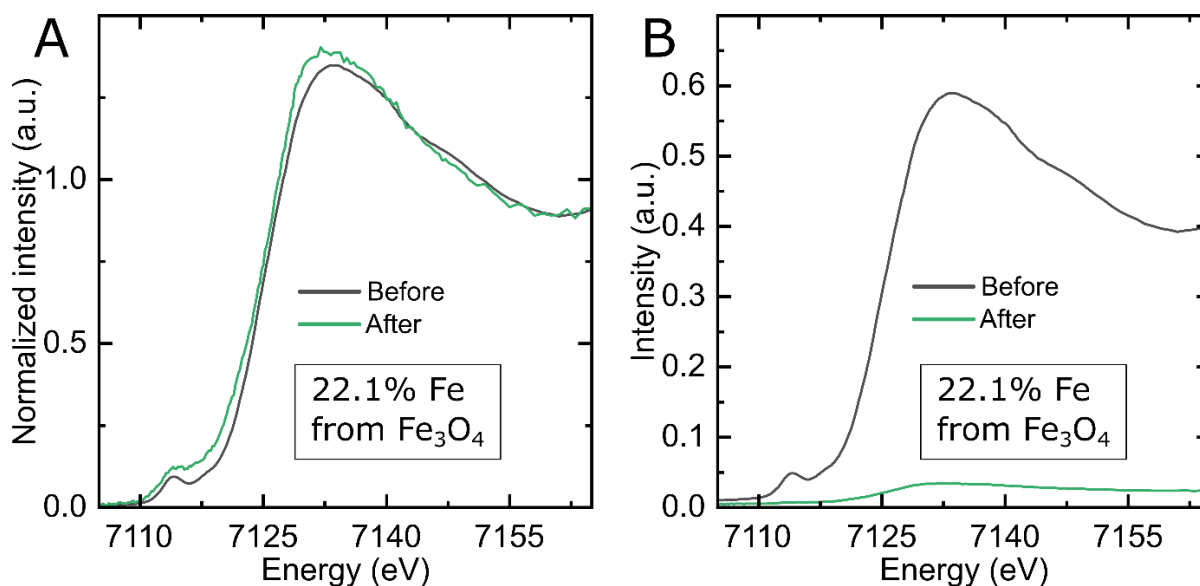


Figure 3-15. X-ray absorption spectra as normalized data **(A)** and raw data **(B)** collected on an FePc/Fe₃O₄-modified electrode before and after two-hour electrolysis at -1.1 V vs. RHE. Fe₃O₄ contributed 22.1% of the iron content in the sample.

3.4.4 Discussion

Overall, the result from experiments with Fe₃O₄ nanoparticles showed that when FePc contained a small amount of Fe₃O₄ nanoparticles, the resulting XAS spectra exhibited significant changes. Although this experiment could not completely rule out the formation of every iron species, the reversibility of the XAS spectra on an electrode with only FePc demonstrated that the degradation of FePc was highly improbable. Moreover, the presence of a Fe₃O₄ species significantly alters the adhesion between the catalyst layer and the glassy carbon plate. Therefore, the outcome of this experiment provided strong evidence of the structural integrity of the catalyst.

3.5 C – C bond formation mechanism

The demonstration that a molecular electrocatalyst can form several consecutive C – C bonds poses the question of their formation mechanism. Since the main product observed upon the reduction of CO₂ was CO, we postulated that the first intermediate for forming C – C bonds could be an FePc-CO species (see Figure 3-19). Indeed, electrolysis with CO as substrate showed the formation of similar hydrocarbon products observed for CO₂, albeit with faradaic efficiencies approximately twice as low (see Figure 3-16). We attributed this lower Faradaic efficiency to the low solubility of CO in water (1 mM) compared to that of CO₂ (33 mM). As observed in other studies,^{15,16} we surmised that the difference in initial concentration of substrate was responsible for this difference in efficiency. According to the finite element analysis calculating the

concentration profiles upon CO_2 reduction in Chapter 2, a supersaturated concentration of CO was observed near the electrode. Specifically, the calculation showed the concentration of CO generated by CO_2 reduction within five μm from the working electrode ranges from 1.5 to 4.5 mM, while the saturated concentration of CO in water is around 1 mM. The CO supersaturation supported a relationship between the amount of C_{2+} products and the local concentration of CO .

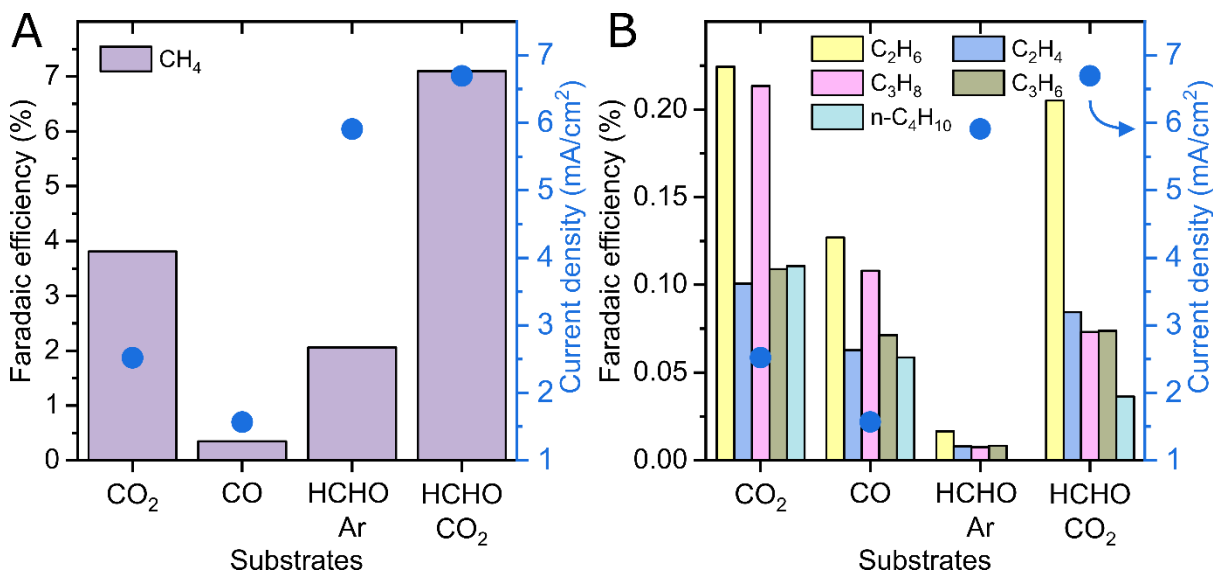


Figure 3-16. **(A)** CH_4 and **(B)** C_{2+} products distribution with faradaic efficiencies after 2h electrolysis at -1.7V vs. Ag/AgCl with different substrates using an FePc -modified electrode. The total current densities at 60 minutes are plotted as a blue dot for each reactant. The amount of ethylene (C_2H_4) is underestimated due to the high background generated by CO_2 in the chromatograph column.

By analogy with what happens during the Fischer-Tropsch synthesis of long-chain hydrocarbons, we hypothesized that a terminal $\text{FePc}=\text{CH}_2$ carbene species could be the precursor to all C_{2+} products. This transient species would be formed, *via* a hydroxycarbene species, by reacting an $\text{FePc}-\text{CO}$ adduct with either H_2 formed locally or with protons and electrons available in large amounts. This species would then further react either with more H_2 (or protons and electrons) to form methane. The putative iron carbene species undergo CO insertion similar to the Fischer-Tropsch mechanism to create a $\text{C}-\text{C}$ bond. This CO insertion pathway is different from the carbene coupling involved in forming ethylene on metallic copper since there are no adjacent active sites in iron phthalocyanine. The process could continue a few times following various pathways and lead to the formation of longer saturated or unsaturated hydrocarbon chains (see Figure 3-19).

To verify this hypothesis, we used formaldehyde as a substrate, expecting it to form an $\text{FePc}=\text{CH}(\text{OH})$ hydroxycarbene species by direct reaction with the activated form of the catalyst (see Figure 3-19). One of the polymerization schemes in the Fischer-Tropsch process is initiated by forming metal-hydroxycarbene intermediates from the hydrogenation of the chemisorbed carbon monoxide.¹⁷ By using HCHO instead of CO_2

as the reactant, creating the hydroxycarbene species would not require the reduction of CO_2 to CO and the hydrogenation of the adsorbed CO . Consequently, we surmised that the hydroxycarbene intermediate would be readily formed on the reduced iron center. With 30 mM of HCHO as the reactant, the product distribution showed similar multi-carbon products as with CO_2 or CO as substrates, although in much lower amounts (Figure 3-16B), as well as methane (2%) and traces of methanol (Figure 3-16A and Figure 3-17). The observed methanol was likely the result of the Cannizzaro reaction between the formaldehyde molecules.¹⁸ While the concentration of formaldehyde (30 mM) was similar to that of saturated CO_2 in water at 25°C (33 mM), the very low faradaic efficiencies observed for C_{2+} products could be explained by the absence of any CO to be inserted in the $\text{FePc}=\text{C}$ bond of the putative carbene species. Without any CO to react further, the carbene species were preferentially reduced into methane, leading to a 6-fold increase in the faradaic yield of methane as compared to the CO substrate.

To confirm the reaction of CO with an FePc carbene species, we performed electrolysis with HCHO in a CO_2 atmosphere, as CO_2 reduction could provide the necessary CO to increase the C_{2+} formation with the carbene species generated from HCHO . Indeed, at -1.1 V vs. RHE, the total faradaic efficiency of C_{2+} products was one order of magnitude higher than observed in HCHO without CO_2 (Figure 3-18A and C), thus confirming our hypothesis of a reaction between CO and a carbene species obtained from formaldehyde. At less negative potentials, where the formation of CO from CO_2 is more favorable, the total C_{2+} faradaic efficiency increased further, reaching a maximum value of 1.5% at -0.9 V vs. RHE, *ca.* three times higher than when only CO_2 was used as substrate (Figure 3-18B and C). The higher selectivity of C_{2+} products after electrolysis of HCHO under CO_2 emphasized the crucial role of the CO insertion step while corroborating the hypothesis that the formation of C_{2+} species involves CO insertion on an intermediate FePc carbene species, as described in Figure 3-19.

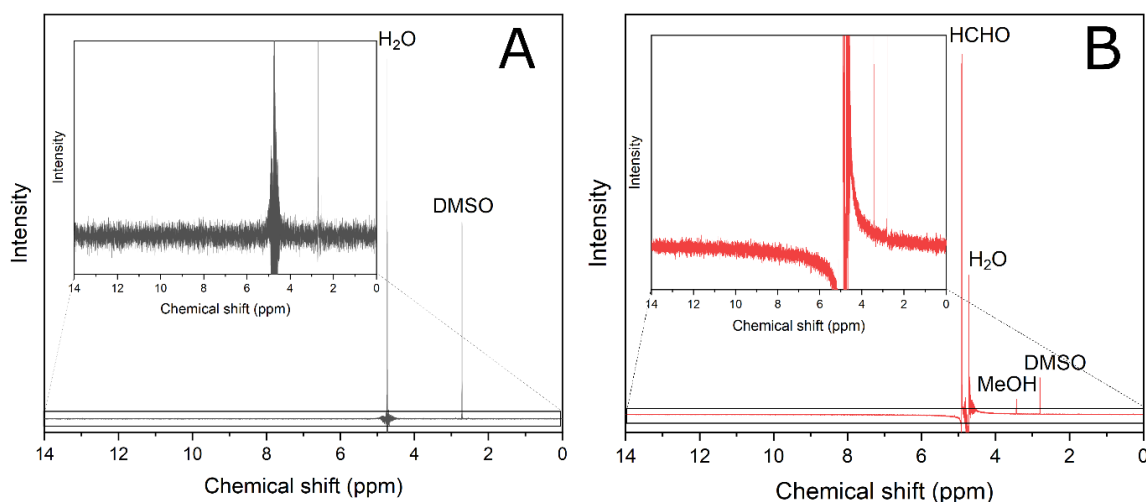


Figure 3-17. ^1H NMR spectra of catholyte after 2-hour electrolysis in CO saturated electrolyte (A), Ar saturated electrolyte with 30 mM HCHO (B) at -0.97 V vs. RHE (-1.7 V vs. Ag/AgCl)

with an FePc-modified electrode.

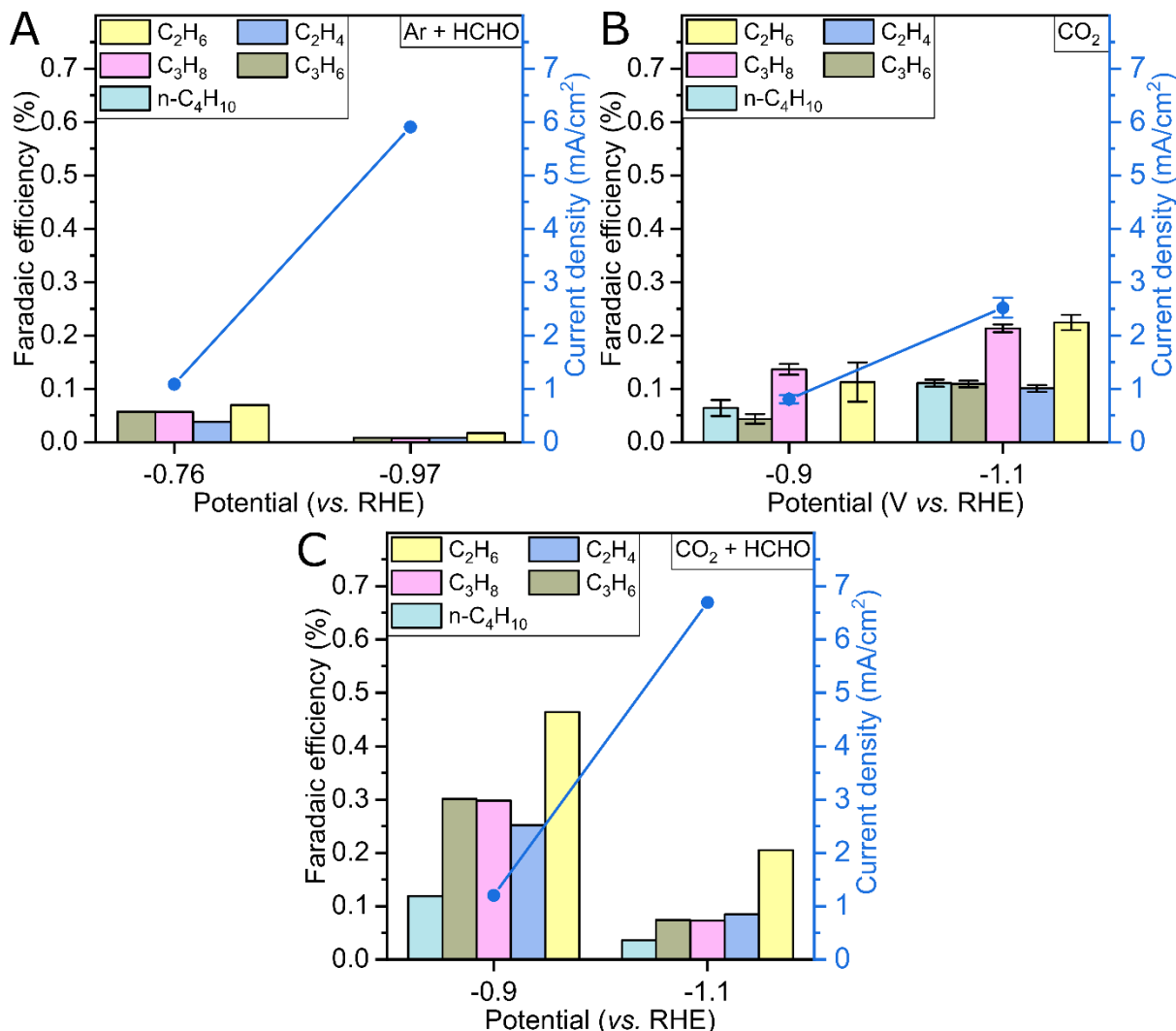


Figure 3-18. C₂₊ products faradaic efficiencies after 2h electrolysis at -0.76 V and -0.97 V vs. RHE (-1.7 V and -1.5 V vs. Ag/AgCl, respectively) with 30 mM HCHO under Ar atmosphere using an FePc-modified electrode (A); at -0.9 V and -1.1 V vs. RHE (-1.7 V and -1.5 V vs. Ag/AgCl, respectively) under only CO₂ (B) and CO₂ with 30 mM HCHO atmosphere (C) using FePc-modified electrodes. The total current densities at 60 minutes are plotted as a blue dot for each potential. The amount of ethylene (C₂H₄) is underestimated due to the high background generated by CO₂ in the chromatograph column.

The existence of an FePc=CH₂ intermediate is supported by the fact that several carbene species of iron porphyrin (a macrocycle similar to FePc) have been reported, either as transient^{19,20} or stable species,²¹ and that FePc itself has been reported as an efficient catalyst for the cyclopropanation of alkenes,²² which involves FePc-carbene intermediates. Iron porphyrins are also known for catalyzing the insertion of carbenes into N-H, S-H, or C-H bonds.^{23,24} These precedents, as well as the experiments described here with alternate substrates, strongly support the involvement of an FePc carbene species on the way to C₂₊ hydrocarbons. To show that the Fe=CH₂ species is

the intermediate of the proposed mechanism, such species could be synthesized and isolated in order to study its single turnover reactivity, i.e., whether it would react with CO and H₂ to form a C – C bond. Spectroscopic studies of such a species would also be beneficial. However, comparison with operando data would be difficult since it is produced in very low amounts and likely very fugacious during the catalytic cycle. However, the identification of a reaction between the iron carbene species and a mixture of CO and H₂ would provide concrete evidence to support the proposed mechanistic pathway for forming C₂₊ products.

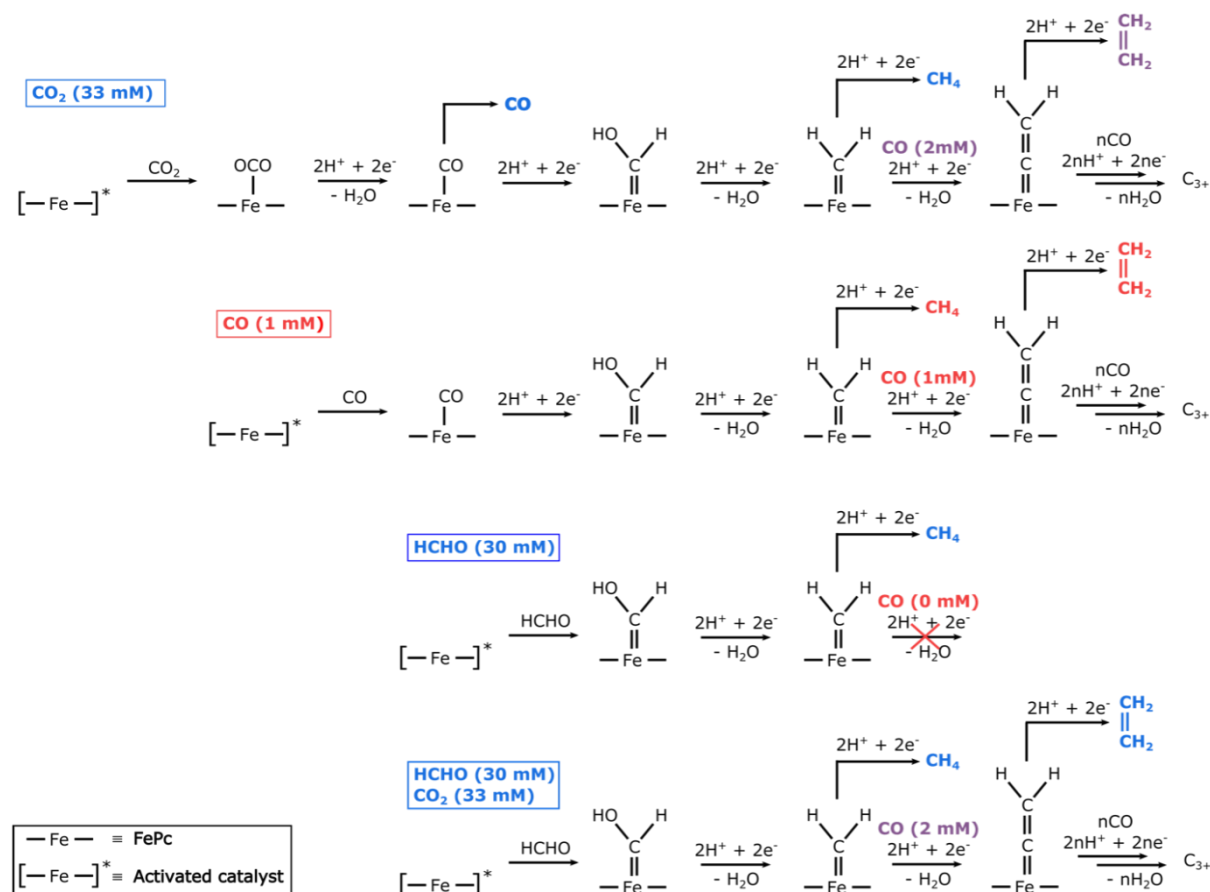


Figure 3-19. Simplified mechanisms proposed for forming C – C bonds by FePc with either CO₂, CO, HCHO, or a mixture of HCHO and CO₂ as substrates. The color code for substrates and products is as follows: blue, purple, and red for high, intermediate, and low concentrations, respectively.

The mechanism we propose is based on a CO insertion step to form C – C bonds, which is similar to one mechanism reported for the Fischer-Tropsch process. Consequently, we surmise that the obtained hydrocarbons would follow the Flory-Schulz distribution, analogous to what happens during the Fischer-Tropsch reaction.²⁵ To verify this hypothesis, we plot the $\ln(W_n/n)$ against n , where n is the number of carbon, and W_n is the mole fraction of all products containing n carbon. This plot is known as the quasi-Anderson-Schulz-Flory plot, which yields the same trend as a standard Flory-Schulz plot (common logarithm of mass fraction vs. the number of carbon) but with improved linearity.²⁶ Figure 3-20A shows our quasi-Anderson-Schulz-Flory, which did

not show a linear relationship. However, the value of C_2 products was underestimated due to the C_2H_4 peak got overlapped with the background of the CO_2 peak in the gas chromatograms. Therefore, we removed the point of the C_2 species, resulting in Figure 3-20B, which shows a clear linear relationship between $\ln(W_n/n)$ and n . The linear trend demonstrated the generation of hydrocarbons was a polymerization process based on the insertion of CO into carbene species.²⁷ We note that our calculations overestimate the mole fractions of all species due to ethylene underestimation and the amount of some C_4 and C_5 being below the level of quantification. However, this is a systemic error that applied to all points, thus the trend would not be affected.

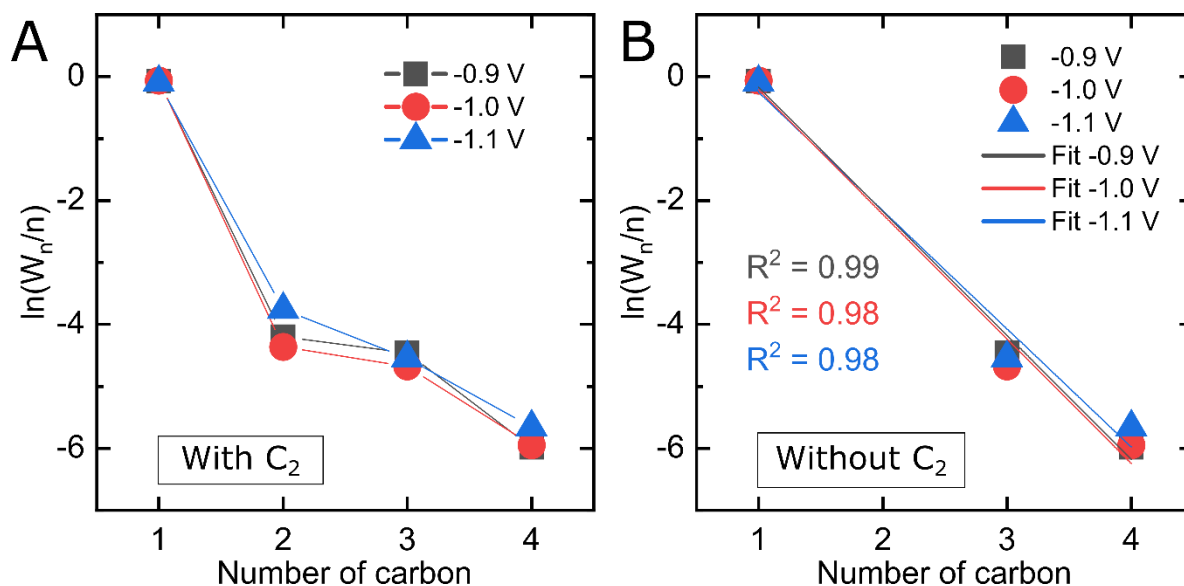


Figure 3-20. Quasi Anderson-Schulz-Flory plot of hydrocarbons formed on FePc-modified electrodes by the electrochemical reduction CO_2 at different potentials, including C_2 products (A) and excluding C_2 products (B). The potentials are reported with the RHE scale.

3.6 Conclusion

In this chapter, we reported the electrocatalytic activity of iron phthalocyanine toward reducing CO_2 in our 3D-printed millifluidic electrochemical flow cell. Upon reducing CO_2 , linear hydrocarbons with up to three C – C bonds were detected, while the main product was CO. The formation of the hydrocarbons depended on the applied potentials, with reliable observations of these products starting from -0.9 V to -1.1 V vs. RHE. Using operando X-ray absorption spectroscopy, we showed that iron phthalocyanine kept its molecular structure throughout the electrocatalytic process. Experiments with Fe_3O_4 corroborate the evidence proving the structural integrity of FePc during catalysis. Based on experiments involving carbon monoxide or formaldehyde and the finite element analysis of the product concentration profiles, we showed that the local concentration of CO is key to the formation of C – C bonds. We proposed a terminal carbene as an intermediate on the way to the C_{2+} products. The hydrocarbon products substantiated the proposed mechanism following the Flory-Schulz distribution. These results indicate that single-site transition metal macrocycles

Chapter 3

can catalyze the formation of several consecutive carbon-carbon bonds under mild electrochemical conditions. The mechanistic insights we provided open a perspective for designing molecular and material-based catalysts with enhanced selectivity towards C_{2+} products.

3.7 Chapter 3 annex

3.7.1 NMR characterization

NMR measurement is used to detect liquid products that might be in the electrolyte. An aliquot of catholyte is sampled after each electrolysis. A solution of 50 mM Phenol and 10 mM DMSO in D₂O is used as the standard for the NMR measurement. 450 µL of the catholyte solution and 50 µL of the standard solution are thoroughly mixed and dropped into an NMR tube for measurement. A 400 MHz Bruker NMR spectrometer with a water suppression program is used for the measurement. Each measurement contains 128 scans.

3.7.2 Isotopic labeling experiments

The Micro GC FUSION® is coupled to the Omni Star GSD 320, O₂ mass spectrometer by connecting the analytical outlet of module B of the gas chromatograph to the capillary of the mass spectrometer. A multiple-ion detection mode with an SEM detector is used to monitor the masses of the theoretical fragments of C₂ to C₄ products based on the NIST database.²⁸ The parameters of the detection method are summarized in Table 3-1.

Table 3-1. Mass spectrometry method parameters

Parameters	Value
Inlet temperature	120°C
Capillary temperature	150°C
Dwell time	200 ms
SEM voltage	900 V
Resolution	50
Pause calibrate	1.00

A standard electrocatalytic experiment with ¹²CO₂ is performed as described in section 3. The mass spectrometer measurement is started simultaneously with the gas chromatograph measurement every 30 minutes during the 2-hour electrolysis. For the labeling experiment, the standard ¹²CO₂ purging gas is changed to 99.9% ¹³CO₂ from Eurisotop, while other steps in the procedure remain unchanged.

Chapter 3

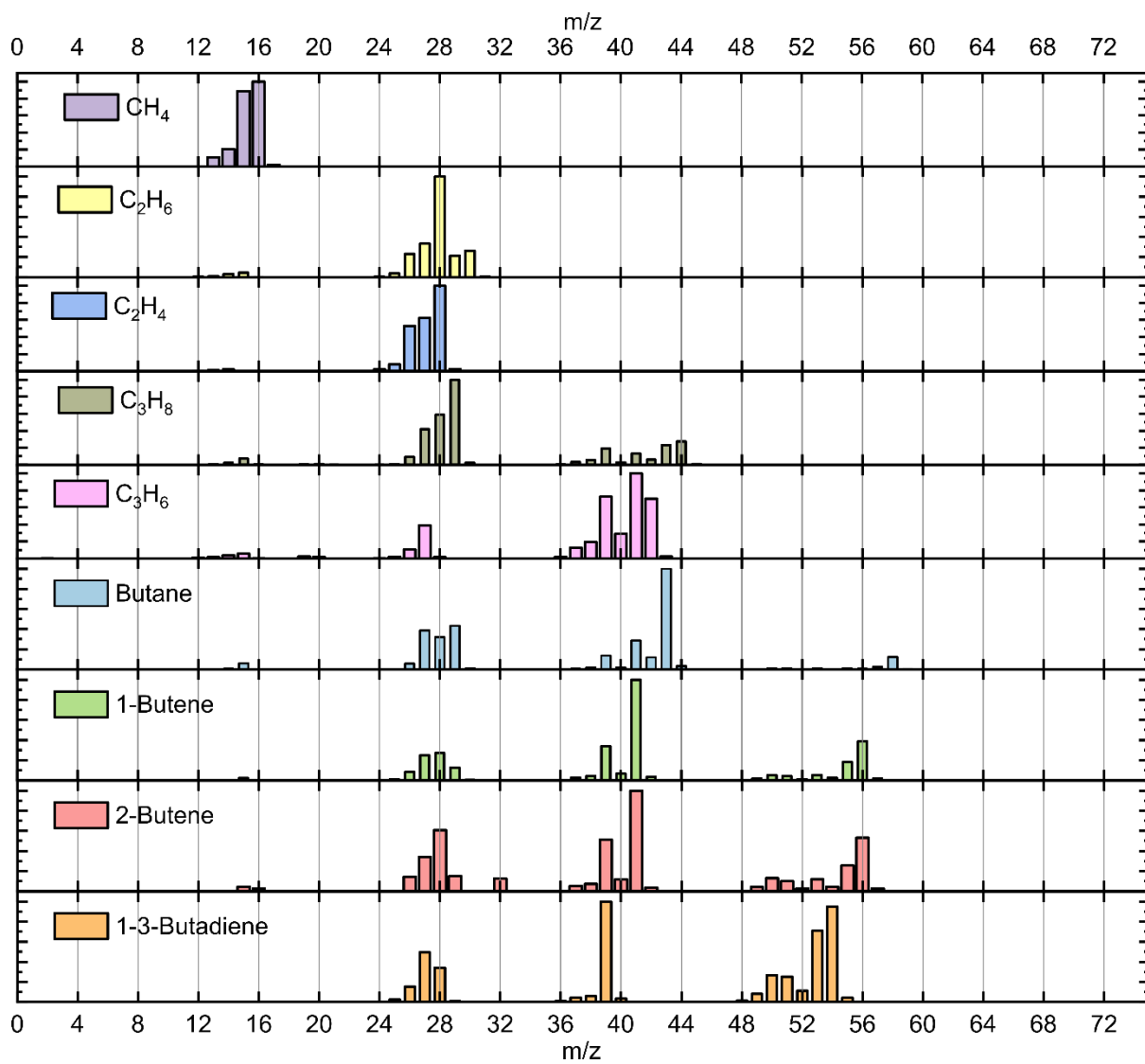


Figure 3-21. Reference mass spectra of C_1 to C_4 linear hydrocarbons. Data were taken from the NIST chemistry WebBook.²⁸

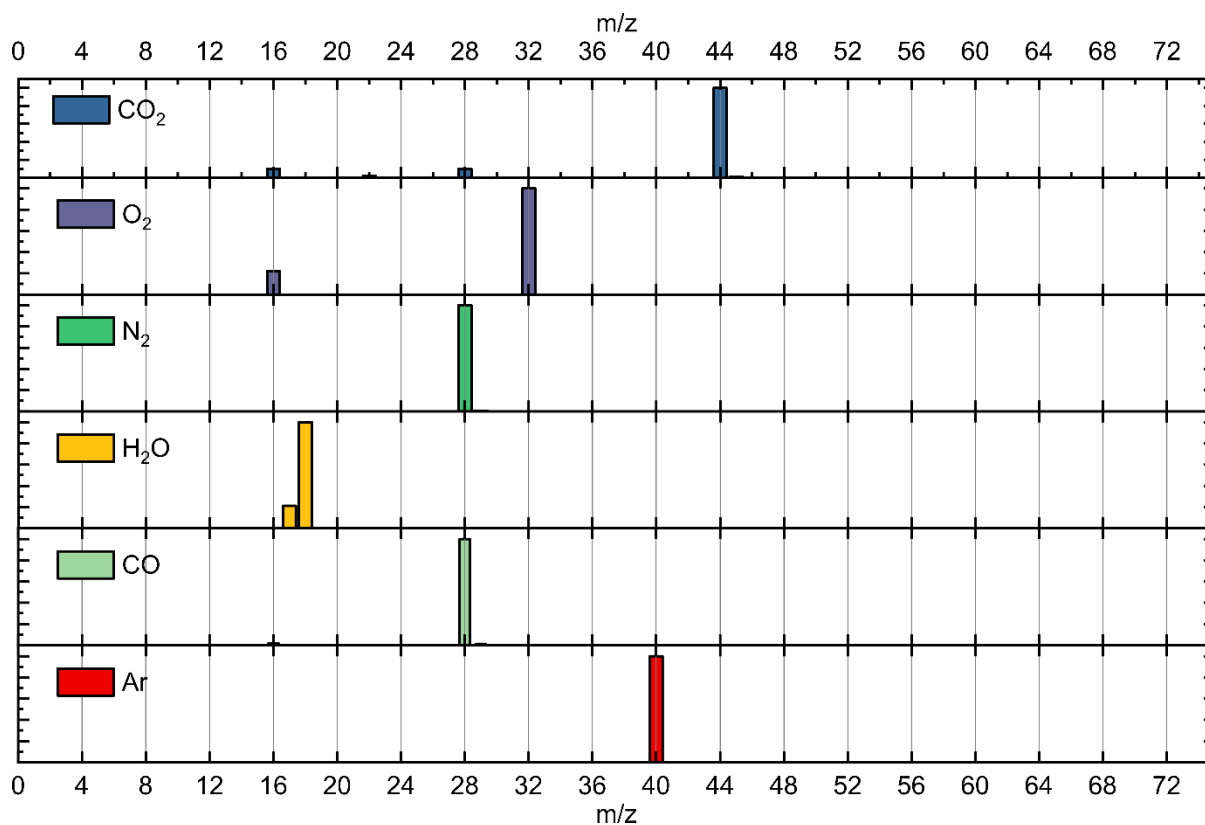


Figure 3-22. Reference mass spectra of species presented in the sample mixture. Data were taken from the NIST chemistry WebBook.²⁸

3.7.3 Cyclic voltammetry and active site estimation

To perform cyclic voltammetry in the electrochemical flow cell, the experimental setup is similar to the one for constant-potential electrolysis described in the general annex. However, the purging gas (CO_2 or Ar) is kept flowing, and the peristaltic pump is stopped during the potential cycling. The cyclic voltammetry is performed using the VSP-300 potentiostat from Biologic.

A homemade glass heart shape electrochemical cell is used to perform cyclic voltammetry in the standard static electrochemical cell. The working electrode is a rotating disk glassy carbon ($d = 5 \text{ mm}$) from Pine research, though the electrode was not rotating when performing the experiment. Before each drop-casting, the electrode is polished using diamond slurry solutions ($6 \mu\text{m} \rightarrow 3 \mu\text{m} \rightarrow 1 \mu\text{m}$, 2 minutes each). The ink and the drop-casting procedure are similar to the ones described in the general annex. However, since the working electrode is smaller than the glassy carbon plate used in the flow cell, to get the surface concentration of 80 nmol/cm^2 , an $8\text{-}\mu\text{L}$ drop is added to the electrode until the total volume of $83 \mu\text{L}$ is reached. The electrode is dried in an oven at 100°C after every drop. The catalyst-free electrode is prepared in a similar fashion using FePc-free ink. The reference electrode is a saturated calomel electrode, and a Pt counter electrode is used. The electrolyte is $0.05 \text{ M H}_2\text{SO}_4$, and the scan rate is 100 mV/s . Before every experiment, the electrolyte is purged with Ar for at least 15 minutes. An Autolab PGSTAT302N potentiostat (Metrohm) is used to perform

Chapter 3

electrochemical experiments.



Figure 3-23. Cyclic voltammetry setup in a homemade glass electrochemical cell.

The charge needed to carry out a 1-electron redox process with all FePc presented on the electrode is:

$$q = c_{surface} \times F = 80 \times 10^{-9} \frac{\text{mol}}{\text{cm}^2} \times 96490 \frac{\text{C}}{\text{mol}}$$

$$q \approx 7.7 \times 10^{-3} \frac{\text{C}}{\text{cm}^2} \approx 7.7 \text{ mC/cm}^2$$

The charges exhibited in a cyclic voltammetry experiment can be obtained by dividing areas under the peak of a cyclic voltammogram by the scan rate (0.1 V/s). With three peak areas obtained from three independent experiments shown in Figure 3-24, the average charge is $q_{average} = 0.604 \pm 0.065 \text{ mC/cm}^2$. Dividing the obtained charge to the charge needed for a 1-electron redox process with all the catalysts, we got the percentage of active catalyst to be $7.8 \pm 0.8\%$.

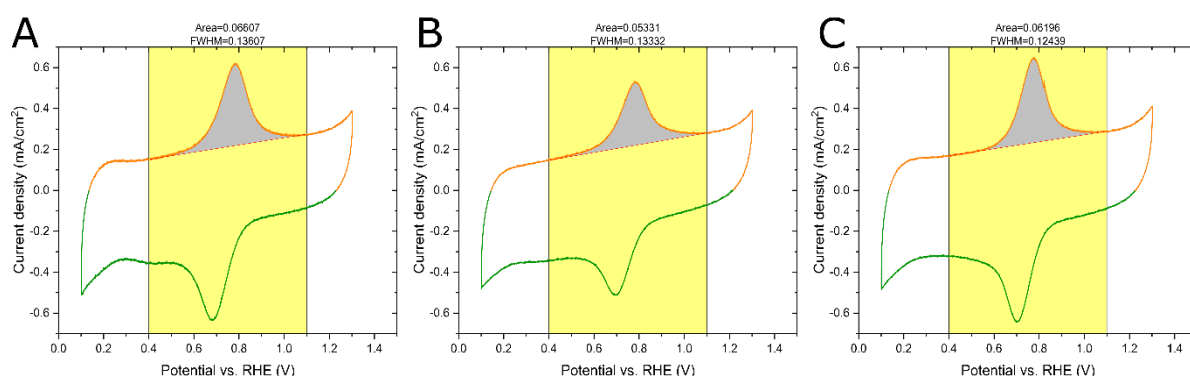


Figure 3-24. CVs peak integration of three independent experiments indicate by the panels (A), (B), and (C)

3.7.4 Infrared spectroscopy

The infrared measurements were performed at the AILES beamline ²⁹ of Synchrotron SOLEIL. The beamline is equipped with a Fourier Transform infrared spectrometer (IFS 125 from Bruker Instruments) working under a vacuum (10^{-4} mbar). The spectra are recorded using a Globar source, a KBr beamsplitter, and a homemade Mercury-Cadmium-Telluride detector cooled at 4.2K ³⁰. Two different set-ups were used for this study. Reference samples (pure powder) were analyzed using attenuated total reflectance technique⁴ with a single reflection on a 2mm diamond crystal. Modified-electrode samples were analyzed using an optical setup (A513-Bruker), allowing reflectivity measurement at grazing angle (70°), the spectrum of the glassy carbon modified with catalyst-free ink being used as a reference.

3.8 Bibliography

- (1) Wu, Y.; Jiang, Z.; Lu, X.; Liang, Y.; Wang, H. Domino Electroreduction of CO₂ to Methanol on a Molecular Catalyst. *Nature* **2019**, *575* (7784), 639–642. <https://doi.org/10.1038/s41586-019-1760-8>.
- (2) Boutin, E.; Wang, M.; Lin, J. C.; Mesnage, M.; Mendoza, D.; Lassalle-Kaiser, B.; Hahn, C.; Jaramillo, T. F.; Robert, M. Aqueous Electrochemical Reduction of Carbon Dioxide and Carbon Monoxide into Methanol with Cobalt Phthalocyanine. *Angewandte Chemie International Edition* **2019**, *58* (45), 16172–16176. <https://doi.org/10.1002/anie.201909257>.
- (3) Rao, H.; Schmidt, L. C.; Bonin, J.; Robert, M. Visible-Light-Driven Methane Formation from CO₂ with a Molecular Iron Catalyst. *Nature* **2017**, *548* (7665), 74–77. <https://doi.org/10.1038/nature23016>.
- (4) Weng, Z.; Jiang, J.; Wu, Y.; Wu, Z.; Guo, X.; Materna, K. L.; Liu, W.; Batista, V. S.; Brudvig, G. W.; Wang, H. Electrochemical CO₂ Reduction to Hydrocarbons on a Heterogeneous Molecular Cu Catalyst in Aqueous Solution. *J. Am. Chem. Soc.* **2016**, *138* (26), 8076–8079. <https://doi.org/10.1021/jacs.6b04746>.
- (5) Weng, Z.; Wu, Y.; Wang, M.; Jiang, J.; Yang, K.; Huo, S.; Wang, X.-F.; Ma, Q.; Brudvig, G. W.; Batista, V. S.; Liang, Y.; Feng, Z.; Wang, H. Active Sites of Copper-Complex Catalytic Materials for Electrochemical Carbon Dioxide Reduction. *Nat Commun* **2018**, *9* (1), 415. <https://doi.org/10.1038/s41467-018-02819-7>.
- (6) Creissen, C. E.; Fontecave, M. Keeping Sight of Copper in Single-Atom Catalysts for Electrochemical Carbon Dioxide Reduction. *Nat Commun* **2022**, *13* (1), 1–4. <https://doi.org/10.1038/s41467-022-30027-x>.
- (7) Magdesieva, T. V.; Yamamoto, T.; Tryk, D. A.; Fujishima, A. Electrochemical Reduction of CO₂ with Transition Metal Phthalocyanine and Porphyrin Complexes Supported on Activated Carbon Fibers. *J. Electrochem. Soc.* **2002**, *149* (6), D89. <https://doi.org/10.1149/1.1475690>.
- (8) Liu, Y.; Deb, A.; Yee Leung, K.; Nie, W.; S. Dean, W.; E. Penner-Hahn, J.; L. McCrory, C. C. Determining the Coordination Environment and Electronic Structure of Polymer-Encapsulated Cobalt Phthalocyanine under Electrocatalytic CO₂ Reduction Conditions Using in Situ X-Ray Absorption Spectroscopy. *Dalton Transactions* **2020**, *49* (45), 16329–16339. <https://doi.org/10.1039/D0DT01288B>.
- (9) Ziminov, A. V.; Ramsh, S. M.; Terukov, E. I.; Trapeznikova, I. N.; Shamanin, V. V.; Yurre, T. A. Correlation Dependences in Infrared Spectra of Metal Phthalocyanines. *Semiconductors* **2006**, *40* (10), 1131–1136. <https://doi.org/10.1134/S1063782606100022>.
- (10) Zhang, X.; Zhang, Y.; Jiang, J. Towards Clarifying the N-M Vibrational Nature of Metallo-Phthalocyanines. *Spectrochimica Acta Part A: Molecular and Biomolecular Spectroscopy* **2004**, *60* (10), 2195–2200. <https://doi.org/10.1016/j.saa.2003.11.015>.
- (11) Ha, S. Y.; Park, J.; Ohta, T.; Kwag, G.; Kima, S. In Situ Iron K-Edge XANES Study of Iron Phthalocyanine Irreversibly Adsorbed on an Electrode Surface. *Electrochem. Solid-State Lett.* **1999**, *2* (9), 461. <https://doi.org/10.1149/1.1390871>.

- (12) Corbin, N.; Zeng, J.; Williams, K.; Manthiram, K. Heterogeneous Molecular Catalysts for Electrocatalytic CO₂ Reduction. *Nano Res.* **2019**, *12* (9), 2093–2125. <https://doi.org/10.1007/s12274-019-2403-y>.
- (13) Zhu, M.; Ye, R.; Jin, K.; Lazouski, N.; Manthiram, K. Elucidating the Reactivity and Mechanism of CO₂ Electroreduction at Highly Dispersed Cobalt Phthalocyanine. *ACS Energy Letters* **2018**, *3* (6), 1381–1386. <https://doi.org/10.1021/acseenergylett.8b00519>.
- (14) Han, S.; Kim, C.; Kwon, D. Thermal/Oxidative Degradation and Stabilization of Polyethylene Glycol. *Polymer* **1997**, *38* (2), 317–323. [https://doi.org/10.1016/S0032-3861\(97\)88175-X](https://doi.org/10.1016/S0032-3861(97)88175-X).
- (15) Gurudayal; Perone, D.; Malani, S.; Lum, Y.; Haussener, S.; Ager, J. W. Sequential Cascade Electrocatalytic Conversion of Carbon Dioxide to C–C Coupled Products. *ACS Appl. Energy Mater.* **2019**, *2* (6), 4551–4559. <https://doi.org/10.1021/acsaem.9b00791>.
- (16) Louisia, S.; Kim, D.; Li, Y.; Gao, M.; Yu, S.; Roh, I.; Yang, P. The Presence and Role of the Intermediary CO Reservoir in Heterogeneous Electroreduction of CO₂. *Proc. Natl. Acad. Sci. U.S.A.* **2022**, *119* (18), e2201922119. <https://doi.org/10.1073/pnas.2201922119>.
- (17) Mahmoudi, H.; Mahmoudi, M.; Doustdar, O.; Jahangiri, H.; Tsolakis, A.; Gu, S.; LechWyszynski, M. A Review of Fischer Tropsch Synthesis Process, Mechanism, Surface Chemistry and Catalyst Formulation. *Biofuels Engineering* **2017**, *2* (1), 11–31. <https://doi.org/10.1515/bfuel-2017-0002>.
- (18) Boutin, E.; Salamé, A.; Merakeb, L.; Chatterjee, T.; Robert, M. On the Existence and Role of Formaldehyde During Aqueous Electrochemical Reduction of Carbon Monoxide to Methanol by Cobalt Phthalocyanine. *Chemistry – A European Journal* **2022**, *28* (27), e202200697. <https://doi.org/10.1002/chem.202200697>.
- (19) Lexa, D.; Savéant, J.-M.; Battioni, J.-P.; Lange, M.; Mansuy, D. Redox Relationship between Carbeneiron And σ -Alkyliron Porphyrins. *Angew. Chem. Int. Ed. Engl.* **1981**, *20* (67), 578–579. <https://doi.org/10.1002/anie.198105781>.
- (20) Artaud, I.; Gregoire, N.; Leduc, P.; Mansuy, D. Formation and Fate of Iron-Carbene Complexes in Reactions between a Diazoalkane and Iron-Porphyrins: Relevance to the Mechanism of Formation of N-Substituted Hemes in Cytochrome P-450-Dependent Oxidation of Sydnones. *J. Am. Chem. Soc.* **1990**, *112* (19), 6899–6905. <https://doi.org/10.1021/ja00175a025>.
- (21) Zhao, Y.; Wang, Y.-J.; Wang, N.; Zheng, P.; Fu, H.-R.; Han, M.-L.; Ma, L.-F.; Wang, L.-Y. Tetraphenylethylene-Decorated Metal-Organic Frameworks as Energy-Transfer Platform for the Detection of Nitro-Antibiotics and White-Light Emission. *Inorg. Chem.* **2019**, *58* (19), 12700–12706. <https://doi.org/10.1021/acs.inorgchem.9b01588>.
- (22) Liu, J.-Z.; Wang, T.-L.; Ji, L.-N. Enhanced Dye Decolorization Efficiency by Citraconic Anhydride-Modified Horseradish Peroxidase. *Journal of Molecular Catalysis B: Enzymatic* **2006**, *41* (3), 81–86. <https://doi.org/10.1016/j.molcatb.2006.04.011>.
- (23) Lewis, R. D.; Garcia-Borràs, M.; Chalkley, M. J.; Buller, A. R.; Houk, K. N.; Kan, S. B. J.; Arnold, F. H. Catalytic Iron-Carbene Intermediate Revealed in a Cytochrome c Carbene Transferase. *PNAS* **2018**, *115* (28), 7308–7313. <https://doi.org/10.1073/pnas.1807027115>.

Chapter 3

- (24) Empel, C.; Jana, S.; Koenigs, R. M. C-H Functionalization via Iron-Catalyzed Carbene-Transfer Reactions. *Molecules* **2020**, *25* (4), 880. <https://doi.org/10.3390/molecules25040880>.
- (25) Henrici-Olivé, G.; Olivé, S. The Fischer-Tropsch Synthesis: Molecular Weight Distribution of Primary Products and Reaction Mechanism. *Angewandte Chemie International Edition in English* **1976**, *15* (3), 136–141. <https://doi.org/10.1002/anie.197601361>.
- (26) Tavakoli, A.; Sohrabi, M.; Kargari, A. Application of Anderson–Schulz–Flory (ASF) Equation in the Product Distribution of Slurry Phase FT Synthesis with Nanosized Iron Catalysts. *Chemical Engineering Journal* **2008**, *136* (2), 358–363. <https://doi.org/10.1016/j.cej.2007.04.017>.
- (27) Kudo, A.; Nakagawa, S.; Tsuneta, A.; Sakata, T. Electrochemical Reduction of High Pressure CO₂ on Ni Electrodes. <https://iopscience.iop.org/article/10.1149/1.2221599>.
- (28) NIST Chemistry WebBook. <https://webbook.nist.gov/chemistry/> (accessed 2022-10-24). <https://doi.org/10.18434/T4D303>.
- (29) Roy, P.; Rouzières, M.; Qi, Z.; Chubar, O. The AILES Infrared Beamline on the Third Generation Synchrotron Radiation Facility SOLEIL. *Infrared Physics & Technology* **2006**, *49* (1–2), 139–146. <https://doi.org/10.1016/j.infrared.2006.01.015>.
- (30) Faye, M.; Bordessoule, M.; Kanouté, B.; Brubach, J.-B.; Roy, P.; Manceron, L. Improved Mid Infrared Detector for High Spectral or Spatial Resolution and Synchrotron Radiation Use. *Review of Scientific Instruments* **2016**, *87* (6), 063119. <https://doi.org/10.1063/1.4954405>.

Chapter 3

4 CHAPTER 4: OPTIMIZING ELECTROLYSIS PARAMETERS OF FEPC AND SCREENING VARIOUS CATALYSTS

4.1	Introduction.....	114
4.2	Influence of external factors on FePc.....	115
4.2.1	Flow rate.....	115
4.2.2	Electrolyte concentration and pH.....	118
4.2.3	FePc concentration.....	121
4.2.4	Conductive carbon support concentration.....	124
4.3	Metal phthalocyanines.....	126
4.3.1	Metal center effects.....	126
4.3.2	Ligand effects on FePc.....	129
4.4	Iron porphyrins and derivatives.....	134
4.5	Conclusion.....	138
4.6	Bibliography.....	140

4.1 Introduction

The metal center and the ligands of a molecular catalyst can be tuned to achieve specific properties. As discussed in Chapter 1, the nature of the metal and ligands of many phthalocyanine species have been studied and optimized for CO₂ reduction for several decades. Concerning the influence of the metal center on the CO₂-to-CO reducing activity, cobalt phthalocyanine is the most active species, followed by iron and nickel phthalocyanine.^{1,2} Other metal phthalocyanines could produce CO, but their performances are generally worse than Co, Ni, and FePc. Further reduced products such as methane and methanol have been reported. The formation of species with C–C bonds is much rarer, with only one report mentioning the presence of low amounts of methane, ethane, and ethylene with CoPc and CuPc without further investigation.³ The porphyrin family behaves similarly, with iron and nickel porphyrin being the most active species for CO₂-to-CO reduction.⁴ The nature of the ligand also plays a prominent role in the performance of porphyrin and phthalocyanine species. Multiple properties of a substituent group, including its inductive effect, steric hindrance, charge, or proton relaying site, can influence the catalytic activity of a catalyst.^{2,5,6} Consequently, the direct substituents-activity relationship is complicated to establish and can differ from case to case.

Besides the nature of the catalyst, many parameters surrounding CO₂ electrolysis can significantly affect its performance. Some of these parameters have been discussed in Chapter 1, namely electrolyte flow rate, catalyst concentration, electrolyte concentration, and the nature of the conductive carbon support. In an electrolysis flow system where CO₂ is dissolved into the electrolyte, the electrolyte flow rate can change the amount of CO₂ coming in contact with the electrode surface, altering the selectivity of species products.⁷ The catalyst loading in heterogeneous electrocatalysis affects the dispersity of the active sites, leading to different turnover frequencies and current densities at different loading.⁸ For carbonate and bicarbonate electrolytes, their buffer capacity depends on their concentration, influencing the local pH in close proximity to the electrode surface.^{8–10} Finally, the type and amount of the conductive carbon supports have wide-ranging effects on the current density and selectivity of the CO₂ reduction process.^{11,12}

In the previous chapter, we provided evidence showing that FePc could produce a small amount of CH₄ and C₂₊ products from CO₂ reduction. The applied potential significantly affected the product distribution of CO₂ electrolysis. In this chapter, we further explore the impacts of other factors on the CO₂ reduction activity of FePc, aiming to increase the selectivity of the catalyst towards C₂₊ products. The investigated parameters include the electrolyte flow rate, the concentrations of catalyst, electrolyte, and conductive carbon support. We then conducted a preliminary study to see the effect of ligands of FePc, and different metal phthalocyanines to produce C₂₊ species. Finally, we used iron tetraphenyl porphyrin and its derivatives as catalysts for CO₂ reduction, focusing on whether other iron macrocycles would yield C₂₊ products.

4.2 Influence of external factors on FePc

4.2.1 Flow rate

Figure 4-1 shows the electrolysis curves of FePc-modified electrodes at applied potentials of -0.9 to -1.1 V vs. RHE with the electrolyte flow rate of 0.25, 1, and 4 mL/min. Other parameters were similar to experiments with FePc described in Chapter 3 and the annex, with a catalyst loading of 80 nmol/cm^2 and a KHCO_3 0.1 M electrolyte. The lower flow rate limit was chosen to ensure the bubbles generated from electrolysis can be evacuated fast enough to avoid disrupting the electrolysis. The higher flow rate limit was the maximum rate where the catalyst layer could adhere well to the working electrode without undergoing significant mechanical erosion.

At both potentials, the fastest flow rate of 4 mL/min displayed a slightly higher current density, while the values at 0.25 and 1 mL/min were similar. The higher current density at a higher flow rate might suggest that the CO_2 -reducing activity was higher due to more reactants being in contact with the electrode surface. However, the effect was insignificant, as only minor changes were observed.

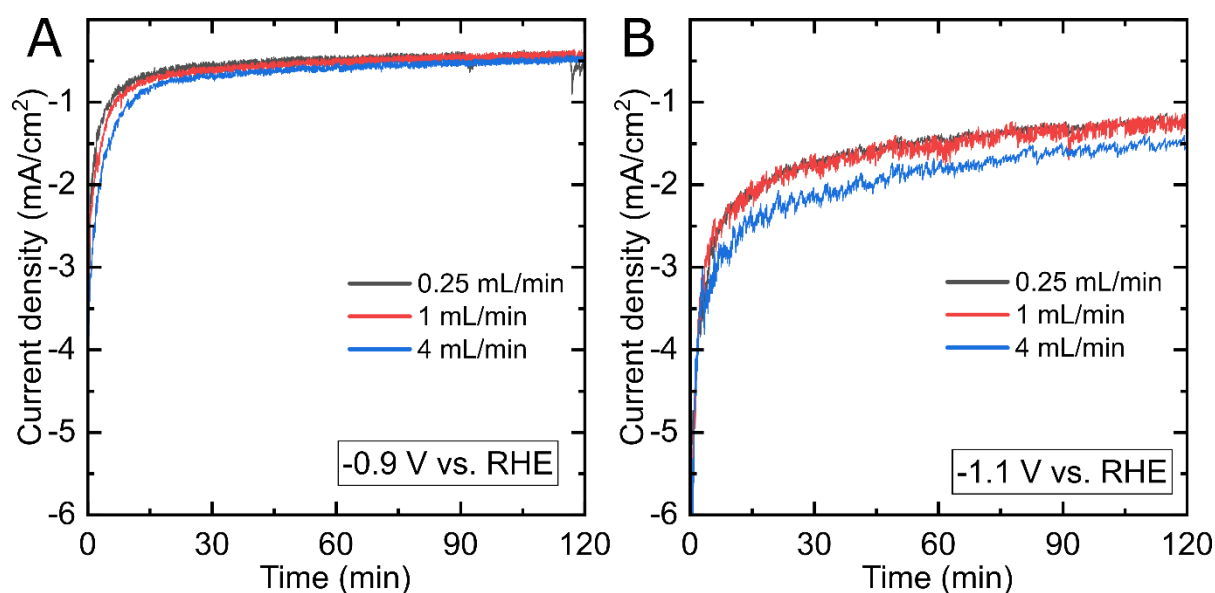


Figure 4-1. Electrolysis curves of FePc-modified electrodes at -0.9 V vs. RHE (**A**), and -1.1 V vs. RHE (**B**) under CO_2 in 0.1 M KHCO_3 performed at different flowrate for two hours.

Figure 4-2 shows the faradaic efficiencies (FE) of CO , H_2 , CH_4 , and C_{2+} products obtained after 2-hour electrolysis at -0.9 and -1.1 V vs. RHE with FePc-modified electrodes under CO_2 at a flow rate ranging from 0.25 to 4 mL/min. When the flow rate increased from 0.25 to 4 mL/min, the CO_2 reduction activity increased, and the hydrogen evolution activity was further suppressed. While this phenomenon was observed at both applied potentials, the rise in CO selectivity, from 30% to 50%, was more pronounced at a more negative potential of -1.1 V vs. RHE. The high flow rate enhanced the CO_2 mass transport to the electrode surface, resulting in more CO_2

Chapter 4

reduction activity and less side reaction with water. This CO₂ availability effect played a more prominent role at high overpotentials, as the electrode consumes more CO₂ at this condition. Therefore, an electrolysis system with higher CO₂ availability, such as a high-pressure or gas diffusion setup, would enhance the selectivity of the FePc catalyst towards CO₂ reduction.

Interestingly, the selectivity-flow rate trend appears to reverse concerning the more reduced hydrocarbon species. The most selective condition for CH₄ generation was at 1 mL/min at -0.9 V vs. RHE (1.5%) and 0.25 mL/min at -1.1 V vs. RHE (4.5%). The total C₂₊ products consistently decreased with increasing flow rate at both electrolysis potentials, from 0.35% to 0.23% at -0.9 V and from 0.66% to 0.56% at -1.1 V vs. RHE.

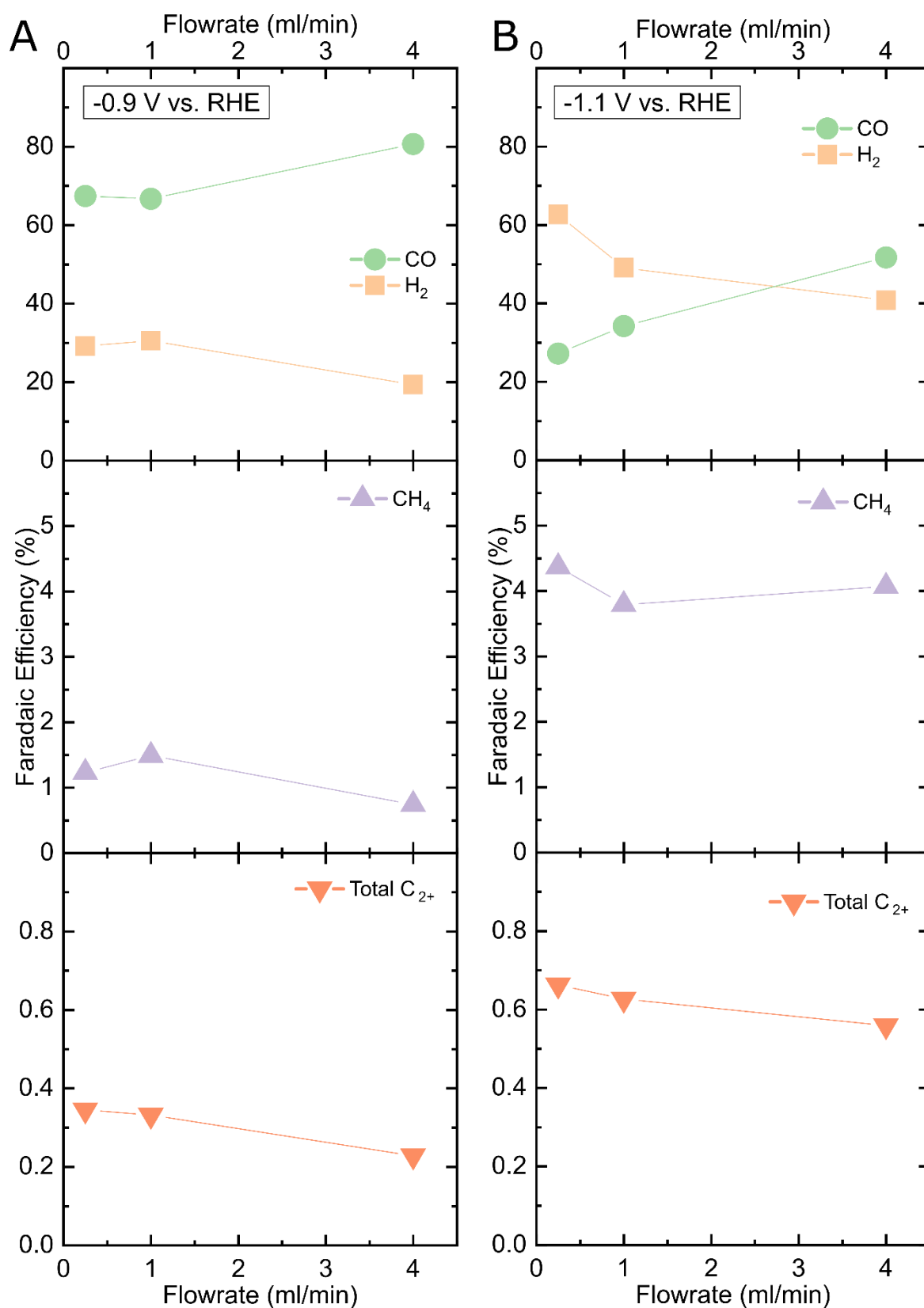


Figure 4-2. Product distribution observed with FePc-modified electrodes as faradaic efficiencies at -0.9 V vs. RHE (**A**) and -1.1 V vs. RHE (**B**) as a function of flow rate. The amount of ethylene (C₂H₄) is underestimated due to the high background generated by CO₂ in the chromatograph column.

The full distribution of individual C_{2+} products is shown in Figure 4-3. The evolution of the hydrocarbon species is generally correlated with the evolution trend of hydrogen. The correlation indicated that the formation of the highly reduced species was more limited by the hydrogen availability than CO. Therefore, a setup with higher CO_2 availability can increase the CO selectivity of FePc, but it may also hinder the formation of products with C – C bonds. Overall, the choice of a flow rate value could considerably alter the product distribution of CO and H_2 . However, the flow rate effect toward CH_4 was marginal. Concerning the C_{2+} products, C_2H_6 exhibited the most significant changes, increasing from 0.2 to 0.3% when the flow rate was decreased from 4 to 0.25 mL/min and the potential poised at -1.1 V.

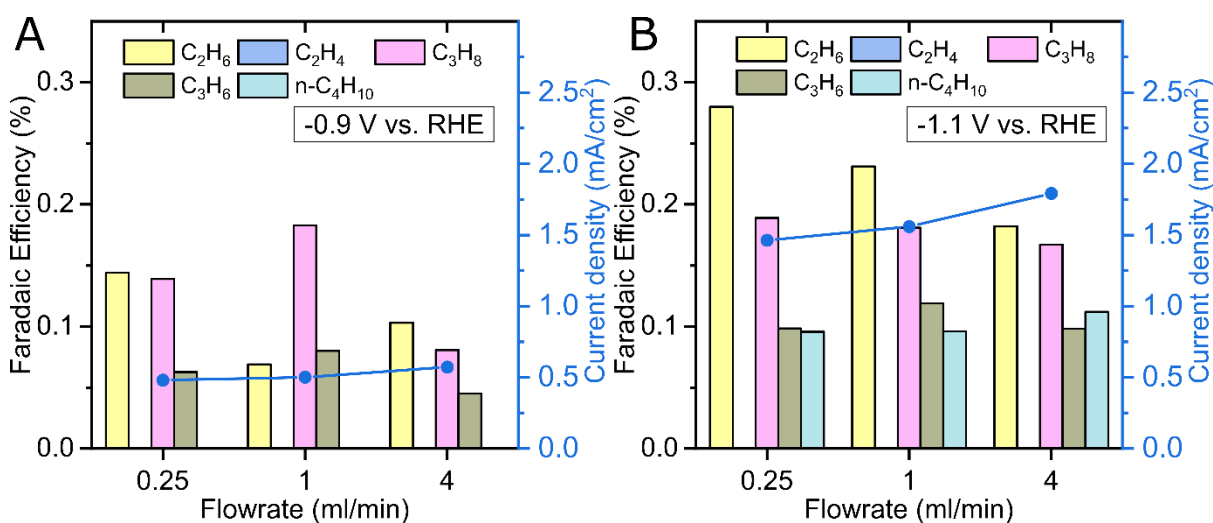


Figure 4-3. C_{2+} product distribution observed with FePc-modified electrodes as faradaic efficiencies at -0.9 V vs. RHE (A) and -1.1 V vs. RHE (B) as a function of flow rate. The total current density at 60 minutes is plotted as a blue dot for each flow rate. Although no ethylene (C_2H_4) was plotted, its peak was likely underestimated due to the high background generated by CO_2 in the chromatograph column.

4.2.2 Electrolyte concentration and pH

To study the effect of $KHCO_3$ electrolyte concentration on the CO_2 -reducing activity of FePc, we perform electrolysis experiments at -1.7 V vs. Ag/AgCl with FePc-modified electrodes under CO_2 at $KHCO_3$ concentration ranging from 0.02 M to 2.5 M. Since the bulk pH of the electrolyte is dependent on the salt concentration, the applied potential in the scale of the reversible hydrogen electrode is slightly different depending on the electrolyte concentration. Table 4-1 summarizes the pH and the applied potentials on the RHE scale. Other conditions were kept similar to experiments with FePc described in Chapter 3 and the annex, with a catalyst loading of 80 nmol/cm² and a flow rate of 1 mL/min.

Table 4-1. pH and applied potential on RHE scale as a function of KHCO_3 concentration

KHCO_3 concentration (M)	Initial pH	pH after 15-minute CO_2 bubbling	V vs. RHE at -1.7 V vs. Ag/AgCl
0.02	8.76	5.87	-1.15
0.1	8.75	6.80	-1.09
0.5	8.55	7.43	-1.06
1	9.50	7.76	-1.04
2.5	9.39	9.08	-0.96

Figure 4-4 shows the current densities and faradaic efficiencies of CO , H_2 , CH_4 , and C_2^+ products obtained after the 2-hour electrolysis experiments at different electrolyte concentrations. As observed in Figure 4-4A, the current density increased with the electrolyte concentration. However, starting from 0.5 M, the electrolysis becomes unstable as the current increased over time. The instability was most substantial at the highest concentration of 2.5 M, as the noise and the rising trend were greatly exacerbated. The increase in current density over time was likely the result of a corrosive side reaction. Therefore, the total faradaic efficiencies under these conditions did not reach one hundred percent. In addition, the high amount of hydrogen generated in these conditions considerably increased the pressure in the headspace. Since the faradaic efficiency calculation assumed the head space pressure to equal atmospheric pressure, the amount of gas products in these conditions was likely underestimated.

When the electrolyte concentration increased, the CO_2 reduction activity of FePc drastically decreased. The highest CO selectivity was obtained at 0.02 M KHCO_3 , which then falls to around 20% at 0.1 M and less than 10% at higher electrolyte concentrations. On the contrary, the hydrogen evolution activity rises with electrolyte concentration, peaking at 80% at 0.5 M. At higher electrolyte concentrations, the hydrogen selectivity was likely to be underestimated, as explained above. At first, these trends seemed counter-intuitive, as hydrogen yield was higher in concentrated bicarbonate electrolytes with higher bulk pH. However, the observed trends were consistent with previous studies in the literature.^{9,10} The concentrated bicarbonate electrolyte has a higher bulk pH, but it also has a higher buffer capacity. The high buffer capacity would prevent the rise of local pH caused by CO_2 reduction activity consuming protons. Therefore, concentrated electrolytes would have lower local pH than dilute electrolytes, hence the higher hydrogen evolution and lower CO_2 reduction activity.

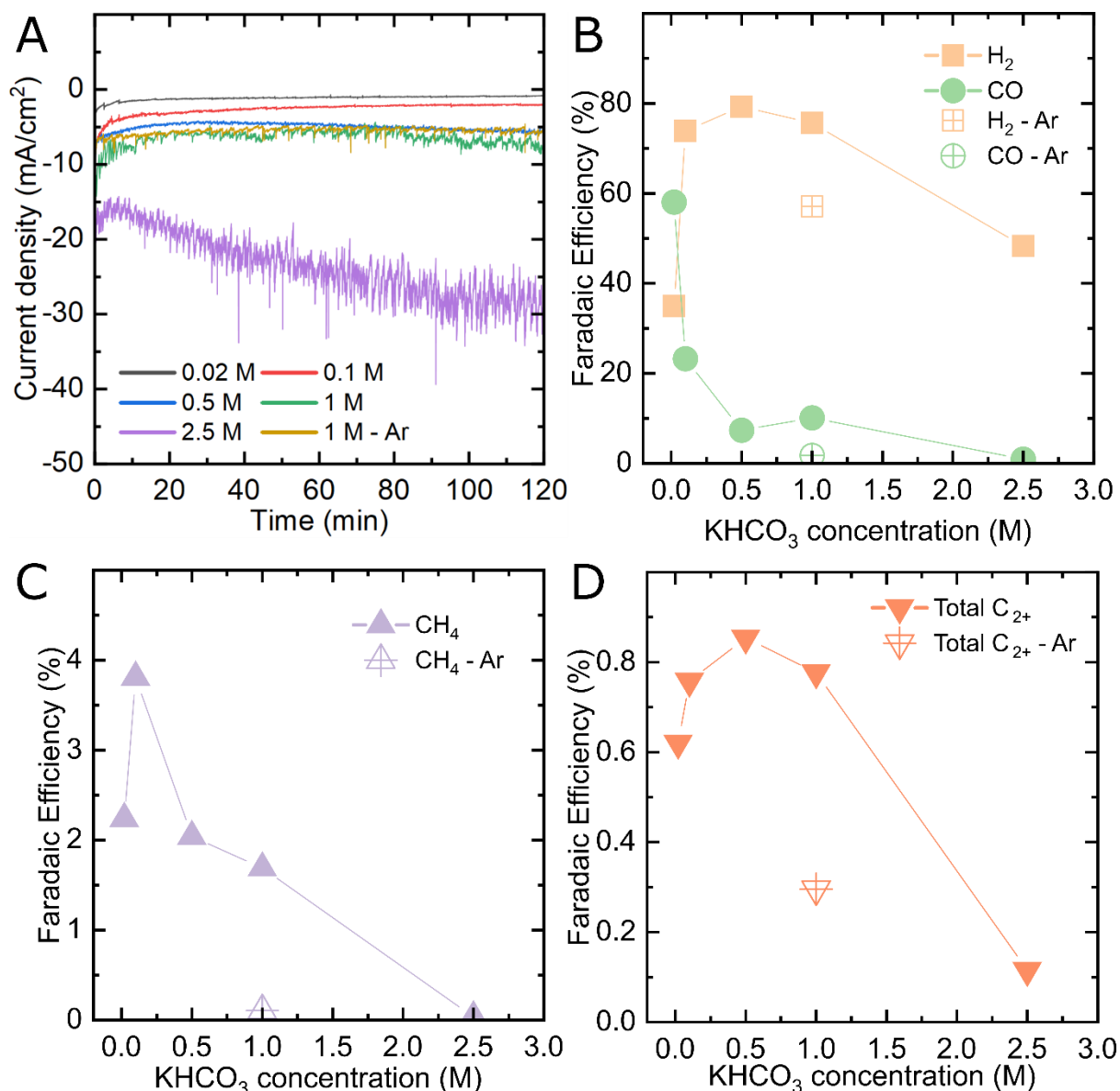


Figure 4-4. Electrolysis curves of FePc-modified electrodes at -1.7 V vs. Ag/AgCl (**A**) and product distribution observed with FePc-modified electrodes as faradaic efficiencies at -1.7 V vs. Ag/AgCl (**B-D**) as a function of KHCO_3 concentration. The amount of ethylene (C_2H_4) is underestimated due to the high background generated by CO_2 in the chromatograph column.

The high electrolyte concentration also did not favor the formation of hydrocarbon species, as little to no CH_4 and C_{2+} species were observed at 2.5 M concentration. However, instead of a monotonic decrease, as in the case of CO, the evolution of CH_4 and C_{2+} products follow a volcano trend. The total distribution of individual C_{2+} products is shown in Figure 4-5. CH_4 peaks around 4% at 0.1 M, while C_{2+} peaks around 0.85% at 0.5 M. Nevertheless, controlled electrolysis in an Ar-saturated 1 M KHCO_3 electrolyte showed that all the carbon products are present, albeit in much lower amounts compared to a CO_2 -saturated electrolyte despite the similar current density. In contrast, a control experiment with 0.1 M KHCO_3 (Chapter 3) yielded only a trace amount of CO and no traces of CH_4 or C_{2+} products. The presence of these highly reduced species suggests that at high bicarbonate concentrations, the bicarbonate

itself is also a feedstock and can be reduced to hydrocarbon species. Therefore, excluding the amount of C_{2+} products generated from bicarbonate, the optimized concentration to produce species with C – C bonds from CO_2 would lie around 0.1 M.

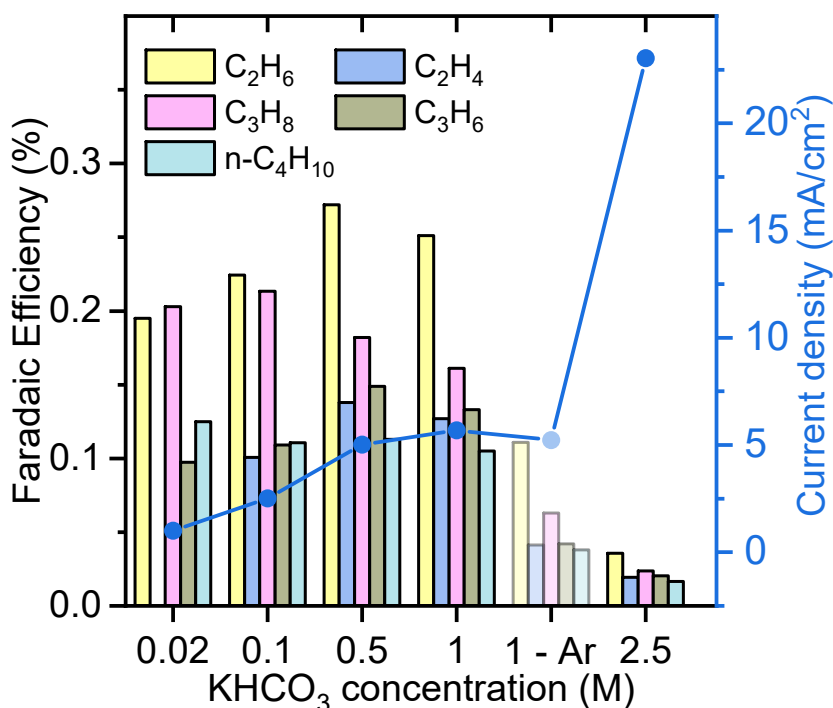


Figure 4-5. C_{2+} product distribution observed with FePc-modified electrodes as faradaic efficiencies at -1.7 V vs. Ag/AgCl as a function of $KHCO_3$ electrolyte concentration. The total current density at 60 minutes is plotted as a blue dot for each bicarbonate concentration. The amount of ethylene (C_2H_4) is underestimated due to the high background generated by CO_2 in the chromatograph column.

4.2.3 FePc concentration

Figure 4-6 shows the electrolysis curves of FePc-modified electrodes at applied potentials of -0.7 , -0.9 , and -1.1 V vs. RHE with different FePc loading. The experimental conditions were similar to experiments with FePc described in Chapter 3 and the annex, with a catalyst loading of 80 nmol/cm², a $KHCO_3$ 0.1 M electrolyte, and a flow rate of 1 mL/min. Regardless of the catalyst concentrations, the current density was higher at more negative potential. At -0.7 and -1.1 V vs. RHE, no significant difference in current density was displayed by electrodes with different amounts of FePc. However, at -0.9 V vs. RHE, the highest current density (~ 1.5 mA/cm²) was observed with the electrode having the highest catalyst loading, while the values of the two others were around one and a half times lower.

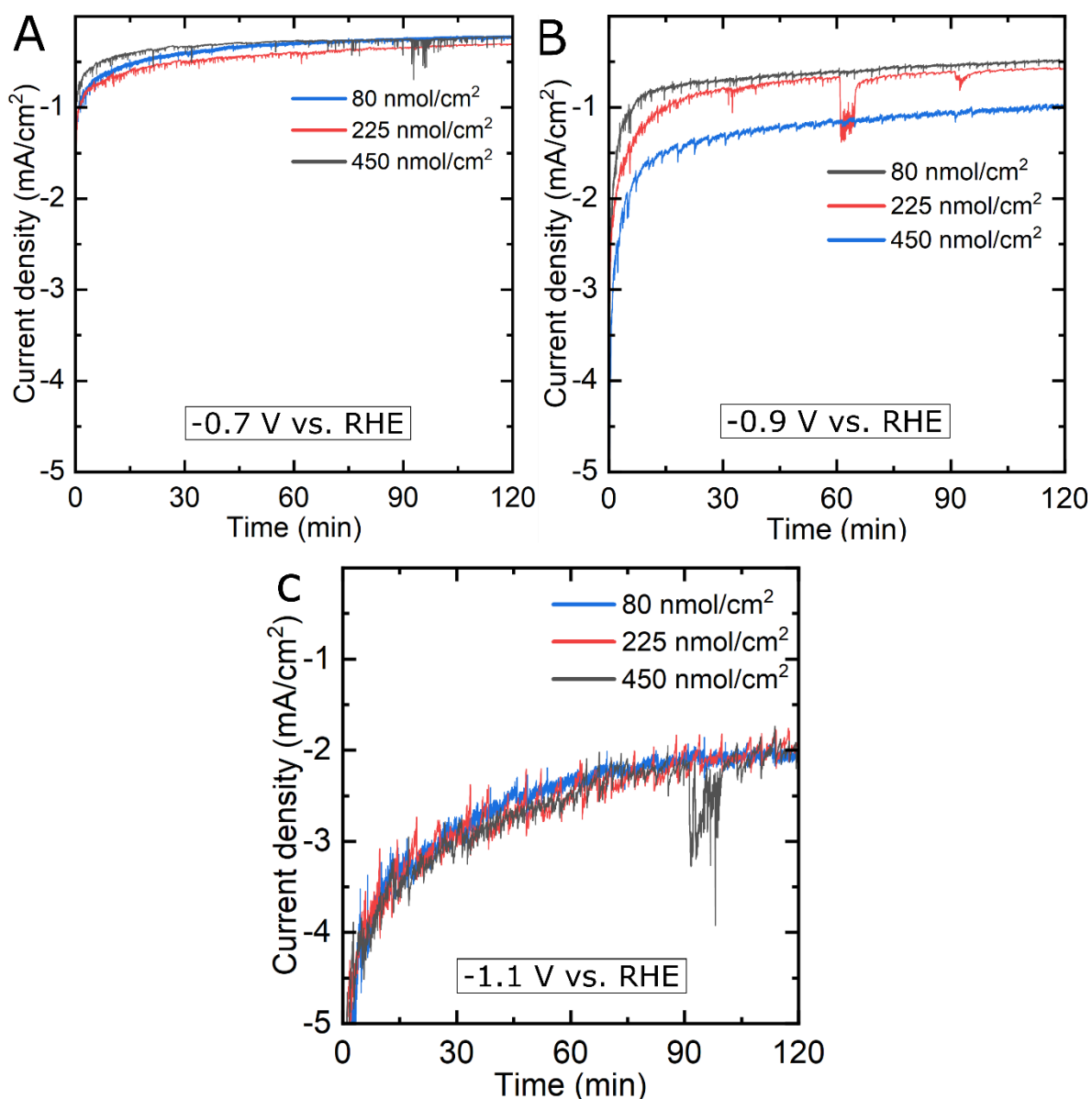


Figure 4-6. Electrolysis curves of FePc-modified electrodes at -0.7 V vs. RHE (A), -0.9 V vs. RHE (B), and -1.1 V vs. RHE (C) under CO₂ in 0.1 M KHCO₃ performed at different FePc concentrations for two hours.

Figure 4-7. Product distribution observed with FePc-modified electrodes as faradaic efficiencies at -0.9 V vs. RHE (A) and -1.1 V vs. RHE (B) as a function of FePc concentration. The amount of ethylene (C₂H₄) is underestimated due to the high background generated by CO₂ in the chromatograph column.

Figure 4-7 shows the faradaic efficiencies (FE) of CO, H₂, CH₄, and C₂⁺ products obtained after 2-hour electrolysis at -0.9 and -1.1 V vs. RHE with FePc-modified electrodes under CO₂ at FePc concentrations ranging from 80 to 450 nmol/cm². At -1.1 V vs. RHE, the selectivity of CO and H₂ exhibited a moderate variation at different FePc concentrations, but no clear trend emerged. On the other hand, at -0.9 V vs. RHE, the faradaic efficiency of CO decreased, while that of H₂ increased with higher catalyst

loading. Since CO_2 reduction is more favored than hydrogen evolution at this moderate potential, the amount of CO_2 near the electrode might be depleted too quickly with high catalyst concentrations. Therefore, water reduction could happen more readily as the CO_2 mass transfer was not quick enough. A similar trend was observed at a potential of -0.7 V vs. RHE (Figure 4-8). At this potential, CO and H_2 were the only products observed, indicating that a sufficient potential was necessary to reduce CO_2 further than CO.

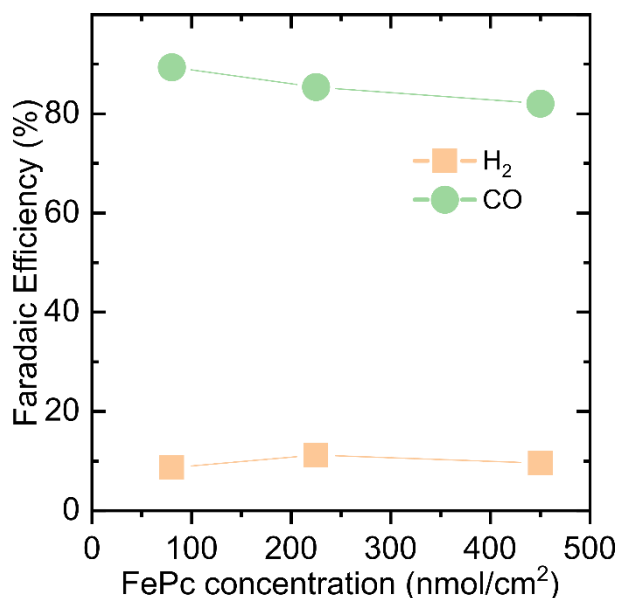


Figure 4-8. Product distribution observed with FePc-modified electrodes as faradaic efficiencies at -0.7 V vs. RHE as a function of FePc concentration.

When the applied potential was sufficiently negative, CH_4 tended to be favored at lower catalyst loading. At -1.1 V vs. RHE, the highest CH_4 amount obtained was at the lowest FePc concentration. At -0.9 V vs. RHE, both the highest and the lower FePc concentrations yielded a similar amount of CH_4 , while the lowest CH_4 faradaic efficiency was observed at the moderate FePc loading.

Concerning the C_{2+} products, at a high overpotential of -1.1 V vs. RHE, the total selectivity increased, but it appeared to reach a saturating value of around 1.2 % at 225 nmol/cm². A similar trend was observed at a less negative potential of -0.9 V vs. RHE as the total C_{2+} products saturated when the catalyst concentrations increased. The entire distribution of individual C_{2+} products is shown in Figure 4-9. The saturation effect of C_{2+} products observed with increasing FePc concentrations suggested that catalyst degradation could not be the source of the observed hydrocarbons, as higher catalyst loading did not lead to equally higher observed products.

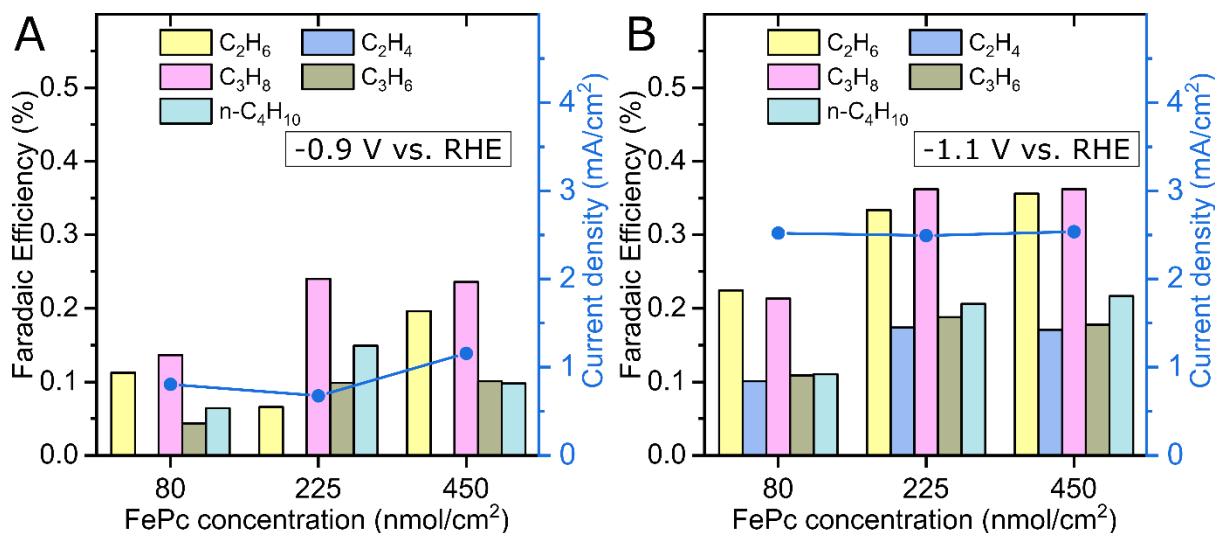


Figure 4-9. C₂₊ product distribution observed with FePc-modified electrodes as faradaic efficiencies at -0.9 V vs. RHE (A) and -1.1 V vs. RHE (B) as a function of FePc concentration. The total current density at 60 minutes is plotted as a blue dot for each catalyst concentration. The amount of ethylene (C₂H₄) is underestimated due to the high background generated by CO₂ in the chromatograph column.

4.2.4 Conductive carbon support concentration

Figure 4-10 shows the faradaic efficiencies (FE) of CO, H₂, CH₄, and C₂₊ products obtained after 2-hour electrolysis experiments at -1.1 V vs. RHE with FePc-modified electrodes under CO₂ at different carbon support concentrations. The standard carbon black concentration was one milligram per milliliter of ink. This concentration results in a thick catalyst layer of a few microns after drop-casting, which adheres well to the surface of the glassy carbon plate. Other conditions were kept similar to experiments with FePc described in Chapter 3 and the annex, with a catalyst loading of 80 nmol/cm², a KHCO₃ 0.1 M electrolyte, and a flow rate of 1 mL/min.

The increase in carbon black concentration correlated with the rise in CO and CH₄ concentration. However, the evolutions of H₂ and C₂₊ exhibited a reverse trend. Similar to the flow rate series, the high yield of C₂₊ products coincided with the high yield of H₂. The correlation corroborates the hypothesis that C₂₊ species are more favored in an environment with an abundance of hydrogen. However, in this case, CH₄ was not favorable when there was high availability of hydrogen.

We propose a hypothesis concerning the observed behavior of FePc with different amounts of carbon support. The low carbon black concentration means higher proximity of the catalytic centers, potentially forming clusters. The FePc in close proximity leads to a higher local concentration of CO generated, producing more C₂₊ products. The higher carbon black concentration renders the FePc catalyst more dispersed, leading to a lower local CO concentration to carry out the CO insertion step on the carbene species. Therefore, the observed C₂₊ products were low, and the obtained methane was high.

Although the selectivity of products with C – C bonds is favored at low concentrations of carbon black, the catalyst layer is not stable as it is peeled off after one electrolysis experiment. Consequently, a sufficient amount of conductive carbon support is necessary to preserve the mechanical stability of the catalyst layer.

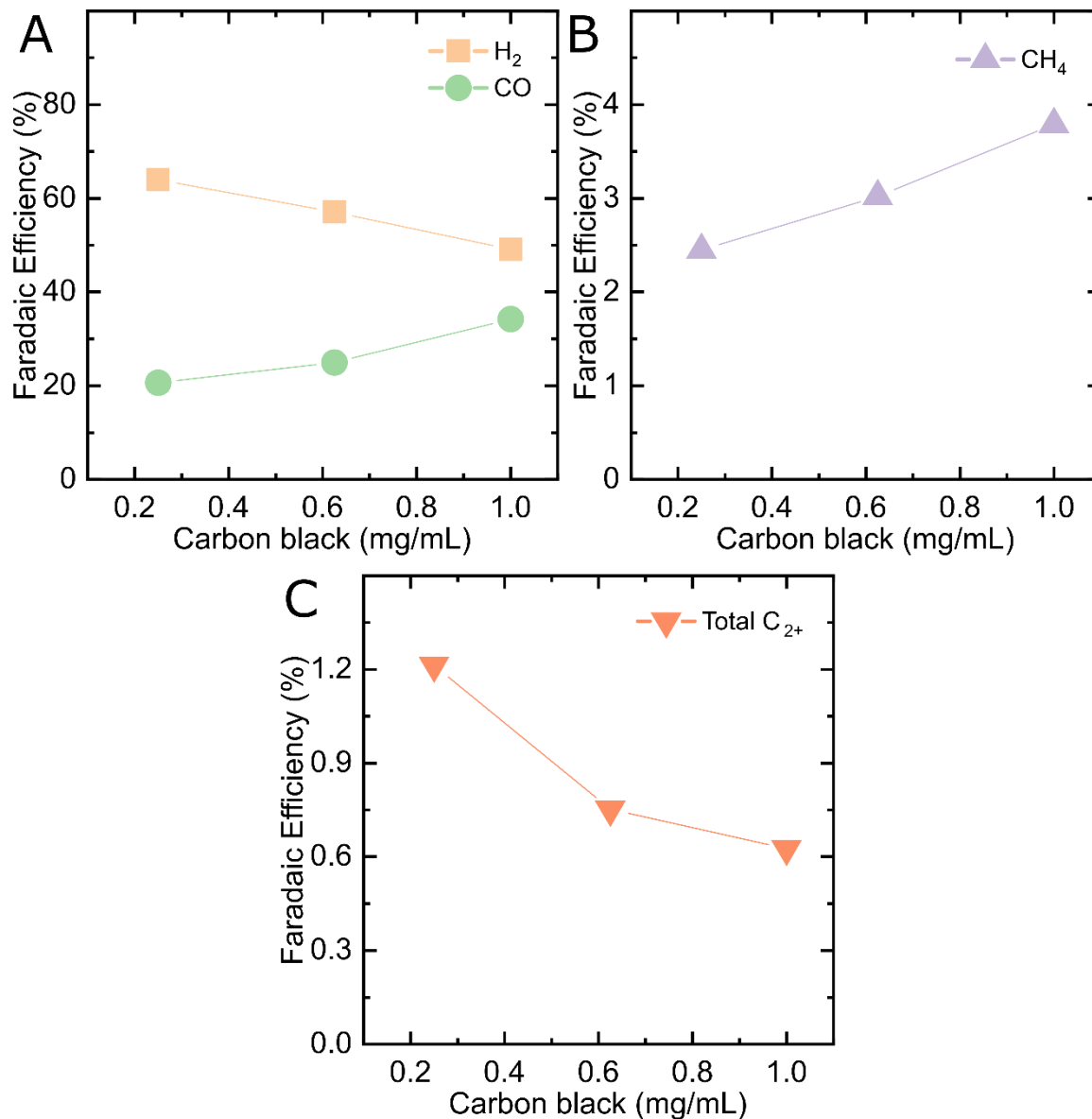


Figure 4-10. Product distribution observed with FePc-modified electrodes as faradaic efficiencies at -1.1 V vs. RHE as a function of carbon black concentration. The amount of ethylene (C_2H_4) is underestimated due to the high background generated by CO_2 in the chromatograph column.

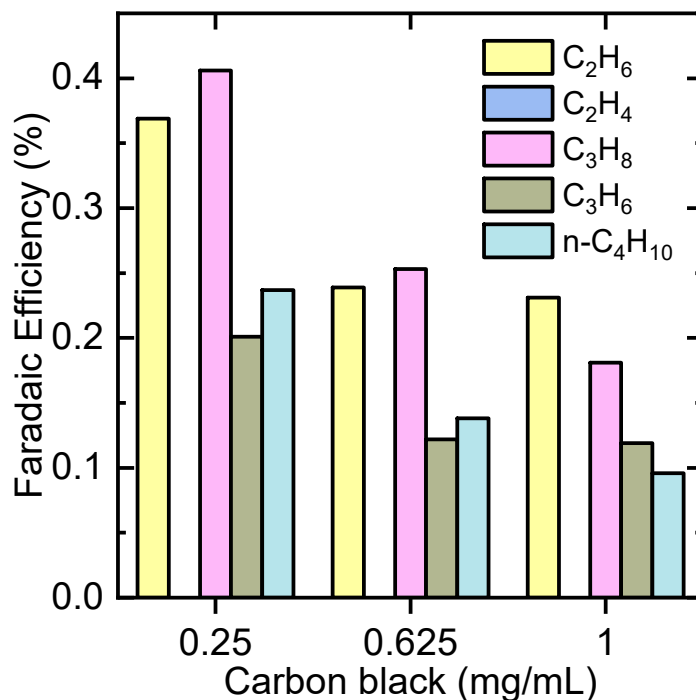


Figure 4-11. C₂₊ product distribution observed with FePc-modified electrodes as faradaic efficiencies at -1.1 V vs. RHE as a function of carbon black concentration. Although no ethylene (C₂H₄) was plotted, its peak was likely underestimated due to the high background generated by CO₂ in the chromatograph column.

4.3 Metal phthalocyanines

In this section, we investigated the influence of metal centers on the CO₂-reducing activity of metal phthalocyanines, focusing on the hydrocarbon products with C – C bonds. Then we studied the impact of various substituent groups on the catalytic activity of FePc.

4.3.1 Metal center effects

We examined six first-row transition metal phthalocyanines for their CO₂-reducing activity: Mn, Fe, Co, Ni, Cu, and Zn. The experimental conditions were similar to experiments with FePc described in Chapter 3 and the annex, with a catalyst loading of 80 nmol/cm², a KHCO₃ 0.1 M electrolyte, and a flow rate of 1 mL/min. Figure 4-12 shows the electrolysis curves of the studied metal phthalocyanines at applied potentials ranging from -0.7 to -1.1 V vs. RHE. CoPc exhibited the highest stable current density in all potentials. The high current density came with a considerable noise level, likely due to the large amount of gas bubbles generated. At -0.7 V vs. RHE, all metal phthalocyanines exhibited current densities one order of magnitude lower than CoPc (CuPc was not examined at this potential). At the moderate potential of -0.9 V vs. RHE, CoPc was followed by CuPc, NiPc, and FePc, while MnPc and ZnPc were inactive. The electrolysis curve of NiPc displayed a sharp decline in current density. The same trend can be observed at -1.1 V vs. RHE. However, MnPc and NiPc became unstable at this

negative potential as their electrolysis curves sloped down over time.

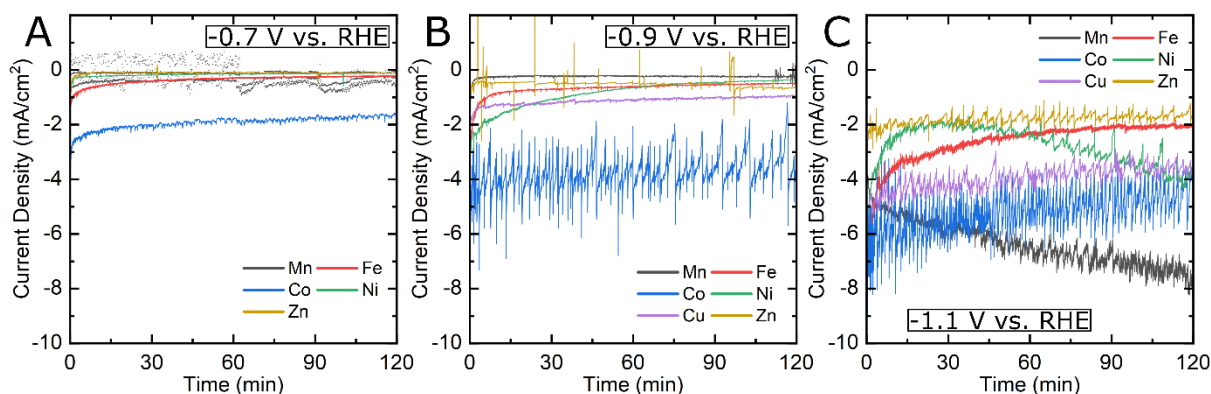


Figure 4-12. Electrolysis curves of different metal phthalocyanines modified electrodes at -0.7 V vs. RHE (A), -0.9 V vs. RHE (B), and -1.1 V vs. RHE (C) under CO_2 in 0.1 M KHCO_3 for two hours.

Figure 4-13 shows the CO and H_2 faradaic efficiency of the investigated M-Pc after 2-hour electrolysis. In agreement with previous reports in the literature, Fe, Co, and NiPc show the highest selectivity for CO , greater than 70%, at potentials of -0.7 and -0.9 V vs. RHE. At these moderate potentials, Mn, Cu, and ZnPc produce more H_2 than CO . The CO_2 -reducing activity on these metal Pc is low, resulting in the current density being close to the background current value and the total faradaic efficiencies not reaching close to a hundred percent. Although the liquid products were not characterized in all experiments, based on the literature, we would expect at most a few percent of methanol generated from electrolysis on CoPc. At a more negative potential of -1.1 V vs. RHE, CoPc was the only catalyst maintaining CO as the primary product. Other catalysts mainly produced hydrogen, except for ZnPc, generating CO and H_2 at roughly equal selectivity.

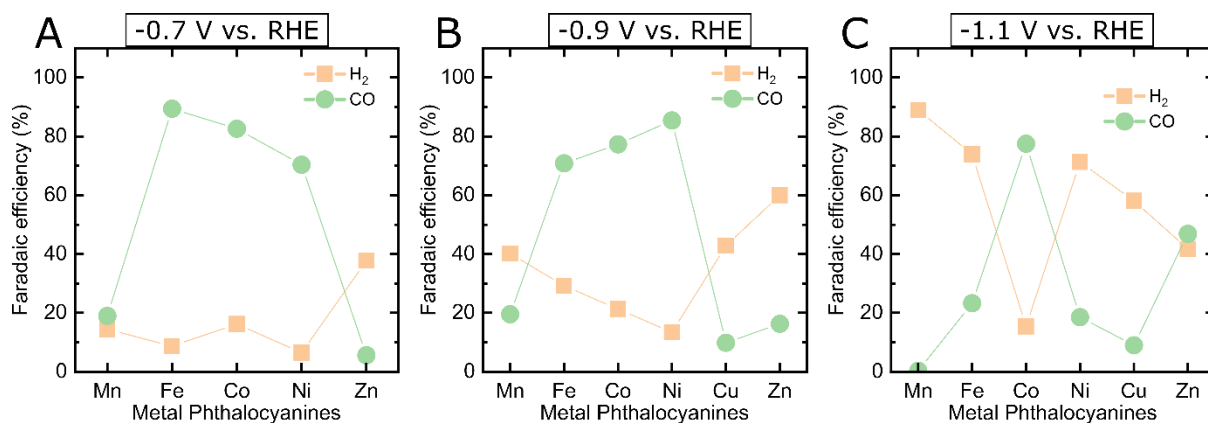


Figure 4-13. CO and H_2 distribution observed with metal phthalocyanines electrodes as faradaic efficiencies after 2-hour electrolysis at -0.7 V vs. RHE (A), -0.9 V vs. RHE (B), and -1.1 V vs. RHE (C)

Figure 4-14 shows the methane distribution of the studied metal phthalocyanines. No hydrocarbons were detected at -0.7 V vs. RHE. At -0.9 V vs. RHE, only FePc and CuPc

produced methane. At a more negative potential of -1.1 V vs. RHE, Mn, Fe, and NiPc are the catalysts that yield methane, with the highest methane faradaic efficiency of around 4% coming from FePc. Interestingly, methane was only presented when CuPc was poised at -0.9 V instead of -1.1 V vs. RHE.

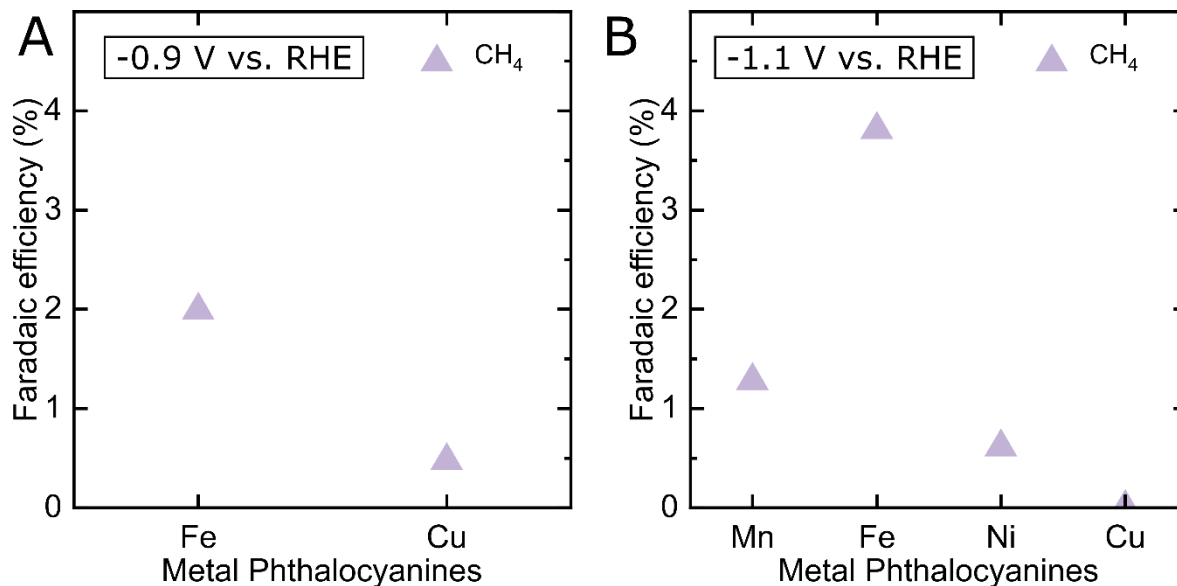


Figure 4-14. CH₄ distribution observed with metal phthalocyanines electrodes as faradaic efficiencies after 2-hour electrolysis at -0.9 V vs. RHE (**A**), and -1.1 V vs. RHE (**B**)

Figure 4-15 shows the faradaic efficiencies of all C₂₊ products coming from the examined metal phthalocyanines. At -0.9 V vs. RHE, only FePc produced the hydrocarbon products with C – C bonds, with their distributions presented in Chapter 3. When the potential is more negative at -1.1 V vs. RHE, Mn, Fe, and CuPc produce hydrocarbon species. C₂H₄ accounted for the majority of hydrocarbons coming from CuPc. However, as discussed in Chapter 1, the molecular nature of CuPc may not be preserved during catalysis; thus, the actual active sites where the C – C bonds formed was likely metal site. FePc and MnPc generated a range of C₂₊ products, with the total accounting for 0.76% and 0.21%, respectively.

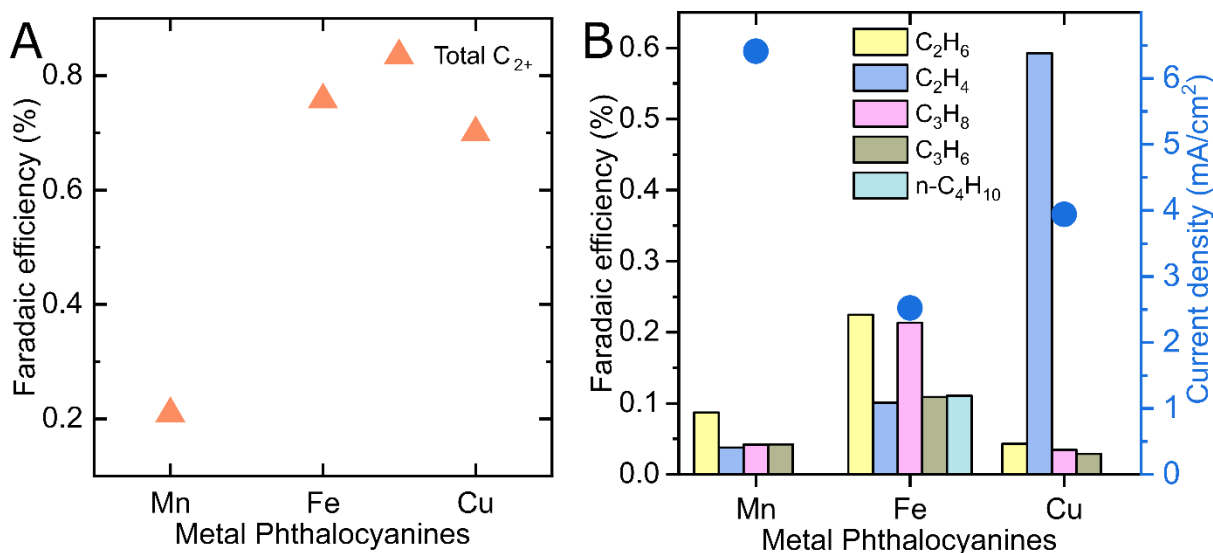


Figure 4-15. C₂₊ product distribution as total C₂₊ products (A) and individual C₂₊ products (B) observed with metal phthalocyanine electrodes as faradaic efficiencies after 2-hour electrolysis at -1.1 V vs. RHE. The total current density at 60 minutes is plotted as a blue dot for each metal species. The amount of ethylene (C₂H₄) is underestimated due to the high background generated by CO₂ in the chromatograph column.

The observation that FePc was the most active metal phthalocyanine in reducing CO₂ to hydrocarbon products emphasizes the distinct properties of the iron center. Amongst metal catalysts, copper is the unique species that can form products with C – C bonds in high quantities. This specific ability comes from copper being the only metal to possess mild binding energy with both CO* and H* intermediates. Therefore, on a copper surface, a CO* species can remain for a sufficient amount of time to form a C – C bond (through a carbene species) without separating quickly to form CO like silver or binding too strongly, leading to catalyst poisoning like platinum. Although the binding energy of iron metal with CO* and H* do not fall into this sweet spot, this property can change when the iron is complexed as an ion by organic ligands. Using DFT calculations, Rossmeisl and co-workers showed that a porphyrin-like structure of an Fe-N-C species possesses binding energies for CO* and H* similar to metallic Cu.¹³ Similarly, Mn-N-C and Cu-N-C are the only other common transition metals to fall into this category. This calculation result completely matches our experimental results, as MnPc, FePc, and CuPc were the only species in the series that could form products with C – C bonds from CO₂ reduction. These findings emphasize that the surrounding environment of metal can alter its properties and demonstrate the prospect of a copper-free catalyst for forming products with C – C bonds from CO₂ reduction.

4.3.2 Ligand effects on FePc

We studied the substituents' effects on the CO₂-reducing activity of FePc using four species shown in Figure 4-16. The Cl and COOH groups are electron-withdrawing, which helps to lower the overpotential needed to reduce CO₂. However, these groups also decrease the electron density around the metal center, potentially hindering the

electron transfer to CO_2 . On the other hand, the NH_2 donating group has the opposite effect of increasing the electron density around the metal center while also increasing the overpotential of the reaction. The standard experimental conditions were used, with catalyst loading of 80 nmol/cm^2 , a 0.1 KHCO_3 electrolyte, and a flow rate of 1 mL/min .

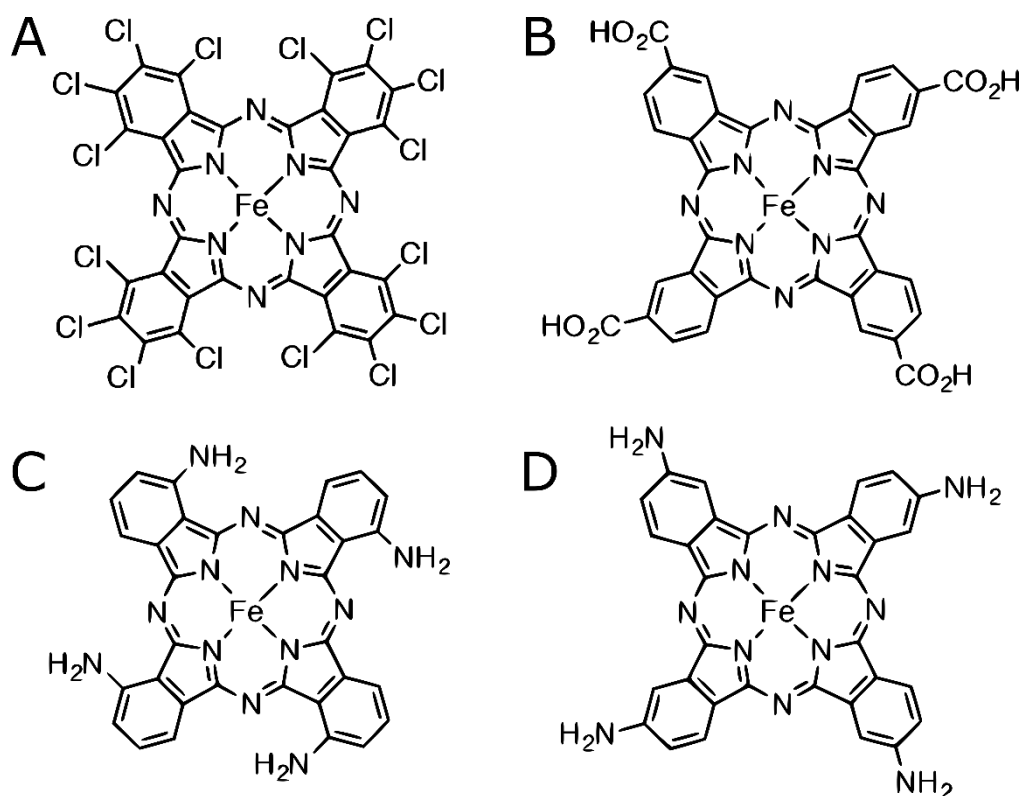


Figure 4-16. Chemical structures of iron phthalocyanine with different substituents: Cl_{16} (**A**), $(m\text{-COOH})_4$ (**B**), $(o\text{-NH}_2)_4$ (**C**), and $(m\text{-NH}_2)_4$ (**D**)

Figure 4-17 shows the electrolysis curves of FePc-substituted electrodes at -0.9 and -1.1 V vs. RHE (FePc- Cl_{16} was tested at -0.8 V vs. RHE instead). At -0.9 V vs. RHE , the highest current densities are observed for the amino substituted at the ortho position, followed by the meta-amino and the carboxylic acid species, while the unmodified FePc and the chloro-substituted FePc were the least active. The trend was analogous to that at -1.1 V vs. RHE .

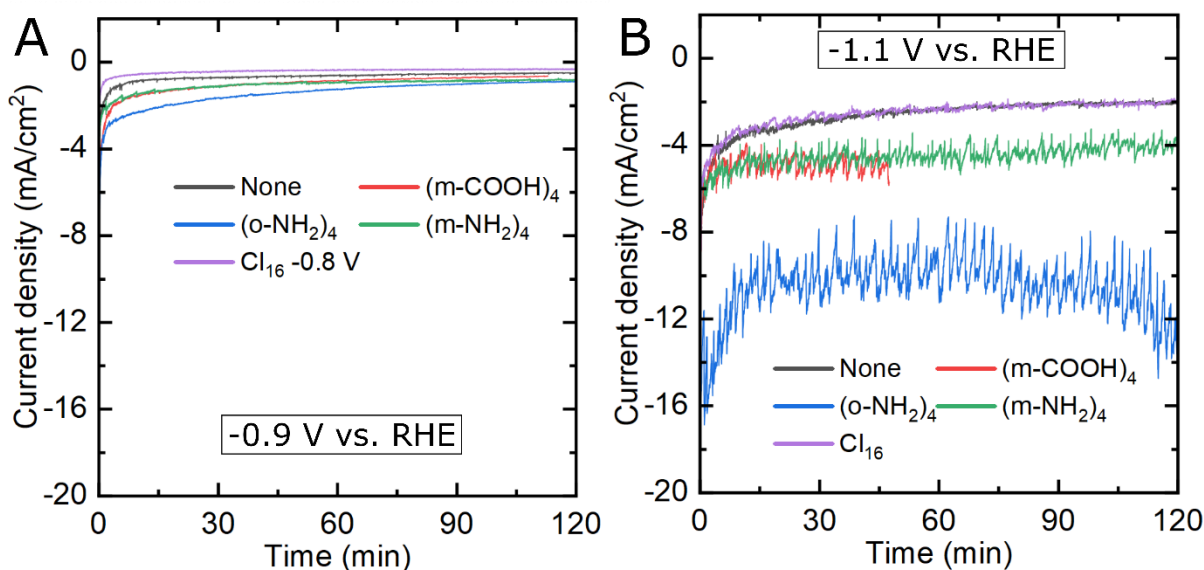


Figure 4-17. Electrolysis curves of FePc-substituted modified electrodes at -0.9 V vs. RHE (**A**), and -1.1 V vs. RHE (**B**) under CO₂ in 0.1 M KHCO₃ for two hours. The potential applied to the FePc-Cl₁₆ catalyst in panel A was -0.8 V vs. RHE. The data file of the FePc-COOH species corrupted after 50 minutes.

Figure 4-18 shows the faradaic efficiencies of H₂, CO, CH₄, and C₂₊ products from the studied substituted FePc. The non-substituted FePc exhibited the highest CO selectivity at both applied potentials, accounting for 70% and 20% at -0.9 and -1.1 V vs. RHE, respectively. Interestingly, all substituted FePc were not highly active at reducing CO₂ to CO. Catalysts with Cl and COOH functional groups produced CO with faradaic efficiency higher than 10%, while the amino-substituted FePc hardly yielded any CO. The poor performance may arise from the drop-casting process and the solubility of these species in DMF. Out of the analyzed catalysts, FePc is the most soluble, followed by FePc-Cl₁₆, and then the rest of the catalyst. In fact, FePc-COOH and FePc-NH₂(m) were hardly soluble in DMF. Consequently, the insoluble species were not well-dispersed on the electrode surface and stayed in the form of large particles, leading to the poor performance observed. This result reflects the complication in studying the influence of ligand functional groups on the CO₂-reducing activity of metal complexes, as secondary phenomena can interfere with the intended effect of the study.

Although the substituted FePc did not produce a considerable amount of CO, CH₄, and C₂₊ products were present in the products of these catalysts at both applied potentials. The complete distribution of individual C₂₊ products is shown in Figure 4-19. At -1.1 V vs. RHE, the unmodified FePc produced the most significant amount of methane, followed by the chloro, the m-amino, and the carboxylic acid substituted FePc. This order was similar concerning the total selectivity of the C₂₊ products. Interestingly, FePc-(o-NH₂)₄ produced a negligible amount of both methane and the C₂₊ hydrocarbons. However, at the less negative potential of -0.9 V vs. RHE, the trend

Chapter 4

seemed to be reversed as the non-substituted FePc has the least amount of CH₄ and C₂₊ while the amino-substituted had the most. This result indicates that, despite the low amount of CO produced, when hydrogen is abundant, C₂₊ products are favored.

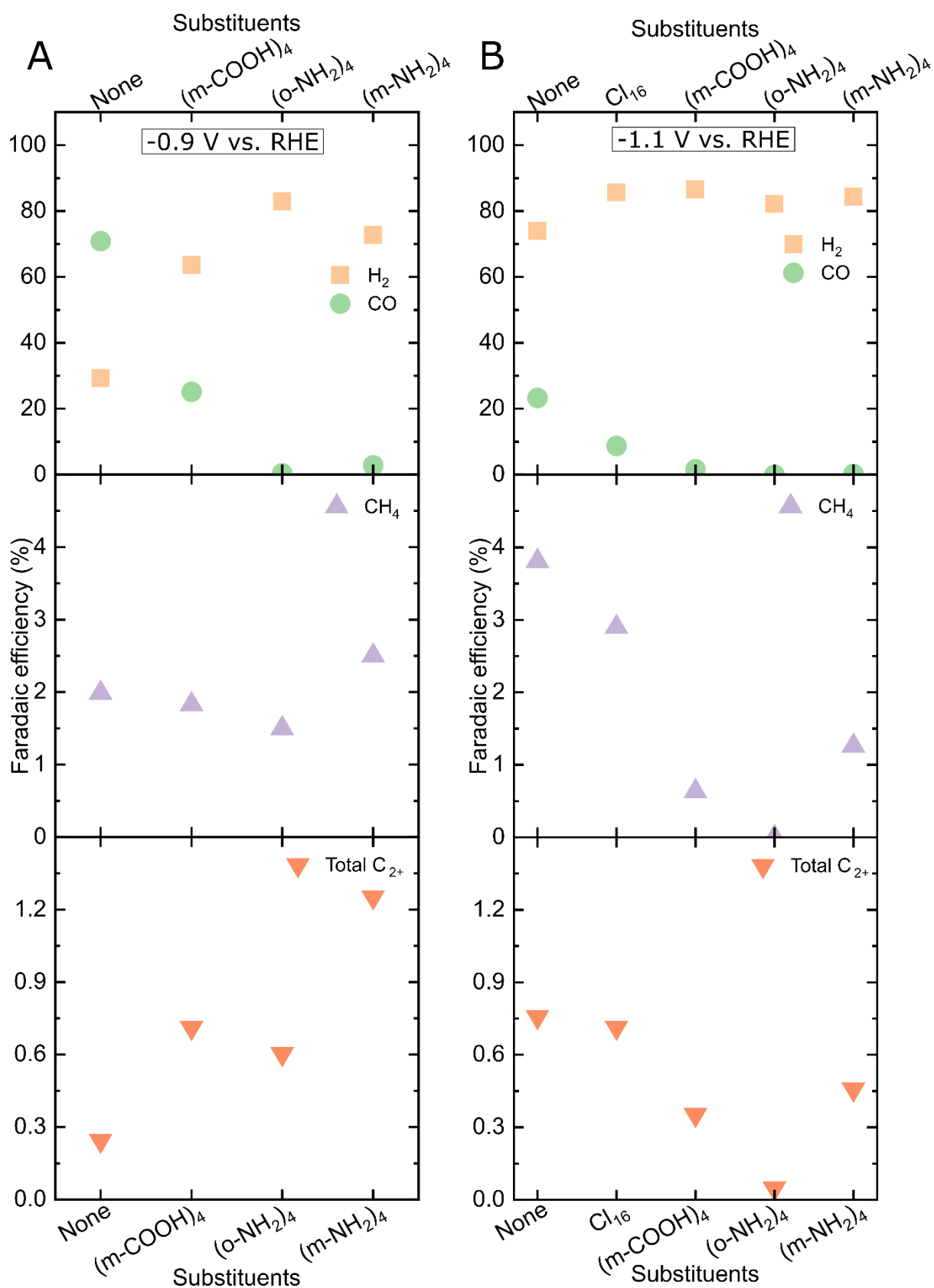


Figure 4-18. Product distribution observed with FePc-modified electrodes as faradaic efficiencies after 2-hour electrolysis at -0.9 V vs. RHE (**A**) and -1.1 V vs. RHE (**B**) as a function of substituents of FePc. The amount of ethylene (C₂H₄) is underestimated due to the high background generated by CO₂ in the chromatograph column.

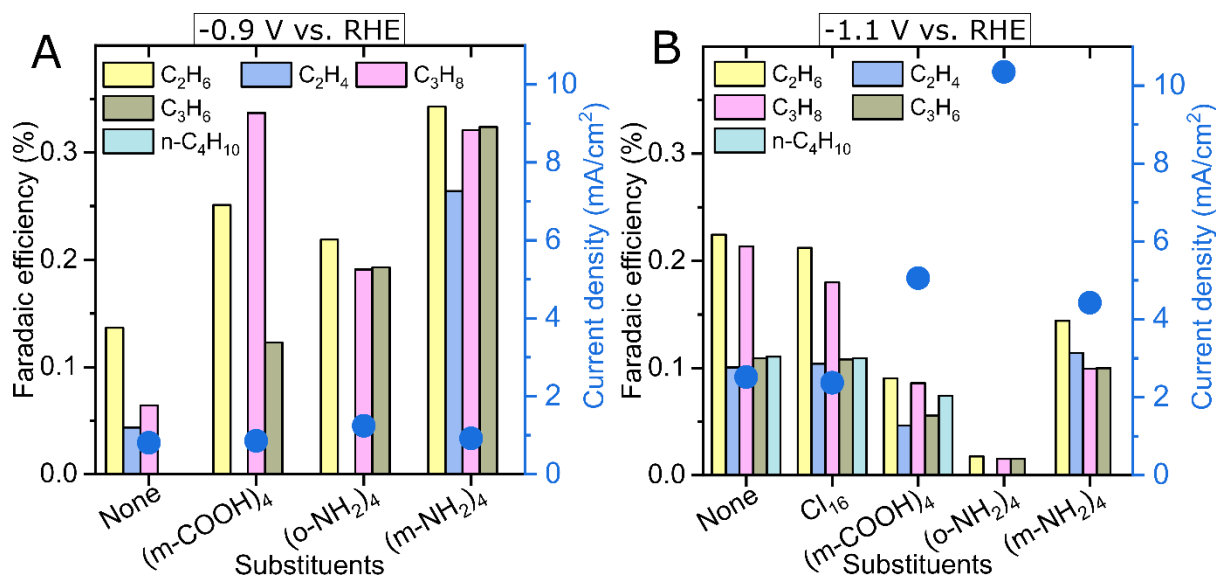


Figure 4-19. C₂₊ product distribution observed with FePc-modified electrodes as faradaic efficiencies after 2-hour electrolysis at -0.9 (A) and -1.1 V vs. RHE (B) as a function of substituents of FePc. The total current density at 60 minutes is plotted as a blue dot for each substituent. The amount of ethylene (C₂H₄) is underestimated due to the high background generated by CO₂ in the chromatograph column.

4.4 Iron porphyrins and derivatives

As discussed in Chapter 1, metal phthalocyanines and porphyrins are the two molecular macrocycles with the highest CO₂-to-CO activity. Since we found that iron phthalocyanine produces methane and hydrocarbon products with C – C bonds, iron porphyrin is a promising candidate to study whether it can form C – C bonds from CO₂ reduction. We examined four iron porphyrin species shown in Figure 4-21: a commonly used iron tetraphenyl porphyrin (FeTPP), then two FeTPP substituted with electron-withdrawing groups (fluoro – FeTPP-F₂₀), and electron-donating group (methyl – FeTTP). Finally, we studied a bimetallic iron porphyrin species where the porphyrin rings are fused on the same plane (Fe₂FP). The last two porphyrins were provided by the group of Prof. Gary F. Moore from Arizona State University in the United States of America. The idea behind the two adjacent iron sites is that their proximity may facilitate the formation of products with C – C bonds in a mechanism similar to the coupling of the carbene species on metallic copper that yield ethylene.

The experimental conditions were similar to those described above, with a catalyst loading of around 80 nmol/cm², a 0.1 KHCO₃ electrolyte, and a 1 mL/min flow rate. Since the fused porphyrin has two iron per molecule, the iron content doubled that of the other catalysts.

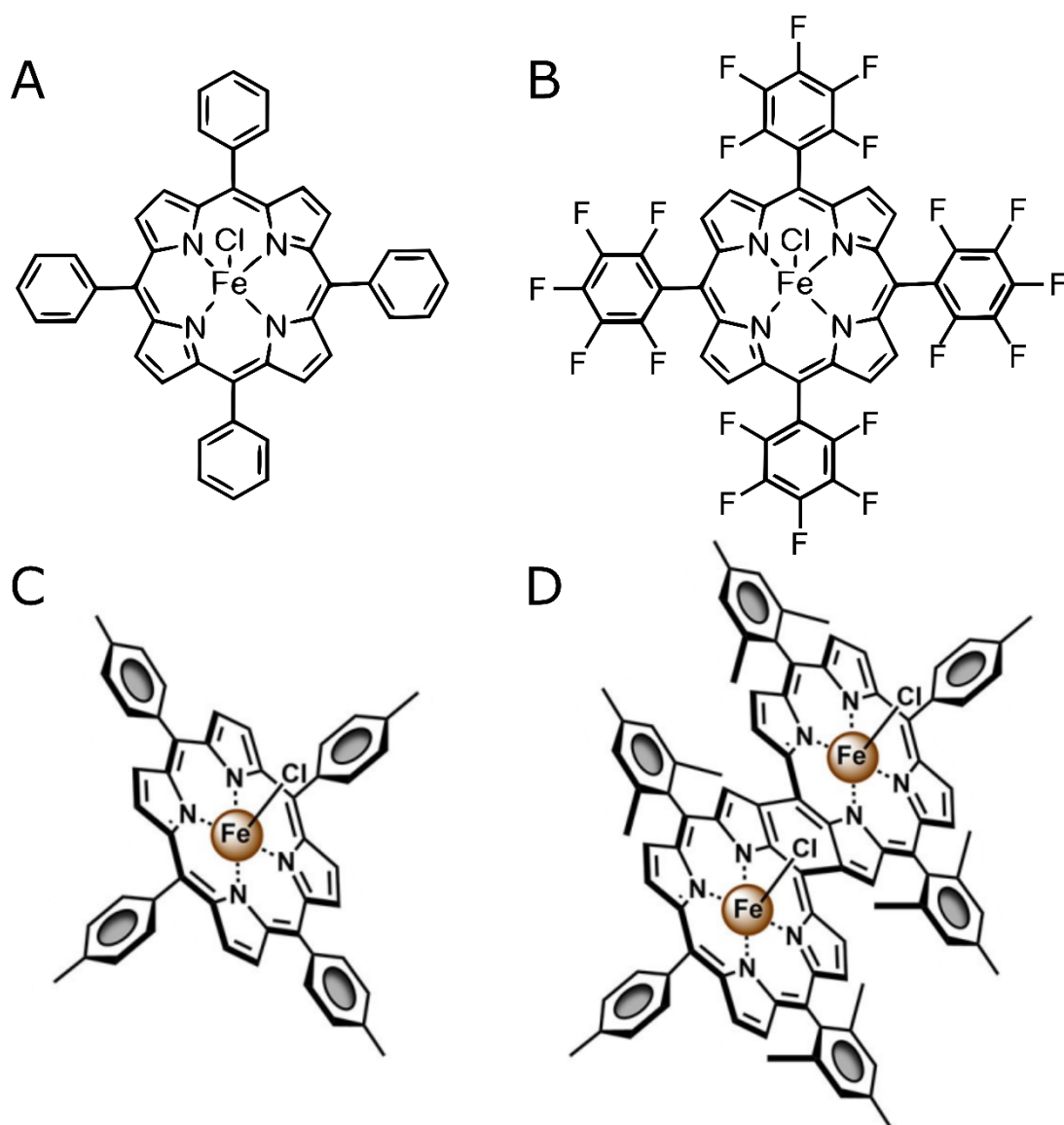


Figure 4-20. Chemical structures of iron tetraphenyl porphyrin (FeTPP) **(A)** and its derivatives: FeTPP-F₂₀ **(B)**, FeTTP **(C)**, and Fe₂FP **(D)**. Panel C and D were reproduced from an article by Moore and co-workers.¹⁴

Figure 4-21 shows the electrolysis curves of electrodes modified with FeTPP and its derivatives at -0.8 and -1.1 V vs. RHE. At -0.8 V vs. RHE, Fe₂FP exhibited the highest current density, followed by FeTPP and FeTTP, and FeTPP-F₂₀ was the least active species. Interestingly, at -1.1 V vs. RHE, Fe₂FP became the species with the lowest current densities, while FeTPP became the most active species. FeTTP and FeTPP-F₂₀ displayed similar electrolysis curves at this potential.

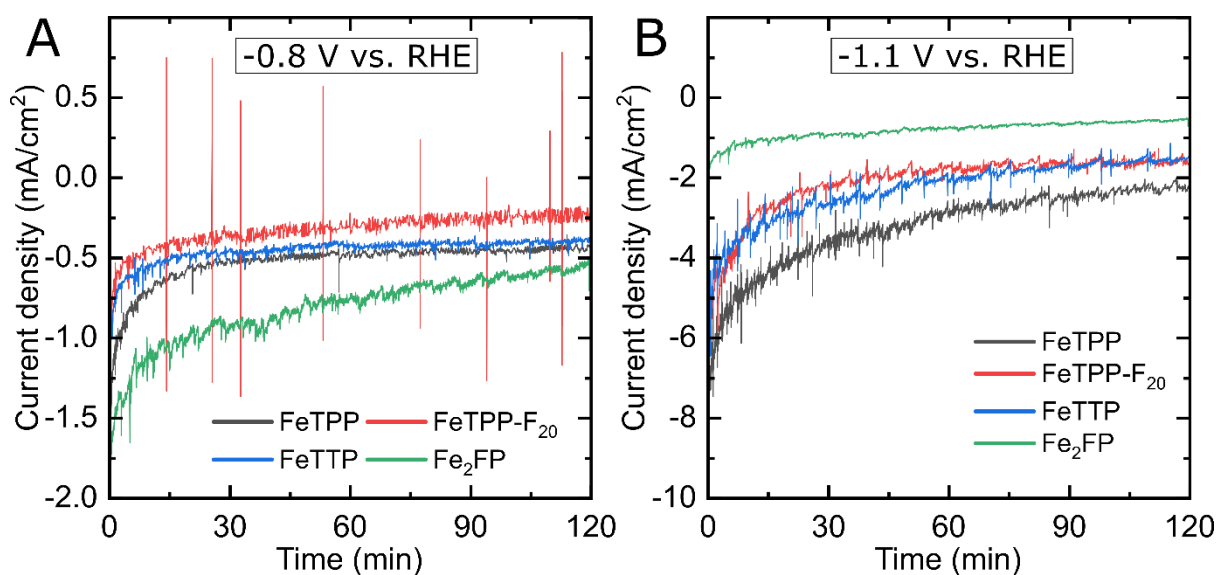


Figure 4-21. Electrolysis curves of electrodes modified with various iron-based macrocycles at -0.8 V vs. RHE (**A**), and -1.1 V vs. RHE (**B**) under CO_2 in 0.1 M KHCO_3 for two hours.

Figure 4-22 shows the faradaic efficiencies of CO , H_2 , CH_4 , and C_{2+} observed with the four iron porphyrin species at -0.8 V vs. RHE and -1.1 V vs. RHE. At the low overpotential of -0.8 V vs. RHE, CO and H_2 are the only products detected. Fe_2FP was the most selective catalyst toward CO , while other iron porphyrin species also showed high CO selectivity. The substituents did not clearly influence the CO_2 -reducing activity of these catalysts. At -1.1 V vs. RHE, Fe_2FP was still the most CO -selective catalyst, with CO accounting for around 60% of the products. Other catalysts all produced more H_2 than CO at this highly negative potential. However, under these conditions, all catalysts produced more reduced hydrocarbon products. Methane was present with all iron porphyrin catalysts at around 1.5%, with FeTTP having the highest selectivity of 2%. Only FeTPP-F_{20} and FeTTP yielded C_{2+} products, with FeTPP-F_{20} having the highest total C_{2+} faradaic efficiency of around 0.6%. The distribution of individual C_{2+} products is shown in Figure 4-23.

While the reason why only FeTTP and FeTPP-F_{20} produced C_{2+} is unclear, the fact that not all iron macrocyclic compounds produced molecules with $\text{C}-\text{C}$ bonds indicated that the ligand plays a crucial role in the CO_2 -reducing activity of these catalysts. Moreover, the complexes with adjacent sites did not yield C_{2+} . This result indicates that the proximity of two potential active sites is insufficient (at least in this geometric configuration) to promote the formation of $\text{C}-\text{C}$ bonds. However, the mechanistic route proposed in Chapter 3 suggested that only one metal active site is involved in forming multiple $\text{C}-\text{C}$ bonds by CO insertion into an iron carbene species. The absence of C_{2+} products from the Fe_2FP compound supports this single-site hypothesis.

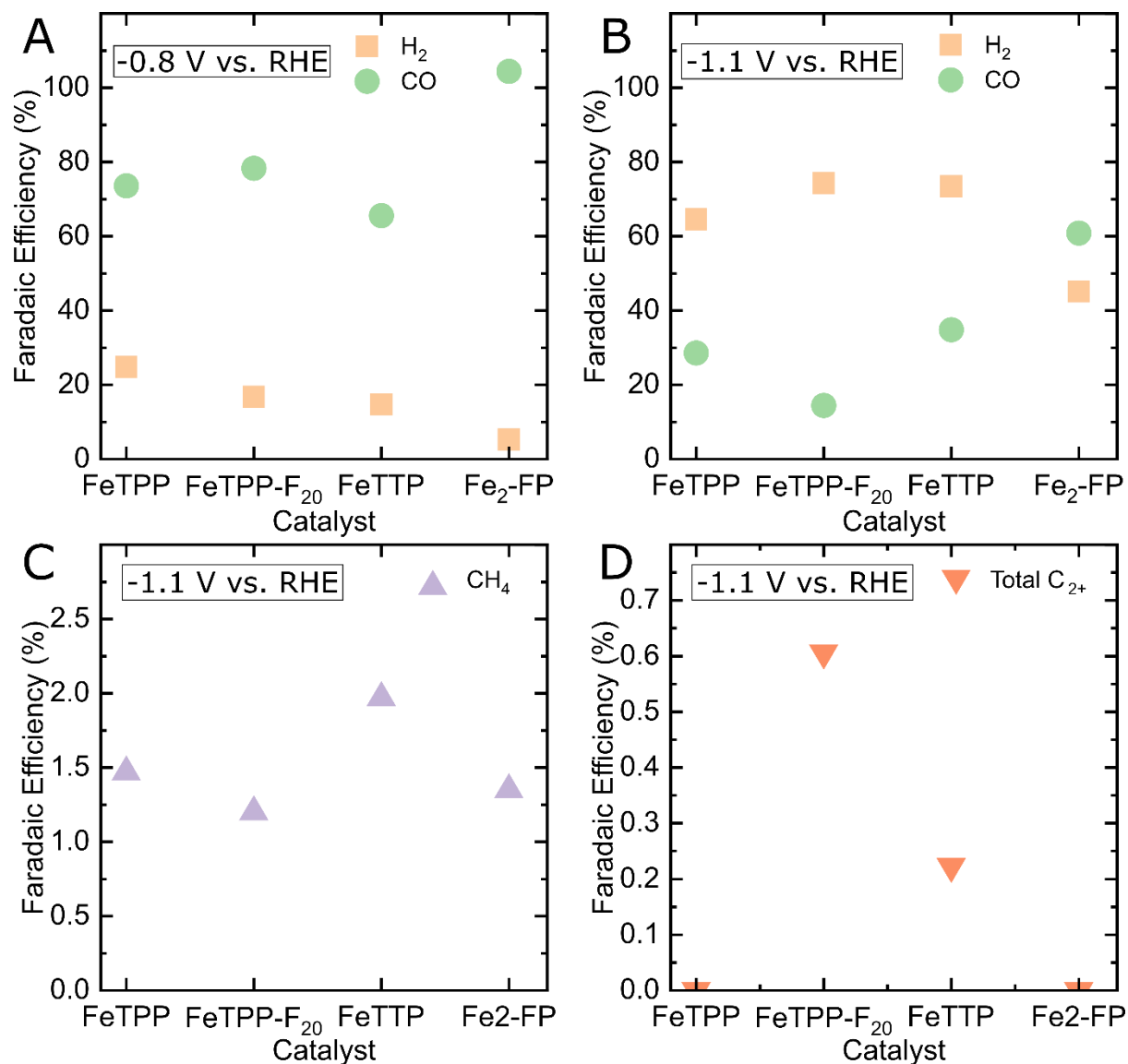


Figure 4-22. Product distribution observed with electrodes modified with various iron-based macrocycles as faradaic efficiencies after 2-hour electrolysis at -0.8 V vs. RHE (**A**) and -1.1 V vs. RHE (**B-D**). The amount of ethylene (C₂H₄) is underestimated due to the high background generated by CO₂ in the chromatograph column.

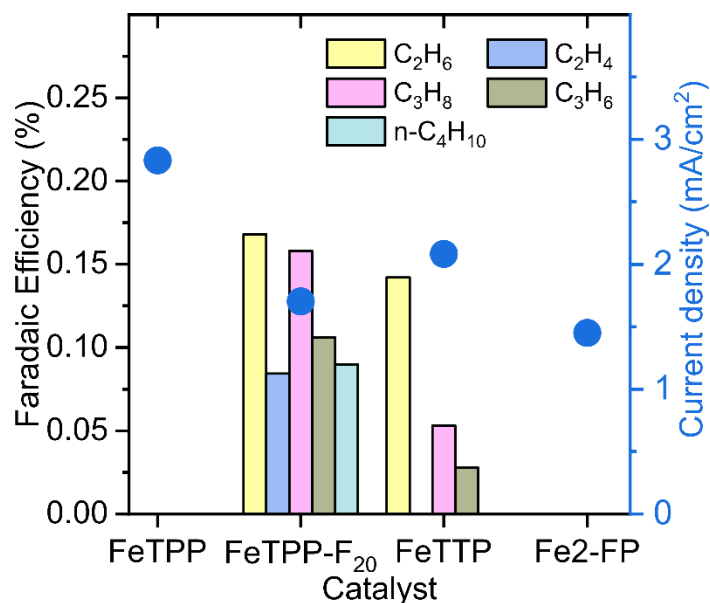


Figure 4-23. C₂₊ product distribution observed with electrodes modified with various iron-based macrocycles as faradaic efficiencies after 2-hour electrolysis at -1.1 V vs. RHE as a function of substituents of FePc. The total current density at 60 minutes is plotted as a blue dot for each catalyst. The amount of ethylene (C₂H₄) is underestimated due to the high background generated by CO₂ in the chromatograph column.

4.5 Conclusion

In this chapter, we first reported on the influences of the electrolyte flow rate and the concentrations of catalyst, electrolyte, and carbon support on the CO₂-reducing activity of FePc. The flow rate influenced the amount of CO₂ reaching the electrode, altering the product distribution of the catalysis. The high catalyst loading leads to the depletion of CO₂ near the electrode, hindering CO₂ reduction while benefiting hydrogen evolution. Higher catalyst loading did not significantly increase the C₂₊ production, confirming catalyst degradation was not the source of the observed hydrocarbons. The high electrolyte concentration provides high buffer capacity, keeping the local pH low near the electrode and thus facilitating hydrogen evolution. The highly reduced products were detected at sufficiently high concentrations, suggesting that bicarbonate may be a reactant in appropriate conditions. Finally, the amounts of carbon black support affected the proximity of the catalyst active site, favoring C₂₊ products with less carbon while promoting CH₄ with higher amounts of carbon.

In the second part, we investigated the behavior of different metal macrocycles modified with several functional groups for their activities in reducing CO₂ to hydrocarbon products. Six metal phthalocyanines were tested, and except for CuPc producing C₂H₄, only FePc and MnPc yielded C₂₊ products. The favored binding energy with CO* and H* intermediates of the Fe-N-C and Mn-N-C species could facilitate the formation of C – C bonds, emphasizing the role of the metal center. No clear trend emerged regarding the impact of electron-donating and electron-withdrawing groups

Chapter 4

on the performance of FePc, although some substituents clearly showed better performances toward C_{2+} formation. Analogous iron porphyrin counterparts only produced C_{2+} products when substituent groups were presented. Finally, a bi-metallic center fused iron porphyrin did not yield C_{2+} products, supporting the single-site mechanism to form C – C bond proposed in Chapter 3 rather than a dimerization similar to what happens in metallic copper.

4.6 Bibliography

- (1) Zhang, Z.; Xiao, J.; Chen, X.-J.; Yu, S.; Yu, L.; Si, R.; Wang, Y.; Wang, S.; Meng, X.; Wang, Y.; Tian, Z.-Q.; Deng, D. Reaction Mechanisms of Well-Defined Metal–N₄ Sites in Electrocatalytic CO₂ Reduction. *Angewandte Chemie International Edition* **2018**, 57 (50), 16339–16342. <https://doi.org/10.1002/anie.201808593>.
- (2) Corbin, N.; Zeng, J.; Williams, K.; Manthiram, K. Heterogeneous Molecular Catalysts for Electrocatalytic CO₂ Reduction. *Nano Res.* **2019**, 12 (9), 2093–2125. <https://doi.org/10.1007/s12274-019-2403-y>.
- (3) Magdesieva, T. V.; Yamamoto, T.; Tryk, D. A.; Fujishima, A. Electrochemical Reduction of CO₂ with Transition Metal Phthalocyanine and Porphyrin Complexes Supported on Activated Carbon Fibers. *J. Electrochem. Soc.* **2002**, 149 (6), D89. <https://doi.org/10.1149/1.1475690>.
- (4) Sonoyama, N.; Kirii, M.; Sakata, T. Electrochemical Reduction of CO₂ at Metal-Porphyrin Supported Gas Diffusion Electrodes under High Pressure CO₂. *Electrochemistry Communications* **1999**, 1 (6), 213–216. [https://doi.org/10.1016/S1388-2481\(99\)00041-7](https://doi.org/10.1016/S1388-2481(99)00041-7).
- (5) Abe, T.; Imaaya, H.; Yoshida, T.; Tokita, S.; Schlettwein, D.; Wöhrle, D.; Kaneko, M. Electrochemical CO₂ Reduction Catalysed by Cobalt Octacyanophthalocyanine and Its Mechanism. *J. Porphyrins Phthalocyanines* **1997**, 01 (04), 315–321. [https://doi.org/10.1002/\(SICI\)1099-1409\(199710\)1:4<315::AID-JPP35>3.0.CO;2-V](https://doi.org/10.1002/(SICI)1099-1409(199710)1:4<315::AID-JPP35>3.0.CO;2-V).
- (6) Zhu, M.; Yang, D.-T.; Ye, R.; Zeng, J.; Corbin, N.; Manthiram, K. Inductive and Electrostatic Effects on Cobalt Porphyrins for Heterogeneous Electrocatalytic Carbon Dioxide Reduction. *Catal. Sci. Technol.* **2019**, 9 (4), 974–980. <https://doi.org/10.1039/C9CY00102F>.
- (7) Gurudayal; Perone, D.; Malani, S.; Lum, Y.; Haussener, S.; Ager, J. W. Sequential Cascade Electrocatalytic Conversion of Carbon Dioxide to C–C Coupled Products. *ACS Appl. Energy Mater.* **2019**, 2 (6), 4551–4559. <https://doi.org/10.1021/acsaem.9b00791>.
- (8) Zhu, M.; Ye, R.; Jin, K.; Lazouski, N.; Manthiram, K. Elucidating the Reactivity and Mechanism of CO₂ Electroreduction at Highly Dispersed Cobalt Phthalocyanine. *ACS Energy Letters* **2018**, 3 (6), 1381–1386. <https://doi.org/10.1021/acseenergylett.8b00519>.
- (9) Varela, A. S.; Kroschel, M.; Leonard, N. D.; Ju, W.; Steinberg, J.; Bagger, A.; Rossmeisl, J.; Strasser, P. PH Effects on the Selectivity of the Electrocatalytic CO₂ Reduction on Graphene-Embedded Fe–N–C Motifs: Bridging Concepts between Molecular Homogeneous and Solid-State Heterogeneous Catalysis. *ACS Energy Letters* **2018**. <https://doi.org/10.1021/acseenergylett.8b00273>.
- (10) Kas, R.; Kortlever, R.; Yilmaz, H.; Koper, M. T. M.; Mul, G. Manipulating the Hydrocarbon Selectivity of Copper Nanoparticles in CO₂ Electroreduction by Process Conditions. *ChemElectroChem* **2015**, 2 (3), 354–358. <https://doi.org/10.1002/celec.201402373>.
- (11) Hu, X.-M.; Rønne, M. H.; Pedersen, S. U.; Skrydstrup, T.; Daasbjerg, K. Enhanced Catalytic Activity of Cobalt Porphyrin in CO₂ Electroreduction upon Immobilization on Carbon Materials. *Angewandte Chemie International Edition* **2017**, 56 (23), 6468–6472. <https://doi.org/10.1002/anie.201701104>.

Chapter 4

- (12) Zhang, X.; Wu, Z.; Zhang, X.; Li, L.; Li, Y.; Xu, H.; Li, X.; Yu, X.; Zhang, Z.; Liang, Y.; Wang, H. Highly Selective and Active CO₂ Reduction Electrocatalysts Based on Cobalt Phthalocyanine/Carbon Nanotube Hybrid Structures. *Nature Communications* **2017**, *8* (1), 14675. <https://doi.org/10.1038/ncomms14675>.
- (13) Bagger, A.; Ju, W.; Varela, A. S.; Strasser, P.; Rossmeisl, J. Single Site Porphyrine-like Structures Advantages over Metals for Selective Electrochemical CO₂ Reduction. *Catalysis Today* **2017**, *288*, 74–78. <https://doi.org/10.1016/j.cattod.2017.02.028>.
- (14) Reyes Cruz, E. A.; Nishiori, D.; Wadsworth, B. L.; Khusnutdinova, D.; Karcher, T.; Landrot, G.; Lassalle-Kaiser, B.; Moore, G. F. Six-Electron Chemistry of a Binuclear Fe(III) Fused Porphyrin. *ChemElectroChem* **2021**, celc.202100550. <https://doi.org/10.1002/celec.202100550>.

5 CHAPTER 5: CONCLUSIONS AND PERSPECTIVES

5.1 Chapter 1

In the first chapter, we looked at the importance of energy storage regarding the transition from fossil fuels to renewable energy. Inspired by natural photosynthesis, we explored why carbon dioxide reduction is a promising method to store renewable energy and produce valuable fuels and chemicals. By reviewing the literature focusing on metal phthalocyanines and porphyrins, we made a case for studying molecular catalysts to understand better the detailed mechanisms of the CO₂ reduction reaction. We then laid out the strategy of the thesis in designing and fabricating an electrochemical flow system in an attempt to generate highly reduced products from CO₂ reduction on molecular catalysts

5.2 Chapter 2

In chapter 2, we first presented a strategy for using a cascade catalysis system to reduce CO₂ to highly reduced products using a series of microfluidic devices. We reported on designing and fabricating a PDMS microfluidic flow cell prototype. We learned that despite the apparent benefit of the microfluidics conditions for electrochemical energy applications, a microfluidics device was not the appropriate choice for handling a fluid with high amounts of dissolved gas. The microscopic channel prevented the gas bubbles from being evacuated quickly, leading to unstable electrochemistry. To alleviate the problem, we 3D-printed a millifluidic electrochemical flow cell, anticipating the larger dimension of the flow channel would allow bubbles to escape faster. The 3D printing process allows for quick modifications, enabling us to adapt the cell for spectroelectrochemistry applications with X-ray absorption spectroscopy. Although having larger dimensions, laminar flow conditions were still achieved in the cell, similar to the microfluidic conditions. However, a CO₂-saturated solution still caused the turbulent flow in the cell's channels by generating bubbles. A membrane was then employed, and CO₂ electrolysis using an FePc catalyst could last at least two hours with a lower noise level than the PDMS cell. The concentration profiles of the reduced products were characterized using finite element analysis based on laminar flow and transport of diluted species physics. The calculation showed that CO concentration existed in a supersaturated concentration near the electrode surface, but the CO₂ conversion rate was relatively poor.

For perspectives, we propose an alternate design for the microfluidic cell. The cell uses a Teflon gasket instead of PDMS to form the flow channel. Although the bubble problem proves tricky to solve, reducing CO₂ in a thin channel is still an attractive idea. First, under appropriate conditions (i.e., flow rate, CO₂ pressure, and electrolyte), the total consumption of CO₂, which is challenging to achieve in a cell employing a gas

diffusion electrode, could be achieved. Under these conditions, a small amount of pure CO can be generated in place and on demand. This pure stream of CO can serve as a feedstock in the subsequent reactor of a sequential reduction system. Moreover, creating a controlled amount of CO in a safe concentration is helpful in multiple applications, as handling CO in a compressed tank is complicated and risky due to its toxicity. Finally, the complete conversion of reactant is not desirable to only CO₂. In X-ray spectroelectrochemistry for homogeneous catalysis, the total transformation of a reactant is required to obtain a signal solely from the intended species. The millifluidic 3D-printed flow cell could be fabricated with more robust materials such as PEEK or Teflon to accommodate more extreme experimental conditions. The cell could also be converted to use in a gas-diffusion setup.

5.3 Chapter 3

In chapter 3, we reported the electrocatalytic activity of iron phthalocyanine toward reducing CO₂ in our 3D-printed millifluidic electrochemical flow cell. We learned that upon reducing CO₂, in addition to CO, a small amount of linear hydrocarbons with up to three C – C bonds were detected at appropriate potentials. Control experiments and GC-MS characterization confirmed that CO₂ was the source of carbon atoms in the detected hydrocarbons. We demonstrated the integrity of the iron phthalocyanine molecular nature throughout the electrocatalytic process using *operando* X-ray absorption spectroscopy. Based on experiments involving carbon monoxide or formaldehyde and the finite element analysis of the product concentration profiles, we showed that the local concentration of CO is key to the formation of C – C bonds. We proposed a terminal carbene as an intermediate on the way to C₂₊ products.

These results indicate a novel finding that single-site transition metal macrocycles could catalyze the formation of several consecutive carbon-carbon bonds under mild electrochemical conditions. We propose a strategy to validate the hypothesis of the C – C bond formation mechanism by CO insertion into an iron carbene intermediate. The Fe=CH₂ species could be synthesized and isolated to study its single turnover reactivity, i.e., whether it would react with CO and H₂ to form a C – C bond. Spectroscopic studies of such a species would also be beneficial. However, matching those spectra with *operando* data would be challenging since the intermediate existed in low amounts during the catalytic cycle. However, the *e* of a reaction between CO and H₂ on an iron carbene species would provide concrete proof to support the proposed mechanistic pathway for forming C₂₊ products. In addition to experimental data, DFT calculation could provide valuable information regarding the thermodynamics favorability of each intermediate species, as well as the kinetic pathway of the transformation between each step. The effect of external factors such as conductive carbon support, electrolyte, and flow rate is tricky to incorporate into the DFT model. Overall, the fact that C – C bond formation could happen on single-site species opens a perspective for the design of both molecular and material-based catalysts with enhanced selectivity towards C₂₊ products.

5.4 Chapter 4

In chapter 4, we learned about the influences of external factors on the CO₂-reducing activity of FePc: the electrolyte flow rate and the concentrations of catalyst, electrolyte, and carbon support. The higher the flow rate, the higher the amount of CO₂ reaching the electrode, and the more CO₂ is reduced to CO. The higher the catalyst loading, the lower the CO produced due to CO₂ being depleted near the electrode. The amount of C₂₊ hydrocarbon increased, but not in a linear relationship with the catalyst concentration, thus proving that catalyst degradation was not the source of the observed hydrocarbons. Hydrogen evolution was favored at high electrolyte concentration, as the local pH was kept low near the electrode surface due to the high buffer capacity of the electrolyte. The highly reduced products were detected even without CO₂ at sufficiently high bicarbonate concentrations, indicating that bicarbonate may be a reactant in appropriate conditions. Finally, the increasing amounts of carbon black support correlated with the rising amount of CH₄ and the decreasing of C₂₊ products. We attributed the observation to the proximity of the catalyst's active site induced by different amounts of the carbon support. In all the series tested, the high yield of C₂₊ products correlated with high hydrogen selectivity. This observation suggests that the availability of hydrogen plays a role in forming C – C bonds. Therefore, a sequential setup where the amount of CO and H₂ could be precisely tuned may prove beneficial to produce C₂₊ products more selectively.

We then investigated the behavior of different metal macrocycles modified with several functional groups for their activities in reducing CO₂ to hydrocarbon products. Six metal phthalocyanines were tested: Mn, Fe, Ni, Co, Cu, and Zn. Except for CuPc that produced C₂H₄, C₂₊ products were detected only on FePc and MnPc. We attribute the activity of FePc and MnPc to their unique binding energy with CO* and H* intermediates. Like metallic copper, FePc and MnPc can bind with CO* and H* not too strongly or weakly, providing the ideal condition for forming C – C bonds. Chloro and amino substituent groups were grafted on FePc, but their influence on the production of C₂₊ was unclear. Analogous iron porphyrin counterparts only produced C₂₊ products when substituent groups were present, signifying the importance of the ligands in molecular catalysts. Finally, a bi-metal center fused iron porphyrin did not yield C₂₊ products, supporting the single-site mechanism forming the C – C bond proposed in Chapter 3.

5.5 General discussion of the thesis

As discussed in Chapter 1, molecular catalysts may not be the ideal candidate to reduce CO₂ on an industrial scale. Still, they provide a platform for studying detailed mechanisms of the CO₂ reduction reaction. Previously, this application of molecular catalysts was limited to only C₁ products. The discovery of C₂₊ products on a single-site molecular macrocycle, even in low amounts, helps to inspire the development of molecular catalysts to form products with C – C bonds. While the formation of the C₂₊

products could begin with CO₂, starting from a mixture of CO and H₂, or CO and HCHO with the optimum ratio, it would be much more efficient. In this case, cascade catalysis would be an appealing approach. Based on the reactivity we have shown for several metal macrocycles and iron phthalocyanine in particular, a sequential catalytic system could be constructed. The first reactor will consist of a highly active catalyst like CoPc to produce an optimum mixture of CO and H₂ to feed to the second reactor, which contains catalysts (FePc or MnPc) capable of forming hydrocarbon products. Alternatively, a tandem catalyst containing multiple active species can be designed and synthesized. One species would be responsible for generating CO and H₂, which serve as the feedstock for a neighboring species to convert into C₂₊ products.

While we identified several influencing trends of electrolysis parameters and catalysts' nature on the generation of C₂₊ products, the optimum conditions have not been combined. The best conditions of all investigated parameters should give several percent of C₂₊ products, which could be higher if a cascade system is employed. The high selectivity toward the hydrocarbon products would allow the collection of *operando* spectroscopic data with a higher signal-to-noise ratio. The high-quality spectroscopy data could then be compared with data obtained from single-turnover experiments with the metal carbene intermediate, providing robust evidence for the proposed mechanism. Even without industrial applications, the mechanistic insights gained from studying molecular species would benefit the design and optimization of more applicable candidates. Finally, a gas-diffusion setup could help to enhance the activity of the investigated catalysts.

5.6 The big picture

Developing and implementing energy storage systems are the crucial missing links in the energy transition from fossil fuels to renewable sources. Presently, fossil fuels are the standard choice to fill the intermittent gap between wind and solar power. As the share of wind and solar increases in the energy mix, energy storage systems must replace gas-fired power plants as the primary method to make up for renewable sources' intermittency. In immediate terms, batteries are the most matured electrochemical storage devices and should be heavily invested to accommodate society's rapid electrification. In the medium term, green hydrogen from water electrolysis will be a substantial factor in energy storage, helping to decarbonize the economy. Hydrogen can make use of the existing infrastructure for natural gas, and it could be a solution to fields that are challenging to electrify, such as aviation and heavy industry. In the long run, carbon capture, utilization, and storage will play a significant role in reaching a net-zero society. As the share of carbon-emitting technology falls, capturing carbon, either from the source or the atmosphere, will become an attractive solution. When the fossil fuels industry shrinks, carbon dioxide may become the alternative carbon source to produce essential fuels, materials, and chemicals. Carbon utilization represents both an environmental solution and an economic opportunity.

Climate change, the most significant challenge humanity has ever faced, requires an all-hands-on-deck approach to tackle. A silver bullet to solve global warming does not and will not exist. Every decarbonization solution should be impartially considered and studied, from employing energy storage and nuclear power to redesigning transportation infrastructure and changing everyday behaviors. Technical solutions are just one piece of the bigger puzzle, as it takes political will to implement sensible technologies and policies to combat climate change. Therefore, people living in democratic systems should rally around the leaders with the most pragmatic approaches to enact rational environmental laws and regulations. As Russia, Saudi Arabia, and other authoritarian regimes continue to wield oil and gas as weapons, the democratic nations should accelerate the decoupling of fossil fuels from the global economy. It will not be a trivial task, but it is possible, and it must be done.

6 ANNEX

6.1	Supplementary figure	149
6.2	Millifluidic cell assembly procedure	149
6.3	Ink and electrodes preparation procedure	152
6.4	Constant-potential electrolysis experimental setup	154
6.5	Gas chromatograph characterization	155
6.6	Faradaic efficiency calculation and electrode potential conversion	157
6.7	X-ray absorption spectroscopy experiments	158
6.8	Bibliography	158

6.1 Supplementary figure

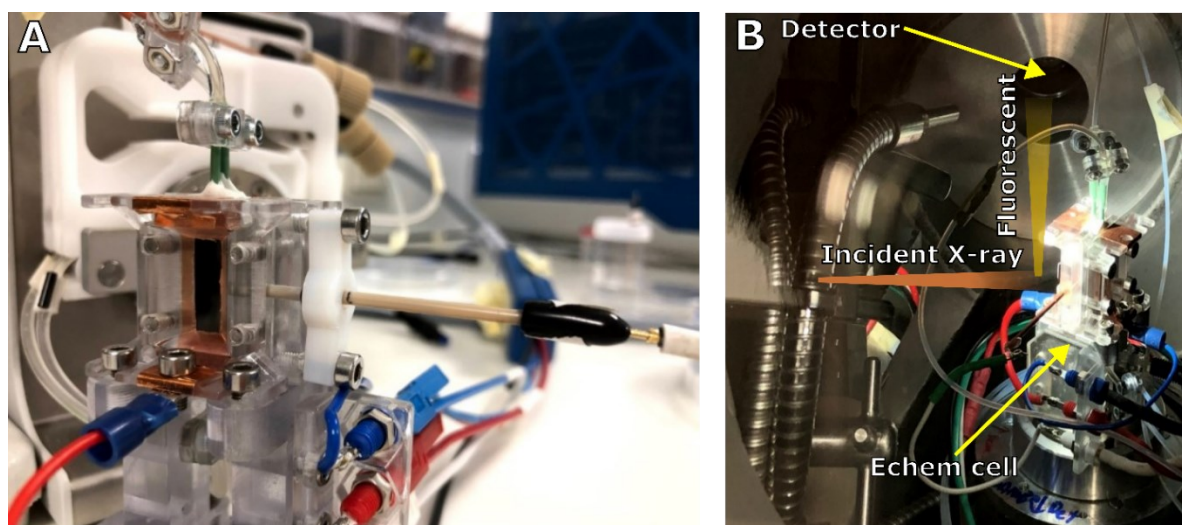


Figure 6-1. Actual photos of the 3D-printed electrochemical flow cell **(A)** and the flow cell in the experimental chamber of the LUCIA beamline **(B)**.

6.2 Millifluidic cell assembly procedure

1. All cell components are sonicated for 10 minutes in water purified by reverse osmosis to 18 M Ω before each experiment to remove any possible contaminants. They are dried with compressed air.
2. Place the working electrode (glassy carbon) on the bottom cover (Figure 6-2A), with the catalyst layer facing up and the electrode sitting on the copper tape in the middle of the cover (Figure 6-2B). M3 threads are tapped directly into the four corresponding holes of the bottom cover.
3. Place a silicone gasket on the cathodic flow plate, aligning the slot of the gasket with the flow plate channel (Figure 6-2C). The silicone gasket (0.127 mm, Fuel Cell Store) is cut with a scalpel, having the slot dimensions of 18 x 6 mm². Each catalyst has a specific gasket to avoid cross-contamination.
4. Mount the reference electrode cover on the side of the flow plate with two M3 bolts. Three 1 x 1 mm² O-rings (FKM) are placed under the cover (Figure 6-2C).

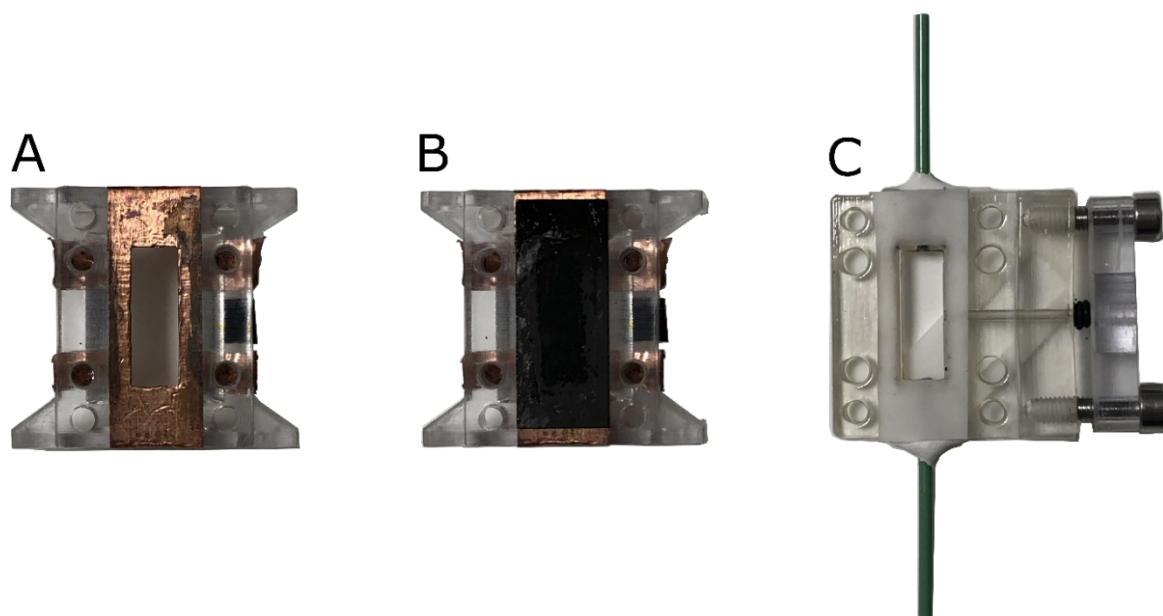


Figure 6-2. Millifluidic cell assembly 1

5. Stack the cathodic flow plate on top of the working electrode, with the gasket pressing down on the glassy carbon plate, and the catalyst layer is centered in the flow channel. Two pins are inserted into two alignment holes to hold the stack together during assembly (Figure 6-3A).
6. The Ag/AgCl mini reference electrode is inserted into the designated hole, protruding about 1 mm in the flow channel. The electrode is marked where it touches the cover so it can sit at the proper depth when assembled. This step is necessary when the electrode is new, or the mark is not visible.
7. Place a silicone gasket on the cathodic plate, similar to step 3. Wash the Nafion membrane with DI water, and put the membrane on top of the gasket, ensuring it is centered with the flow channel (Figure 6-3B). The gaskets that are not touching the working electrode are used in all experiments.
8. Place a silicone gasket on the anodic plate, similar to the previous step (Figure 6-3C).

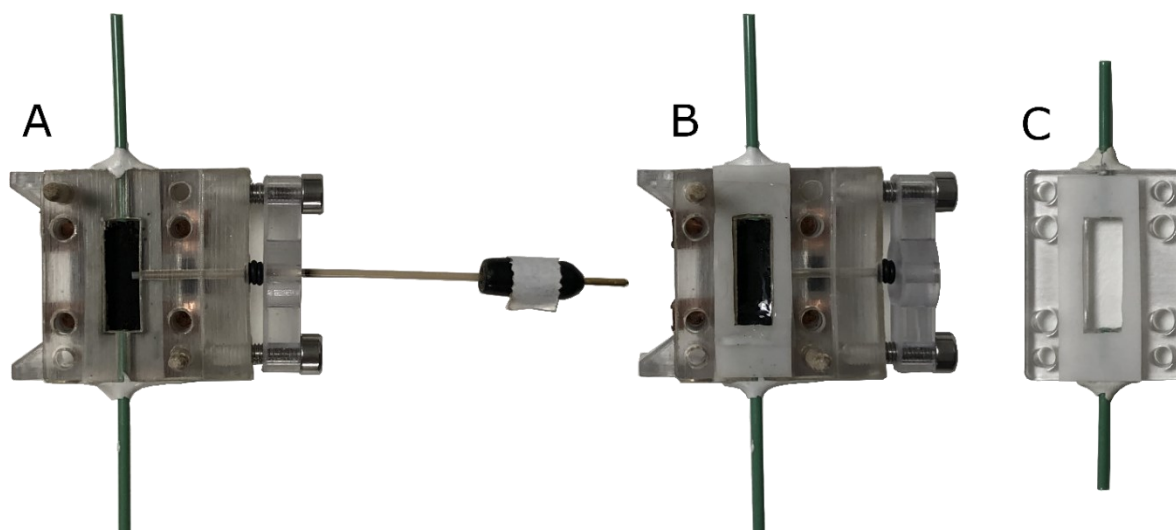


Figure 6-3. Millifluidic cell assembly 2

9. Place the anodic plate on top of the cathodic plate with the help of the alignment pins, making sure the membrane is sandwiched between the two gaskets. Then add a silicone gasket on top of the anodic plate. A nickel plate, acting as the counter electrode, is then placed on this gasket (Figure 6-4A).
10. Place the top cover on the assembly with the help of the alignment pins. Insert four M3 bolts (16 mm) in the designated holes (Figure 6-4B). Tighten the bolts in a criss-cross pattern to apply pressure evenly and seal the cell. The bolt holes are covered with copper tape to avoid the beam interfering with the iron in the bolts in a spectro-electrochemical experiment (Figure 6-2A).
11. Insert the reference electrode into its designated hole, with the mark in step 6 lined up with the cover. Gradually tighten the M3 (10mm) bolts to apply pressure and seal the connection (Figure 6-4C).

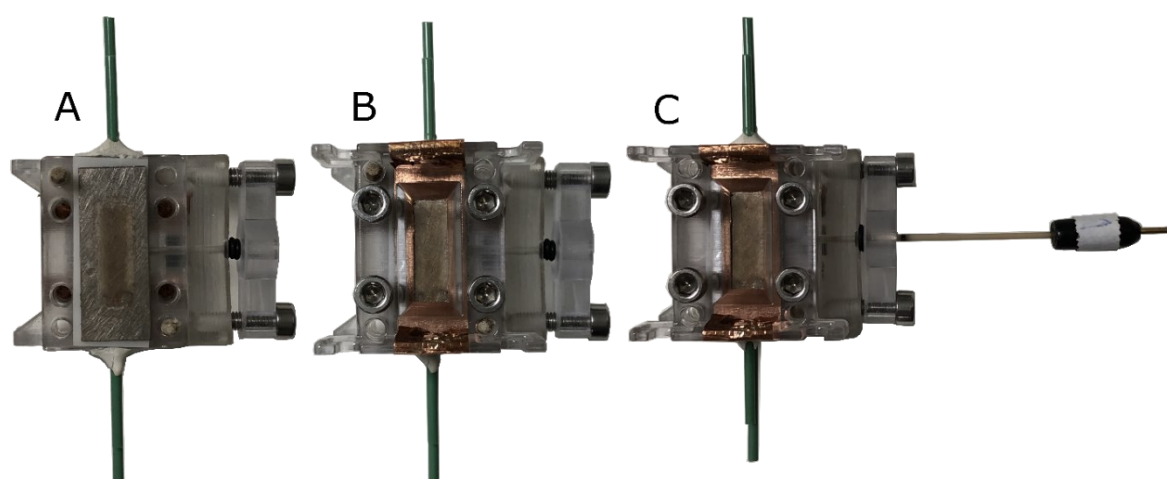


Figure 6-4. Millifluidic cell assembly 3

12. The cell is now ready. The experimental setup is described in detail in Chapter 3.
3. After each experiment, the cell is sonicated in water purified by reverse osmosis to 18 M Ω to remove any possible contaminants.

6.3 Ink and electrodes preparation procedure

8 mg of carbon black (Vulcan XC72 – Fuel Cell Store) is dispersed in 6 mL of dimethylformamide (DMF – 99.8% – VWR) by sonicating the mixture for 30 minutes at high power (FB11209 Fischer brand sonicator). 0.74 mg of FePc (Porphychem) dissolved into 2 mL of DMF is added to the carbon black dispersion, and the mixture is then sonicated for 10 minutes at low power. 80 μ L of Nafion D-520 solution (Alfa Aesar) is added, with another 10 minutes of sonication at low power. This standard ink solution is made for electrodes having the FePc surface concentration of 80 nmol/cm² and the carbon black concentration of 1 mg/mL. Table 6-1. summarizes the parameters For electrodes with different parameters: FePc concentration, carbon black concentration, different metal phthalocyanines, different substituted FePc, and FeTPP and its derivatives.

All the phthalocyanines and porphyrins species were purchased from Porphychem, except for FeTTP and Fe₂FP, which Prof. Gary Moore provided. The Fe₃O₄ nanoparticles were purchased from Sigma Aldrich. The nanoparticles are stabilized by modified polyethylene glycol (PEG) ligands covalently bonded to the particle by a hydroxamic acid on the end of the PEG chain. The PEG concentration is less than 1 % in weight. Their density is 1 mg/1 mL of H₂O, and their molecular weight is 231.53 g/mol.

The drop-casting procedure for an electrode is shown in Figure 6-5. The working electrodes are cast right after the ink is made to avoid the aggregation of the carbon black. A glassy carbon plate (HTW) with a dimension of 25 x 10 x 0.3 mm³ is kept on a hotplate at 80°C. A 70- μ L drop of ink is cast onto the glassy carbon plate, covering the whole surface of the electrode. The total volume cast on one electrode is 1167 μ L, yielding a surface concentration of the catalyst around 80 nmol/cm². After adding the ink, the excess catalyst that would not be in contact with the electrolyte is removed. Then the electrode is kept in a vacuum desiccator at 80°C overnight to evaporate the DMF solvent fully.

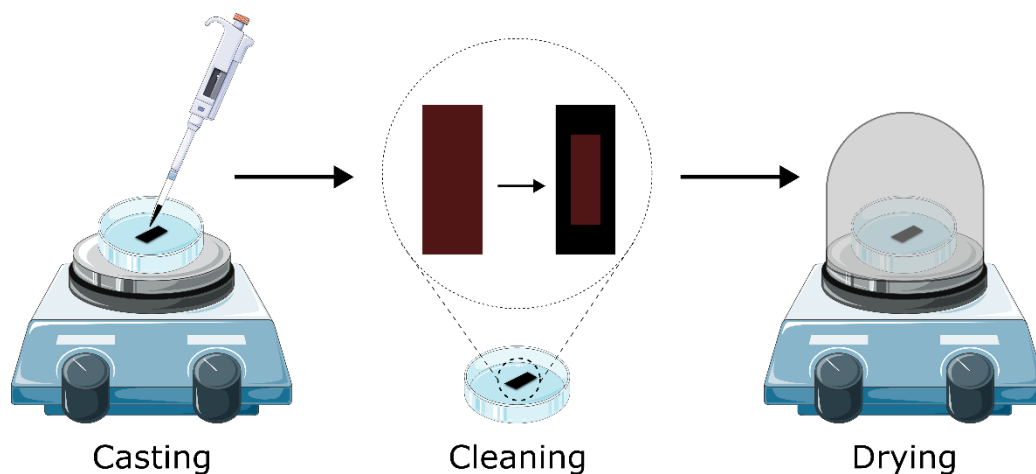


Figure 6-5. Drop-casting procedure

A nickel plate (99.9% trace metal basis, Sigma-Aldrich) with a dimension of 25 x 10 x 0.5 mm³ is used as the counter electrode. The electrode is polished gradually with 9 μm , 6 μm , and 3 μm liquid diamond suspensions (Bio DIAMANT®) and repolished with 3 μm liquid diamond suspension after each electrolysis experiment.

Table 6-1. Ink parameters of different electrode

Sample	Change from standard parameters (for 8 mL of ink)
H ₂ Pc – 80 nmol/cm ²	Catalyst mass: 0.67 mg
Fe ₃ O ₄ – 27 nmol/cm ²	Catalyst mass: 0.1 mg (0.1 mL solution)
Fe ₃ O ₄ /FePc; 40 nmol/cm ² of Fe each catalysts	Catalyst mass: 0.37 mg FePc and 0.05 mg Fe ₃ O ₄ (50 μL solution)
Fe ₃ O ₄ /FePc: 76 nmol/cm ² from FePc, 1.3 nmol/cm ² from Fe ₃ O ₄	Catalyst mass: 0.70 mg FePc and 0.005 mg Fe ₃ O ₄ (5 μL solution)
FePc – 225 nmol/cm ²	Catalyst mass: 2.22 mg
FePc – 450 nmol/cm ²	Catalyst mass: 4.44 mg
FePc – 0.25 C mg/mL	Carbon black mass: 5 mg
FePc – 0.625 C mg/mL	Carbon black mass: 2 mg
MnPc – 80 nmol/cm ²	Catalyst mass: 0.70 mg
NiPc – 80 nmol/cm ²	Catalyst mass: 0.80 mg
CoPc – 80 nmol/cm ²	Catalyst mass: 0.74 mg

CuPc – 80 nmol/cm ²	Catalyst mass: 0.74 mg
ZnPc – 80 nmol/cm ²	Catalyst mass: 0.80 mg
FePc-(m-COOH) ₄ – 80 nmol/cm ²	Catalyst mass: 0.96 mg
FePc-(m-NH ₂) ₄ – 80 nmol/cm ²	Catalyst mass: 0.82 mg
FePc-(o-NH ₂) ₄ – 80 nmol/cm ²	Catalyst mass: 0.82 mg
FePc-Cl ₁₆ – 80 nmol/cm ²	Catalyst mass: 1.45 mg
FeTPP – 80 nmol/cm ²	Catalyst mass: 0.91 mg
FeTPP-F ₂₀ – 80 nmol/cm ²	Catalyst mass: 1.4 mg
FeTTP – 100 nmol/cm ²	Catalyst mass: 1.32 mg
Fe ₂ FP – 100 nmol/cm ²	Catalyst mass: 2.51 mg

An LF-1 leak free 3.4 M Ag/AgCl reference electrode from Innovative Instruments is used as the reference electrode in all experiments. It is kept in a 0.05 M solution of H₂SO₄ and is thoroughly washed before and after each experiment with water purified by reverse osmosis to 18 MΩ.

6.4 Constant-potential electrolysis experimental setup

The assembly of the electrochemical flow cell is described in detail in chapter 2. Figure 6-6 shows the setup of the electrolysis and product characterization system. PEEK tubing (1/16" OD, 0.5 mm ID from Cluzeau) connects the electrolyte bottles with the peristaltic pump and the electrochemical cell. The PEEK tubings of the fully-assembled cell are connected to the PEEK tubings of the system using flexible silicone peristaltic pump tubing (1.02 mm ID, TYGON 2001 from Ismatec). The catholyte and anolyte bottles contain 25 mL of 0.1 M KHCO₃ (VWR) electrolyte. A peristaltic pump (Ismatec) circulates the electrolyte solution from the bottles to the cell and back to the bottles. Before an experiment, the catholyte solution is bubbled with CO₂ (Alphagaz 1 – Air Liquide) for at least 15 minutes while the solution is circulating. The pump's flow rate is 1 mL/min, which is calibrated before each experiment. When the gas purging finishes, the vent valve is closed while the purge valve is kept open for around 5 minutes, keeping the system with a slight overpressure to check for leakage. When no leakage is detected, the purge valve is closed, and the vent valve is quickly opened to depressurize the system, then closed immediately afterward. After that, constant-potential electrolysis is performed using the VSP-300 potentiostat from Biologic.

In control experiments in a CO₂-free environment, Ar (Alphagaz 2 – Air Liquide) is

purged instead of CO₂ before the electrolysis. In experiments with CO, instead of CO₂ as the reactant, CO (Air Liquide) is purged. When HCHO is used as the reactant, a solution of 30 mM HCHO in 0.1 M KHCO₃ is prepared using 16% HCHO (methanol-free, Thermo Scientific). The solution is used as the catholyte, and either Ar or CO₂ is purged in the HCHO/KHCO₃ solution for at least 15 minutes before the experiments.

A gas chromatograph (Inficon MicroGC) is connected directly to the catholyte bottle using similar PEEK tubing to analyze the gas products. The chromatograph analyzes the gas composition in the bottle's headspace. The headspace volume of the catholyte container is derived from the mass difference of water between a filled versus a 25-mL-filled container, yielding 9.5 mL.

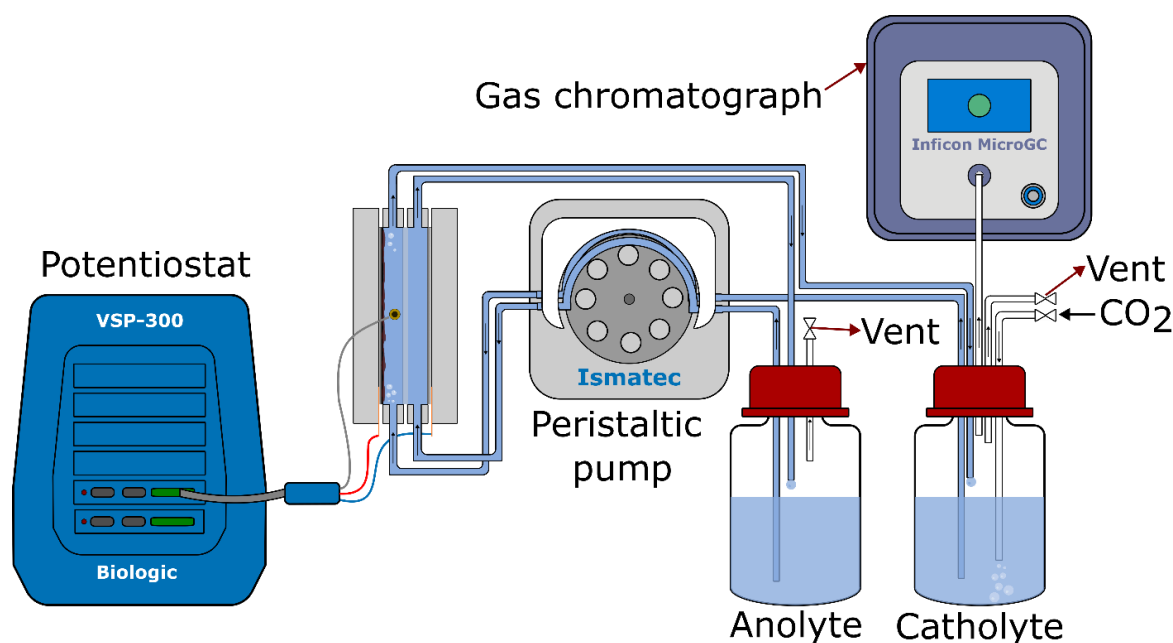


Figure 6-6. The electrochemical and gas detection setup used in this study

6.5 Gas chromatograph characterization

This study uses a 2-module Micro GC FUSION® Gas analyzer to characterize gaseous products. Module A has a 10-meter Rt-Molsieve 5A column, while module B has a 12-meter Rt-Q-bond column. Module A analyzes “light” gases, while module B analyzes “heavier” gases and some volatile organic compounds. Both modules use a thermal conductivity detector. The parameters of each module are shown in Table 6-2.

Table 6-2. Gas chromatograph method parameters

Parameters	Module A	Module B
Carrier gas	Argon	Helium
Column temperature	55°C (hold 20s) to 100°C (hold 185s), ramp rate 1°C/s	50°C (hold 50s) to 100°C (hold 100s), ramp rate 1°C/s
Backflush time	10.9 s	N/A
Column pressure	20 psi	17 psi
Inlet temperature	50°C	50°C
Detector temperature	70°C	70°C
Sample pump time	10s	10 s
Injector temperature	70°C	90°C
Inject time	120 ms	90 ms

While the exact elution time of a gas depends on a method's parameters, the appearance order in both modules is fixed. For module A, the order of appearance is $H_2/He \rightarrow O_2/Ar \rightarrow N_2 \rightarrow CH_4 \rightarrow CO$. Module B can analyze more species, so the order of appearance is more complicated as there are more chances for peaks to overlap. However, common species in module B follow a general trend: module A mixture $\rightarrow CO_2 \rightarrow C_2 \rightarrow H_2O \rightarrow C_3 \rightarrow C_4 \rightarrow C_n$. For multi-carbon species with isomers, unsaturated isomers generally elute before saturated isomers. If H_2 and CH_4 are presented in high amounts, the peak representing the module A mixture will have a negative peak at the beginning corresponding to H_2 and a shoulder at the end corresponding to CH_4 . The chromatograms of both modules exhibit a peak at the beginning due to the injection process. The direction of the peak depends on the carrier gas, and the peak in module A is more pronounced due to the backflush process to prevent unwanted gas from entering the column.

The gas chromatograph is calibrated using mixtures of gases with known concentrations. A 2.9% (v/v) mixture of H_2 in Ar and a 0.5% (v/v) mixture of CO in He from Air Liquide are used to calibrate CO and H_2 . For CH_4 , C_2H_4 , C_2H_6 , C_3H_6 , and C_3H_8 , a mixture of 100 ppm (v/v) of each gas in N_2 from Air Products are used. For $n-C_4H_{10}$, a pure sample of the gas from Messer is used. A linear forced through zero regression is performed to establish the relationship between the peak area and the volume concentration for each gas product, as recommended by the chromatograph manufacturer. The peak corresponding to pentane (C_5H_{12}) was identified by sampling

the headspace of a flask containing liquid pentane. However, it was not calibrated due to the difficulties in calibrating volatile liquid organic products with the gas chromatograph in the low-concentration region observed in our experiments.

6.6 Faradaic efficiency calculation and electrode potential conversion

A gas chromatograph measurement is performed every 30 minutes during the 2-hour electrolysis. The volume percentages of each gas are derived from the calibration line obtained from the procedure described above. The mole numbers of each product are calculated using the ideal gas law:

$$n = \frac{P \times (\%V \times V)}{R \times T}$$

where P , V , and T are the headspace pressure, volume, and temperature, of the catholyte container, respectively. $\%V$ is the volume percentage measured by the gas chromatograph, and R is the gas constant ($8.314 \text{ J}\cdot\text{mol}^{-1}\cdot\text{K}^{-1}$). Due to the low amount of generated products compared to the headspace volume, as well as the climate-controlled condition of the laboratory, the values of the pressure and the temperature in the headspace are assumed to be the values of atmospheric pressure (1.013 hPa) and room temperature (298K).

The Faradaic efficiency of all gaseous products is then calculated using the formula:

$$\%FE = \frac{n \times e \times F}{Q}$$

where n is the mole number of the corresponding products, e is the number of electrons needed to reduce CO_2 (or H_2O in the case of H_2) to that product, F is the Faraday constant ($96490 \text{ C}\cdot\text{mol}^{-1}$), and Q (C) is the total charge passed through the system at the time of the gas sampling, given by the potentiostat.

The procedure for calculating the Faradaic efficiency of liquid products is similar, except that the mole number is calculated directly using the molar concentration measured by NMR with a DMSO internal standard.

The conversion of potential from 3.4 M Ag/AgCl reference electrode to reversible hydrogen electrode is performed using the formula:

$$E_{RHE} = E_{Ag/AgCl} + 0.205 \text{ V} + 0.0591 \times pH$$

where the pH of 0.1 M KHCO_3 is 6.8 when saturated with CO_2 and 8.5 when saturated with Ar; the pH of 0.1 M KCl is 6.3 when saturated with Ar. All potential values are rounded to the first decimal place.


6.7 X-ray absorption spectroscopy experiments

XAS experiments were performed on the LUCIA¹ beamline of Synchrotron SOLEIL, with a ring current of 500 mA and nominal energy of 2.3 GeV. On LUCIA, The beamline energy was selected using a Si (111) double-crystal monochromator, and the beam size was 2 x 2 mm². Figure 6-1B shows the electrocatalytic flow cell in the experimental chamber under vacuum, with a 25° outgoing angle with respect to the detector, which is located at a 90° angle from the incident beam path. The experimental setup is similar to the one described in Section 6.4. However, a silver wire glued in the cell was used as the pseudo reference electrode since the mini Ag/AgCl reference electrode is not vacuum-compatible. In addition, the gas is kept bubbling during the whole measurement, as the gas products were not characterized during the spectro-electrochemical measurement. XANES data were collected as fluorescence excitation spectra using an SDD Bruker detector. The reference spectra of FePc, Fe metal, and Fe₃O₄ are measured with 6-mm round pellets containing 1 mg of sample and 40 mg of graphite window materials. All XAS data were normalized to the intensity of the incoming beam and reduced using the Athena software.²

6.8 Bibliography

- (1) Vantelon, D.; Trcera, N.; Roy, D.; Moreno, T.; Mailly, D.; Guilet, S.; Metchalkov, E.; Delmotte, F.; Lassalle, B.; Lagarde, P.; Flank, A.-M. The LUCIA Beamline at SOLEIL. *J Synchrotron Rad* **2016**, 23 (2), 635–640. <https://doi.org/10.1107/S1600577516000746>.
- (2) Ravel, B.; Newville, M. ATHENA and ARTEMIS: Interactive Graphical Data Analysis Using IFEFFIT. *Phys. Scr.* **2005**, 2005 (T115), 1007. <https://doi.org/10.1238/Physica.Topical.115a01007>.

6.9 Publications

Cite this: *Chem. Sci.*, 2023, 14, 550 All publication charges for this article have been paid for by the Royal Society of ChemistryReceived 24th August 2022
Accepted 14th December 2022DOI: 10.1039/d2sc04729b
rsc.li/chemical-science

Multiple C–C bond formation upon electrocatalytic reduction of CO₂ by an iron-based molecular macrocycle†

Si-Thanh Dong, Chen Xu and Benedikt Lassalle-Kaiser *

Molecular macrocycles are very promising electrocatalysts for the reduction of carbon dioxide into value-added chemicals. Up to now, most of these catalysts produced only C₁ products. We report here that iron phthalocyanine, a commercially available molecule based on earth-abundant elements, can produce light hydrocarbons upon electrocatalytic reduction of CO₂ in aqueous conditions and neutral pH. Under applied electrochemical potential, C₁ to C₄ saturated and unsaturated products are evolved. Isotopic labelling experiments unambiguously show that these products stem from CO₂. Control experiments and *in situ* X-ray spectroscopic analysis show that the molecular catalyst remains intact during catalysis and is responsible for the reaction. On the basis of experiments with alternate substrates, a mechanism is proposed for the C–C bond formation step.

Introduction

Atmospheric carbon dioxide (CO₂) has been used as a feedstock to produce all biomass,¹ including fossil fuels, since photosynthesis developed on Earth more than two billion years ago. Industrialized societies are eagerly searching for such a solar-to-chemical conversion process, which would help mitigate their carbon dioxide emissions while providing alternative ways to produce staple chemicals.² The electrochemical CO₂ reduction reaction (CO₂RR) has been proposed as a viable technology to convert this gas into valuable chemicals. At present, the most common products of CO₂ reduction are carbon monoxide (CO) and formic acid (HCOOH). Although these C₁ products are near the market-ready level, they only reflect a few of the chemicals that can be generated from CO₂.³ Great efforts have been directed to further reduce CO₂ to higher value products, particularly those including C–C bonds. Starting from the work of Hori and co-workers⁴ in the 80s, copper-based catalysts have shown remarkable activity towards the formation of light hydrocarbons, such as methane and ethylene.⁵ Despite these performances, the precise nature of the active sites involved remains debatable,⁶ partly because of the restructuring of copper during catalysis.^{7,8} Recently, single-atom catalysts (SACs) have gained significant attention in the field of CO₂ reduction due to their low metal content and high activity.⁹ While the reduction of CO₂ on SACs yields mostly CO, other more reduced products have been obtained,^{10,11} including C₂₊ products such

as ethanol¹² and acetone.¹³ Although SACs properties are expected to be favorable to the reduction of CO₂ beyond CO,¹⁴ the heterogeneity of their structures⁹ prevents establishing detailed reaction mechanisms.

Molecular complexes catalyze the reduction of CO₂ to CO with high efficiency and stability,^{15,16} and the homogeneity of their chemical structure allows establishing precise reaction mechanisms.^{17,18} Transition metal macrocycles such as porphyrins¹⁹ or phthalocyanines^{20–23} have shown very promising results in the electrochemical reduction of CO₂, both as homogeneous²³ and heterogeneous systems.²⁴ Beside their efficiency and robustness, these molecular catalysts also offer chemical tunability, which allows orienting their reactivity towards higher turnover numbers (TONs),²⁵ higher selectivity,²⁶ or the synthesis of a specific compound.²⁷ While most molecular species catalyzed the CO₂ to CO reduction, a handful of examples have shown that C₁ products such as methane^{28,29} or methanol^{21,30} can be produced by catalysts with M–N₄ structure. Ethanol and acetic acid were found as a product of CO₂ reduction on cobalt and manganese corrole species, respectively.^{31,32} There is, however, no example of C₂₊ compounds produced from CO₂ reduction by a catalyst for which the molecular nature during catalysis is demonstrated.

We report here on the electrocatalytic formation of saturated and unsaturated light hydrocarbons (C₁–C₄) from CO₂ using a heterogenized molecular iron phthalocyanine catalyst in a flowing system (see Fig. 1 and S1†). The analysis of the products formed under applied electrochemical potential shows that, besides CO and H₂, small amounts of methane, ethylene, ethane, propene, propane, and *n*-butane are detected along with traces of C₅ products. Electrocatalytic experiments using alternate substrates such as carbon monoxide (CO) or

Synchrotron SOLEIL, Route Départementale 128, l'Orme des Merisiers, 91190 Saint-Aubin, France. E-mail: benedikt.lassalle@synchrotron-soleil.fr

† Electronic supplementary information (ESI) available. See DOI: <https://doi.org/10.1039/d2sc04729b>



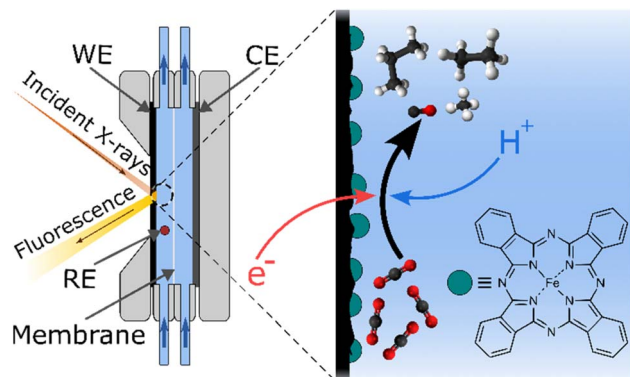


Fig. 1 Schematic side view of the electrochemical cell and simplified CO₂ reduction process on the surface of the working electrode. The dark green circles represent iron phthalocyanine (FePc), the molecular catalyst used in this study, whose structure is shown in the right corner. WE, CE, and RE stand for "working electrode", "counter electrode", and "reference electrode", respectively. The scheme is not drawn to scale.

formaldehyde (HCHO) support a mechanism involving a terminal carbene as a critical species on the way to C₂₊ compounds.

Results and discussion

Electrocatalysis and distribution of products

Based on the design of Ager and co-workers,³³ CO₂ reduction experiments were performed in an electrocatalytic flow cell consisting of two chambers for the cathodic and anodic reactions, separated by a Nafion® membrane (see Fig. 1 and S1†). The cathode consists of a glassy carbon electrode, on which an ink containing iron phthalocyanine (FePc) and a carbon powder is drop-casted with a surface concentration of around 80 nmol cm⁻² (see ESI† for electrode preparation procedure). A reference electrode is arranged in the cathode chamber, and the anode consists of a nickel plate. Two independent reservoirs contain the catholyte and anolyte (KHCO₃, 0.1 M), which are flown independently in the anodic and cathodic chambers. The headspace of the cathodic compartment is analyzed during the experiment by an online gas chromatograph that performs automatic sampling every thirty minutes (see Fig. S2A†).

Fig. 2A shows the chronoamperometric curves of constant potential electrolysis under Ar or CO₂ for two hours. After poisoning an FePc-modified electrode at -1.1 V vs. RHE under a CO₂ atmosphere, peaks corresponding to ethylene (C₂H₄), ethane (C₂H₆), propene (C₃H₆), propane (C₃H₈) and *n*-butane (C₄H₁₀) clearly stand out in the chromatogram (see Fig. 2B). Other peaks corresponding to unsaturated C₄ as well as *n*-pentane and unsaturated C₅ products can also be observed, although with a lower intensity. Methane (CH₄) is also clearly present on another module of the gas chromatograph (see Fig. S3†). The catholyte was analyzed by ¹H NMR to check for liquid products, but none was detected (see Fig. S4†). Control experiments were performed to ensure that FePc catalyzed the reduction of CO₂ into the products observed. When a FePc-modified electrode was set under catalytic conditions in an

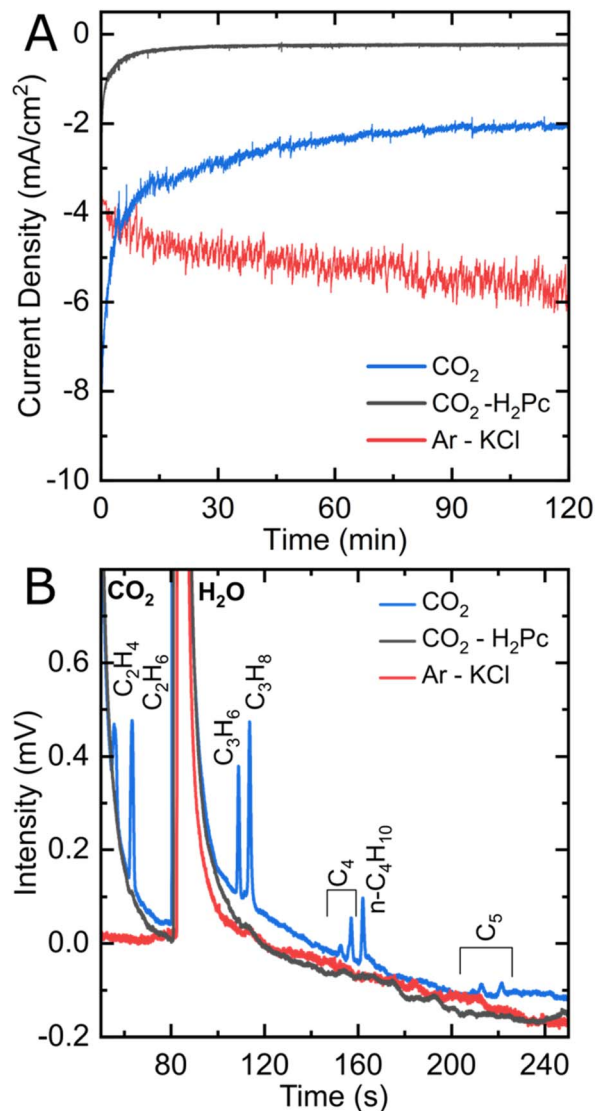


Fig. 2 (A) Chronoamperometric curves and (B) module B gas chromatograms of FePc-modified electrodes under Ar in 0.1 M KCl (red) and CO₂ in 0.1 M KHCO₃ (blue) and an H₂Pc-modified electrode under CO₂ in KHCO₃ (black). Chronoamperometric experiments are performed at -1.1 V vs. RHE for two hours, after which a gas chromatograph (GC) samples their resulting gaseous products.

Ar-saturated KHCO₃ electrolyte, hydrogen was the major product detected after two hours of electrolysis, with a trace amount of CO and hydrocarbons (see Fig. S5†). The observed carbon products can be attributed to the small amount of CO₂ that exists in equilibrium with the KHCO₃ electrolyte. In fact, a similar FePc-modified electrode, at the same potential, under a CO₂-free environment (Ar-saturated 0.1 M KCl electrolyte), produces only H₂ (see Fig. 2B and S3†). The current density observed is higher than under CO₂ (see Fig. 2A), indicating a high activity of FePc towards hydrogen evolution in a CO₂-free environment at high overpotential. When an H₂Pc-modified electrode was poised at -1.1 V in a CO₂-saturated KHCO₃ electrolyte, a twenty-fold decrease in current density was observed as compared to an FePc-modified electrode, indicating



a negligible catalytic activity without the Fe center. In agreement with the low catalytic activity, the main product detected was H_2 , with a miniscule amount of CO (Fig. S3†). These results strongly indicate CO_2 as the source of the carbon products observed and underline the essential role of the metal center in the catalytic process.

To confirm the origin of the carbon atoms in the C_{2+} products observed in the chromatograms, gas chromatography coupled mass spectrometry (GC-MS) experiments were performed. Fig. 3 shows the GC-MS chromatograms corresponding to the retention time of C_4 products (190–240 s). We focus on the C_4H_8 signal since it has the highest intensity of all C_4 products without overlapping the signal of CO_2 or CO . The $m/z = 56$ mass, which corresponds to a C_4H_8 species containing four

^{12}C atoms, shows a peak when $^{12}\text{CO}_2$ is used as the substrate, while it does not appear in the presence of $^{13}\text{CO}_2$. The opposite behavior is observed with the $m/z = 60$ mass, which corresponds to a C_4H_8 species with four ^{13}C atoms. The GC-MS chromatogram of the $m/z = 41$ mass at the region of the retention time of C_3 and C_4 products is shown on Fig. S6.† The $m/z = 41$ mass, which corresponds to a C_3H_5 fragment (originating from both C_3 and C_4 products) shows two distinguishable peaks when $^{12}\text{CO}_2$ is used, which disappear with $^{13}\text{CO}_2$. These isotopic labelling experiments demonstrate that the origin of the carbon atoms in the hydrocarbons observed is indeed CO_2 .

Fig. 4 shows the product distribution in terms of faradaic efficiency (FE) for each of the products obtained after a 2 hours electrocatalytic experiment under CO_2 . The potential range is chosen where there is significant CO_2 reduction activity without generating hydrogen bubbles that would make the system unstable. Between -0.7 V and -0.9 V, CO and H_2 are the only products observed. Although the current density at high overpotential slightly decreases over time, the selectivity of all products remains constant (see Fig. S7†). The amount of hydrogen increases steadily from -0.7 V to -1.1 V up to 65% FE at the expense of CO . Noticeable amounts of hydrocarbons can be observed starting from -0.9 V, methane being the main of them with up to 4% at -1.0 and -1.1 V. Ethylene, ethane, propene, propane and *n*-butane are produced with faradaic efficiencies of 0.1–0.25% each, making the total of C_{2+} products to be around 1%. It should be noted that the amount of ethylene is underestimated because of the high background generated by CO_2 in the chromatograph column. Despite the low amounts of products generated, their distribution was reproducible, as shown by the replicates performed on three different electrodes.

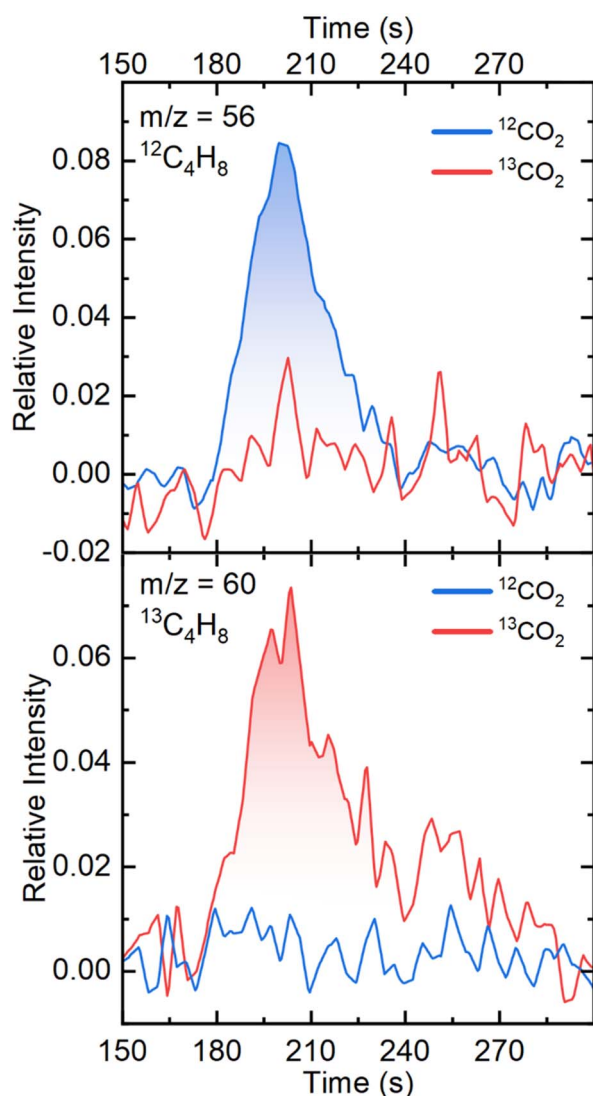


Fig. 3 GC-MS chromatograms for mass $m/z = 56$ of $^{12}\text{C}_4\text{H}_8$ and mass $m/z = 60$ of $^{13}\text{C}_4\text{H}_8$ at the retention time of C_4 products. Chronoamperometric experiments were performed on FePc-modified electrodes at -1.1 V vs. RHE for two hours, after which the GC-MS sampled the resulting gaseous products. The chromatograms were averaged from three independent experiments.

Catalyst characterization

In order to determine the nature of the catalyst under operating conditions and check its integrity, we performed *in situ* and *operando* X-ray absorption spectroscopy (XAS) experiments at the iron K-edge in the exact same electrochemical cell (see Fig. 1, S1 and S2B†). Fig. 5 shows the X-ray absorption near-edge structure (XANES) spectra of the FePc-modified electrode under open circuit potential (OCP) and under catalytic conditions, in a CO_2 atmosphere, with the corresponding non-normalized spectra in Fig. S8.† The spectrum of the electrode under resting state presents the same features as the pure, starting compound, showing the chemical robustness of the FePc catalyst after dropcasting and in the presence of an electrolyte. When poisoning the electrode at a potential of -1.1 V (at which C_{2+} products are observed), the spectrum shows a shift to lower energies (-2.7 eV at half-edge jump) while keeping the features that are characteristic of phthalocyanines,³⁴ *i.e.* two pre-edge peaks at 7114 eV and 7118 eV. A XANES spectrum was also recorded *in situ* after performing electrocatalytic experiments under a CO_2 atmosphere, and it was remarkably similar to the one collected on the starting electrode. The non-normalized spectra indicate a 10% material loss after 4.5 hours of continuous flowing, which is standard in this type of experiment.³⁵ The comparison between the spectra collected under *in situ* and



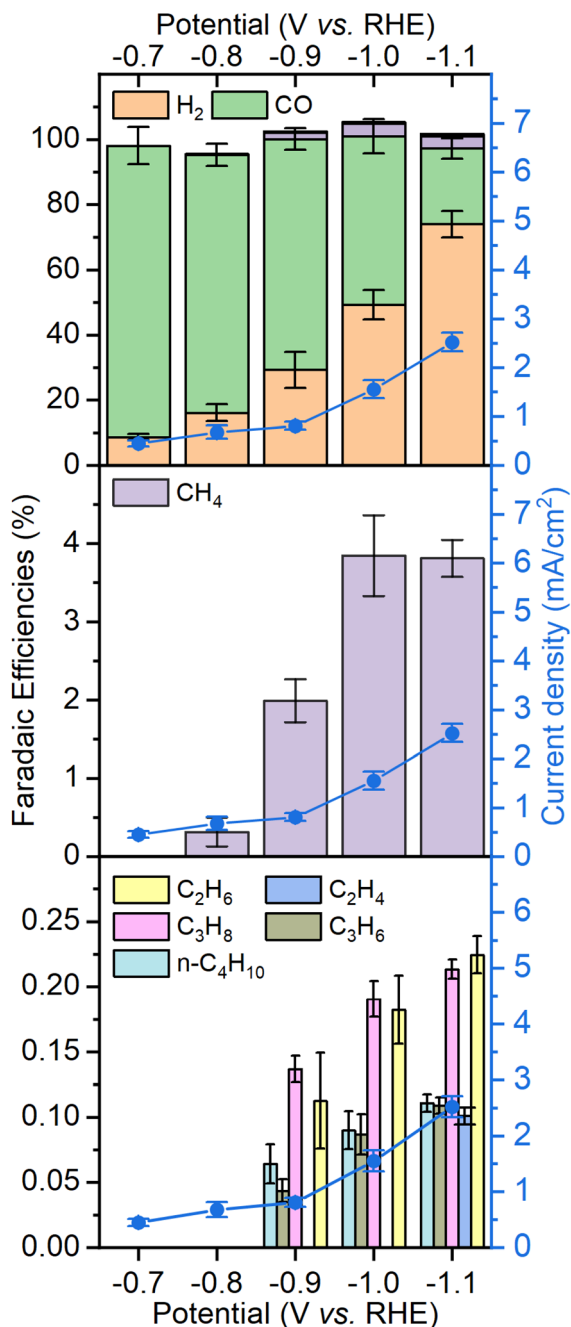


Fig. 4 Product distribution observed as faradaic efficiencies with FePc-modified electrodes as a function of applied potential. The total current density is plotted for each potential as the blue lines. The amount of ethylene (C_2H_4) is underestimated due to the high background generated by CO_2 in the chromatograph column.

operando conditions and those of reference compounds (metallic iron, Fe_3O_4) clearly rule out the presence of metallic iron or iron oxide nanoparticles that would be produced by the decomposition of the molecular catalyst. Altogether, these spectroscopic data collected under *in situ* conditions clearly demonstrate the molecular nature and the stability of the catalyst throughout the experiment.

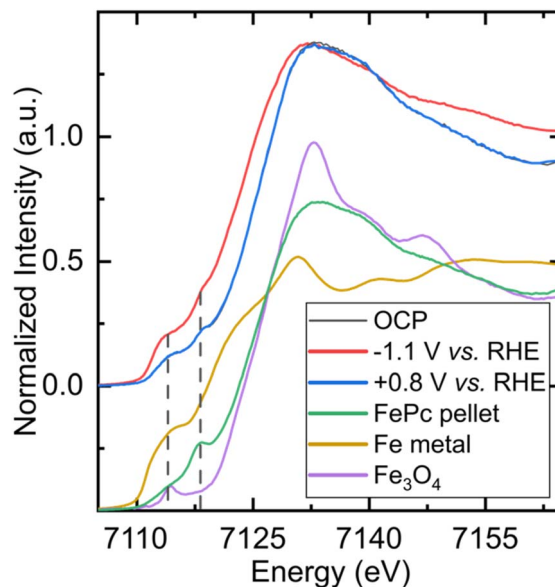


Fig. 5 *In situ* and *operando* X-ray absorption spectra collected on an FePc-modified electrode under different conditions and on reference samples. The spectra at the top correspond to an FePc-modified electrode under a CO_2 atmosphere poised at of FePc (green), on a metallic sheet of iron (gold), and on a pellet of Fe_3O_4 (purple). The two dashed lines indicate the pre-edge features of FePc at 7114 eV and 7118 eV. OCP (black), at -1.1 V vs. RHE (red) and going back at $+0.8$ V vs. RHE (blue). The spectra at the bottom correspond to *ex situ* reference spectra collected on a pellet.

In addition, infrared (IR) spectra were recorded on the FePc catalyst powder and FePc-modified electrodes before and after electrolysis at -1.1 V vs. RHE (see Fig. S9[†]). The spectra recorded show close similarity, agreeing with the XAS results concerning the stability of the catalyst during electrolysis.

C–C bond formation mechanism

The demonstration that a molecular electrocatalyst can form several consecutive C–C bonds poses the question of their formation mechanism. Since the major product observed upon reduction of CO_2 is CO, we postulated that the first intermediate for the formation of C–C bonds could be an FePc–CO species (see Fig. 6). Indeed, electrolysis with CO as substrate shows the formation of similar hydrocarbon products as observed for CO_2 , albeit with faradaic efficiencies approximately twice as low (see Fig. S10[†]). We attribute this lower faradaic efficiency to the low solubility of CO in water (1 mM) as compared to that of CO_2 (33 mM). As observed in other studies,^{33,36} we surmised that the difference in initial concentration of substrate was responsible for this difference in efficiency and performed finite element calculations to simulate concentration profiles upon CO_2 reduction. The results show that the concentration of CO generated by CO_2 reduction within 5 μm from the working electrode ranges from 1.5 to 4.5 mM (see ESI[†]), supporting a relationship between the amount of C_{2+} products and the local concentration of CO. These experiments confirm that FePc–CO is indeed an intermediate on the way to C_{2+} products.



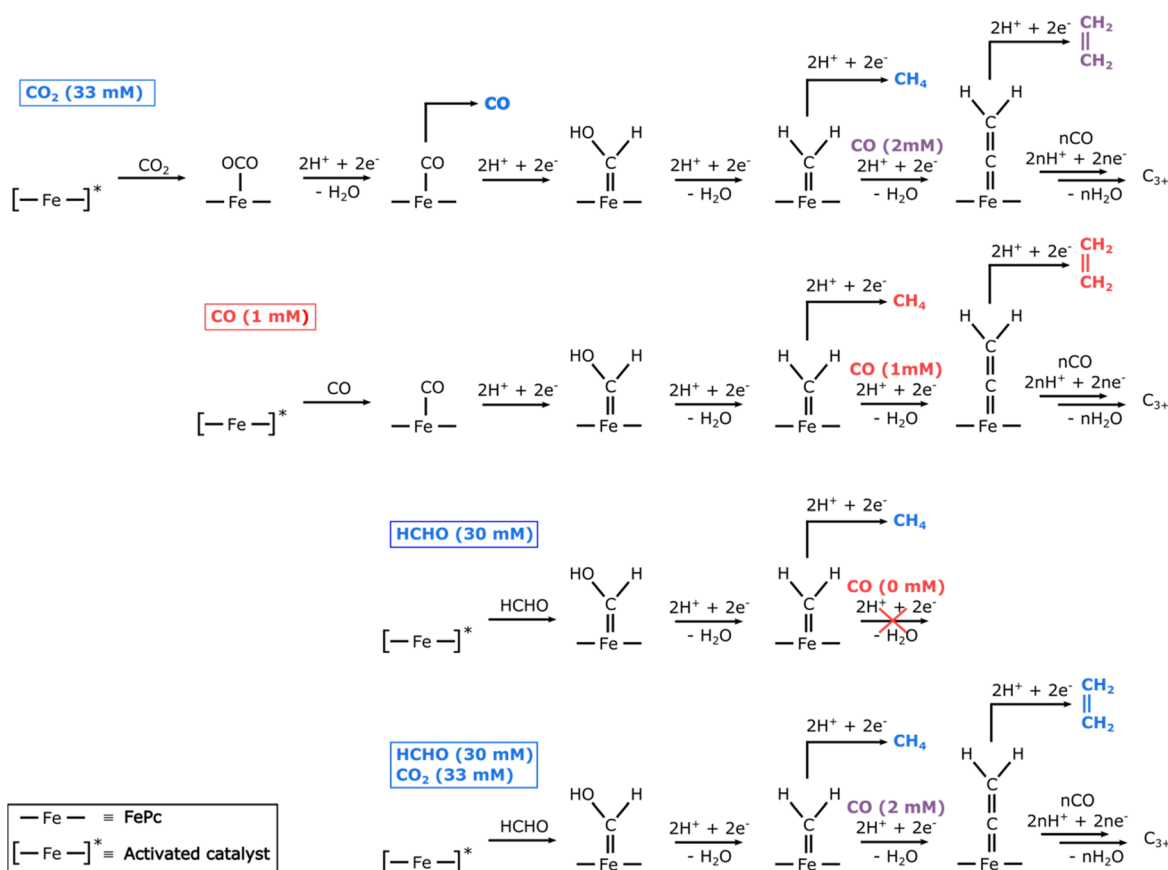


Fig. 6 Simplified mechanisms proposed for the formation of C–C bonds by FePc with either CO₂, CO, HCHO, or a mixture of HCHO and CO₂ as substrates. The colour code for substrates and products is as follow: blue, purple, and red for high, intermediate, and low concentrations, respectively.

By analogy with what happens during the Fischer–Tropsch synthesis of long-chain hydrocarbons, we hypothesized that a terminal FePc=CH₂ carbene species could be the precursor to all C₂₊ products. This transient species would be formed, *via* a hydroxycarbene species, by reaction of an FePc–CO adduct with either H₂ formed locally or with protons and electrons available in large amounts. This species would then further react either with more H₂ (or protons and electrons) to form methane. To form a C–C bond, the iron carbene species undergo CO insertion similar to Fischer–Tropsch mechanism. This CO insertion pathway is different from the carbene coupling involved in the formation of ethylene on metallic copper since there are no adjacent active sites in iron phthalocyanine. The process could continue a few times following various pathways and lead to the formation of longer saturated or unsaturated hydrocarbon chains (see Fig. 6).

To verify this hypothesis, we used formaldehyde as a substrate, expecting it to form an FePc=CH(OH) hydroxycarbene species by direct reaction with the activated form of the catalyst³⁷ (see Fig. 6). In these conditions, the product distribution shows similar multi-carbon products as with CO₂ or CO as substrates, although in much lower amounts (Fig. S10[†]), as well as methane (2%) and traces of methanol

(Fig. S10 and S13[†]). While the concentration of formaldehyde (30 mM) is similar to that of saturated CO₂ in water at 25 °C (33 mM), the very low faradaic efficiencies observed for C₂₊ products can be explained by the absence of any CO to be inserted in the FePc=C bond of the putative carbene species. Without any CO to react further, the carbene species is preferentially reduced into methane, leading to a 6-fold increase in the faradaic yield of methane as compared to the CO substrate. In order to confirm the reaction of CO with an FePc carbene species, we performed electrolysis with HCHO in a CO₂ atmosphere, as CO₂ reduction could provide the necessary CO to increase the C₂₊ formation with the carbene species generated from HCHO. Indeed, at –1.1 V vs. RHE, the total faradaic efficiency of C₂₊ products is one order of magnitude higher than observed in HCHO without CO₂ (see Fig. S11 and S12[†]), thus confirming our hypothesis of a reaction between CO and a carbene species obtained from formaldehyde. At less negative potentials, where the formation of CO from CO₂ is more favorable, the total C₂₊ faradaic efficiency increases further, reaching a maximum value of 1.5% at –0.9 V vs. RHE, *ca.* three times higher than when only CO₂ is used as substrate (see Fig. S12[†]). The higher selectivity of C₂₊ products after electrolysis of HCHO under CO₂ clearly supports the hypothesis that the formation of C₂₊ species



involves CO insertion on an intermediate FePc carbene species, as described in Fig. 6.

The existence of an FePc=CH₂ intermediate on the way to C₂₊ products is supported by the fact that several carbene species of iron porphyrin (a macrocycle similar to FePc) have been reported, either as transient^{38,39} or stable species,⁴⁰ and that FePc itself has been reported as an efficient catalyst for the cyclopropanation of alkenes,⁴¹ which involves FePc–carbene intermediates. Iron porphyrins are also known for catalyzing the insertion of carbenes into N–H, S–H, or C–H bonds.^{42,43} These precedents, as well as the experiments described here with alternate substrates, strongly support the involvement of an FePc carbene species on the way to C₂₊ hydrocarbons.

Conclusions

We reported in this paper on the electrocatalytic activity of iron phthalocyanine, a molecular macrocycle based on earth-abundant elements, towards the reduction of CO₂ into light hydrocarbons with up to three C–C bonds. Using *operando* X-ray absorption spectroscopy, we showed that the catalyst keeps its molecular structure throughout the electrocatalytic process. Based on experiments involving carbon monoxide or formaldehyde, we showed that the local concentration of CO is key to the formation of C–C bonds and propose a terminal carbene as an intermediate on the way to C₂₊ products. These results indicate that the formation of several consecutive carbon–carbon bonds can be catalyzed by single-site transition metal macrocycles under mild electrochemical conditions. The mechanistic insights that we provided open a perspective for the design of both molecular and material-based catalysts with enhanced selectivity towards C₂₊ products.

Data availability

The authors confirm that the data supporting the findings of this study are available within the article and its ESI material.† Raw data that support the findings of this study are available from the corresponding author, upon reasonable request.

Author contributions

Conceptualization: STD, BLK investigation: STD, CX funding acquisition: BLK supervision: BLK writing – original draft: STD, BLK writing – review & editing: STD, BLK.

Conflicts of interest

There are no conflicts to declare.

Acknowledgements

We express our gratitude to Dr Jean-Blaise Brubach of the AILES beamline of Synchrotron SOLEIL for his help during infrared spectra collection. We are indebted to Ms. Chanjuan Zhang and Dr Zakaria Halime at the Institut de Chimie Moléculaire et des Matériaux d'Orsay, Université Paris-Saclay for their assistance

in performing ¹H-NMR measurements. The Agence Nationale de la recherche is acknowledged for a young researcher grant to B. L.-K. (grant no. 18-CE05-0007).

References

- 1 A. A. Benson, J. A. Bassham, M. Calvin, T. C. Goodale, V. A. Haas and W. Stepka, *J. Am. Chem. Soc.*, 1950, **72**, 1710–1718.
- 2 J. Cheon, J. Y. Yang, M. Koper and O. Ishitani, *Acc. Chem. Res.*, 2022, **55**, 931–932.
- 3 O. S. Bushuyev, P. De Luna, C. T. Dinh, L. Tao, G. Saur, J. van de lagemaat, S. O. Kelley and E. H. Sargent, *Joule*, 2018, **2**, 825–832.
- 4 Y. Hori, K. Kikuchi, A. Murata and S. Suzuki, *Chem. Lett.*, 1986, **15**, 897–898.
- 5 S. Nitopi, E. Bertheussen, S. B. Scott, X. Liu, A. K. Engstfeld, S. Horch, B. Seger, I. E. L. Stephens, K. Chan, C. Hahn, J. K. Nørskov, T. F. Jaramillo and I. Chorkendorff, *Chem. Rev.*, 2019, **119**, 7610–7672.
- 6 D. Raciti and C. Wang, *ACS Energy Lett.*, 2018, **3**, 1545–1556.
- 7 J. Vavra, T.-H. Shen, D. Stoian, V. Tileli and R. Buonsanti, *Angew. Chem.*, 2021, **133**, 1367–1374.
- 8 Y.-G. Kim, J. H. Baricuatro and M. P. Soriaga, *Electrocatalysis*, 2018, **9**, 526–530.
- 9 J. Zhang, W. Cai, F. Xin Hu, H. Yang and B. Liu, *Chem. Sci.*, 2021, **12**, 6800–6819.
- 10 L. Han, S. Song, M. Liu, S. Yao, Z. Liang, H. Cheng, Z. Ren, W. Liu, R. Lin, G. Qi, X. Liu, Q. Wu, J. Luo and H. L. Xin, *J. Am. Chem. Soc.*, 2020, **142**, 12563–12567.
- 11 W. Ju, A. Bagger, X. Wang, Y. Tsai, F. Luo, T. Möller, H. Wang, J. Rossmeisl, A. S. Varela and P. Strasser, *ACS Energy Lett.*, 2019, **4**, 1663–1671.
- 12 Y. Jiao, Y. Zheng, P. Chen, M. Jaroniec and S.-Z. Qiao, *J. Am. Chem. Soc.*, 2017, **139**, 18093–18100.
- 13 K. Zhao, X. Nie, H. Wang, S. Chen, X. Quan, H. Yu, W. Choi, G. Zhang, B. Kim and J. G. Chen, *Nat. Commun.*, 2020, **11**, 2455.
- 14 A. Bagger, W. Ju, A. S. Varela, P. Strasser and J. Rossmeisl, *Catal. Today*, 2017, **288**, 74–78.
- 15 S. Ren, D. Joulié, D. Salvatore, K. Torbensen, M. Wang, M. Robert and C. P. Berlinguette, *Science*, 2019, **365**, 367–369.
- 16 X. Zhang, Y. Wang, M. Gu, M. Wang, Z. Zhang, W. Pan, Z. Jiang, H. Zheng, M. Lucero, H. Wang, G. E. Sterbinsky, Q. Ma, Y.-G. Wang, Z. Feng, J. Li, H. Dai and Y. Liang, *Nat. Energy*, 2020, **5**, 684–692.
- 17 J. Bonin, A. Maurin and M. Robert, *Coord. Chem. Rev.*, 2017, **334**, 184–198.
- 18 Y. Kuramochi, O. Ishitani and H. Ishida, *Coord. Chem. Rev.*, 2018, **373**, 333–356.
- 19 G. F. Manbeck and E. Fujita, *J. Porphyrins Phthalocyanines*, 2015, **19**, 45–64.
- 20 K. Kusuda, R. Ishihara and H. Yamaguchi, *Electrochim. Acta*, 1986, **31**, 657–663.



- 21 E. Boutin, M. Wang, J. C. Lin, M. Mesnage, D. Mendoza, B. Lassalle-Kaiser, C. Hahn, T. F. Jaramillo and M. Robert, *Angew. Chem., Int. Ed.*, 2019, **58**, 16172–16176.
- 22 Z. Jiang, Y. Wang, X. Zhang, H. Zheng, X. Wang and Y. Liang, *Nano Res.*, 2019, **12**, 2330–2334.
- 23 R. Francke, B. Schille and M. Roemelt, *Chem. Rev.*, 2018, **118**, 4631–4701.
- 24 N. Corbin, J. Zeng, K. Williams and K. Manthiram, *Nano Res.*, 2019, **12**, 2093–2125.
- 25 C. Costentin, S. Drouet, M. Robert and J.-M. Savéant, *Science*, 2012, **338**, 90–94.
- 26 W. W. Kramer and C. C. L. McCrory, *Chem. Sci.*, 2016, **7**, 2506–2515.
- 27 P. Gotico, Z. Halime and A. Aukauloo, *Dalton Trans.*, 2020, **49**, 2381–2396.
- 28 B. Li, L. Sun, J. Bian, N. Sun, J. Sun, L. Chen, Z. Li and L. Jing, *Appl. Catal., B*, 2020, **270**, 118849.
- 29 J. Shen, R. Kortlever, R. Kas, Y. Y. Birdja, O. Diaz-Morales, Y. Kwon, I. Ledezma-Yanez, K. J. P. Schouten, G. Mul and M. T. M. Koper, *Nat. Commun.*, 2015, **6**, 8177.
- 30 Y. Wu, Z. Jiang, X. Lu, Y. Liang and H. Wang, *Nature*, 2019, **575**, 639–642.
- 31 S. Gonglach, S. Paul, M. Haas, F. Pillwein, S. S. Sreejith, S. Barman, R. De, S. Müllegger, P. Gerschel, U.-P. Apfel, H. Coskun, A. Aljabour, P. Stadler, W. Schöfberger and S. Roy, *Nat. Commun.*, 2019, **10**, 3864.
- 32 R. De, S. Gonglach, S. Paul, M. Haas, S. S. Sreejith, P. Gerschel, U.-P. Apfel, T. H. Vuong, J. Rabeah, S. Roy and W. Schöfberger, *Angew. Chem., Int. Ed.*, 2020, **59**, 10527–10534.
- 33 Gurudayal, D. Perone, S. Malani, Y. Lum, S. Haussener and J. W. Ager, *ACS Appl. Energy Mater.*, 2019, **2**, 4551–4559.
- 34 Y. Liu, A. Deb, K. Yee Leung, W. Nie, W. S. Dean, J. E. Penner-Hahn and C. C. L. McCrory, *Dalton Trans.*, 2020, **49**, 16329–16339.
- 35 T. Zhao, Y. Wang, S. Karuturi, K. Catchpole, Q. Zhang and C. Zhao, *Carbon Energy*, 2020, **2**, 582–613.
- 36 S. Louisia, D. Kim, Y. Li, M. Gao, S. Yu, I. Roh and P. Yang, *Proc. Natl. Acad. Sci. U. S. A.*, 2022, **119**, e2201922119.
- 37 H. Mahmoudi, M. Mahmoudi, O. Doustdar, H. Jahangiri, A. Tsolakis, S. Gu and M. LechWyszynski, *Biofuels Engineering*, 2017, vol. 2, pp. 11–31.
- 38 D. Lexa, J.-M. Savéant, J.-P. Battioni, M. Lange and D. Mansuy, *Angew. Chem., Int. Ed. Engl.*, 1981, **20**, 578–579.
- 39 I. Artaud, N. Gregoire, P. Leduc and D. Mansuy, *J. Am. Chem. Soc.*, 1990, **112**, 6899–6905.
- 40 Y. Liu, W. Xu, J. Zhang, W. Fuller, C. E. Schulz and J. Li, *J. Am. Chem. Soc.*, 2017, **139**(14), 5023–5026.
- 41 H.-H. Liu, Y. Wang, Y.-J. Shu, X.-G. Zhou, J. Wu and S.-Y. Yan, *J. Mol. Catal. A: Chem.*, 2006, **246**, 49–52.
- 42 R. D. Lewis, M. Garcia-Borràs, M. J. Chalkley, A. R. Buller, K. N. Houk, S. B. J. Kan and F. H. Arnold, *Proc. Natl. Acad. Sci. U. S. A.*, 2018, **115**, 7308–7313.
- 43 C. Empel, S. Jana and R. M. Koenigs, *Molecules*, 2020, **25**, 880.





In situ/operando X-ray spectroscopy applied to electrocatalytic CO₂ reduction: Status and perspectives

Daniela Mendoza, Si-Thanh Dong and Benedikt Lassalle-Kaiser

Abstract

X-ray spectroscopy is a powerful tool to understand the electronic and local structure of electrocatalysts under operating conditions. Although catalysis itself is performed by electroactive species, other, non-electroactive ones play a critical role in electrocatalytic reactions as well. Cations, anions, solvents or reactants all have significant effects in the efficiency of electrocatalytic reactions. Focusing on the electrochemical reduction of carbon dioxide, we give a short summary of the current status of the *in situ/operando* X-ray spectroscopy experiments performed on electroactive species, as well as a perspective on the techniques and setups that could be used to probe non-electroactive ones.

Addresses

Synchrotron SOLEIL, L'Orme des Merisiers, Route Départementale 128, 91190, Saint-Aubin, France

Corresponding author: Lassalle-Kaiser, Benedikt (benedikt.lassalle@synchrotron-soleil.fr)

Current Opinion in Colloid & Interface Science 2022, 61:101635

This review comes from a themed issue on **Colloid & Interfacial Phenomena in Electrochemical Systems (2022)**

Edited by **Gabriel Loget** and **Yann Leroux**

For complete overview about the section, refer [Colloid & Interfacial Phenomena in Electrochemical Systems \(2022\)](#)

<https://doi.org/10.1016/j.cocis.2022.101635>

1359-0294/© 2022 Elsevier Ltd. All rights reserved.

Keywords

CO₂ reduction reaction, Electrocatalysis, X-ray spectroscopy, *In situ/operando* techniques.

Introduction

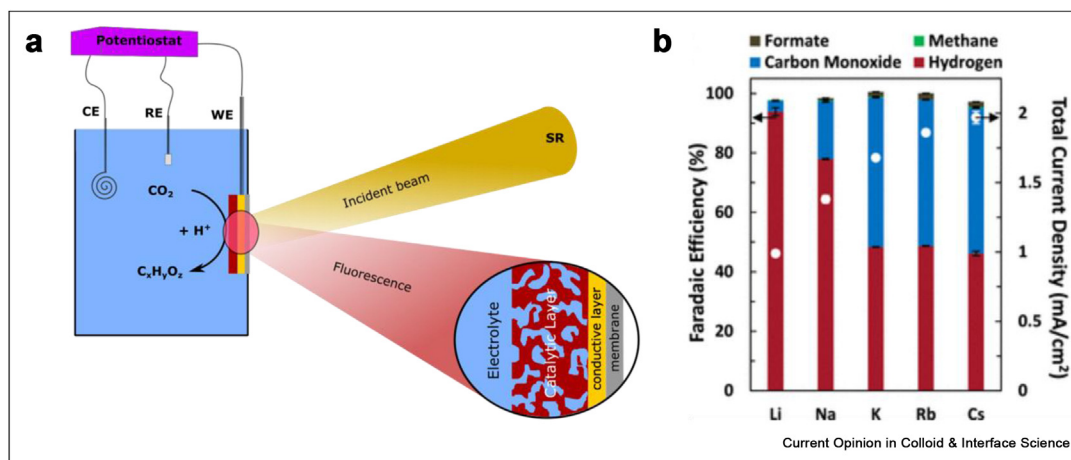
The electrocatalytic CO₂ reduction reaction (CO₂RR) is a promising process to convert this industrial by-product into value-added chemicals [1]. Synthetic building blocks such as carbon monoxide, formic acid, formaldehyde or methanol are used industrially at the megaton level and can be produced through this process. The CO₂RR actually entails several reactions, which can occur in parallel (and therefore compete with each other), or in series (also competing with each other).

CO₂ can be reduced by two electrons into carbon monoxide (CO) or formic acid (HCOOH), CO can be reduced to formaldehyde (HCHO) and formaldehyde can be further reduced to methanol (CH₃OH) or directly to methane (CH₄). A few catalysts are also able to form C₂₊ products, such as ethylene [2] or ethanol [3]. Out of these products, only carbon monoxide [4] and formic acid [5] are obtained with a very high selectivity (>95%), while other products are usually obtained as mixtures, preventing their large-scale use and industrial application (among other constraints). The production of hydrogen concomitantly to carbon-based products is also a very frequent phenomenon that is deleterious to applications requiring high purity products. The improvement of the efficiency (the total current density) and selectivity (the faradaic yields) of the CO₂RR requires a fundamental understanding of the parameters that influence this reaction.

One aspect of these fundamental studies is the field of spectroelectrochemistry, which aim is to provide spectroscopic information on species that appear, disappear or evolve under an electrochemical stimulus. These techniques provide information on the chemical nature, the local and electronic structure and the long-range order of the species that are present in the vicinity of the electrode–electrolyte interface. They are therefore complementary to the thermodynamic and kinetic information that can be obtained from electrochemical techniques and allow building structure–activity relationships that can be used for the optimization of a reaction. In this paper, we will focus on the use of X-ray spectroelectrochemistry for the study of the CO₂ reduction reaction, with a special emphasis on non-electroactive species. A simplified scheme of an *in situ/operando* X-ray absorption spectroelectrochemical setup is shown in [Figure 1a](#). A very exhaustive review of X-ray absorption spectroscopy applied to electrocatalysis in general was recently published by Timoshenko and Roldan Cuenya [6], we invite the readers to consult it for a more complete view of the topic.

The nature of the catalyst used in the CO₂RR is obviously critical for both the efficiency and selectivity of the reaction, depending on the nature of the metal used

Figure 1



(a) Simplified scheme of an *in situ/operando* XAS spectroelectrochemical experiment applied to the CO₂RR. (b) Product distribution (plotted as Faradaic efficiency) in the CO₂RR on copper in the presence of different cations. Reprinted with permission from Ref. [10]. Copyright 2020 American Chemical Society.

as the primary catalytic site, its composition, its morphology and crystallinity as well as many other electronic and structural parameters. In the first part of this article, we will give an overview of the works that used *in situ/operando* X-ray spectroscopies to probe the structure of *electroactive species* involved in the CO₂RR.

Other components such as the solvent [7], the electrolytes [8,9], the reactants or other additives [10] can also have a significant impact on its outcome. For example, the product distribution in the electrocatalytic reduction of CO₂ by heterogeneous copper catalysts was shown to vary as a function of the cations used in the electrolyte [10–12] (see Figure 1b). The detailed effects of these and other non-electroactive components on the CO₂RR have been reviewed recently elsewhere [13]. In the second part of this paper, we will present a selection of X-ray-based photon-in/photon-out techniques that could be used to probe *non-electroactive species* involved in the CO₂RR and provide valuable information on the reaction mechanism.

State of the art: understanding the structure of CO₂-reducing electrocatalysts under operating conditions with *in situ/operando* X-ray absorption spectroscopy

Principles of *in situ/operando* XAS applied to CO₂RR

Among spectroelectrochemical techniques, X-ray-based spectroscopies have received a lot of attention in the last decade, particularly in the field of electrocatalysis [6]. This is due to advances in instrumentation that made possible experiments with strong experimental constraints, but also very likely to the electrocatalysis community realizing that these tools were the ones that

could actually answer their questions. XAS is a very complete technique that provides both structural (from the picometer to the nanometer range) and electronic (oxidation and spin states) information on electrocatalysts, with the ability to probe them under *in situ* or *operando* conditions thanks to the high penetration depth of the photons used. This property of X-rays leads to probing a significant volume of the electrode/electrolyte assembly, which can be an advantage to have an average view of the sample, but also a drawback when it comes to probing only the solid or liquid part of the solid–liquid interface [14].

In the vast majority of X-ray spectroelectrochemical studies, electroactive species have been the point of focus, because they are those primarily involved in electron transfer processes, and also because they are the most easily observed. Changes in oxidation states or structural rearrangements usually have obvious signatures, with shifts in absorption edge positions in the XANES spectra and changes in the peak positions and intensities of the Fourier transform spectra of the EXAFS signal. It is therefore possible to determine the chemical nature of an electrode material under applied electrochemical bias, which can significantly differ from their starting structure. The same is true for electroactive species in solution (homogeneous catalysis), in which chemical structure upon oxidation or reduction can be probed *in situ* under applied potential. These information are extremely important to determine the nature of the species that are responsible for catalysis.

The CO₂ reduction reaction has been studied in the past decade with various spectroscopic tools, in order to

identify the intermediate species involved in the reaction [15]. X-ray spectroscopy has been a tool of choice for this type of studies, especially for heterogeneous systems which can be observed under operating conditions with very few techniques. Pure metals, such as copper, metal/nitrogen-doped carbon (MNC) materials or discrete molecules have all been used as heterogeneous electrocatalysts for the reduction of CO₂ and to some extent studied with X-ray techniques. The next paragraphs give an overview of the most essential work done in this field, with a focus on the fate of the electroactive species.

Pure metals

A large variety of metals can reduce CO₂ [16], mostly into formic acid (such as Sn, Cd or In) or carbon monoxide (such as Ag, Au or Zn). In a few cases, the structure of these metals has been probed by XAS under functioning conditions [17,18]. We will, however, focus our attention on the case of copper, which has been thoroughly investigated with X-ray spectroscopy.

Pure copper is a very interesting electrocatalyst for the reduction of CO₂, mostly because it is able to produce significant amounts of products beyond CO, such as methane or ethylene, as well as other more reduced products [19]. For this reason, it has been widely investigated with various spectroelectrochemical techniques [15]. To summarize briefly, the use of XAS at the copper K-edge has been used extensively [20–22] to assess the oxidation state of copper under catalytic conditions, the conclusion being that it is essentially purely metallic, while a small fraction of oxide still exists in some cases. On the basis of X-ray photoelectron Spectroscopy (XPS) and theoretical calculations, the presence of remaining oxygen under reducing conditions has been assigned to a sub-surface layer of oxygen [23], which could play a role in tuning the reactivity of copper towards ethylene. This hypothesis is, however, the subject of debates [24], because the presence of traces of oxide at the surface of copper that could contribute to the signal (rather than sub-surface oxygen) is extremely challenging to avoid experimentally. The presence of oxygen at the surface of copper under electrocatalytic conditions has also been evidenced with *operando* XAS [25], the presence of oxides favoring the formation of ethylene. It is, however, not clear yet whether this reactivity is directly linked to the chemical nature of the catalyst or to the nanostructuring induced by the *in situ* reduction of the oxide phases [26,27].

Understanding the nature of the catalytic sites of metals or materials-based catalysts remains challenging with X-ray absorption, because the reactivity only occurs at the solid–liquid interface, while XAS probes the whole material. Complementary techniques more sensitive to

the surface or to specific species are often required, such as XPS [28].

Molecular systems

Transition metal molecular complexes have been known to reduce CO₂ efficiently for several decades, mostly under homogeneous conditions [29,30]. For example, polypyridyl complexes of rhenium [31] or manganese [32] were shown to reduce CO₂ in organic solvents and water as early as the 80's [33]. Macrocyclic complexes of transition metals such as cyclams [34,35], porphyrins [36] or phthalocyanines [37] were also shown to be very efficient CO₂ reduction catalysts in the same period, with a surge of interest in recent years. Although industrial application of electrochemical reactions in homogeneous conditions is very unlikely, molecules in solutions are ideal systems to study the mechanism of a chemical reaction [38]. Indeed, their structure can be precisely determined as compared to metals or inorganic materials that present a heterogeneity of sites. Changes in oxidation state and/or structure as well as interactions with reactants, solvent or products can therefore be precisely followed. Recently, molecular systems (particularly transition metal macrocycles) have been heterogenized to meet the requirements of large-scale applications [4,39–41]. Incidentally, the possibility of performing *in situ/operando* X-ray spectroscopic experiments has increased [41–43] because the diffusion of molecules to/from the electrode is suppressed in these systems and simplifies the data collection and analysis processes. One of the main lessons learned from X-ray spectroscopic experiments is that these molecules seem to be robust enough to withstand the electrocatalytic conditions of CO₂ reduction for a few hours at least [44]. There are, however, exceptions to this statement, with a few molecular systems for which the active species were proposed to be nanoparticles that are reversibly formed during catalysis. For example, copper molecular species were shown to evolve into nanoparticles under CO₂-reducing catalytic conditions. When the original molecular complex used was based on a phthalocyanine ligand, the Cu clusters were shown to revert to their original structure after catalysis, as shown by *in situ* X-ray absorption spectroscopy [45]. Indeed, both the Cu K-edge XANES and EXAFS features showed an evolution from a molecular species to a metallic one (edge position shift and appearance of metal–metal interactions) upon application of cathodic potentials. These changes were reversible upon the application of anodic potentials. It should be noted that a fraction of the initial metal amount was not recovered eventually (as seen by the fluorescence raw signal), indicating a partial dissolution/decomposition of the copper ions. This unexpected behavior has been observed in a few other cases [46,47] has been the matter of debates [48,49], but in all instances, it shows that the stability of CO₂RR molecular

systems needs to be carefully monitored for each specific case. Perspective articles were recently published by Rooney et al. [50] and Creissen et al. [51], describing how the degradation/restructuring of molecular catalysts should be carefully monitored under operating conditions, and how X-ray spectroscopy is an ideal tool for this purpose.

Apart from these critical stability issues, many questions still need to be answered on the local and electronic structure of the intermediates involved, mostly because of a lack of detailed spectroscopic information on the local and electronic structure of the reduced forms of these molecular species. Although it was not performed under conditions directly relevant to catalysis, the study of Römelt et al. on the electronic structure of reduced forms of Fe tetraphenyl porphyrin in the solid state by Fe K-edge XANES is a first and important step in this direction [52].

Metal/nitrogen-doped carbon hybrid materials

A class of materials that has emerged in the last decade is metal/nitrogen doped carbon (MNC), which lies somewhere between materials and molecules. These systems are usually obtained by calcination of a matrix containing both metallic salts and organic components, yielding a graphitic-like material with nitrogen-substituted coordination pockets that are filled with metallic ions [53]. The coordination sites are very heterogeneous, with a combination of pyrrolic and pyridinic nitrogen sites that can form cavities with 2–6 potential ligands and the presence of metallic clusters or nanoparticles is very difficult to rule out [54,55]. Similarly to the molecular species described above, it was shown (using X-ray absorption spectroscopy) that, in some cases, their structure is reversibly going from a molecular-like species to metallic nanoparticles under applied potential [55]. These nanoparticles would recover their starting molecular structure when the potential is left at open circuit potential or left at air. This behavior once again raises the question of the actual active sites and stresses the importance of *operando* measurements to obtain a mechanistic understanding. One study, however, showed that the number of coordination sites around a cobalt ion could regulate the selectivity towards CO [56], giving credit to a purely molecular (*i.e.* free of nanoclusters) behavior of MNCs.

Although XAS proved very useful in determining the presence or absence of metallic clusters under applied potential, it has not allowed yet to determine the structure of the species that are present under catalytic conditions. Besides their tendency to evolve into metallic clusters, MNCs are heterogeneous material in nature with a variety of coordination sites, geometries and nuclearities, which can hardly be disentangled with XAS [57]. Unless a rationale is found for the synthesis and stability of MNCs

and their structure are properly described (and XAS can help for that), the mechanism by which these materials are able to reduce CO₂ will not be understood.

Perspective: probing non-electroactive species in CO₂-reducing electrocatalysis with *in situ/operando* X-ray spectroscopies

As briefly described in the introduction, the role of the solvent, the electrolytes (cations and anions) as well as other non-electroactive components can be critical in the efficiency and selectivity of the CO₂RR [13]. These species are essentially composed of light elements (C, N, O, Li, K, Na, Mg, Ca), with the exception of heavy alkali (Rb and Cs) and alkali-earth (Sr and Ba). The reactant (CO₂) and products (which can in turn become reactants in cascade reactions) are also composed of light elements only. Probing these elements can provide critical information on their oxidation state, geometry, or binding mode and their implication in non-covalent bonds. The next paragraphs are dedicated to describing advanced X-ray techniques [58,59] that can be used to probe light elements under electrocatalytic conditions.

Tender X-rays XANES

The definition of the tender X-ray range is far from being accurate. It could be summarized as “too high for a soft X-ray beamline and too low for a hard X-ray beamline”, *i.e.* from 1000 to 4000 eV. Which essentially means that it is not easily accessible and that only a few beamlines are specifically optimized for it. Alkali metals and alkali earth metals can have a drastic effect on the efficiency and selectivity of the CO₂RR, which makes it worth studying their structure. The XANES and EXAFS spectra at the K-edge of several of these elements (Na, K, Mg, Ca) can be collected at tender X-ray beamlines, while those of others (Rb, Cs, Sr, Ba) can be obtained at hard X-rays beamlines. The L-edges of the high Z (Rb, Cs, Sr, Ba) elements can also be collected at tender X-ray beamlines. These data can provide information on the geometry of these elements under operating conditions, their ligands, coordination number, and first and second shell neighbors. Such information can help determine the actual role of these ions, whether they act as Lewis acids, as structural templates or as docking stations for reactants (reactant, solvent, or other electrolytes). As an example, the role of cations (in particular calcium) in natural [60] and artificial [61] water oxidizing systems was largely determined with the help of X-ray absorption spectroscopy in the tender X-ray range. The application of tender XAS to CO₂RR under operating conditions is, however, not trivial. The penetration depth is indeed too high (from a few μm at 1000 eV to *ca.* 100 μm at 4000 eV in water) to probe only the electrocatalytic material in the case of a heterogeneous system. The contribution of interfacial

vs. bulk cations would therefore be very difficult, unless grazing incidence [62] or microfluidic electrochemical cells [63] are used.

Soft X-rays XANES

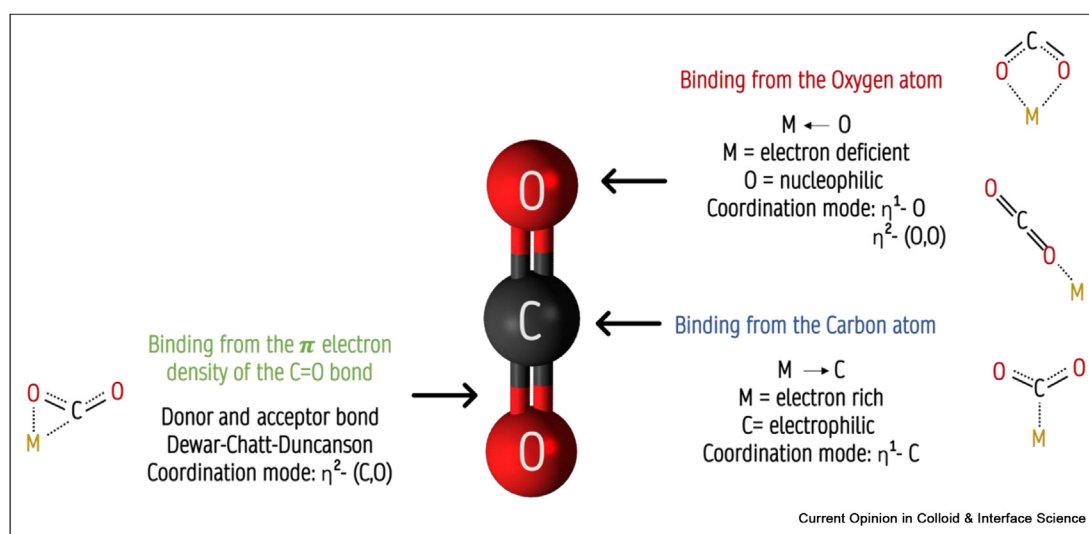
X-ray absorption spectroscopy in the soft X-ray range is the primary tool to study light elements, whose K-edge ionization energy lies approximately between 200 and 1000 eV. As far as CO₂ reduction is concerned, the main elements of interest, *i.e.* carbon and oxygen, have their K-edges at 284 and 543 eV. At these energies, the penetration depth of X-rays is very low, with an attenuation length of *ca* 100 nm (at 284 eV) and 250 nm (at 543 eV) in silicon nitride (Si₃N₄), a material that is very often used as a vacuum compatible membrane for liquid or electrochemical cells in the soft X-ray energy range. In a solvent with a density of 1, these numbers increase slightly but never go above the micron. This is a drawback when it comes to designing and operating *in situ* electrochemical cells but becomes an advantage when considering the volume of sample probed. Indeed, a thin film of electrocatalytic material deposited on an electrode will contribute to a much larger extent to the signal than the bulk of the solution. By subtracting or comparing the blank signal of a solvent/electrolyte component with the signal of an electrocatalytic component under *in situ* conditions, it is possible to extract the contribution of light components (*e.g.* solvent, electrolyte, CO₂ or its reduction products) in contact with the catalyst. This procedure is nevertheless tedious and requires spectroelectrochemical cells specifically designed for the soft X-rays energy range, which implies compatibility to vacuum and a very thin membrane/electrode assembly to allow X-rays to penetrate.

Such cells exist [64–66] but, as far as we know, have only been used once for the study of the CO₂ reduction reaction under operating conditions [67]. The conditions used for such measurements are, however, quite far from potential applications, since they require the use of a very thin (5–50 nm) conductive layer of noble metals (typically Au) to provide conductivity to the X-ray transparent window.

The ability to probe the oxidation state of carbon under catalytic conditions is a very powerful tool that should provide very valuable information concerning the CO₂ reduction reaction. Indeed, the C K-edge signals of CO₂, CO and more reduced forms of carbon are very distinctive. This technique could therefore be used to probe the presence of specific adsorbed species such as M-CO. There are several hypotheses as to the binding mode of CO₂ on catalytic sites prior to its reduction [68,69], with terminal, bridging, C-bound or O-bound configurations and several combinations of these modes (see Figure 2).

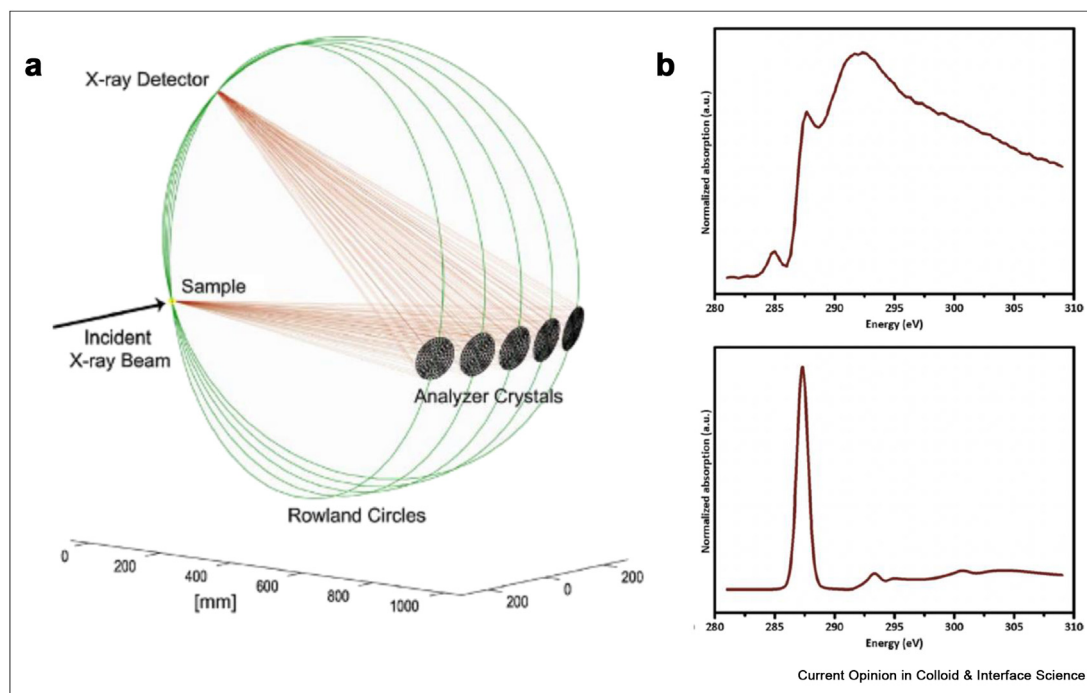
A combination of XAS data at the carbon and oxygen K-edges collected under *in situ* conditions should provide the information required to discriminate between these species. For example, Yan *et al.* studied the adsorption of CO₂ on CeO₂ with C K-edge XANES and identified two different adsorbates, *i.e.* CO₃²⁻ and CO₂ depending on the nature of the surface [70]. Another study used C K-edge XANES to show that CO binds much more strongly on nanostructured Au than on its flat counterparts [71]. In a somewhat opposite concern to the CO₂ reduction reaction, Knop-Gericke and collaborators studied the oxidation of methanol on copper with *in situ*

Figure 2



Different possible binding modes of CO₂ on a single metal site.

Figure 3



(a) Multi-crystal analyzer setup for X-ray emission and X-ray Raman spectroscopies. Reprinted from Ref. [59]. Copyright (2009), with permission from Elsevier. (b) Carbon K-edge XANES spectra collected with X-ray Raman on a carbon-containing wax (SX-100) used for Fischer–Tropsch catalysis (top) and on carbon monoxide (bottom). Reprinted with permission from Ref. [76]. Copyright 2021 American Chemical Society.

soft x-ray spectroscopy [72]. Thanks to the large energy difference observed for carbon species (see Figure 3b for a similar example), it was possible to deconvolute the spectra obtained *in situ* and quantify each component. Measurements at the O K-edge have never been performed on CO₂-reducing systems but could prove useful to determine the presence of oxide phases in metallic catalysts and their potential role in catalysis.

Another significant advantage of the soft X-ray range is that it also allows probing the L-edges of transition metals used as catalysts, which contains a wealth of information on their structure. This possibility has been used by De Luna et al. to study the structural and morphological evolution of a copper-based CO₂-reducing electrocatalyst [67].

X-ray Raman

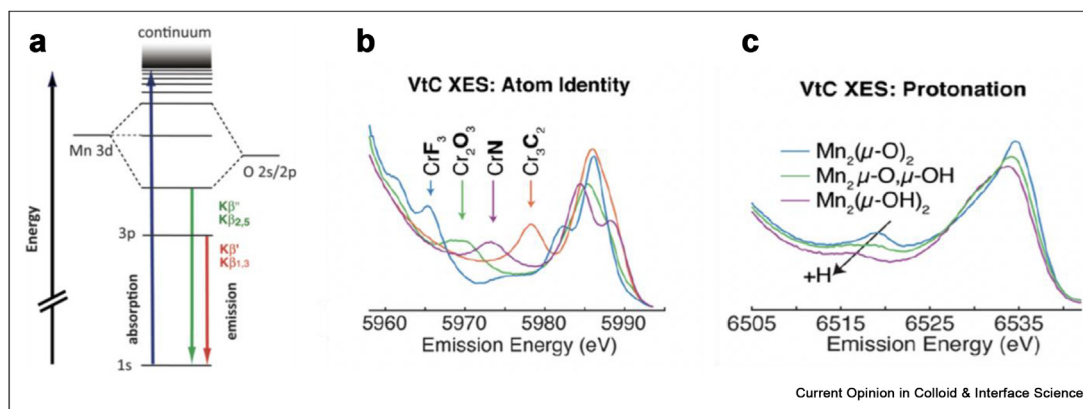
Another X-ray technique that can probe light elements while avoiding the experimental constraints imposed by soft X-rays is X-ray Raman Scattering (XRS) [73]. This method uses hard X-ray photons that interact with the sample and are collected after losing an amount of energy corresponding to the light element of interest. It requires a spectrometer (see Figure 3a) that can collect a large fraction of the solid angle around the sample, since the amount of photons emitted through this process is very

low. It has been used to probe light elements embedded into complex matrices involving higher elements, such as glasses [74], tissues [75] or catalysts [76].

Because of the high penetration depth of the hard X-rays used, it is very appropriate for *in situ* experiments in which experimental conditions cannot be adapted to the vacuum environment required for soft X-rays. This type of experiments have been used by Moya-Cancino et al. to determine the nature of carbon (both as a support, a reactant and a ligand) in Fischer–Tropsch catalysts under operating conditions [76]. Interestingly, these authors used XRS to probe the L_{3,2}-edges of cobalt as well, demonstrating the formation of a carburized cobalt species under operating conditions. XRS could therefore be very useful to track the fate of carbon or oxygen (contained in reactants, products or other components of the reaction) in the electrocatalytic reduction of CO₂, under conditions that are closer to the potential application than those used for soft X-rays experiments.

It should, however, be noted that XRS is a poorly efficient spectroscopic process, thus requiring high catalyst loading and/or measurement times. Notwithstanding the advantages of the experiments mentioned above, they remain challenging and require a significant instrumental and methodological expertise.

Figure 4



(a) Simplified scheme representing the X-ray absorption and X-ray emission processes in the case of manganese. Reprinted with permission from Ref. [80]. Copyright 2013 American Chemical Society (b) X-ray emission V2C spectra of a series of chromium complexes with different types of ligands. Reprinted from Ref. [81] licensed under Creative Commons BY 4.0. (c) X-ray emission V2C spectra of a series of [Mn(salpn)₂O₂H_x] (x = 0–2) complexes with different protonation states for the bridging oxygens. Reprinted from Ref. [81] licensed under Creative Commons BY 4.0.

Valence-to-Core X-ray emission

X-ray emission spectroscopy is another technique based on inelastic X-ray scattering and requires an instrumentation similar to XRS (see Figure 3a). Multiple analyzer crystals located on the so-called Rowland circle are aligned to collect the fluorescence photons emitted from the sample with a high energy resolution [58]. The resolution obtained of the spectra obtained (*ca.* 1 eV) allows differentiating the different recombination processes that occur during the fluorescence phenomenon. One of these processes corresponds to the recombination of valence electrons (3*d* in the case of a first row transition metal) into the core hole (1*s*) orbitals, the so-called valence-to-core (V2C) emission process [77]. A specific feature of the V2C emission spectra is the so-called crossover peak, located at a lower energy than the main feature. While the main feature corresponds to the recombination of electrons located in the 3*d* block, the crossover peak corresponds to the recombination of electrons located in the *ligand's* orbitals into the core hole of the metal excited. As such, it is a direct probe of the nature, the valence and protonation state of the ligands *that are bound to the metal* (see Figure 4b,c) [78]. Unlike soft X-ray XANES or XRS, this technique provides information on light elements that are directly bound to the element probed, hence avoiding the contribution of these elements that are not in contact with the metal involved in catalysis. It has proved extremely powerful in determining the nature or protonation state of ligands in bioinorganic [79] or biomimetic [80] active sites.

As for XRS, V2C XES is very appropriate for *in situ* experiments applied to catalysis [81], since it is based on

hard X-ray photons for both excitation and fluorescence processes. As far as we know, this technique has only been applied once to understand the structure of a CO₂-reducing catalyst, although not under catalytic conditions [82]. With a combination of V2C XES and theoretical calculations, Sun *et al.* managed to identify H₂O/OH ligands bound to a nitrogen-doped carbon material with iron sites. This type of information obtained under operating conditions would help decipher the binding mode of CO₂ and related species to catalytic sites and understand the structure of critical intermediates.

Conclusion

We have given an overview of the current situation of *in situ/operando* X-ray spectroscopy techniques applied to the electrocatalytic reduction of CO₂. The large majority of the studies performed so far focus their attention on the fate of the catalytic centers involved, which are essentially transition metals. There is an increasing interest in the influence that non-electroactive components such as the solvent, electrolytes or reactants can have on the efficiency and product selectivity of the CO₂RR [9,13]. These effects have not been studied so far with X-ray spectroscopy, although a lot of information could be extracted from it. We therefore provided a perspective on potential evolutions of this field and described a few X-ray techniques that are either well established or still developing and can be used to extract information specifically from non-electroactive species. This type of information is complementary to those that are typically collected on electrocatalysts and can shed new light on the parameters that influence the efficiency and product distribution of the electrochemical CO₂ reduction reaction.

Declaration of competing interest

The authors declare that they have no known competing financial interests or personal relationships that could have appeared to influence the work reported in this paper.

Data availability

No data was used for the research described in the article.

Acknowledgements

The Agence Nationale de la Recherche is acknowledged for a starting grant to BLK and STD (n°18-CE05-0007) and a Michem/synchrotron SOLEIL LABEX doctoral fellowship to DM.

References

Papers of particular interest, published within the period of review, have been highlighted as:

* of special interest

** of outstanding interest

- Cheon J, Yang JY, Koper M, Ishitani O: **From pollutant to chemical feedstock: valorizing carbon dioxide through photo- and electrochemical processes.** *Acc Chem Res* 2022, **55**:931–932, <https://doi.org/10.1021/acs.accounts.2c00129>.
- Hori Y, Kikuchi K, Murata A, Suzuki S: **Production of methane and ethylene in electrochemical reduction of carbon-dioxide at copper electrode in aqueous hydrogenocarbonate solution.** *Chem Lett* 1986:897–898, <https://doi.org/10.1246/cl.1986.897>.
- Xu H, Rebollar D, He H, Chong L, Liu Y, Liu C, Sun C-J, Li T, Muntean V. J, Winans RE, Liu D-J, Xu T: **Highly selective electrocatalytic CO(2)reduction to ethanol by metallic clusters dynamically formed from atomically dispersed copper.** *Nat Energy* 2020, **5**:623–632, <https://doi.org/10.1038/s41560-020-0666-x>.
- Ren S, Joulie D, Salvatore D, Torbensen K, Wang M, Robert M, Berlinguette CP: **Molecular electrocatalysts can mediate fast, selective CO2 reduction in a flow cell.** *Science* 2019, **365**:367+, <https://doi.org/10.1126/science.aax4608>.
- Ding P, Zhao H, Li T, Luo Y, Fan G, Chen G, Gao S, Shi X, Lu S, Sun X: **Metal-based electrocatalytic conversion of CO2 to formic acid/formate.** *J Mater Chem A* 2020, **8**:21947–21960, <https://doi.org/10.1039/d0ta08393c>.
- Timoshenko J, Cuenya BR: **In situ/operando electrocatalyst characterization by X-ray absorption spectroscopy.** *Chem Rev* 2021, **121**:882–961, <https://doi.org/10.1021/acs.chemrev.0c00396>.
This paper is an extensive review of all the X-ray absorption spectroscopic studies applied to electrocatalytic reactions, including CO₂ reduction.
- Kosugi K, Kondo M, Masaoka S: **Quick and easy method to dramatically improve the electrochemical CO2 reduction activity of an iron porphyrin complex.** *Angew Chem Int Ed* 2021, **60**:22070–22074, <https://doi.org/10.1002/anie.202110190>.
- Pan B, Wang Y, Li Y: **Understanding and leveraging the effect of cations in the electrical double layer for electrochemical CO2 reduction.** *Chem Catal* 2022, **2**:1267–1276, <https://doi.org/10.1016/j.checat.2022.03.012>.
- Marcandalli G, Monteiro MCO, Goyal A, Koper MTM: **Electrolyte effects on CO2 electrochemical reduction to CO.** *Acc Chem Res* 2022, **55**:1900–1911, <https://doi.org/10.1021/acs.accounts.2c00080>.
This article reviews the work done by the group of Koper on the effects that electrolytes (including cations, anions and acids) can have on the rate and selectivity of the CO₂RR.
- Malkani AS, Anibal J, Xu B: **Cation effect on interfacial CO2 concentration in the electrochemical CO2 reduction reaction.** *ACS Catal* 2020, **10**:14871–14876, <https://doi.org/10.1021/acscatal.0c03553>.
This paper uses *in situ* IR spectroscopy to show how the nature and concentration of cations can influence the efficiency of the CO₂RR.
- Aran-Ais RM, Gao D, Roldan Cuenya B: **Structure- and electrolyte-sensitivity in CO2 electroreduction.** *Acc Chem Res* 2018, **51**:2906–2917, <https://doi.org/10.1021/acs.accounts.8b00360>.
- Monteiro MCO, Dattila F, Lopez N, Koper MTM: **The role of cation acidity on the competition between hydrogen evolution and CO2 reduction on gold electrodes.** *J Am Chem Soc* 2022, **144**:1589–1602, <https://doi.org/10.1021/jacs.1c10171>.
- Deng B, Huang M, Zhao X, Mou S, Dong F: **Interfacial electrolyte effects on electrocatalytic CO2 reduction.** *ACS Catal* 2022, **12**:331–362, <https://doi.org/10.1021/acscatal.1c03501>.
This review article gathers work that the studied the effects of electrolytes and the electrode–electrolyte interface and the subsequent efficiency of the CO₂RR.
- Kerr V. B, King HJ, Garibello CF, Dissanayake PR, Simonov AN, Johannessen B, Eldridge DS, Hocking RK: **Characterization of energy materials with X-ray absorption spectroscopy—advantages, challenges, and opportunities.** *Energy Fuels* 2022, **36**:2369–2389, <https://doi.org/10.1021/acs.energyfuels.1c04072>.
- Jin L, Seifitokaldani A: **In situ spectroscopic methods for electrocatalytic CO2 reduction.** *Catalysts* 2020, **10**, <https://doi.org/10.3390/catal10050481>.
- Hori Y, Kikuchi K, Suzuki S: **Production of CO and CH4 in electrochemical reduction of CO2 at metal-electrodes in aqueous hydrogenocarbonate solution.** *Chem Lett* 1985: 1695–1698, <https://doi.org/10.1246/cl.1985.1695>.
- Jeon HS, Sinev I, Scholten F, Divins NJ, Zegkinoglou I, Pielsticker L, Roldan Cuenya B: **Operando evolution of the structure and oxidation state of size-controlled Zn nanoparticles during CO2 electroreduction.** *J Am Chem Soc* 2018, **140**:9383–9386, <https://doi.org/10.1021/jacs.8b05258>.
- Zhang XY, Li WJ, Chen J, Wu XF, Liu YW, Mao F, Yuan HY, Zhu M, Dai S, Wang HF, Hu P, Sun C, Liu PF, Yang HG: **In operando identification of in situ formed metalloid Zincδ+ active sites for highly efficient electrocatalyzed carbon dioxide reduction.** *Angew Chem Int Ed* 2022, **61**, e202202298, <https://doi.org/10.1002/anie.202202298>.
- Nitopi S, Bertheussen E, Scott SB, Liu X, Engstfeld AK, Horch S, Seger B, Stephens IEL, Chan K, Hahn C, Nørskov JK, Jaramillo TF, Chorkendorff I: **Progress and perspectives of electrochemical CO2 reduction on copper in aqueous electrolyte.** *Chem Rev* 2019, **119**:7610–7672, <https://doi.org/10.1021/acs.chemrev.8b00705>.
This exhaustive review gives a picture of the current status of the work done on the CO₂RR on copper in aqueous electrolyte within the last fifty years.
- Lee SH, Lin JC, Farmand M, Landers AT, Feaster JT, Acosta JEA, Beeman JW, Ye Y, Yano J, Mehta A, Davis RC, Jaramillo TF, Hahn C, Drisdell WS: **Oxidation state and surface reconstruction of Cu under CO2 reduction conditions from in situ X-ray characterization.** *J Am Chem Soc* 2021, **143**: 588–592, <https://doi.org/10.1021/jacs.0c10017>.
- Timoshenko J, Jeon HS, Sinev I, Haase FT, Herzog A, Roldan Cuenya B: **Linking the evolution of catalytic properties and structural changes in copper-zinc nanocatalysts using operando EXAFS and neural-networks.** *Chem Sci* 2020, **11**: 3727–3736, <https://doi.org/10.1039/d0sc00382d>.
- Vavra J, Shen T-H, Stoian D, Tileli V, Buonsanti R: **Real-time monitoring reveals dissolution/redeposition mechanism in copper nanocatalysts during the initial stages of the CO2 reduction reaction.** *Angew Chem Int Ed* 2021, **60**:1347–1354, <https://doi.org/10.1002/anie.202011137>.
- Favaro M, Xiao H, Cheng T, Goddard W, Yano J, Crumlin E: **Subsurface oxide plays a critical role in CO2 activation by Cu(111) surfaces to form chemisorbed CO2, the first step in reduction of CO2.** *Proc Natl Acad Sci USA* 2017, **114**: 6706–6711, <https://doi.org/10.1073/pnas.1701405114>.

24. Permyakova AA, Herranz J, El Kazzi M, Diercks JS, Povia M, Mangani LR, Horisberger M, Patru A, Schmidt TJ: **On the oxidation state of Cu₂O upon electrochemical CO₂ reduction: an XPS study.** *ChemPhysChem* 2019, **20**:3120–3127, <https://doi.org/10.1002/cphc.201900468>.
25. Mistry H, Varela AS, Bonifacio CS, Zegkinoglou I, Sinev I, Choi Y-W, Kisslinger K, Stach EA, Yang JC, Strasser P, Cuenya BR: **Highly selective plasma-activated copper catalysts for carbon dioxide reduction to ethylene.** *Nat Commun* 2016, **7**, <https://doi.org/10.1038/ncomms12123>.
26. Ren D, Deng Y, Handoko AD, Chen CS, Malkhandi S, Yeo BS: **Selective electrochemical reduction of carbon dioxide to ethylene and ethanol on copper(I) oxide catalysts.** *ACS Catal* 2015, **5**:2814–2821, <https://doi.org/10.1021/cs502128q>.
27. Popovic S, Smiljanic M, Jovanovic P, Vavra J, Buonsanti R, Hodnik N: **Stability and degradation mechanisms of copper-based catalysts for electrochemical CO₂ reduction.** *Angew Chem Int Ed* 2020, **59**:14736–14746, <https://doi.org/10.1002/anie.202000617>.
- This paper reviews the current knowledge and theories about the restructuring of copper-based CO₂-reducing electrocatalysts, including with *operando* XAS.
28. Kaya S, Friebel D, Ogasawara H, Anniyev T, Nilsson A: **Electronic structure effects in catalysis probed by X-ray and electron spectroscopy.** *J Electron Spectrosc Relat Phenom* 2013, **190**:113–124, <https://doi.org/10.1016/j.elspec.2013.04.015>.
29. Francke R, Schille B, Roemelt M: **Homogeneously catalyzed electroreduction of carbon dioxide—methods, mechanisms, and catalysts.** *Chem Rev* 2018, **118**:4631–4701, <https://doi.org/10.1021/acs.chemrev.7b00459>.
30. Boutin E, Merakeb L, Ma B, Boudy B, Wang M, Bonin J, Anxolabéhère-Mallart E, Robert M: **Molecular catalysis of CO₂ reduction: recent advances and perspectives in electrochemical and light-driven processes with selected Fe, Ni and Co aza macrocyclic and polypyridine complexes.** *Chem Soc Rev* 2020, **49**:5772–5809, <https://doi.org/10.1039/d0cs00218f>.
31. Sampson MD, Froehlich JD, Smieja JM, Benson EE, Sharp ID, Kubiak CP: **Direct observation of the reduction of carbon dioxide by rhenium bipyridine catalysts.** *Energy Environ Sci* 2013, **6**:3748–3755, <https://doi.org/10.1039/C3EE42186D>.
32. Bourrez M, Molton F, Chardon-Noblat S, Deronzier A: **{[Mn(bipyridyl)(CO)(3)Br]}: an abundant metal carbonyl complex as efficient electrocatalyst for CO₂ reduction.** *Angew Chem Int Ed* 2011, **50**:9903–9906, <https://doi.org/10.1002/anie.201103616>.
33. Hawecker J, Lehn J, Ziessel R: **Electrocatalytic reduction of carbon-dioxide mediated by Re(bipy)(CO)3Cl(BIPY=2,2-Bipyridine).** *J Chem Soc, Chem Commun* 1984:328–330, <https://doi.org/10.1039/c39840000328>.
34. Beley M, Collin JP, Ruppert R, Sauvage JP: **Nickel(II) cyclam - an extremely selective electrocatalyst for reduction of CO₂ in water.** *J Chem Soc, Chem Commun* 1984:1315–1316, <https://doi.org/10.1039/c39840001315>.
35. Schneider J, Jia H, Kobiros K, Cabelli DE, Muckerman JT, Fujita E: **Nickel(II) macrocycles: highly efficient electrocatalysts for the selective reduction of CO₂ to CO.** *Energy Environ Sci* 2012, **5**:9502–9510, <https://doi.org/10.1039/C2EE22528J>.
36. Gotico P, Halime Z, Aukauloo A: **Recent advances in metalloporphyrin-based catalyst design towards carbon dioxide reduction: from bio-inspired second coordination sphere modifications to hierarchical architectures.** *Dalton Trans* 2020, **49**:2381–2396, <https://doi.org/10.1039/c9dt04709c>.
- This article reviews the different chemical structures of transition metal porphyrins that show catalytic activity towards CO₂ reduction under homogeneous conditions.
37. Kusuda K, Ishihara R, Yamaguchi H, Izumi I: **Electrochemical investigation of thin-films of cobalt phthalocyanine and cobalt-4,4',4''-tetracarboxyphthalocyanine and the reduction of carbon-monoxide, formic-acid and formaldehyde mediated by the co(I) complexes.** *Electrochim Acta* 1986, **31**: 657–663, [https://doi.org/10.1016/0013-4686\(86\)87032-3](https://doi.org/10.1016/0013-4686(86)87032-3).
38. Costentin C, Robert M, Saveant J-M: **Current issues in molecular catalysis illustrated by iron porphyrins as catalysts of the CO₂-to-CO electrochemical conversion.** *Acc Chem Res* 2015, **48**:2996–3006, <https://doi.org/10.1021/acs.accounts.5b00262>.
39. Corbin N, Zeng J, Williams K, Manthiram K: **Heterogeneous molecular catalysts for electrocatalytic CO₂ reduction.** *Nano Res* 2019, **12**:2093–2125, <https://doi.org/10.1007/s12274-019-2403-y>.
- This paper reviews the recent work where molecular systems for the CO₂RR have been heterogenized to improve applicability.
40. Wang M, Torbensen K, Salvatore D, Ren S, Joulie D, Dumoulin F, Mendoza D, Lassalle-Kaiser B, Isci U, Berlinguette CP, Robert M: **CO₂ electrochemical catalytic reduction with a highly active cobalt phthalocyanine.** *Nat Commun* 2019, **10**, <https://doi.org/10.1038/s41467-019-11542-w>.
41. Zhang X, Wang Y, Gu M, Wang M, Zhang Z, Pan W, Jiang Z, Zheng H, Lucero M, Wang H, Sterbinsky GE, Ma Q, Wang Y-G, Feng Z, Li J, Dai H, Liang Y: **Molecular engineering of dispersed nickel phthalocyanines on carbon nanotubes for selective CO₂ reduction.** *Nat Energy* 2020, **5**:684–692, <https://doi.org/10.1038/s41560-020-0667-9>.
42. Liu Y, Deb A, Leung KY, Nie W, Dean WS, Penner-Hahn JE, McCrory CCL: **Determining the coordination environment and electronic structure of polymer-encapsulated cobalt phthalocyanine under electrocatalytic CO₂ reduction conditions using in situ X-Ray absorption spectroscopy.** *Dalton Trans* 2020, **49**:16329–16339, <https://doi.org/10.1039/d0dt01288b>.
43. Lu X, Ahsaine HA, Dereli B, Garcia-Esparza AT, Reinhard M, Shinagawa T, Li D, Adil K, Tchalala MR, Kroll T, Eddaoudi M, Sokaras D, Cavallo L, Takanabe K: **Operando elucidation on the working state of immobilized fluorinated iron porphyrin for selective aqueous electroreduction of CO₂ to CO.** *ACS Catal* 2021, **11**:6499–6509, <https://doi.org/10.1021/acscatal.1c01157>.
44. Boutin E, Wang M, Lin JC, Mesnage M, Mendoza D, Lassalle-Kaiser B, Hahn C, Jaramillo TF, Robert M: **Aqueous electrochemical reduction of carbon dioxide and carbon monoxide into methanol with cobalt phthalocyanine.** *Angew Chem Int Ed* 2019, **58**, <https://doi.org/10.1002/anie.201909257>.
45. Weng Z, Wu Y, Wang M, Jiang J, Yang K, Huo S, Wang X-F, Ma Q, Brudvig GW, Batista VS, Liang Y, Feng Z, Wang H: **Active sites of copper-complex catalytic materials for electrochemical carbon dioxide reduction.** *Nat Commun* 2018, **9**, <https://doi.org/10.1038/s41467-018-02819-7>.
46. Karapinar D, Zitolo A, Huan TN, Zanna S, Taverna D, Galvao Tizei LH, Giaume D, Marcus P, Mougél V, Fontecave M: **Carbon-nanotube-supported copper polyphthalocyanine for efficient and selective electrocatalytic CO₂ reduction to CO.** *ChemSusChem* 2020, **13**:173–179, <https://doi.org/10.1002/cssc.201902859>.
47. Cai Y, Fu J, Zhou Y, Chang Y-C, Min Q, Zhu J-J, Lin Y, Zhu W: **Insights on forming N,O-coordinated Cu single-atom catalysts for electrochemical reduction CO₂ to methane.** *Nat Commun* 2021, **12**, <https://doi.org/10.1038/s41467-020-20769-x>.
48. Boutin E, Salamé A, Robert M: **Confined molecular catalysts provide an alternative interpretation to the electrochemically reversible demetallation of copper complexes.** *Nat Commun* 2022, **13**:4190, <https://doi.org/10.1038/s41467-022-31661-1>.
49. Weng Z, Wu Y, Wang M, Brudvig GW, Batista VS, Liang Y, Feng Z, Wang H: **Reply To: confined molecular catalysts provide an alternative interpretation to the electrochemically reversible demetallation of copper complexes.** *Nat Commun* 2022, **13**:4191, <https://doi.org/10.1038/s41467-022-31662-0>.
50. * C.L. Rooney, Y. Wu, D.J. Gallagher, H. Wang, Restructuring and integrity of molecular catalysts in electrochemical CO₂ reduction, *Nat. Sci.* n/a (n.d.) e20210628. <https://doi.org/10.1002/ntls.20210628>. This article stresses the importance of using X-ray absorption spectroscopy to monitor the presence of nanoclusters when using molecular or MNC catalysts for the CO₂RR.
51. Creissen CE, Fontecave M: **Keeping sight of copper in single-atom catalysts for electrochemical carbon dioxide reduction.**

Nat Commun 2022, **13**:2280, <https://doi.org/10.1038/s41467-022-30027-x>.

This article discusses a few examples of molecular and MNC CO₂RR catalysts which presented a reversible formation of nanoclusters under applied potential and stresses the importance of operando characterisation, including using X-ray spectroscopy.

52. Romelt C, Song J, Tarrago M, Rees JA, van Gastel M, Weyhermueller T, DeBeer S, Bill E, Neese F, Ye S: **Electronic structure of a formal iron(0) porphyrin complex relevant to CO₂ reduction.** *Inorg Chem* 2017, **56**:4745–4750, <https://doi.org/10.1021/acs.inorgchem.7b00401>.
53. Sofia Varela A, Ju W, Bagger A, Franco P, Rossmeisl J, Strasser P: **Electrochemical reduction of CO₂ on metal-nitrogen-doped carbon catalysts.** *ACS Catal* 2019, **9**: 7270–7284, <https://doi.org/10.1021/acscatal.9b01405>.
54. Huan TN, Ranjbar N, Rousse G, Sougrati M, Zitolo A, Mougél V, Jaouen F, Fontecave M: **Electrochemical reduction of CO₂ catalyzed by Fe-N-C materials: a structure-selectivity study.** *ACS Catal* 2017, **7**:1520–1525, <https://doi.org/10.1021/acscatal.6b03353>.
55. Karapinar D, Huan NT, Sahraie NR, Li J, Wakerley D, Touati N, Zanna S, Taverna D, Tizei LHG, Zitolo A, Jaouen F, Mougél V, Fontecave M: **Electroreduction of CO₂ on single-site copper-nitrogen-doped carbon material: selective formation of ethanol and reversible reconstruction of the metal sites.** *Angew Chem Int Ed* 2019, **58**:15098–15103, <https://doi.org/10.1002/anie.201907994>.
56. Wang X, Chen Z, Zhao X, Yao T, Chen W, You R, Zhao C, Wu G, Wang J, Huang W, Yang J, Hong X, Wei S, Wu Y, Li Y: **Regulation of coordination number over single Co sites: triggering the efficient electroreduction of CO₂.** *Angew Chem Int Ed* 2018, **57**:1944–1948, <https://doi.org/10.1002/anie.201712451>.
57. Zhang J, Cai W, Hu FX, Yang H, Liu B: **Recent advances in single atom catalysts for the electrochemical carbon dioxide reduction reaction.** *Chem Sci* 2021, **12**:6800–6819, <https://doi.org/10.1039/D1SC01375K>.
58. Glatzel P, Bergmann U: **High resolution 1s core hole X-ray spectroscopy in 3d transition metal complexes - electronic and structural information.** *Coord Chem Rev* 2005, **249**:65–95, <https://doi.org/10.1016/j.ccr.2004.04.011>.
59. Glatzel P, Sikora M, Smolentsev G, Fernandez-Garcia M: **Hard X-ray photon-in photon-out spectroscopy.** *Catal Today* 2009, **145**:294–299, <https://doi.org/10.1016/j.cattod.2008.10.049>.
60. Yachandra VK, Yano J: **Calcium in the oxygen-evolving complex: structural and mechanistic role determined by X-ray spectroscopy.** *J Photochem Photobiol B Biol* 2011, **104**:51–59, <https://doi.org/10.1016/j.jphotobiol.2011.02.019>.
61. Risch M, Klingan K, Ringleb F, Chernev P, Zaharieva I, Fischer A, Dau H: **Water oxidation by electrodeposited cobalt oxides. Role of anions and redox-inert cations in structure and function of the amorphous catalyst.** *ChemSusChem* 2012, **5**: 542–549, <https://doi.org/10.1002/cssc.201100574>.
62. Farmand M, Landers AT, Lin JC, Feaster JT, Beeman JW, Ye Y, Clark EL, Higgins D, Yano J, Davis RC, Mehta A, Jaramillo TF, Hahn C, Drisdell WS: **Electrochemical flow cell enabling operando probing of electrocatalyst surfaces by X-ray spectroscopy and diffraction.** *Phys Chem Chem Phys* 2019, **21**: 5402–5408, <https://doi.org/10.1039/c8cp07423b>.
63. Kwon G, Cho Y-H, Kim K-B, Emery JD, Kim IS, Zhang X, Martinson ABF, Tiede DM: **Microfluidic electrochemical cell for in situ structural characterization of amorphous thin-film catalysts using high-energy X-ray scattering.** *J Synchrotron Radiat* 2019, **26**:1600–1611, <https://doi.org/10.1107/S1600577519007240>.
64. Jiang P, Chen J-L, Borondics F, Glans P-A, West MW, Chang C-L, Salmeron M, Guo J: **In situ soft X-ray absorption spectroscopy investigation of electrochemical corrosion of copper in aqueous NaHCO₃ solution.** *Electrochem Commun* 2010, **12**: 820–822, <https://doi.org/10.1016/j.elecom.2010.03.042>.
65. Nagasaka M, Yuzawa H, Horigome T, Kosugi N: **In operando observation system for electrochemical reaction by soft X-ray absorption spectroscopy with potential modulation method.** *Rev Sci Instrum* 2014, **85**, <https://doi.org/10.1063/1.4898054>.
66. M.F. Tesch, S.A. Bonke, R. Golnak, J. Xiao, A.N. Simonov, R. Schlögl, Vacuum compatible flow-cell for high-quality in situ and operando soft X-ray photon-in–photon-out spectroelectrochemical studies of energy materials, *Electrochem. Sci. Adv.* n/a (n.d.) e2100141. <https://doi.org/10.1002/elsa.202100141>.
67. De Luna P, Quintero-Bermudez R, Dinh C-T, Ross MB, Bushuyev OS, Todorović P, Regier T, Kelley SO, Yang P, Sargent EH: **Catalyst electro-redeposition controls morphology and oxidation state for selective carbon dioxide reduction.** *Nat. Catal.* 2018, **1**:103–110, <https://doi.org/10.1038/s41929-017-0018-9>.
68. Leitner W: **The coordination chemistry of carbon dioxide and its relevance for catalysis: a critical survey.** *Coord Chem Rev* 1996, **153**:257–284, [https://doi.org/10.1016/0010-8545\(95\)01226-5](https://doi.org/10.1016/0010-8545(95)01226-5).
69. Mascetti J: **Carbon dioxide coordination chemistry and reactivity of coordinated CO₂.** In *Carbon dioxide chem. Feedstock*. John Wiley & Sons; 2010:55–88, <https://doi.org/10.1002/9783527629916.ch4>.
70. Yang C, Bebensee F, Chen J, Yu X, Nefedov A, Woell C: **Carbon dioxide adsorption on CeO₂(110): an XPS and NEXAFS study.** *ChemPhysChem* 2017, **18**:1874–1880, <https://doi.org/10.1002/cphc.201700240>.
In this article, soft X-rays carbon K-edge NEXAFS is used to determine the fate of CO₂ adsorbed on a CeO₂ surface. They show that it is only physisorbed but does not react.
71. Hoffmann PM, Hrbek J, Ma S, Park JB, Rodriguez JA, Stacchiola DJ, Senanayake SD: **Enhancing the reactivity of gold: nanostructured Au(111) adsorbs CO.** *Surf Sci* 2016, **650**: 17–23, <https://doi.org/10.1016/j.susc.2015.11.021>.
72. Knop-Gericke A, Havecker M, Schedel-Niedrig T, Schlögl R: **High-pressure low-energy XAS: a new tool for probing reacting surfaces of heterogeneous catalysts.** *Top Catal* 2000, **10**:187–198, <https://doi.org/10.1023/A:1019101109313>.
73. Suzuki T: **X-ray Raman scattering. Experiment. I.** *J Phys Soc Jpn* 1967, **22**:1139, <https://doi.org/10.1143/JPSJ.22.1139>.
74. Petitgirard S, Sahle CJ, Malfait WJ, Spiekermann G, Blanchard I, Jennings ES, Cotte M, Murakami M: **Anomalous density, sound velocity, and structure of pressure-induced amorphous quartz.** *Phys Rev B* 2022, **105**, <https://doi.org/10.1103/PhysRevB.105.134106>.
75. Gueriau P, Rueff J-P, Bernard S, Kaddissy JA, Goler S, Sahle CJ, Sokaras D, Wogelius RA, Manning PL, Bergmann U, Bertrand L: **Noninvasive synchrotron-based X-ray Raman scattering discriminates carbonaceous compounds in ancient and historical materials.** *Anal Chem* 2017, **89**:10819–10826, <https://doi.org/10.1021/acs.analchem.7b02202>.
76. Moya-Cancino JG, Honkanen A-P, van der Eerden AMJ, Oord R, Monai M, ten Have I, Sahle CJ, Meirer F, Weckhuysen BM, de Groot FMF, Huotari S: **In situ X-ray Raman scattering spectroscopy of the formation of cobalt carbides in a Co/TiO₂ Fischer-Tropsch synthesis catalyst.** *ACS Catal* 2021, **11**: 809–819, <https://doi.org/10.1021/acscatal.0c04509>.
In this paper, X-Ray Raman is used to probe the evolution of a Fischer-Tropsch catalyst from the carbon point of view under operating conditions.
77. Gallo E, Glatzel P: **Valence to core X-ray emission spectroscopy.** *Adv Mater* 2014, **26**:7730–7746, <https://doi.org/10.1002/adma.201304994>.
78. Pollock CJ, DeBeer S: **Insights into the geometric and electronic structure of transition metal centers from valence-to-core X-ray emission spectroscopy.** *Acc Chem Res* 2015, **48**:2967–2975, <https://doi.org/10.1021/acs.accounts.5b00309>.
79. Lancaster KM, Roemelt M, Ettenhuber P, Hu Y, Ribbe MW, Neese F, Bergmann U, DeBeer S: **X-Ray emission spectroscopy evidences a central carbon in the nitrogenase iron-molybdenum cofactor.** *Science* 2011, **334**:974–977, <https://doi.org/10.1126/science.1206445>.

80. Lassalle-Kaiser B, Boron TT, Krewald V, Kern J, Beckwith MA, Delgado-Jaime MU, Schroeder H, Alonso-Mori R, Nordlund D, Weng T-C, Sokaras D, Neese F, Bergmann U, Yachandra VK, DeBeer S, Pecoraro VL, Yano J: **Experimental and computational X-ray emission spectroscopy as a direct probe of protonation states in oxo-bridged Mn(IV) dimers relevant to redox-active metalloproteins.** *Inorg Chem* 2013, **52**, <https://doi.org/10.1021/ic400821g>.
81. Cutsail III GE, DeBeer S: **Challenges and opportunities for applications of advanced X-ray spectroscopy in catalysis research.** *ACS Catal* 2022:5864–5886, <https://doi.org/10.1021/acscatal.2c01016>.

This perspective article describes the fundamentals of X-Ray Emission Spectroscopy and progresses made in its use for catalytic applications.

82. Sun X, Wang R, Ould-Chikh S, Osadchii D, Li G, Aguilar A, Hazemann J, Kapteijn F, Gascon J: **Structure-activity relationships in metal organic framework derived mesoporous nitrogen-doped carbon containing atomically dispersed iron sites for CO₂ electrochemical reduction.** *J Catal* 2019, **378**: 320–330, <https://doi.org/10.1016/j.jcat.2019.09.013>.

This is, to our knowledge, the first example of XES applied to CO₂RR, where the nature of the ligand of a catalyst is determined under *operando* conditions with V2C XES.

 Very Important Paper

In situ X-ray Absorption Spectroscopy in Homogeneous Conditions Reveals Interactions Between CO₂ and a Doubly and Triply Reduced Iron(III) Porphyrin, then Leading to Catalysis

Daniela Mendoza,^[a, b] Si-Thanh Dong,^[a] Nikolaos Kostopoulos,^[b] Victor Pinty,^[a] Orestes Rivada-Wheelaghan,^[b] Elodie Anxolabéhère-Mallart,^{*[b]} Marc Robert,^{*[b, c]} and Benedikt Lassalle-Kaiser^{*[a]}

In memory of Doris Lexa

Iron porphyrins are attractive catalysts for the electrochemical reduction of carbon dioxide (CO₂), owing to their high activity and selectivity while being tunable through ligand functionalization. Iron tetraphenyl porphyrin (FeTPP) is the simplest of them, and its catalytic behavior toward CO₂ has been studied for decades. Although kinetic information is available, spectroscopic signatures are lacking to describe intermediate species along the catalytic cycle. *In situ* UV-Visible and X-ray absorption near edge spectroscopy (XANES) were used to monitor the local and electronic structure of FeTPP homogeneously dissolved in

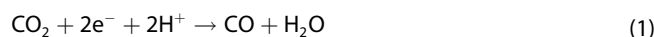
dimethyl formamide (DMF) under reductive potentials. The Fe(III) starting species was identified, together with its one, two and three electron-reduced counterparts under both argon and CO₂ atmospheres. Under argon, the second and third reductions lead to species with electronic density shared between the metal and the porphyrin backbone. In the presence of CO₂ and with a low amount of protons, the doubly and triply reduced species interact with CO₂ at the metallic site. In light of these results, an electronic structure for a key intermediate along the catalytic cycle of the CO₂-to-CO reduction is proposed.

Introduction

The massive use of fossil fuels to supply the global energy demand has increased the CO₂ atmospheric levels to alarming values, as recently presented by the Intergovernmental Panel on Climate Change (IPCC).^[1] Research has shown that CO₂ can be electrochemically reduced into carbon building blocks such as carbon monoxide (CO), which is the first and most critical step in the CO₂ upcycling process. Because of the high chemical stability of CO₂,^[2] the CO₂-to-CO conversion is energetically very costly, requiring the use of efficient catalysts to lower energetic barriers.

Several molecular catalyst families based on earth-abundant transition metals have been proposed as efficient CO₂-to-CO

reducing catalysts. They offer good catalytic activities, both in terms of efficiency and selectivity, and provide convenient platforms for molecular engineering.^[3–5] Among them, iron porphyrins, such as iron tetraphenyl porphyrin (FeTPP, Figure 1A), have been reported as a class of selective, stable, and efficient catalysts for the reduction of CO₂ into CO, both in aprotic solvents and water.^[6–12] Doris Lexa, together with Jean-Michel Savéant and their collaborators, pioneered the electrochemical study of iron porphyrins and their reduced counterparts as early as the '80s.^[6,13,14] Using cyclic voltammetry (CV), they showed that, in dimethyl formamide (DMF) and under inert conditions, FeTPP undergoes three consecutive reduction processes (see Figure 1B), which correspond to the reversible storage of three reducing equivalents. In the presence of CO₂, the third reduction process becomes irreversible and increases in intensity, which is due to the catalytic reduction of CO₂ into CO following Equation (1):



Despite numerous investigations of the CO₂-to-CO reaction mechanism *via* kinetic analysis,^[13–18] the exact nature and structure of the intermediate species involved still need to be deciphered. There is, however, no doubt that understanding the local and electronic structure of such intermediates is required to optimize their catalytic activity. In this regard, early work by Lexa and co-workers showed that the reactivity of the three-electron-reduced species of iron porphyrins is centered on the metal rather than on the ligand.^[19] These observations,

[a] Dr. D. Mendoza, S.-T. Dong, V. Pinty, Dr. B. Lassalle-Kaiser
Science Division
Synchrotron SOLEIL
L'Orme des Merisiers, Départementale 128
91190, Saint-Aubin (France)
E-mail: benedikt.lassalle@synchrotron-soleil.fr

[b] Dr. D. Mendoza, Dr. N. Kostopoulos, Dr. O. Rivada-Wheelaghan,
Dr. E. Anxolabéhère-Mallart, Prof. M. Robert
Université Paris Cité, CNRS
Laboratoire d'Electrochimie Moléculaire
F-75013 Paris (France)
E-mail: elodie.anxolabehere@u-paris.fr
robert@u-paris.fr

[c] Prof. M. Robert
Institut Universitaire de France (IUF)
F-75005 Paris, France

 Supporting information for this article is available on the WWW under <https://doi.org/10.1002/cctc.202201298>

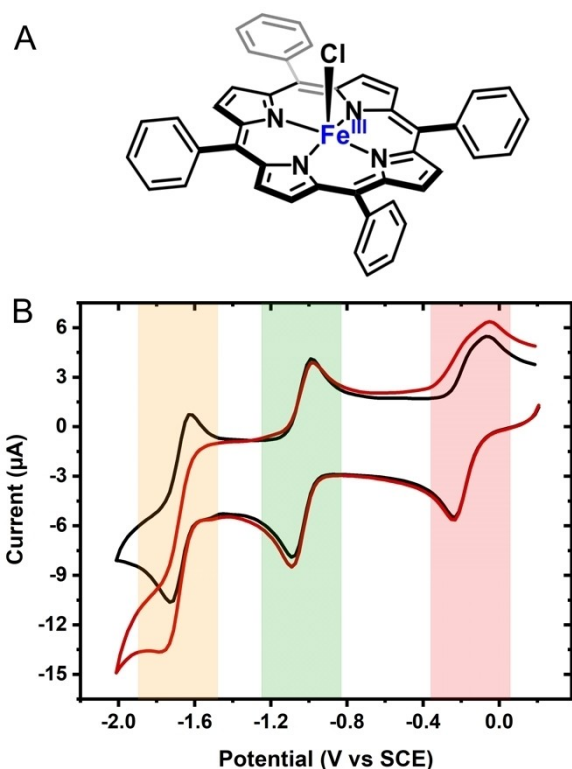


Figure 1. Structure (A) and cyclic voltammogram (B) of iron tetraphenyl porphyrin chloride [Fe^{III}TPP(Cl)] in DMF/TBAPF₆ (0.1 M) under Ar (black line) and CO₂ (red line). Colored areas indicate the first (red), second (green) and third (yellow) electron transfer processes. CVs were recorded in a conventional electrochemical cell at room temperature and a scan rate of $\nu = 100 \text{ mV s}^{-1}$.

associated with *in situ* UV-Vis, resonance Raman and EPR spectroelectrochemistry,^[20–22] led to the conclusion that the three-electron reduced species should be considered as an Fe(0) complex. More recently, Römel *et al.* proposed, on the basis of X-ray Absorption Near Edge Spectroscopy (XANES) performed on solid-state samples and Density Functional Theory (DFT) calculations, that the second and third electrons injected in [Fe^{III}TPP]⁺ are localized on the porphyrin ring rather than on the metal.^[23] They, therefore, formulated the two- and three-electron reduced species as [Fe^{II}TPP·][–] and [Fe^ITPP·]^{2–}.

As shown from this work and many others, XANES is an ideal tool to probe the local and electronic structure of transition metals.^[24–27] It provides information on the oxidation state (through the main edge position) and on the geometry and spin state (through the shape and position of the pre-edge) of the element being probed. In combination with electrochemical techniques, it allows for observing species that would otherwise be difficult to isolate. Such *in situ* measurements, however, require specific instrumentation to couple the two techniques. Up to now, spectroelectrochemical cells for X-ray spectroscopies were mostly developed for heterogeneous systems.^[28–32] Unfortunately, *in situ/operando* analysis on immobilized materials lacks precision when it comes to identifying intermediates. Indeed, the high catalyst loading leads to a

signal that can be dominated by inactive material rather than the active one.^[33] In addition, the electrochemical analysis of immobilized catalysts by cyclic voltammetry is challenging, with electron transfer processes being hidden by electrode effects. The stepwise generation of reduced intermediates on the way to catalytic potentials is therefore hampered, jeopardizing the identification of the catalytic species involved. On the contrary, the study of molecular catalysts in homogeneous conditions allows a better correlation with electrochemical measurements, thus providing more accurate information on the chemical state of the catalysts as a function of the electrode applied potential.

Herein, we present an *in situ* spectroelectrochemical study of the CO₂-reducing molecular electrocatalyst [Fe^{III}TPP(Cl)] in a DMF solution. We describe a custom-made vacuum-compatible X-ray spectroelectrochemical flow cell for the *in situ* study of homogeneous systems in organic solvents and provide XANES and UV-Vis spectra relative to the four oxidation states involved in the redox process, both under argon and carbon dioxide atmospheres (as identified in Table 1).

Results

A vacuum-compatible X-ray spectroelectrochemical flow cell for the study of homogeneous organic solutions

A handful of cells have been reported for the study of electroactive species in solution with a thin-layer configuration,^[34–37] with the possibility to flow the sample for some of them.^[38–43] In order to study the FeTPP complex in DMF, we have developed a novel thin layer spectroelectrochemical flow cell suitable for X-ray spectroscopic experiments (see Figure 2 and Figures S1 and S2), inspired by the work of Jiang *et al.*^[44] This cell allows performing *in situ* measurements in homogeneous conditions with organic solvents under primary vacuum.

Briefly, the cell consists of a main body made in polyether ether ketone (PEEK), a solvent-resistant polymer, to which two polytetrafluoroethylene (PTFE) tubes are connected as liquid inlet and outlet. The electrochemical chamber of the cell consists of a thin layer (200 μm) of liquid that can be circulated between a working (a 60 μm -thick glassy carbon film) and a counter (platinum film) electrode. A reference electrode (silver pseudo-reference) is inserted from the side in the liquid path. The small cell volume ensures the total electrochemical conversion of the species of interest within a short time (<5 min), preventing excessive X-ray dose and subsequent damage. It ensures a laminar flow of the circulating liquid,

Table 1. Identification of the species generated and studied in this study.

e [–] transferred	Ar	CO ₂
0	1	5
1	2 a, 2 b, 2 c	6
2	3	7
3	4	8

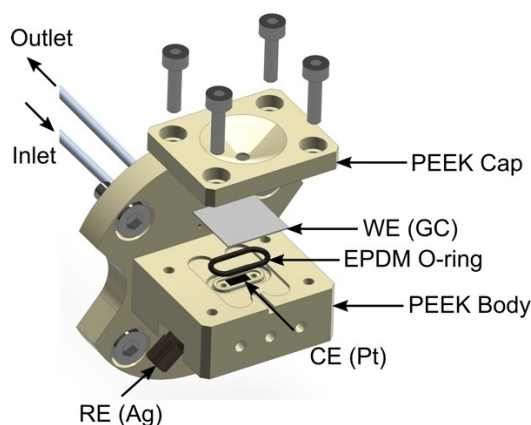


Figure 2. 3D scheme of the spectroelectrochemical cell. PEEK stands for “polyethylene ether ketone”, WE for “working electrode”, GC for “glassy carbon”, EPDM for “ethylene propylene diene monomer”, CE for “counter electrode” and RE for “reference electrode”.

preventing the formation of bubbles and allowing a complete renewal of the sample.

To assess the behavior of the X-ray spectroelectrochemical cell, an initial study in the presence of iron chloride was carried out. Iron(III) chloride hexahydrate ($\text{Fe}^{\text{III}}\text{Cl}_3 \cdot 6\text{H}_2\text{O}$) and iron(II) chloride ($\text{Fe}^{\text{II}}\text{Cl}_2$) reference samples were considered due to previously reported XANES data in the solid state and aqueous solutions for these compounds.^[41,45,46] Therefore, samples were prepared under anaerobic conditions in DMF and tetrabutylammonium hexafluorophosphate (TBAPF_6 , 0.1 M) as supporting electrolyte.

Fe K-edge XANES spectra were recorded *in situ* on both the Fe^{III} and Fe^{II} reference solutions. As shown in Figure 3, the spectrum of the Fe^{III} sample (blue line) presents a low-intensity

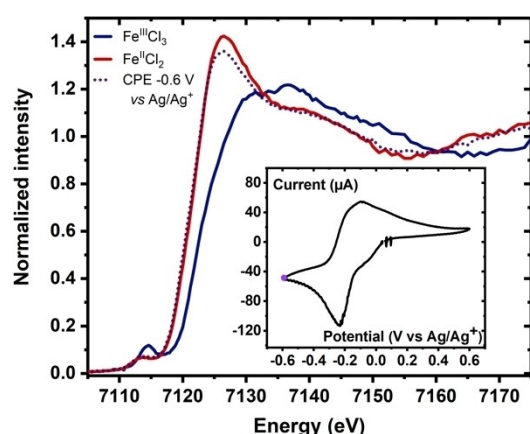


Figure 3. Fe K-edge XANES spectra recorded on 2 mM solution of $\text{Fe}^{\text{III}}\text{Cl}_3$ (blue line) and $\text{Fe}^{\text{II}}\text{Cl}_2$ (red line) in DMF/ TBAPF_6 (0.1 M) under Ar atmosphere. The spectrum of the $\text{Fe}^{\text{II}}\text{Cl}_2$ species obtained after a 15 min constant potential electrolysis at -0.6 V vs. Ag/Ag^+ under the same conditions is also shown (dotted purple line). Inset: Cyclic voltammogram of the 2 mM solution of $\text{Fe}^{\text{III}}\text{Cl}_3 \cdot 6\text{H}_2\text{O}$ in DMF/ TBAPF_6 (0.1 M) under Ar atmosphere recorded in the X-ray spectroelectrochemical cell ($v = 100$ mV.s⁻¹, room temperature).

white line (main edge peak top) as well as a pronounced pre-edge peak at 7114.6 eV (all pre-edge positions are measured at the peak top) and a main edge at 7122.3 eV (all main edge energies are measured at the half-edge jump, where the normalized intensity is equal to 0.5). The ferrous compound (Figure 3 – red line) presents a spectrum with a main edge that is shifted by 2 eV towards lower energies in comparison with the spectrum of the ferric compound (Figure 3 – blue line). Such a downshift in edge energy position is indicative of a reduction of the element probed. In addition, the intensity of the pre-edge peak clearly decreases and is also shifted towards lower energies to 7113.0 eV. The main edge energy shift, as well as the changes observed in the pre-edge intensities for the solutions of $\text{Fe}^{\text{III}}\text{Cl}_3$ and $\text{Fe}^{\text{II}}\text{Cl}_2$ are in agreement with previously reported data^[46] and confirm an oxidation state difference of one unit between these two species. A cyclic voltammogram (CV) was performed in the spectroelectrochemical cell under an Ar atmosphere (Figure 3, insert) on the $\text{Fe}^{\text{III}}\text{Cl}_3$ solution. The CV shows an anodic peak at -0.10 V and a cathodic peak at -0.22 V vs. Ag/Ag^+ . When $\text{Fe}^{\text{III}}\text{Cl}_3$ is electrochemically reduced by applying a constant potential of -0.6 V vs. Ag/Ag^+ during approximately 15 minutes, the main edge energy of XANES spectrum shifts by 2 eV towards lower values (Figure 3 – dotted line). The spectrum obtained matches closely the one of the $\text{Fe}^{\text{II}}\text{Cl}_2$ reference sample. Linear combination fittings (LCF) were performed on the XANES spectrum of the final species, using the spectra of the $\text{Fe}^{\text{III}}\text{Cl}_3$ and $\text{Fe}^{\text{II}}\text{Cl}_2$ reference solutions, indicating a conversion of 96% from Fe^{III} to Fe^{II} (see Figure S3).

In situ XANES and UV-Vis spectroelectrochemistry of $[\text{Fe}^{\text{III}}\text{TPP}(\text{Cl})]$ and its reduced species under Ar atmosphere

The Fe K-edge XANES spectrum of an Ar saturated 2 mM solution of $[\text{Fe}^{\text{III}}\text{TPP}(\text{Cl})]$ (named 1) in DMF/ TBAPF_6 (0.1 M) was recorded and compared with the one of the solid sample (see Figure S4). The two spectra are very similar, indicating that, under these conditions, the chloride ligand remains bound to the metal center.

The cyclic voltammogram (CV) of the initial $[\text{Fe}^{\text{III}}\text{TPP}(\text{Cl})]$ complex recorded in the X-ray spectroelectrochemical cell (Figure 4A) in DMF/ TBAPF_6 under Ar exhibits three well-defined reversible waves. They correspond to three consecutive one-electron reduction processes, ascribed to the $\text{Fe}^{\text{III}}/\text{Fe}^{\text{II}}$, $\text{Fe}^{\text{II}}/\text{Fe}^{\text{I}}$ and $\text{Fe}^{\text{I}}/\text{Fe}^{\text{0}}$ formal couples.^[6,22] The initial UV-Vis spectrum of the $[\text{Fe}^{\text{III}}\text{TPP}(\text{Cl})]$ species presents a Soret band at $\lambda = 416$ nm and Q-bands at $\lambda = 509$ nm and 575 nm, which correspond to previously reported values in the same solvent.^[22]

Controlled potential electrolysis (CPE) were performed at the potentials indicated by arrows in the CV shown in Figure 4A, *i.e.* -0.8 V, -1.6 V and -2.0 V vs. Ag/Ag^+ , corresponding to the first, second and third electron reductions, respectively. Figure 4B shows the normalized Fe K-edge XANES spectra of the starting $[\text{Fe}^{\text{III}}\text{TPP}(\text{Cl})]$ species in DMF/ TBAPF_6 0.1 M and of the species obtained under various applied potentials. Measurements were performed when the electrolysis currents were

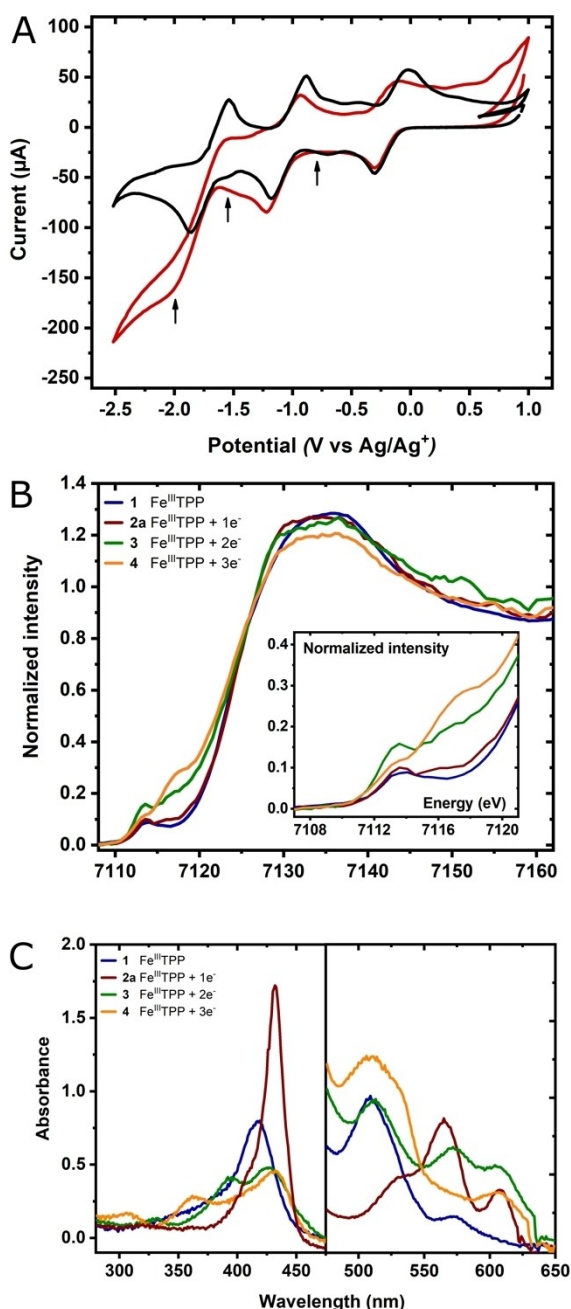


Figure 4. A. Cyclic voltammogram of a 2 mM solution of [Fe^{III}]TPP(Cl) in DMF/TBAPF₆ (0.1 M) under Ar recorded in the X-ray spectroelectrochemical cell at $v = 100 \text{ mV}\cdot\text{s}^{-1}$ (room temperature). Reduction potentials applied during spectroelectrochemical measurements are indicated by black arrows. B. Fe K-edge XANES spectra recorded on [Fe^{III}]TPP(Cl) solution, under the conditions described above (blue) and while applying a constant potential of $E = -0.8 \text{ V}$ (red), -1.6 V (green) and -2.0 V vs. Ag/Ag⁺ (orange). C. UV-Vis spectra (Soret Bands, left, Q-bands, right) for a solution of [Fe^{III}]TPP(Cl) in DMF/TBAPF₆ (0.1 M) under Ar (blue) and electrochemically reduced at $E = -0.8 \text{ V}$ (red), -1.6 V (green) and -2.0 V (orange) vs. Ag/Ag⁺ respectively.

stabilized (after ca. 2–5 min) and the possible occurrence of radiation-induced damages was carefully monitored.

The XANES spectra analysis of iron porphyrins may be divided into two different sections. First, a pre-edge region

extending from 7111 to 7120 eV corresponds to transitions from the 1s to 3d/4p orbitals, while the main edge region from 7120 to 7140 eV corresponds to transitions from the 1s to the 4p orbitals.

One electron reduction species. The first reduction step was performed by applying a constant electrode potential of ca. -0.8 V vs. Ag/Ag⁺. No energy shift was observed in the main edge of the Fe K-edge XANES spectrum upon reduction of [Fe^{III}]TPP(Cl) by one electron (named complex **2a**), as can be seen in Figure 4B. On the contrary, the UV-Vis spectroelectrochemical data recorded upon one-electron reduction of [Fe^{III}]TPP(Cl) leads to a shift of the Soret band from $\lambda = 416 \text{ nm}$ for the [Fe^{III}]TPP(Cl) complex to a sharp Soret band at $\lambda = 432 \text{ nm}$ for the one-electron reduced species as well as to the evolution of the Q-band region into three peaks at $\lambda = 530, 565$ and 603 nm respectively (see Figure 4C and Figure S5 for intermediate spectra).

As shown in the work of Wilson *et al.*,^[47] Fe^{II}TPP can adopt three different spin states, namely, high spin (HS, $S = 2$), intermediate spin (IS, $S = 1$) and low spin (LS, $S = 0$). These three species exhibit very different main edge and pre-edge features in their Fe K-edge XANES spectra.

In order to confirm the nature of the species electro-generated at -0.8 V vs. Ag/Ag⁺, we synthesized the [Fe^{II}]TPP species by chemical reduction of [Fe^{III}]TPP(Cl), as previously described, generating **2b**.^[23,48] When compared with the spectrum of the initial [Fe^{III}]TPP(Cl) complex, the main edge position of the chemically reduced solid sample (see Figure S6) shows a 2 eV shift towards lower energies (from 7123.0 to 7121.0 eV). It also presents a high-intensity shoulder at around 7118.0 eV, which corresponds to a low-lying 1s to 4p_z transition, as previously suggested by Römelt and co-workers.^[23] These features indicate that **2b** in the solid state is in a four-coordinated, square planar environment with an intermediate spin ($S = 1$), as previously discussed.^[23,47] The spectrum of this chemically reduced species is very different from that of complex **2a**, indicating that the two species have different spin states arising from the presence of DMF solvent molecule(s) in the coordination sphere of the complex generated in homogeneous conditions. Indeed, the loss of the feature at around 7118.0 eV in the electrogenerated species shows that the 4p_z orbital is shifted towards higher energies due to the axial coordination of DMF. To confirm this interpretation, we dissolved the chemically reduced [Fe^{II}]TPP solid sample in DMF under anaerobic conditions (named complex **2c**) and got a new spectrum that closely matches the one of the electrochemically reduced species (**2a**). These results illustrate that DMF plays a critical role in the electronic structure of the [Fe^{II}]TPP(Cl) species. Consistent with previously reported data,^[47] **2a** and **2c** are in a low-spin ($S = 0$) configuration, while **2b** is in an intermediate spin ($S = 1$) configuration. Such change in spin configuration explains the similarity between the XANES spectra of [Fe^{II}]TPP(Cl) and **2b** (generated electrochemically *in situ*), the edge shift towards lower energies expected from the reduction of Fe(III) to Fe(II) being compensated by an upshift due to the spin change.

Two and three electrons reduced species. The second reduction step was performed by applying constant electrode potential of *ca.* -1.6 V vs. Ag/Ag^+ to obtain the $[\text{Fe}^{\text{III}}\text{TPP}(\text{Cl})] + 2\text{e}^-$ species (named **3**). As observed in Figure 4B, the main edge energy is slightly shifted to lower values (0.7 eV) when compared to the initial sample, while the pre-edge feature increases in intensity. In addition, a low-intensity shoulder appears at *ca.* 7118.0 eV. The presence of this feature, arising from a $1s$ to $4p_z$ transition (similar to the one found in the intermediate spin $[\text{Fe}^{\text{II}}\text{TPP}]$ species), points towards a square planar environment around the Fe center.

The UV-Vis spectroelectrochemical data recorded upon reduction of $[\text{Fe}^{\text{II}}\text{TPP}(\text{Cl})]$ by a second electron leads to a decrease in intensity and splitting of the Soret band, with two peaks at $\lambda = 392$ nm and $\lambda = 425$ nm (see Figure 4C and S5 for intermediate spectra). The Q-bands of **3** present three bands located at $\lambda = 510$ nm, 575 nm and 608 nm, respectively. These results are in line with previously reported data on complex **3**.^[21]

Finally, a third reduction step is carried out by applying a constant electrode potential of *ca.* -2.0 V vs. Ag/Ag^+ (formation of the species named **4**). The spectrum (see Figure 4B) shows a shift of the main edge position of *ca.* 0.3 eV towards lower values when compared with the 2e^- reduced species, indicating a further reduction of the system. The pre-edge feature at 7113.6 eV decreases in intensity with respect to **3**, while the shoulder at *ca.* 7118.0 eV grows significantly. This increased intensity indicates a higher contribution of $4p_z$ character in the final molecular orbitals of the $1s \rightarrow 4p_z$ transition. The UV-Vis spectroelectrochemical data recorded on complex **4** leads to slight shifts of the Soret bands to $\lambda = 362$ nm and 433 nm (see Figure 4C and Figure S5 for intermediate spectra). More important modifications are observed in the Q-band region, with the presence of a broad band at $\lambda = 514$ nm. These values are in line with those previously reported for **4** in DMF.^[21,22]

***In situ/operando* XANES and UV-Vis spectroelectrochemistry of $[\text{Fe}^{\text{III}}\text{TPP}(\text{Cl})]$ and its reduced species under CO_2 atmosphere**

One electron reduced species. Figure 4A shows the comparison between the CVs obtained for the initial $[\text{Fe}^{\text{III}}\text{TPP}(\text{Cl})]$ complex in DMF/TBAPF₆ (0.1 M) under Ar (black line) and CO_2 atmospheres. Under CO_2 , the third reduction wave presents a current increase and a loss of reversibility as compared to the one in Ar atmosphere, indicating a catalytic process. Although a proton source is usually required to catalyze the CO_2RR , such as protons from residual water, CO_2 itself can play the role of a Lewis acid and lead to catalysis.^[9,15]

Figure 5A shows the normalized Fe K-edge XANES spectra recorded *in situ* on $[\text{Fe}^{\text{III}}\text{TPP}(\text{Cl})]$ and its reduced species under CO_2 atmosphere, while Figure 5B shows the corresponding UV-Vis spectra (see Figure S7 for intermediate spectra). A comparison of the XANES spectrum of the initial $[\text{Fe}^{\text{III}}\text{TPP}(\text{Cl})]$ complex and its one-electron reduced species under CO_2 atmosphere (**5** and **6** respectively) with the ones obtained in the presence of

Ar (see Figures S8–9) shows that they are identical, indicating that there are no interactions between CO_2 and the Fe metal center at these oxidation states. This is confirmed by the UV-Visible spectra of $[\text{Fe}^{\text{III}}\text{TPP}(\text{Cl})]$ and its one-electron reduced species, which are comparable to their counterparts in Ar.

Two and three electrons reduced species. Further reduction of **6** with a second electron under CO_2 atmosphere (complex **7**) yields a XANES spectrum that is almost identical to the one of **6**. It presents, however, clear differences with the one of **3**, obtained under Ar, as can be seen in Figure 5C. The shoulder around 7118.0 eV is absent in the spectrum recorded under CO_2 , which indicates that the square planar geometry observed under Ar has changed, hence pointing towards an interaction between CO_2 and the Fe center. It is worth mentioning that an interaction between CO_2 and an Fe(II) porphyrin was recently reported,^[49] although in a different solvent (acetonitrile). The UV-Vis spectra of complex **7** present a similar Soret band splitting as the one observed under Ar, with peaks at $\lambda = 392$ nm and 425 nm. Q-bands were also located at the same position as those obtained under Ar, *i.e.* at $\lambda = 510$ nm, 575 nm, 608 nm, 667 nm and 712 nm.

A XANES spectrum was recorded after the catalytic wave, at -2.0 V vs. Ag/Ag^+ , where $[\text{Fe}^{\text{III}}\text{TPP}(\text{Cl})]$ is reduced with three electrons to yield complex **8**. Significant changes are observed in the pre-edge region when compared with the two electrons reduced species **7** (Figure 5A), but also with the three-electron reduced species under Ar, **4** (Figure 5E). The pre-edge region of the XANES spectrum is clearly different, not only with the disappearance of the shoulder at 7118.0 eV, but also with a shift of the pre-edge peak from 7113.6 eV (under Ar) to 7115.0 eV (under CO_2). It indicates an important structural modification around the metal center at this potential, pointing towards the coordination of CO_2 to the iron center. Moreover, the main edge position shifts to higher energies by *ca.* 0.7 eV when compared with the two-electron-reduced species in CO_2 . This shift is even more pronounced when the spectra of the three-electron reduced species obtained under Ar (7122.0 eV) and CO_2 (7123.7 eV) are compared, with a shift to higher energies of 1.7 eV for the species obtained in CO_2 . These data further support a coordination of CO_2 to the Fe center, which donates part of its electronic density to the incoming coordinating molecule and therefore appears as being less electron rich. The UV-Vis spectra of the species obtained after reduction of $[\text{Fe}^{\text{III}}\text{TPP}(\text{Cl})]$ with three electrons look almost identical to the one obtained for the two-electron reduced species. The spectrum is, however, significantly different from its counterpart observed under Ar atmosphere (see Figure 5F).

Discussion

The pre-edge and main edge positions of the XANES data, as well as the peak positions of the UV-Visible Soret and Q-bands regions of compounds **1–8** are summarized in Table 2.

Electronic structure under Ar. The XANES data collected on the two and three electrons-reduced species of $[\text{Fe}^{\text{III}}\text{TPP}(\text{Cl})]$ under Ar show slight shifts of the main edge energy toward

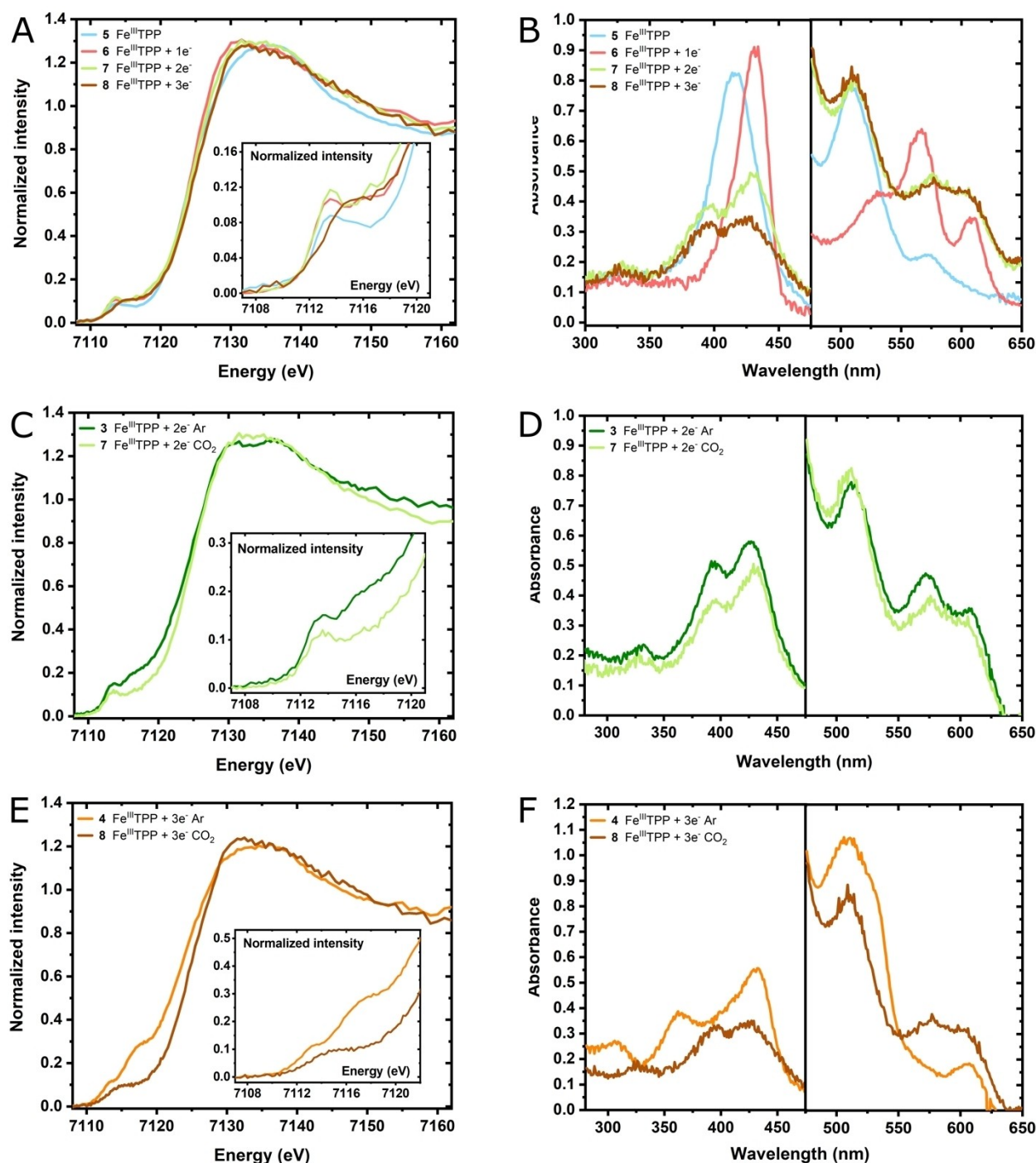


Figure 5. A. Fe K-edge XANES spectra recorded on a 2 mM solution of [Fe^{III}TPP(Cl)] in DMF/TBAPF₆ (0.1 M) under CO₂ (light blue) and while applying a constant electrode potential of $E = -0.8$ V (magenta), -1.6 V (light green) and -2.0 V (brown) vs. Ag/Ag⁺ respectively. B. UV-Vis spectra (Soret Bands on the left, Q-bands on the right) of [Fe^{III}TPP(Cl)] in DMF/TBAPF₆ (0.1 M) under CO₂ (light blue) and while applying a constant electrode potential of $E = -0.8$ V (magenta), -1.6 V (light green) and -2.0 V (brown) vs. Ag/Ag⁺. C. Comparison of the Fe K-edge XANES and D. UV-Visible spectra recorded after controlled potential electrolysis at -1.6 V vs. Ag/Ag⁺ under Ar (green) and CO₂ (light green), respectively. E. Comparison of the Fe K-edge XANES and F. UV-Visible spectra recorded upon applying a constant electrode potential of $E = -2.0$ V vs. Ag/Ag⁺ under Ar (orange) and CO₂ (brown).

lower values as more electrons are injected into the complex. These shifts are notably small (-0.7 and -0.3 eV) and cannot be assigned to full oxidation state changes, suggesting a partial localization of the electrons both on the metal and on the porphyrin ligand. As previously mentioned, the pre-edge

feature observed at 7118.0 eV can be attributed to a $1s \rightarrow 4p_z$ transition. This peak appears in the [Fe^{II}TPP] complex in the solid state, which does not have apical ligands and adopts a square planar geometry, leading to an intermediate spin configuration. When dissolved in solution, one or two DMF

Table 2. XANES pre-edge and main edge energy positions (in eV) and UV-Visible peak positions (in nm) for compounds 1–8.					
e ⁻ transferred Ar saturated solution	Complex	Pre-edge ^[a]	Main edge ^[b]	Soret band(s)	Q-band(s)
0	1	7113.9	7123.0	416	509, 575
1	2a	7113.6	7123.0	432	530, 565, 603
2	3	7113.5, 7118	7122.3	392, 425	510, 575, 608
3	4	7113.6, 7118	7122.0	362, 433	514, 607
CO ₂ saturated solution					
0	5	7113.9	7123.0	417	508, 575
1	6	7113.6	7123.0	430	535, 567, 609
2	7	7113.5	7123.0	392, 425	510, 575, 608
3	8	7115.0	7123.7	395, 424	510, 575, 608

[a] The pre-edge peak positions are measured at the peak maximum. [b] The main edge positions are measured at the half-edge jump (normalized intensity = 0.5).

molecule(s) coordinate the metal, and the feature at 7118.0 eV disappears due to a square (bi)pyramidal structure. When the complex is reduced with a second electron, the shoulder at 7118.0 eV appears with a low intensity, which can be explained by the repulsion of the DMF molecule(s) by the charge (−1) appearing on the Fe porphyrin. Further reduction by a third electron and increase of the charge (−2) lead to the removal of the DMF apical ligands, thus generating a square planar geometry similar to what that observed for the Fe^{II} complex in the solid state, as attested by the presence of the $1s \rightarrow 4p_z$ transition.

Taken together, this *in situ* dataset indicates that the one-electron reduced species of [Fe^{III}TPP(Cl)] in DMF is a low spin Fe(II) complex, while the two and three electrons reduced species have an electronic structure where the additional electrons are shared between the metal and the porphyrin.

Electronic structure under CO₂. Under CO₂ atmosphere, significant differences are observed in the XANES spectra with respect to the Ar atmosphere conditions. The two-electron reduced species (complex 7) presents a XANES spectrum that is different from the one in Ar, with a pre-edge region that misses the shoulder at 7118.0 eV, indicating a deviation from the square planar geometry and thus suggesting an interaction with CO₂. The UV-Vis spectrum obtained under these conditions is, however, almost identical to the one obtained under Ar. This difference may be explained by the lower sensitivity of UV-Vis to valence-level electronic changes. It also suggests that the interaction between 7 and CO₂ is very loose and that no bond is formed with the metallic center.

When reduced with a third electron, more prominent differences can be observed, both by XANES and UV-Visible spectroscopy, when compared to the Ar atmosphere conditions (complexes 8 vs. 4, Figure 5E–F). The pre-edge region of the XANES spectrum is clearly different, not only with the disappearance of the shoulder at 7118.0 eV, but also with a shift of the pre-edge peak from 7113.6 eV (under Ar) to 7115.0 eV (under CO₂). Moreover, the main edge position lies 1.7 eV higher than under Ar. The UV-Visible data show clear differences with the one obtained under Ar, but looks actually very similar to those obtained with 3 and 7, the doubly reduced species observed under Ar or CO₂, respectively. Therefore, both

the XANES and UV-Visible data for complex 8 show differences with respect to those obtained under Ar (complex 4), indicating that CO₂ is bound to the iron center. The disappearance of the peak at 7118.0 eV in the pre-edge region of the XANES spectrum supports a deviation from the square-planar geometry, consistent with a square pyramidal geometry with CO₂ bound to Fe center and sitting on top of the porphyrin plane. The UV-Visible spectrum of 8 is very similar to that 3, which is only reduced with two electrons (vs. three electrons for 8). This suggests an electronic structure for 8 where part of the electronic density is delocalized between the metalloporphyrin system and the CO₂ substrate.

CO₂ reduction mechanism. The cyclic voltammetry experiments shown in Figure 4A indicate that CO₂ reduction catalysis occurs at the third reduction wave (*ca.* −1.8 V vs. Ag/Ag⁺), thanks to the presence of a residual source of protons (and/or with a second CO₂ molecule acting as a Lewis acid to help C–O bond breaking). In such low proton availability conditions, the rate-determining step of the CO₂ reduction reaction is the cleavage of the OC–O bond (see Figure 6).^[18] In other words, the species expected to be observed under these catalytic

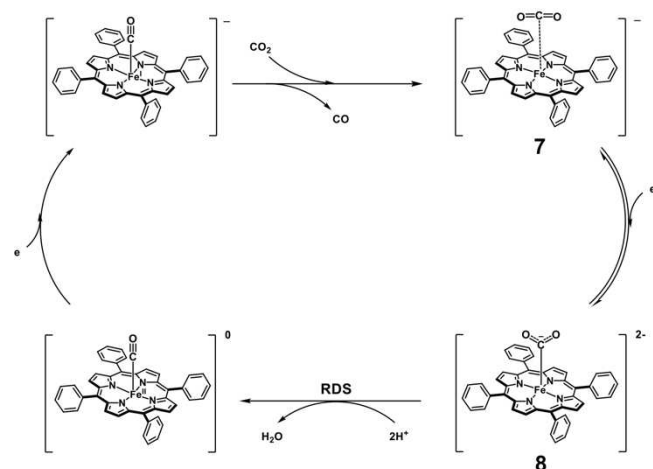


Figure 6. Simplified catalytic cycle for the electrochemical reduction of CO₂ into CO by FeTPP in DMF with species 7 and 8 identified.

conditions is the one accumulating before the rate-limiting step, *i.e.* the triply reduced FeTPP species with CO₂ bound to the metal. The comparison of the *in situ* XANES and UV-Visible data collected under Ar or CO₂ atmospheres provide direct evidence for the coordination of CO₂ to the Fe in the triply reduced form of [Fe^{III}TPP(Cl)]. These results are consistent with the CO₂-to-CO mechanism considered so far (see Scheme S1) and unambiguously demonstrate that, despite an electronic density partly localized on the porphyrin ligand, the reactivity of the triply reduced iron porphyrin towards CO₂ indeed occurs at the metallic center. It implies that the localization of the electronic density is partly shifted from the metalloporphyrin organic backbone to the metal center upon substrate coordination. This behavior may explain the ability of iron porphyrins to store electrons without reacting until a substrate molecule is activated.

Conclusion

Using a custom-made *in situ* X-ray spectroelectrochemical cell, we collected the XANES spectra of the [Fe^{III}TPP(Cl)] complex in a DMF homogeneous solution, together with its one, two and three electrons reduced species. These data were collected both under Ar and CO₂ atmospheres and correlated with the corresponding UV-Vis spectroelectrochemical data. We showed that, when dissolved in DMF, the one-electron reduced species is an Fe(II) complex with a low spin electronic configuration, due to the coordination of DMF to the central Fe ion. The two and three-electrons reduced species generated under Ar are proposed to have electronic structures where the electron density is shared between the metal and the porphyrin ring. Under CO₂ atmosphere, the XAS and UV-Vis spectra collected *in situ* show new features, which indicate that (i) CO₂ is loosely bound to the two electrons reduced species and (ii) CO₂ is coordinated to the iron center in the triply reduced iron porphyrin species, which is the active form of the catalyst. This result is consistent with a rate-limiting step of the reaction corresponding to the cleavage of the OC–O bond and indicates that reactivity towards CO₂ occurs on the metallic center rather on the ligand. Overall, these findings provide a better understanding of the electrocatalytic mechanism for CO₂ reduction with molecular catalysts.

Acknowledgements

We are indebted to the Michem Labex and Synchrotron SOLEIL for a PhD grant to D. M. The peer-review committees of Synchrotron SOLEIL are greatly acknowledged for beamtime allocation. M. R. is thankful to the Institut Universitaire de France (IUF) for partial financial support. O. R–W acknowledges financial support from the Investissement l'Avenir through the MOPGA call N° ANR-18-MPGA-0012.

Conflict of Interest

The authors declare no conflict of interest.

Data Availability Statement

The data that support the findings of this study are available from the corresponding author upon reasonable request.

Keywords: CO₂ reduction · electronic structure · porphyrins · spectroelectrochemistry · X-ray absorption spectroscopy

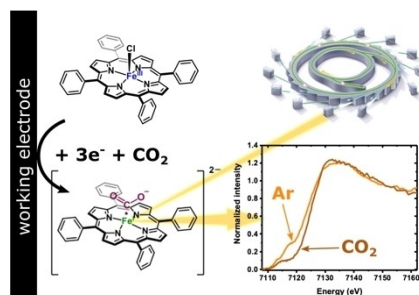
- [1] V. Masson-Delmotte, P. Zhai, A. Pirani, S. L. Connors, C. Péan, S. Berger, N. Caud, Y. Chen, L. Goldfarb, M. I. Gomis, M. Huang, K. Leitzell, E. Lonnoy, J. B. R. Matthews, T. K. Maycock, T. Waterfield, O. Yelekci, R. Yu, B. Zhou (eds.) IPCC, **2021**: Summary for policymakers. In: Climate Change 2021: The physical science basis. Contribution of working group I to the sixth assessment report of the Intergovernmental panel on Climate Change. Cambridge University Press. In Press.
- [2] E. Lamy, L. Nadjo, J.-M. Savéant, *J. Electroanal. Chem. Interfacial Electrochem.* **1977**, *78* (2), 403–407.
- [3] J. P. Collin, J.-P. Sauvage, *Coord. Chem. Rev.* **1989**, *93*(2), 245–268.
- [4] N. W. Kinzel, C. Werlé, W. T. Leitner, *Angew. Chem. Int. Ed.* **2021**, *60* (21), 11628–11686.
- [5] E. Boutin, L. Merakeb, B. Ma, B. Boudy, M. Wang, J. Bonin, E. Anxolabéhère-Mallart, M. Robert, *Chem. Soc. Rev.* **2020**, *49*(16), 5772–5809.
- [6] M. Hammouche, D. Lexa, J.-M. Savéant, M. Momenteau, *J. Electroanal. Chem. Interfacial Electrochem.* **1988**, *249*, 347–351.
- [7] C. Costentin, S. Drouet, M. Robert, J.-M. Savéant, *Science* **2012**, *338*(6103), 90–94.
- [8] P. Gotico, L. Roupnel, R. Guillot, M. Sircoglou, W. Leibl, Z. Halime, A. Aukauloo, *Angew. Chem. Int. Ed.* **2020**, *59*(50), 22451–22455.
- [9] C. Costentin, M. Robert, J.-M. Savéant, A. Tatin, *Proc. Natl. Acad. Sci. USA* **2015**, *112*(22), 6882–6886.
- [10] I. Azcarate, C. Costentin, M. Robert, J.-M. Savéant, *J. Am. Chem. Soc.* **2016**, *138*(51), 16639–16644.
- [11] P. Gotico, B. Boitrel, R. Guillot, M. Sircoglou, A. Quaranta, Z. Halime, W. Leibl, Aukauloo, *Angew. Chem. Int. Ed.* **2019**, *58*(14), 4504–4509.
- [12] A. Khadhraoui, P. Gotico, B. Boitrel, W. Leibl, Z. Halime, A. Aukauloo, *Chem. Commun.* **2018**, *54*(82), 11630–11633.
- [13] M. Hammouche, D. Lexa, M. Momenteau, J.-M. Savéant, *J. Am. Chem. Soc.* **1991**, *113*(22), 8455–8466.
- [14] I. Bhugun, D. Lexa, J.-M. Savéant, *J. Am. Chem. Soc.* **1994**, *116*(11), 5015–5016.
- [15] I. Bhugun, D. Lexa, J.-M. Savéant, *J. Am. Chem. Soc.* **1996**, *118*(7), 1769–1776.
- [16] C. Costentin, G. Passard, M. Robert, J.-M. Savéant, *J. Am. Chem. Soc.* **2014**, *136*(33), 11821–11829.
- [17] I. Bhugun, D. Lexa, J.-M. Savéant, *J. Phys. Chem.* **1996**, *100*(51), 19981–19985.
- [18] C. Costentin, S. Drouet, G. Passard, M. Robert, J.-M. Savéant, *J. Am. Chem. Soc.* **2013**, *135*(24), 9023–9031.
- [19] D. Lexa, J.-M. Savéant, D. Li Wang, *Organometallics*. **1986**, *5*(7), 1428–1434.
- [20] C. Gueutin, D. Lexa, *Electroanalysis* **1996**, *8*(11), 1029–1033.
- [21] E. Anxolabéhère, G. Chottard, D. Lexa, *New J. Chem.* **1994**, *18*, 889–899.
- [22] D. Lexa, M. Momenteau, J. Mispelter, *Biochim. Biophys. Acta.* **1974**, *338*(1), 151–163.
- [23] C. Römelt, J. Song, M. Tarrago, J. A. Rees, M. van Gastel, T. Weyhermüller, S. DeBeer, E. Bill, F. Neese, S. Ye, *Inorg. Chem.* **2017**, *56*(8), 4745–4750.
- [24] J. Kowalska, S. DeBeer, *Biochim. Biophys. Acta.* **2015**, *1853*(6), 1406–1415.
- [25] B. Lassalle-Kaiser, S. Gul, J. Kern, V. Yachandra, J. Yano, *Electron. Spectrosc. Relat. Phenom.* **2017**, *221*, 18–27.
- [26] J. Yano, V. K. Yachandra, *Photosynth. Res.* **2009**, *102*(2–3), 241–254.
- [27] J. Timoshenko, B. Roldan Cuenya, *Chem. Rev.* **2021**, *121*(2), 882–961.
- [28] G. Xuan, S. Jang, G. Kwang, K. Sunghyun *Bull. Korean Chem. Soc.* **2005**, *26*(4), 671–674.

- [29] K. Nakanishi, D. Kato, H. Arai, H. Tanida, T. Mori, Y. Orikasa, Y. Uchimoto, T. Ohta, Z. Ogumi, *Rev. Sci. Instrum.* **2014**, *85*(8), 084103.
- [30] L. León, J. D. Mozo, *Trends Analyt Chem.* **2018**, *102*, 147–169.
- [31] Z. Weng, Y. Wu, M. Wang, J. Jiang, K. Yang, S. Huo, X.-F. Wang, Q. Ma, G. W. Brudvig, V. S. Batista, Y. Liang, Z. Feng, H. Wang, *Nat. Commun.* **2018**, *9*(1), 1–9.
- [32] B. Lassalle-Kaiser, A. Zitolo, E. Fonda, M. Robert, E. Anxolabéhère-Mallart, *ACS Energy Lett.* **2017**, *2*(11), 2545–2551.
- [33] H. J. King, M. Fournier, S. A. Bonke, E. Seeman, M. Chatti, A. N. Jumabekov, B. Johannessen, P. Kappen, A. N. Simonov, R. K. Hocking, *J. Phys. Chem. C* **2019**, *123*(47), 28533–28549.
- [34] H. D. Dewald, J. W. Watkins, R. C. Elder, W. R. Heineman, *Anal. Chem.* **1986**, *58*(14), 2968–2975.
- [35] J. M. Charnock, D. Collison, C. D. Garner, E. J. L. McInnes, J. F. W. Mosselmanns, C. R. Wilson, *J. Phys. IV.* **1997**, *7*(C2), C2–658.
- [36] I. Ascone, A. Cognigni, M. Giorgetti, M. Berrettoni, S. Zamponi, R. Marassi, *J. Synchrotron Radiat.* **1999**, *6*, 384–386.
- [37] E. Anxolabéhère-Mallart, T. Glaser, P. Frank, A. Aliverti, G. Zanetti, B. Hedman, K. O. Hodgson, E. I. Solomon, *J. Am. Chem. Soc.* **2001**, *123*(23), 5444–5452.
- [38] S. Nappini, L. D'Amario, M. Favaro, S. Dal Zilio, F. Salvador, E. Betz-Güttner, A. Fondacaro, I. Piš, L. Romanzin, A. Gambitta, F. Bondino, M. Lazzarino, E. Magnano, *Rev. Sci. Instrum.* **2020**, *92*, 015115.
- [39] A. Ambrosi, R. R. D. Sheng Shi, R. Webster, *J. Mater. Chem. A* **2020**, *8*, 21902–21929.
- [40] E. Achilli, A. Minguzzi, A. Visibile, C. Locatelli, A. Vertova, A. Naldoni, S. Rondinini, F. Auricchio, S. Marconi, M. Fracchia, P. Ghigna, *J. Synchrotron Radiat.* **2016**, *23*(2), 622–628.
- [41] K. Cheaib, B. Maurice, T. Mateo, Z. Halime, B. Lassalle-Kaiser, *J. Synchrotron Radiat.* **2019**, *26*(6), 1980–1985.
- [42] M. F. Tesch, S. A. Bonke, R. Golnak, J. Xiao, A. N. Simonov, R. Schlögl, *Electrochem Sci Adv.* **2021**, *2*, e2100141.
- [43] M. Nagasaka, H. Yuzawa, T. Horigome, N. Kosugi, *Rev. Sci. Instrum.* **2014**, *85*, 104105.
- [44] P. Jiang, J.-L. Chen, F. Borondics, P.-A. Glans, M. W. West, C.-L. Chang, M. Salmeron, J. Guo, *Electrochem. Commun.* **2010**, *12*(6), 820–822.
- [45] T. E. Westre, P. Kennepohl, J. G. DeWitt, B. Hedman, K. O. Hodgson, E. I. Solomon, *J. Am. Chem. Soc.* **1997**, *119*(27), 6297–6314.
- [46] M. J. Apted, G. A. Waychunas, G. E. Brown, *Geochim. Cosmochim. Acta* **1985**, *49*(10), 2081–2089.
- [47] S. A. Wilson, E. Green, I. I. Mathews, M. Benfatto, K. O. Hodgson, B. Hedman, R. Sarangi, *Proc. Natl. Acad. Sci. USA* **2013**, *110*(41), 16333–16338.
- [48] T. Mashiko, C. A. Reed, K. J. Haller, W. R. Scheidt, *Inorg. Chem.* **1984**, *23*(20), 3192–3196.
- [49] S. Masaoka, K. Kosugi, M. Kondo, *Angew. Chem. Int. Ed.* **2021**, *60*(40), 22070–22074.

Manuscript received: October 27, 2022
Accepted manuscript online: December 1, 2022
Version of record online: January 1, 2023

RESEARCH ARTICLE

Catalytic CO₂ reduction: *In situ* X-ray absorption spectroscopy was used to observe the binding of CO₂ on reduced forms of CO₂-reducing iron porphyrins in a homogenous solution. Interactions can be observed on the doubly and triply reduced species of the starting iron(III) complex. Electronic structures are proposed for these species, and implications for the catalytic reduction of CO₂ are discussed.



Dr. D. Mendoza, S.-T. Dong, Dr. N. Kostopoulos, V. Pinty, Dr. O. Rivada-Wheleghan, Dr. E. Anxolabéhère-Mallart*, Prof. M. Robert*, Dr. B. Lassalle-Kaiser*

1 – 10

***In situ* X-ray Absorption Spectroscopy in Homogeneous Conditions Reveals Interactions Between CO₂ and a Doubly and Triply Reduced Iron(III) Porphyrin, then Leading to Catalysis**



Degradation Mechanism of Metal–Organic Framework Drug Nanocarriers Studied by Solid-State Nuclear Magnetic Resonance and X-ray Absorption Near-Edge Structure Spectroscopy

Mai Dang Le Vuong, Ioanna Christodoulou, Marianna Porcino, Si-Thanh Dong, Benedikt Lassalle-Kaiser, Mohamed Haouas, Ruxandra Gref,* and Charlotte Martineau-Corcoc*



Cite This: *Chem. Mater.* 2022, 34, 8178–8189



Read Online

ACCESS |



Metrics & More

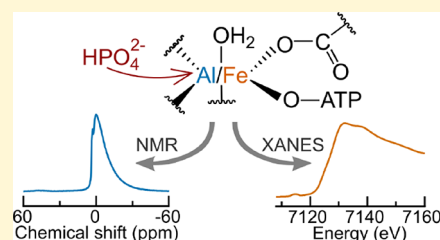


Article Recommendations



Supporting Information

ABSTRACT: Metal–organic framework nanoparticles (nanoMOFs) are novel porous drug delivery systems whose features include high drug loading capacity, versatile functionalization, biocompatibility, and biodegradability. However, little knowledge about the nature of nanoMOF degradation mechanism is one of the many reasons that prevent their clinical use. MIL-100 (MIL stands for Matériaux de l'Institut Lavoisier) is among the most studied nanoMOFs for drug delivery. Here, we investigate at the atomic scale the degradation mechanism of metal(III)-trimesate nanoMIL-100 drug carrier in biological-mimicking phosphate medium. By using solid-state NMR (ssNMR) spectroscopy, we found that the first step of nanoMIL-100(Al) degradation is the substitution of labile water ligands, resulting in new coordination bonds between Al(III) and phosphate ions, followed by the substitution of trimesate ligands, leading to their release. The data indicated that the reaction-limiting step most likely is the formation of an inorganic aluminophosphate layer at the nanoparticle surface and that drug encapsulation and surface coating affect the nanoMIL-100(Al) degradation. The X-ray absorption near-edge structure (XANES) spectroscopy study of nanoMIL-100(Fe) degradation corroborates the hypothesized alteration mechanism of nanoMIL-100(Al). From the ensemble of data, a stepwise degradation mechanism representative for the nanoMIL-100 drug delivery system is proposed.



1. INTRODUCTION

The concept of sustained drug release has been around since the 1960s;¹ the quest to search for the most appropriate drug carriers for the delivery and controlled release of therapeutic molecules to a targeted location in the patient has never stopped. Since the first report in 2010,² metal–organic framework nanoparticles (nanoMOFs) as drug carriers have gained increasing attention as they combine the advantages of both their inorganic and organic constituents. Metal–organic frameworks (MOFs) are porous materials made of metal–ligand coordination units assembled as an ordered crystalline structure with high permanent porosity.^{3–5} This high porosity enables MOFs to capture a large amount of drug within a small amount of carrier, thus potentially reducing the administered dose and related toxicity for the patients.

Among the most studied nanoMOFs for drug delivery to date is nanoMIL-100(Fe), belonging to the MOF family of MIL-100. It consists of trivalent metal cations such as Al(III) or Fe(III) and benzene-1,3,5-tricarboxylate ligands, also called trimesate or BTC.^{6,7} Figure 1 illustrates the structure of MIL-100. Its secondary building unit (SBU), the Fe or Al(III) metal trimer, consists of three metal cations M(III) coordinated with one central bridging oxygen and six carboxylate groups. The 6-fold coordination sphere is completed with hydroxyl and water ligands. Two metal cations coordinate with one water molecule each, and one cation coordinates with one hydroxyl group. Every

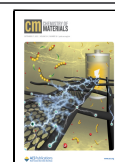
four SBUs connect through trimesate linkers, creating tetrahedra. These tetrahedra build the MTN-type MIL-100 framework, which possesses two kinds of pores: large mesoporous cages of 29 Å diameter, accessible through hexagonal (8.6 Å) and pentagonal windows (4.8–5.5 Å), and small mesoporous cages of 25 Å diameter, accessible exclusively through pentagonal opening windows. The generally accepted formula is $M_3O(H_2O)_2OH(C_6H_3(CO_2)_3)_2$ (M is Fe or Al).^{7,8} In addition, the MIL-100 MOFs consist of coordinative unsaturated metal sites (CUS) with strong Lewis acid properties produced upon thermal activation and departure of labile ligands.^{9,10}

The high drug payload of nanoMIL-100(Fe) has been demonstrated for various drugs,^{12,13} namely, anticancer,^{2,14,15} antibiotic,^{16,17} antiretroviral,¹⁸ and a combination of anti-inflammatory and antibiotics.¹⁹ For example, the anticancer drug busulfan was loaded in nanoMIL-100(Fe) with a payload of 25 wt %, five and sixty times higher than its payload in polymer

Received: April 20, 2022

Revised: August 21, 2022

Published: September 5, 2022



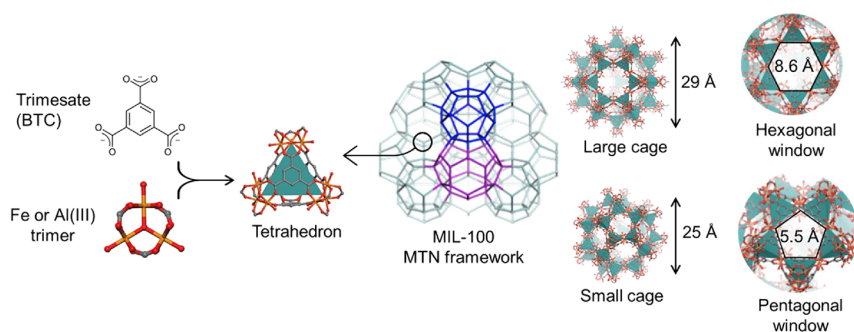


Figure 1. Structure of the MOF family MIL-100. The Fe(III) or Al(III) trimer is 6-coordinate Fe or Al (III) coordinating with bridging oxygen, water, trimesate, and hydroxyl ligands. Tetrahedra, made of Fe or Al(III) trimers on their vertices and trimesates on their faces, are arranged following the MTN framework, creating two types of mesoporous cages: large cages with 29 Å diameter, accessible through hexagonal (8.6 Å) and pentagonal windows (4.8–5.5 Å), and small cages with 25 Å diameter, accessible only through pentagonal windows. Adapted from Figure 1 from ref 11. Copyright 2021 MDPI.

nanoparticles and in liposomes, respectively.^{2,20,21} Recently, the aluminum-trimesate nanoMIL-100(Al) was also explored for drug delivery. The MIL-100(Al) gel loaded with the anticancer drug doxorubicin (DOX) showed a remarkably high payload of 62 wt %.²² More recently, DOX was efficiently encapsulated (74% encapsulation efficiency) in core–shell nanoMIL-100(Al) coated with γ -cyclodextrin (CD) citrate and was released progressively depending on the initial drug loading.²³ Both nanoMIL-100(Al) and nanoMIL-100(Fe) demonstrated high loading capacity for active molecules bearing phosphate moieties because of the strong interaction between Al(III) or Fe(III) CUS and phosphate group.^{14,18,24} Additionally, to improve the nanoMOF's colloidal stability and to modulate their interaction with biological media and cells, the surface of nanoMIL-100(Fe) and nanoMIL-100(Al) was coated covalently with polymers²⁵ or non-covalently with biopolymers, lipids, and carbohydrates.^{15,26–31} More importantly, for biomedical applications, nanoMIL-100(Fe) has been shown non-toxic and biodegradable *in vitro*^{2,32,33} and *in vivo*.^{2,21,34,35} NanoMIL-100(Al) has also been shown non-toxic *in vitro*.³³ Still, many questions remain about the nanoMIL-100 carrier stability, for instance, toxicity might come from nanoMOF's degradation products³² or drug encapsulation can modify nanoMOF's degradation kinetics.²¹ To further progress in the clinical translation of nanoMOFs, a critical aspect that needs to be addressed is deciphering the degradation mechanism of the nanoMIL-100 family.

However, there is little literature on the important topic of nanoMIL-100 degradation in biological-relevant media and the effects of drug encapsulation and surface coating. A popular hypothesis is that the degradation reaction of MIL-100(Fe) produces free iron(III) ions and trimesic acid. Early studies found that the culprit of degradation is the phosphate component of the cell medium.^{18,36} The higher the phosphate concentration, the higher the trimesate release, the more degraded the nanoMOF.¹⁶ Li *et al.* discovered that despite witnessing more than 30% trimesate ligand loss, the MIL-100(Fe) nano- and micro-particles maintained their sizes and shapes upon exposure to phosphate buffer.³⁷ Using Raman and Mossbauer spectroscopy, the authors suspected the formation of an amorphous shell of iron phosphate and/or iron oxide surrounding an intact crystalline core. In addition, using *in situ* atomic force microscopy and high-resolution transmission electron microscopy, Christodoulou *et al.* also found that the nanoMIL-100(Fe) and microMIL-100(Fe) degraded without

collapsing or changing their dimension.¹¹ Degradation of MIL-100(Fe) started at the particle surface, where the crystal planes at the surface disappeared within 2 h of incubation in phosphate buffer saline (PBS) at pH 7.4. However, none of these techniques have given evidence at the atomic scale for the changes in iron coordination.

To study the MOF structure at the atomic scale, solid-state NMR (ssNMR) spectroscopy is a non-destructive and valuable technique to get information about both the long-range crystal structure (when combined with XRD and periodic first-principles calculations)³⁸ and short-range local structure or interactions in MOFs. Deviations from periodic structures in MOFs can happen after chemical modification or functionalization, which are often not detected by routine characterization techniques such as X-ray diffraction and infrared spectroscopy. In this case, ssNMR spectroscopy is a technique of choice for locally probing atoms, their neighboring environments, and chemical bonds while keeping the MOF intact.^{39,40} It has been used extensively to determine the structure of new MOFs^{7,41,42} and the adsorption–desorption mechanism of liquid and gases.^{43,44} For porous drug delivery systems, ssNMR spectroscopy has been mainly used to study mesoporous silica^{45–47} and MOFs.^{48,49} For MIL-100(Fe), ssNMR spectroscopy gave indirect proof about the interaction between the strong paramagnetic Fe(III) and the drug azidothymidine triphosphate or the coating cyclodextrin phosphate (CD-P).^{18,26} For diamagnetic MIL-100(Al), ssNMR spectroscopy provided insights about the host–guest interaction and location of the drugs adenosine triphosphate (ATP) and doxorubicin as well as the surface coating cyclodextrin-phosphate (CD-P).^{23,24}

In this work, we further use solid-state NMR spectroscopy to investigate the degradation mechanism at the atomic scale of this nanoMIL-100(Al) in PBS, revealing a stepwise degradation process. We also study the impact of ATP drug loading and CD-P surface modification on the nanoMOF degradation. ATP and CD-P were chosen based on their well-known interaction between molecules bearing phosphate moieties and the Al(III) cations of nanoMIL-100(Al).^{24,26} The ensemble of ssNMR data (²⁷Al, ³¹P, and ³¹P-²⁷Al) reveals the evolution of the metal coordination sphere in MIL-100 during the degradation reaction as a function of several parameters: MIL-100 structure, concentration of the degradation medium, interaction with surface coating, and loaded drug. To check whether our proposed degradation mechanism applies to the iron MIL-100 analog, we studied the degradation of nanoMIL-100(Fe) in PBS

by XANES spectroscopy, which was selected because it can provide information about the local structure of iron(III) in MOFs.^{50,51} This paper shows that using a combination of ssNMR and XANES spectroscopy allows a better understanding of the chemistry of nanoMIL-100 drug carriers and their degradation.

2. EXPERIMENTAL SECTION

Herein, the most important experimental methods and techniques are summarized. Details are given in the [Supporting Information](#).

2.1. Synthesis of NanoMIL-100(Al) and NanoMIL-100(Fe). NanoMIL-100(Al) and nanoMIL-100(Fe) were synthesized by microwave-assisted synthesis following a published procedure.^{8,52} All reagents and solvents were used without further purification.

2.2. Drug Encapsulation and Surface Coating of NanoMIL-100(Al). NanoMOFs were loaded with ATP with the input loading 30 wt % of initial nanoMOF following a reported soaking procedure.¹⁴ A 1.5 mg mL⁻¹ aqueous solution of ATP disodium salt hydrate was added to a determined milligram of nanoMOF (m_{MOF}). The final nanoMOF concentration was 5 mg mL⁻¹. The weight of drug remaining in the supernatant after drug loading (m_{drug remaining}) was determined by HPLC based on a reported procedure.⁵³ The actual drug payload wt % was calculated as $\frac{m_{\text{drug input}} - m_{\text{drug remaining}}}{m_{\text{MOF}}} \times 100$,

where m_{drug input} is the weight of drug added to nanoMOF.

NanoMOFs were coated with phosphate- β -cyclodextrin (CD-P) at the theoretical coating 30 wt % of initial MOF by adapting a published method.²⁶ A 3 mg mL⁻¹ aqueous solution of phosphated β -cyclodextrin CD-P sodium salt (average 3–4 phosphate groups per cyclodextrin unit) was added to a determined milligram of nanoMOF. The final nanoMOF concentration was 10 mg mL⁻¹. The amount of coating remaining in the supernatant after surface coating (m_{coating remaining}) was determined by quantitative liquid-state NMR spectroscopy. The actual surface coating wt % was calculated as $\frac{m_{\text{coating input}} - m_{\text{coating remaining}}}{m_{\text{MOF}}} \times 100$, where m_{coating input} is the weight of drug added to nanoMOF.

2.3. Degradation of NanoMIL-100(Al) and NanoMIL-100(Fe). NanoMOF was incubated in PBS pH 7.4 at 37 °C for 2–5 days following two conditions: 10 mg mL⁻¹ nanoMOF and PBS 10 mM, and 0.5 mg mL⁻¹ nanoMOF and PBS 1 mM. PBS used was Dulbecco's Phosphate-Buffered Saline 1 \times , *i.e.*, 10 mM, pH 7.0–7.3, composed of 8.1 mM Na₂HPO₄, 1.5 mM KH₂PO₄, 138 mM NaCl, and 2.7 mM KCl.

2.4. Characterization of NanoMIL-100(Al). The morphology and size of nanoMOF were observed by transmission electron microscopy (TEM) under a 120 kV microscope. A particle size of 0.5 mg mL⁻¹ nanoMOF suspension in EtOH abs or deionized (DI) water was measured by dynamic light scattering (DLS). The specific surface area of MOF was measured by the Brunauer–Emmett–Teller technique (BET) after degassing the MOF powder under vacuum at 100 °C overnight. Crystallinity was evaluated by performing powder X-ray diffraction (PXRD) at λ (Cu K α) of 1.5406 Å. Thermal stability was studied by thermogravimetric analysis (TGA). The amount of trimesate and ATP in the supernatant collected after nanoMOF degradation was determined by high-performance liquid chromatography (HPLC) following a published procedure.³⁷ The amount of CD-P in the supernatant was determined by NMR spectroscopy, performed at 9.4 T on a Bruker Avance spectrometer equipped with a probe head of 5 mm. The chemical shifts were referenced to tetramethylsilane for ¹H and ¹³C. The coordination structure of nanoMIL-100(Fe) was studied by XANES spectroscopy recorded at the K-edge of Fe at 7112 eV at the SAMBA beamline in Synchrotron SOLEIL, France. The experimental details are reported in the [Supporting Information](#) (SI).

The coordination structure of nanoMIL-100(Al) was studied by magic-angle spinning (MAS) NMR spectroscopy performed at 11.7 T on a Bruker NEO NMR WB spectrometer equipped with probe heads of 4 and 3.2 mm, except for the ³¹P-²⁷Al 2D NMR measurement, which was recorded at 17.6 T with a 4 mm probe head. The chemical shifts were referenced to tetramethylsilane for ¹H and ¹³C, to Al(NO₃)₃ 1 M

solution for ²⁷Al, and to H₃PO₄ 85 wt % solution for ³¹P. [Table S1](#) in the SI reports the details of NMR experiments.

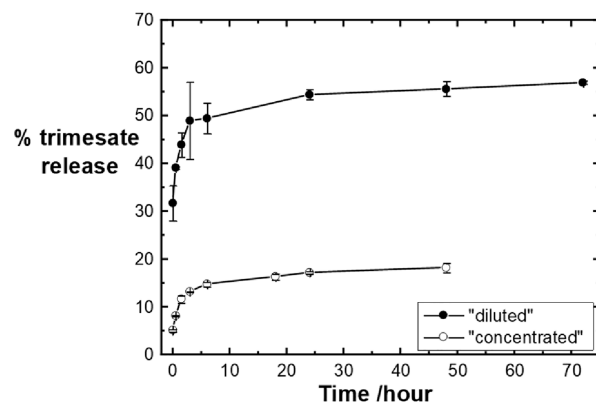


Figure 2. Kinetics of trimesate release, represented by the proportion of trimesate detected in the supernatant after degradation over the initial trimesate content in nanoMIL-100(Al). Two degradation conditions were named “diluted” (0.5 mg mL⁻¹ MOF in PBS 1 mM) and “concentrated” (10 mg mL⁻¹ MOF in PBS 10 mM).

3. RESULTS AND DISCUSSION

3.1. Preparation and Characterization of NanoMIL-100(Al). The first step of this study was the synthesis of nanoMIL-100(Al) suspensions adequate as drug carriers, *i.e.*, having a diameter lower than 200 nm and uniform size distribution. However, following a published procedure,⁵² the obtained MIL-100(Al) suspension had an inhomogeneous size distribution. Therefore, we used an additional size separation step and successfully prepared nanoMIL-100(Al) with a hydrodynamic diameter *Z*-average of 147 ± 14 nm and polydispersity index PDI of 0.10 ± 0.02 ([Figure S1](#)). TEM images ([Figure 3a,c](#) and [Figure S2](#)) also displayed solid nanoMIL-100(Al) particles with a uniform shape and size (88 ± 25 nm). The nanoparticle size was overestimated by DLS because in DLS, the average nanoparticle diameter is determined from scattered light intensity and large objects scatter more light than small ones.⁵⁴ The chemical composition of the obtained nanoMIL-100(Al) was analyzed by TGA ([Figure S4](#)). It also showed good crystallinity (XRD pattern in [Figure S5](#)) and a BET surface area of 1770 m² g⁻¹ (N₂ adsorption isotherm in [Figure S3a](#)), which agree with the published studies of MIL-100(Al).^{7,52} ¹H and ¹³C MAS NMR spectra in [Figures S6](#) and [S7](#) show typical features for MIL-100(Al) materials.

A recent study by our group detected an extra ²⁷Al peak in MIL-100(Al) nanoparticles, which was not detected in the previous study of MIL-100(Al) microparticles.⁷ This extra peak represents the surface Al sites in MIL-100(Al) nanoparticles, indicated by high-field NMR experiments ³¹P-²⁷Al D-HMQC and ²⁷Al 2D MQMAS.²⁴ These surface species were reproduced in this study ([Figure S8](#)) and are expected to play a crucial role in the degradation of nanoMIL-100(Al).

3.2. Degradation Mechanism of NanoMIL-100(Al). In the second step of this study, nanoMIL-100(Al) was incubated in PBS, composed of phosphate monobasic and dibasic salts, at 37 °C to mimic the physiological medium. All measurements were performed *ex situ* by recovering the nanoparticles from suspension in PBS after a given degradation period.

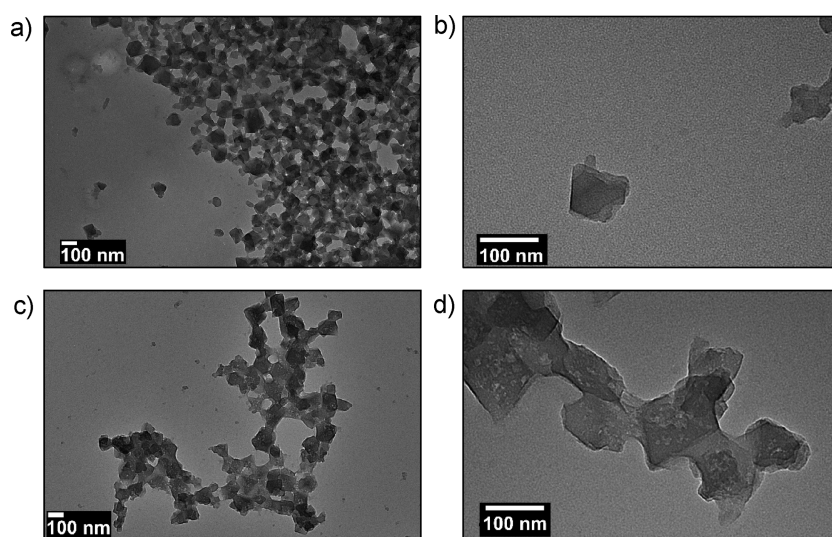


Figure 3. TEM images of intact nanoMIL-100(Al) at (a) 10k and (b) 30k magnification. TEM images of degraded nanoMIL-100(Al) at (c) 10k and (d) 30k magnification. Degradation was carried out with the “diluted” condition: 0.5 mg mL^{-1} nanoMOF in PBS 10 mM.

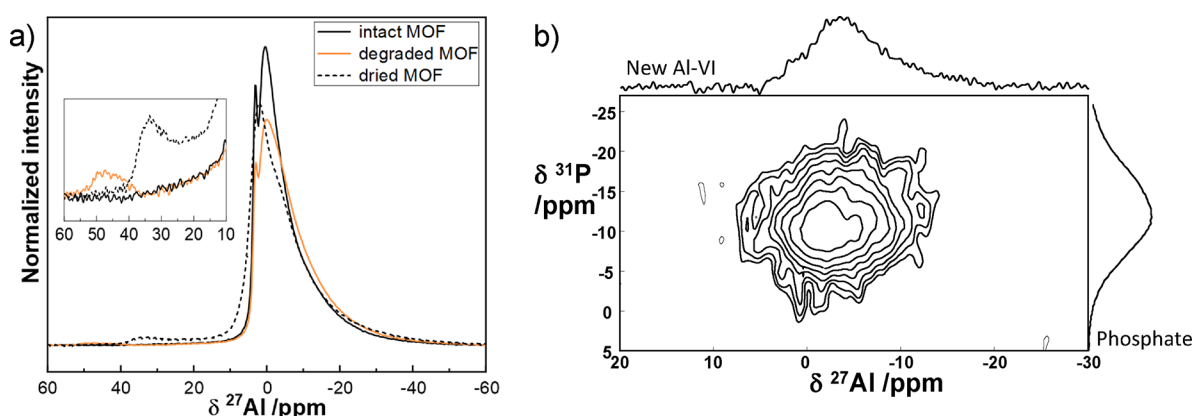


Figure 4. (a) ^{27}Al MAS NMR spectra of intact (solid black line), degraded (orange), and dehydrated (black dash line) nanoMIL-100(Al). The inset graph shows the 40 ppm region corresponding to the 4- and 5-coordinate Al(III). (b) 2D ^{31}P - ^{27}Al 2D MAS NMR spectrum of degraded MOF in excess PBS.

As a first step, to choose the suitable conditions for the NMR investigation, we determined the degradation kinetics of nanoMIL-100(Al) and the formation of trimesate by using HPLC. We chose two degradation conditions, “concentrated” (10 mg mL^{-1} nanoMIL-100(Al) in PBS 10 mM, 2 days) and “diluted” (0.5 mg mL^{-1} nanoMIL-100(Al) in PBS 1 mM, 2 days). In the “concentrated” condition, the molar ratio of phosphate/ Al_3 trimer (P/Al_3) is 0.54:1, meaning that nanoMIL-100(Al) is in excess, whereas in the “diluted” condition, P/Al_3 is 11:1, and PBS is in excess compared to nanoMIL-100(Al). The percentage of released trimesate upon degradation in PBS is shown in Figure 2. As expected, the release profile of trimesate from nanoMIL-100(Al) had a similar pattern with MIL-100(Fe) and consisted of two stages. In the first 3 h after incubation in PBS, there was a rapid generation of trimesic acid. Subsequently, the degradation reaction rate decreased gradually in the next 24 h and reached equilibrium after 48–72 h. This plateau of trimesate release after a given period was also observed in other works dealing with MIL-100(Fe).^{11,16,18}

There could be two explanations for this degradation plateau: (1) insufficient amount of phosphate to react with nanoMIL-100(Al) or (2) another mechanism preventing the reaction from proceeding further. The first explanation was supported by the

fact that the trimesate release was higher in the “diluted” degradation, where the ratio P/Al_3 was higher than in the “concentrated” degradation. To investigate further the limitation step of the nanoMIL-100 degradation reaction, the morphology and structure of the degraded nanoMOF were characterized.

The modification of nanoMIL-100(Al) morphology after 48 h degradation is shown in Figure 3b,d and Figure S9. The degraded nanoMIL-100(Al) retained their initial faceted shape and size distribution $98 \pm 24 \text{ nm}$, similar to the degraded nanoMIL-100(Fe) in ref 37. However, the degraded nanoMIL-100(Al) had holes on its surface, which is somewhat different from the degraded nanoMIL-100(Fe), whose TEM images displayed particles with rounded edges and without holes at the surface. Meanwhile, the crystal structure of the degraded nanoMIL-100(Al) did not change, shown by PXRD (Figure S10), which is similar to MIL-100(Fe) degradation.¹¹

More importantly, solid-state NMR spectroscopy demonstrates significant changes in the coordination sphere of nanoMIL-100(Al) after 48 h degradation, indicated by the evolution of ^{27}Al MAS NMR spectra (Figure 4a). The first noticeable change is the growth of the ^{27}Al resonance around -2 ppm , a chemical shift characteristic of 6-coordinate Al cations

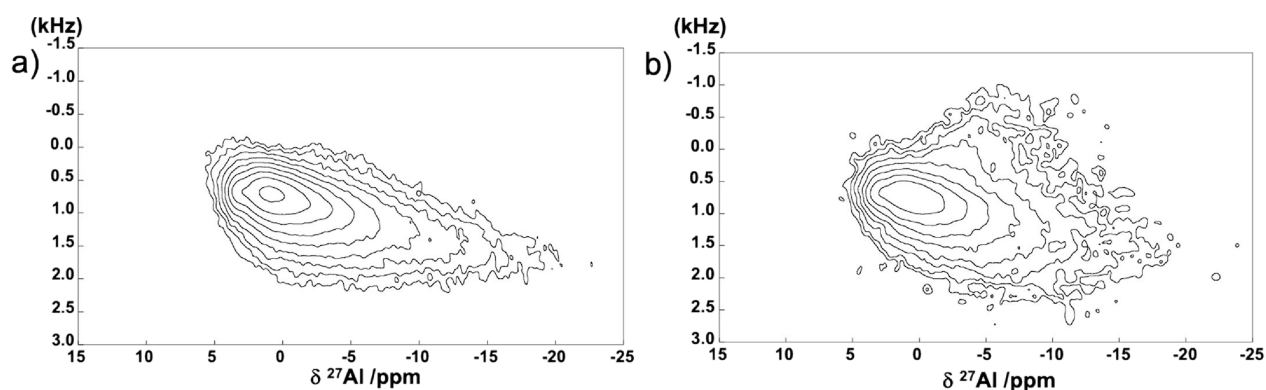


Figure 5. ^{27}Al MQMAS spectra of (a) original and (b) degraded nanoMIL-100(Al).

coordinated to phosphate ions, coming from the MIL-100(Al) trimer and the degradation medium PBS, respectively. The presence of this new coordination mode for the 6-fold aluminum was confirmed in the ^{27}Al multiple-quantum MAS (MQMAS) NMR spectrum of the degraded nanoparticles (Figure 5). The formation of the Al-O-P bond was further evidenced by the ^{31}P - ^{27}Al 2D MAS NMR spectrum (Figure 4b), which showed a correlation peak between this ^{27}Al resonance at -2 ppm and the ^{31}P resonances around -10 ppm (Figure S11). This ^{31}P - ^{27}Al correlation peak indicates close spatial proximity within 5 Å between these two nuclei, which fits the Al-O-P bond distance. It was also confirmed by ^1H - ^{31}P and ^1H - ^{27}Al 2D NMR spectroscopy (Figures S13 and S14), showing, in the degraded MIL-100(Al), the proximity between the phosphorus and the protons of the linker and between the new 6-coordinate Al(III) and the trimesate linker. Note that this degraded Al species still remains in the 6-coordination state as in the original MIL-100(Al) trimer, indicating that substitution of an existing ligand such as water or trimesate occurred. Trimesate is a stronger Lewis base than water, and thus the metal–ligand bond Al-O-H between Al(III) and water is more easily broken than the metal–ligand bond Al-O-C between Al(III) and trimesate. As a result, phosphate ions from PBS should first replace the water ligand and form a strong Al-O-P coordination bond with an Al(III) center. Then, due to an increase in interaction between the Al metal center and the newly bonded phosphate ligand, the interaction of the Al center with the trimesate ligands decreases. As the connection Al-O-C between carboxylic groups of the trimesate and Al weakens, phosphate can also attack and replace the position of carboxylate. Free trimesic acid is liberated when all six Al-O-C bonds between a trimesate linker and Al trimers are disconnected.

Notably, the 1D ^{27}Al MAS NMR spectrum of the degraded nanoMIL-100(Al) (Figure 4) shows another new Al species at 48 ppm, whose chemical shift lies between the range of 4- and 5-coordinate aluminum cations. A decrease in the coordination number of aluminum cations in MIL-100(Al) is a known phenomenon observed when heating the sample above 150 °C. As in the study of Haouas *et al.*,⁵⁵ we also found that the coordinated water ligands were removed by heating, thus creating 5-coordinate Al cations with a ^{27}Al chemical shift of 34 ppm (Figure 4). When the dehydrated MIL-100(Al) re-adsorbed water from ambient air, this 5-coordinate Al cation returned back 6-fold coordination without modifying the framework. However, in the degraded MIL-100(Al), the degraded low-coordinate Al had a higher chemical shift of 48 ppm, and this chemical shift did not change when the sample

was exposed to air or heated above 150 °C (Figure S12), implying that this low-coordinate Al site no longer coordinates with water ligands. As Al(III) species bonded with phosphate usually have lower ^{27}Al chemical shifts than the same coordination number Al(III) species with no phosphate ligand due to a deshielding effect in NMR,⁵⁶ we hypothesize that these Al species at 48 ppm are 4-coordinate Al with at least one phosphate ligand. Such 4-coordinate-Al is favorable in basic pH but not in neutral pH of PBS^{56,57} (further explanation in the SI), which could explain why these species have very low intensity in the ^{27}Al NMR spectrum. When the nanoMIL-100(Al) was degraded in excess PBS (“diluted” condition), the intensity of the 4-coordinate ^{27}Al peak increased slightly, and even a new 5-coordinate ^{27}Al peak was observed around 22–25 ppm (Figure 6). Therefore, we ruled out the possibility of an intermediate

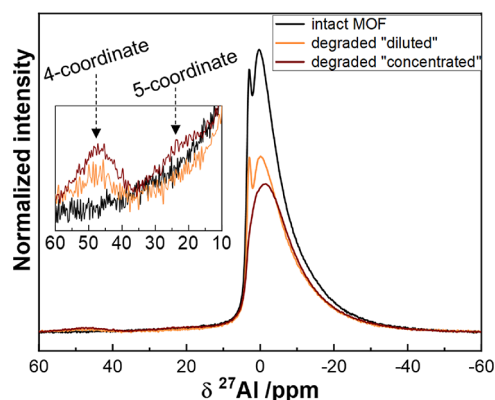


Figure 6. ^{27}Al MAS NMR of the degraded nanoMIL-100(Al) at the “diluted” and “concentrated” conditions, demonstrating the effect of increasing the P/ Al_3 ratio on the nanoMOF degradation reaction. The arrows indicate the position of 4- and 5-coordinate aluminum species.

product, and we assigned these 4- and 5-coordinate ^{27}Al resonances to an inorganic aluminum phosphate AlPO_4 .^{58,59} As the 4- and 5-coordinate ^{27}Al peaks only account for 1% of the total Al amount, the amount of these degradation products is low, and their formation may happen only at the surface. If these 4- and 5-coordinate aluminophosphate form a non-porous layer, this layer can passivate the nanoMIL-100(Al) surface, preventing phosphate from reacting with nanoMIL-100(Al), thus slowing down the degradation reaction. Blocked access to the nanoMIL-100(Al) was supported by a 10-time decrease in BET surface area (Figure S3). The existence of this passivation

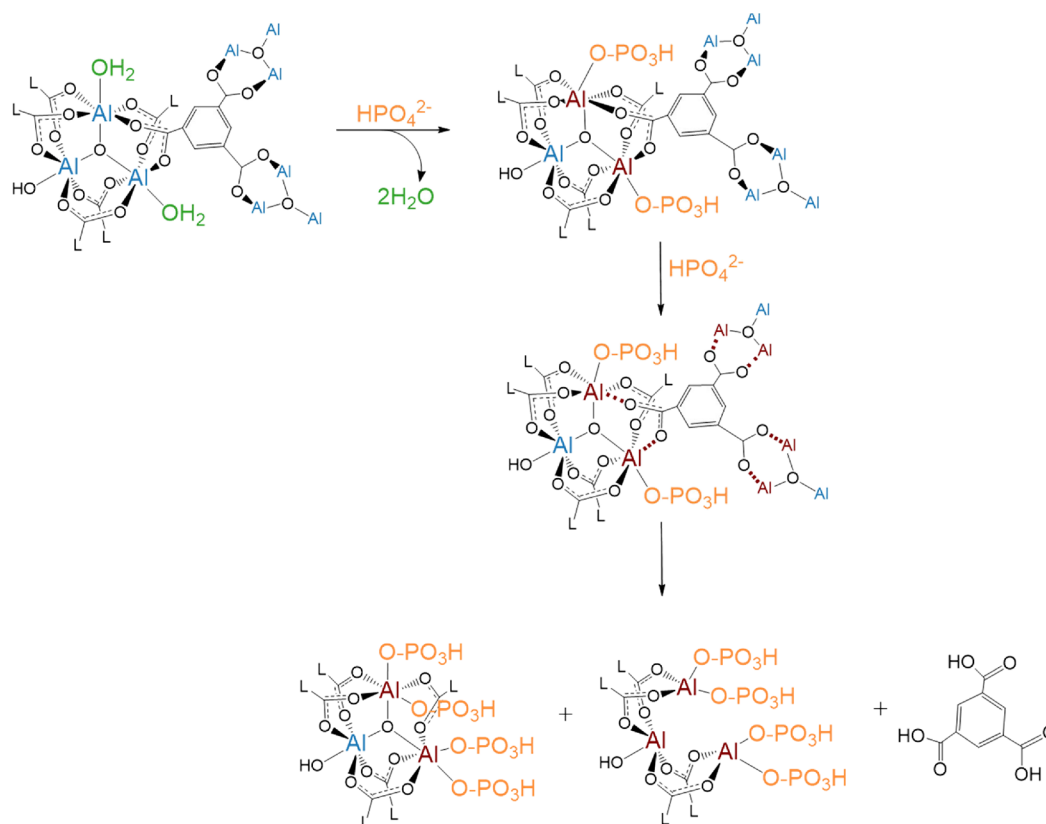


Figure 7. Proposed degradation mechanism of nanoMIL-100(Al) in phosphate buffer solution.

layer may explain why degradation and trimesate release reached a plateau after 48 h as determined by HPLC (Figure 2).

The present ssNMR study about nanoMIL-100(Al) so far agrees with the hypothesis of Li *et al.* about nanoMIL-100(Fe)³⁷ that the aluminum/iron phosphate complex is the degradation product of nanoMIL-100 reacting with phosphate buffer PBS. While Li *et al.* could only hypothesize the formation of iron phosphate and iron oxide hematite and goethite,³⁷ the present study offers concrete evidence about the structure of the degraded nanoMIL-100(Al) by showing the coordination states of Al and the likely formation of the Al-O-P bond in the degradation product.

To summarize, we propose for the first time a molecular mechanism of nanoMIL-100(Al) degradation in the mimicking biological medium PBS as follows (Figure 7):

- 1) Phosphate ions in PBS attack the nanoMIL-100(Al) surface, substitute labile water ligands of MIL-100(Al), and form a coordination Al–O–P bond with MIL-100(Al). Consequently, the Al–O–C coordination bonds between the MIL-100(Al) trimer and trimesate linker are weakened.
- 2) Phosphate ions substitute the carboxylate of a trimesate linker. As the substitution of water and trimesate continues, the formation of 6-fold aluminum atoms with a new coordination sphere (i.e., aluminum bonded with 1 to 2 phosphate groups) continues, producing the main degradation products of nanoMIL-100(Al). The release of free trimesic acid starts when all six Al–O–C bonds between a trimesate linker and Al trimers are broken.
- 3) New 4- and 5-coordinate Al species are produced, most likely as a layer of inorganic aluminum phosphate AlPO_4

on the nanoMIL-100(Al) surface, due to cleavage of the trimesate linker and the aluminum-oxo center.

- 4) After 6 h, the insoluble aluminum phosphate species AlPO_4 passivate the MOF pore and pore window. The intact trimers of nanoMIL-100(Al) are no longer exposed to a high amount of phosphate. As a result, the degradation reaction reaches equilibrium, and the release of trimesate reaches the maximum.

3.3. Degradation Mechanism of Drug-Loaded and Surface-Coated NanoMIL-100(Al)

In the final step, we analyzed the effect of surface coating and drug loading on the nanoMIL-100(Al) degradation processes. As reported in the literature, the presence of loaded drug and surface coating could alter the physicochemical properties of nanoMOF,^{21,26} thus potentially affecting nanoMOF's degradation reaction.

NanoMIL-100(Al) was successfully loaded with adenosine triphosphate (ATP) at 18.6 ± 0.8 wt % and coated with β -cyclodextrin-phosphate (CD-P) at 28.3 ± 0.4 wt %. Before studying the degradation, the drug loading and surface coating quality were evaluated. The results of ²⁷Al and ³¹P MAS NMR in Figure S15a,b agree with our previous study.²⁴ ³¹P MAS NMR (Figure S17b) showed that the drug ATP is captured inside MIL-100(Al) by chemical adsorption through Al–O–P coordination. ²⁷Al MAS NMR (Figure S17a) showed that the CD-P coating is located at the surface and does not penetrate the MOF core. The integrity of the trimesate framework was checked by TEM and ¹³C MAS NMR (see Figures S16 and S18, respectively). From now on, we denote in the figures below the CD-P-surface-coated nanoMIL-100(Al) as MOF-coated, the ATP-drug-loaded nanoMIL-100(Al) as MOF-loaded, and the ATP-drug-loaded-CDP-surface-coated nanoMIL-100(Al) as MOF-loaded-coated.

Degradation of the CD-P coated nanoMIL-100(Al) is similar to degradation of the non-coated one. In Figure 8, the ^{27}Al MAS

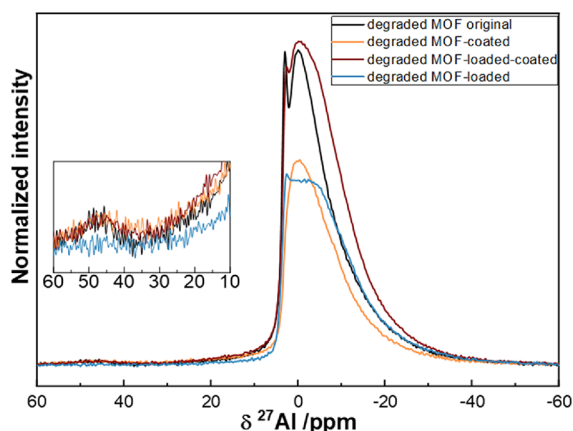


Figure 8. ^{27}Al MAS NMR spectra of degraded original and degraded modified nanoMIL-100(Al), presenting the impact of drug encapsulation and surface coating on the nanoMOF degradation.

NMR spectrum of the degraded MOF-CD-P- shows both the hexa-coordinate Al-O-P around -2 ppm and the tetra-coordinate aluminophosphate at 48 ppm. Observing a similar degradation product, we speculate that, as CD-P covers approximately 30% of the nanoMIL-100(Al) surface,²⁶ a degradation reaction still occurs at the nanoMOF's surface not attached to CD-P, following the reaction mechanism proposed in the previous section.

Additionally, the ^{31}P MAS NMR spectrum of the degraded MOF-CD-P- in Figure 9a displays a shoulder around -10 ppm, which belongs to CD-P, and the dominant signal of the phosphate coordinated with the MIL-100(Al) framework around -15 ppm. The presence of CD-P coating even after 5 days of degradation suggests that CD-P competes with inorganic phosphate ions to complex with Al(III). Consequently, PBS phosphates can only partially displace CD-P.

Meanwhile, the degradation reaction of the ATP-loaded nanoMIL-100(Al) exhibits features distinctive from that of the empty nanoMOF. No sign of low-coordinated Al was detected. ^{27}Al NMR (Figure 8) still showed the 6-coordinate Al species around -2 ppm as the main degradation product, while the Al species bonded with phosphate ATP was still present. Likewise, the ^{31}P MAS NMR spectrum in Figure 9b shows both a peak of

coordinated PBS phosphate and a shoulder signal of ATP. Both ^{27}Al and ^{31}P NMR data consistently suggest that nanoMIL-100(Al) loaded with ATP is less degraded than the empty one, and only a part of ATP is liberated from the framework. Similar to the surface coating CD-P, the loaded drug ATP competes with inorganic PBS phosphates to coordinate the Al(III) of nanoMIL-100(Al). The triphosphate ATP is a much stronger complexing ligand toward Al(III) than the hydrogen phosphate and dihydrogen phosphate ions,⁶⁰ meaning that MIL-100(Al) forms a more stable coordination complex with ATP than with phosphate ions. Therefore, it is difficult to break the coordination between ATP and Al(III) by solely phosphate PBS, which explains the presence of ATP in the ^{31}P NMR spectrum, even after days of degradation. However, the strong Al-O-P bond between Al(III) and ATP makes the Al-O-C bond between Al(III) and the trimesate linker more easily attacked by phosphate. We hypothesize that phosphate attacks the Al-O-C bond with trimesate, forming hexa-coordinate Al-O-P in the region -2 to -5 ppm observed in the ^{27}Al spectrum. When the Al center forms a new coordination bond with inorganic phosphate, its coordination bond with ATP is weakened. As a result, the probability is higher for phosphate to displace ATP from the framework. Another factor to be considered is the steric effect caused by ATP. Bulky ATP possibly hinders phosphate diffusion in the MIL-100(Al) trimer, thus preventing trimesate substitution.

In addition, the notable absence of the low-coordinate aluminophosphate can be explained by the chelating capability of triphosphate ATP.^{61,62} ATP coordinates with MIL-100(Al) through the terminal γ -phosphorus. During the breaking of the Al-O-C bond, the β -phosphorus of ATP can compete with phosphate PBS ions and create a second coordination bond with Al. The bidentate Al-ATP coordination not only halts the formation of low-coordinate Al but also prevents the 100% release of ATP. Consistently, only 60% ATP was released in excessive PBS, while 100% of trimesate ligand was found by HPLC (data not shown).

Finally, combining the effect of drug encapsulation and surface coating, Figure 8 shows that degradation of the ATP-loaded CD-P-surface-coated nanoMIL-100(Al) produces both the 6-coordinate aluminophosphate complex and 4-coordinate inorganic aluminophosphate but with a slightly lower proportion of 4-coordinate degraded complex (1.0%) than that in the surface-coated empty nanoMIL-100(Al) (1.6%). Also, the ^{27}Al peak at 2.5 ppm belonging to the original

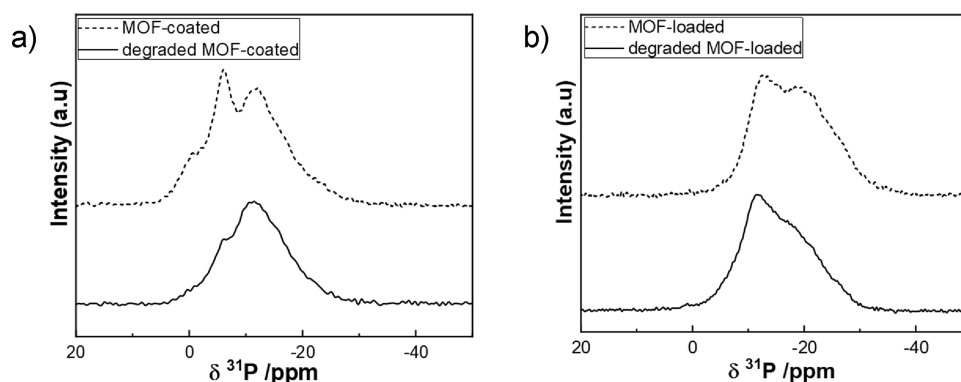


Figure 9. ^{31}P MAS NMR of (a) degraded CD-P-coated MIL-100(Al) compared to CD-P-coated MIL-100(Al) and (b) degraded ATP-loaded-MIL-100(Al) compared to ATP-loaded-MIL-100(Al). CD-P and ATP are still present in the degraded nanoMOF after 4–5 days of degradation.

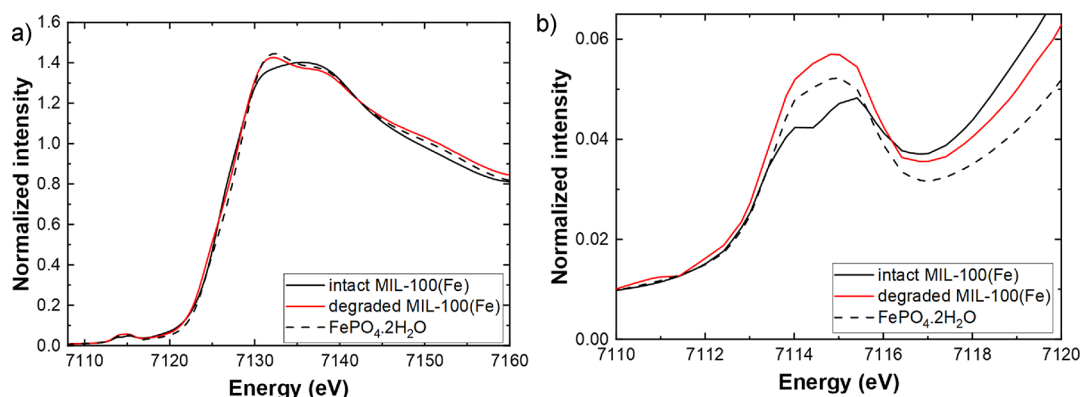


Figure 10. (a) Normalized Fe K-edge XANES spectra and (b) zoomed in pre-edge region of degraded nanoMIL-100(Fe) compared with original nanoMIL-100(Fe) and iron(III) phosphate dihydrate.

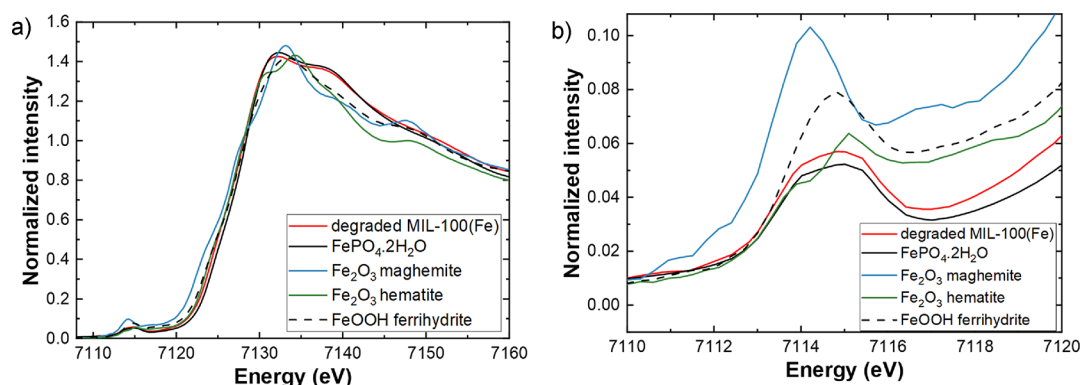


Figure 11. (a) Normalized Fe K-edge XANES spectra and (b) zoomed in pre-edge region of degraded nanoMIL-100(Fe) compared with several Fe(III) possible degradation products, such as iron phosphate, iron oxides, and iron oxyhydroxide.

nanoMIL-100(Al) is more preserved in the degraded one in the presence of the drug ATP.

In summary, the degradation reaction of the modified MOF including the ATP-loaded and the CD-P-surface-coated nanoMIL100(Al) can be summarized as follows:

- 1) Surface coating with CD-P has a negligible effect on the degradation of nanoMIL-100(Al). 6-Coordinate and 4-coordinate aluminum complexes with phosphate are formed as described in the degradation mechanism of the original nanoMIL-100(Al).
- 2) Encapsulation of ATP inside nanoMIL-100(Al) impacts significantly the nanoMOF degradation. Degradation of ATP-loaded nanoMIL-100(Al) starts with the substitution of the trimesate Al-O-C bond, thus producing hexa-coordinate aluminophosphate and free trimesate. However, the bulky ATP limits the amount of trimesate release. The coordination of PBS phosphate with the Al trimer facilitates the dissociation of the Al-O-P bond with ATP. Then, phosphate from PBS replaces the bonded ATP, leading to the release of free ATP. During the bond dissociation process, the coordinated ATP can make the second coordination bond with the degraded Al trimer. Consequently, no low-coordinated Al is created, and ATP is not entirely released.

3.4. Degradation Mechanism of NanoMIL-100(Fe) in Comparison with NanoMIL-100(Al). To evaluate whether our proposed degradation mechanism applies to the iron MIL-100 analog, nanoMIL-100(Fe), XANES spectroscopy was used to study the *ex situ* degradation of the original, CD-P surface-

coated, and ATP-loaded nanoMIL-100(Fe). Similar to nanoMIL-100(Al), nanoMIL-100(Fe) was incubated in PBS at 37 °C, and then, the degraded nanoparticles were recovered after 48 h. A “very diluted” condition (0.5 mg mL⁻¹ nanoMIL-100(Fe) in PBS 10 mM) was used to produce as much as possible degraded MIL-100(Fe) species.

The evolution of original nanoMIL-100(Fe) after degradation is shown in Figure 10. The XANES Fe K-edge spectrum of the degraded nanoMIL-100(Fe) is reminiscent of that of iron(III) phosphate dihydrate, a substance having 6-coordinate iron(III) bonds with phosphate through the Fe-O-P bond.⁶³ This similarity is also observed in the pre-edge region, where the intact MIL-100(Fe) shows two features at 7114 and 7115.4 eV, while the degraded MIL-100(Fe) and FePO₄·2H₂O only show a single, broad peak at 7114.9 eV. Moreover, the XANES spectrum of this degraded nanoMIL-100(Fe) is different from those of iron(III) oxide and iron(III) oxyhydroxide, excluding their presence in the degraded nanoMIL-100(Fe) (Figure 11). Therefore, we propose that the first step of nanoMIL-100(Fe) degradation also forms an iron-phosphate-6-coordinate species with the Fe-O-P coordination bond, in the same way as illustrated in Figure 7, where phosphate from PBS replaces the water ligand of nanoMIL-100(Fe) and coordinates with Fe(III). The 4-coordinate iron phosphate species were not detected due to its low amount, probably 1% of iron in the degraded nanoMIL-100(Fe). Note that nanoMIL-100(Fe) also became less porous after degradation (Figure S19) with a smaller decrease (50% decrease) in the BET surface area than in nanoMIL-100(Al) (90% decrease).

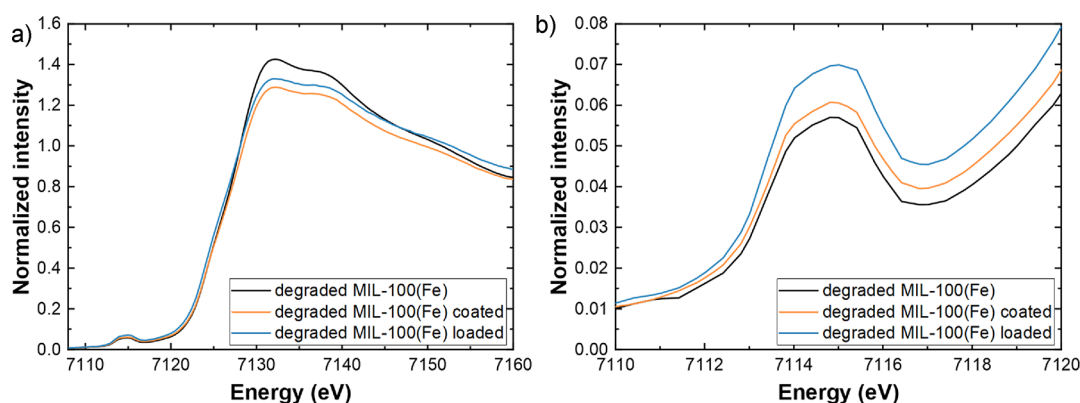


Figure 12. (a) Normalized Fe K-edge XANES spectra of degraded original and modified nanoMIL-100(Fe) and (b) zoomed in pre-edge region.

In addition, after a degradation reaction, the oxidation number of Fe in nanoMIL-100(Fe) does not change and remain as +III, as the degraded and original nanoMIL-100(Fe) have the same edge position (Figure 10a), and the edge position of nanoMIL-100(Fe) is close to the values of Fe(III) compounds (Figure S20). Previously observed by other authors using Mossbauer spectroscopy,³⁷ this maintenance of Fe oxidation number after nanoMIL-100(Fe) degradation is consistent with our proposed degradation mechanism based on the model nanoMIL-100(Al) (Figure 7), which describes degradation as an acid–base reaction.

The effect of ATP drug loading and CD-P surface coating on the nanoMIL-100(Fe) degradation was also investigated. Figure S21 shows that the ATP-drug-loaded and CD-P-surface-coated nanoMIL-100(Fe) share the same XANES features as the original one, indicating that drug loading and surface coating do not degrade nanoMIL-100(Fe). Figure 12 shows that degradation of drug-loaded and surface-coated nanoMIL-100(Fe) produces similar species as obtained from the degradation of the original one, as all three XANES and pre-edge spectra have similar shapes and features. Once again, XANES spectroscopy shows that 6-coordinate iron-phosphate was formed during the degradation reaction of nanoMIL-100(Fe).

This complementary study with XANES suggests that the first step in degradation of nanoMIL-100(Fe) likely follows the degradation reaction of its aluminum analog, corroborating the ssNMR study on nanoMIL-100(Al).

4. CONCLUSIONS

By using solid-state NMR spectroscopy, we obtained novel knowledge about the degradation mechanism of nanoMIL-100(Al) and nanoMIL-100(Fe) in phosphate buffer. For the first time, we find direct evidence about the change of the metal coordination sphere and the limiting reaction step in the nanoMIL-100 degradation mechanism. First, upon substitution of labile water ligands by phosphate, Al-O-P coordination bonds are formed between aluminum species at the surface of nanoMOF and phosphate from the medium, creating 6-coordinate aluminophosphate. Second, the substitution of trimesate by phosphate leads to the release of free trimesate and creates 4-coordinate inorganic aluminum phosphate. This 4-coordinate aluminum, which has not been observed before, can passivate the nanoMOF surface and slow down the degradation reaction. Additionally, our study demonstrates that chemical modification such as drug encapsulation and surface coating can impact the nanoMOF degradation and

hence its drug release process as a function of metal–ligand bond strength.

To conclude, insights about the degradation mechanism of nanoMOF from this work contribute to the understanding of MOF chemistry and help optimizing the performance of nanoMOF drug carriers. This study also highlights the useful role of ssNMR spectroscopy with the support of XANES spectroscopy in investigating in depth the nanoMOF structure. Using ssNMR spectroscopy, we were able to obtain enough evidence about the coordination sphere and the reaction limiting step of nanoMIL-100(Al) degradation, while XANES spectroscopy provided complementary proof on the reaction of nanoMIL-100(Fe). The obtained knowledge in this study prompts new studies on understanding drug delivery chemistry and developing characterization tools for drug nanocarriers. Comparative studies of MIL-100(Al) and MIL-100(Fe) are being carried out to investigate the behaviors of MIL-100 analogs. Various types of drug compounds can be explored when different host–guest interactions and degradation behaviors are expected. In the future, we will develop a new NMR spectroscopy method to monitor *in situ* drug delivery processes of nanoMOF.

■ ASSOCIATED CONTENT

Supporting Information

The Supporting Information is available free of charge at <https://pubs.acs.org/doi/10.1021/acs.chemmater.2c01190>.

- (1) Experimental procedures of nanoMOF preparation and characterization, (2) standard characterization of nanoMIL-100(Al): DLS, TEM, XRD, BET, TGA, and ¹H MAS NMR, ¹³C MAS NMR, ²⁷Al MAS, and MQMAS NMR spectra, and (3) complementary NMR measurements on degraded nanoMIL-100(Al): ³¹P, ¹H-³¹P, and ¹H-²⁷Al (PDF)

■ AUTHOR INFORMATION

Corresponding Authors

Ruxandra Gref – Institut des Sciences Moléculaires d'Orsay, Université Paris-Saclay, CNRS, 91405 Orsay, France; orcid.org/0000-0002-7869-0908; Email: ruxandra.gref@universite-paris-saclay.fr

Charlotte Martineau-Corcoss – Institut Lavoisier de Versailles, Université Paris-Saclay, UVSQ, CNRS, 78000 Versailles, France; Present Address: CortecNet, 7 avenue du Hoggar, 91940 Les Ulis, France (C.M.-C.); orcid.org/0000-0003-1887-1042; Email: ccorcoss@cortecnet.com

Authors

Mai Dang Le Vuong – Institut Lavoisier de Versailles, Université Paris-Saclay, UVSQ, CNRS, 78000 Versailles, France; Institut des Sciences Moléculaires d'Orsay, Université Paris-Saclay, CNRS, 91405 Orsay, France

Ioanna Christodoulou – Institut des Sciences Moléculaires d'Orsay, Université Paris-Saclay, CNRS, 91405 Orsay, France

Marianna Porcino – Conditions Extrêmes et Matériaux: Haute Température et Irradiation (CEMHTI), CNRS UPR 3079, Université d'Orléans, CNRS, 45071 Orléans, France

Si-Thanh Dong – Synchrotron SOLEIL, 91192 Gif-sur-Yvette, France

Benedikt Lassalle-Kaiser – Synchrotron SOLEIL, 91192 Gif-sur-Yvette, France; orcid.org/0000-0003-2141-2496

Mohamed Haouas – Institut Lavoisier de Versailles, Université Paris-Saclay, UVSQ, CNRS, 78000 Versailles, France;

orcid.org/0000-0002-2133-702X

Complete contact information is available at:

<https://pubs.acs.org/10.1021/acs.chemmater.2c01190>

Author Contributions

C.M.-C. and R.G. conceived the idea and designed the experiments. M.V. and I.C. synthesized and characterized the materials. M.P. performed the high-field MAS NMR spectroscopy experiments. M.V., B.L.-K., and S.-T.D. performed and analyzed XANES spectroscopy measurement. M.V. and C.M.-C. analyzed data. All authors participated in the data discussion. M.V. wrote the manuscript, and all authors revised the manuscript. All authors have approved the final version of the manuscript.

Notes

The authors declare no competing financial interest.

ACKNOWLEDGMENTS

Financial support from the IR-RMN-THC Fr3050 CNRS for conducting the research is gratefully acknowledged. This work was also supported by the Paris Ile-de-France Region – DIM “Respire”. The present work has benefited from Imagerie-Gif core facility supported by l'Agence Nationale de la Recherche (ANR-11-EQPX-0029/Morphoscope, ANR-10-INBS-04/FranceBioImaging; ANR-11-IDEX-0003-02/ Saclay Plant Sciences). We also thank the beamline scientists and staffs at the SAMBA beamline for assistance. M.P. and C.M.-C thank Dr. Vincent Sarou-Kanian (CEMHTI Orléans) for support during the high-field NMR experiments.

REFERENCES

- (1) Folkman, J.; Long, D. M. The Use of Silicone Rubber as a Carrier for Prolonged Drug Therapy. *J. Surg. Res.* **1964**, *4*, 139–142.
- (2) Horcajada, P.; Chalati, T.; Serre, C.; Gillet, B.; Sebrie, C.; Baati, T.; Eubank, J. F.; Heurtaux, D.; Clayette, P.; Kreuz, C.; et al. Porous Metal–Organic-Framework Nanoscale Carriers as a Potential Platform for Drug Delivery and Imaging. *Nat. Mater.* **2010**, *9*, 172–178.
- (3) Férey, G. Hybrid Porous Solids: Past, Present. *Future Chem. Soc. Rev.* **2008**, *37*, 191–214.
- (4) Furukawa, H.; Cordova, K. E.; O’Keeffe, M.; Yaghi, O. M. The Chemistry and Applications of Metal–Organic Frameworks. *Science* **2013**, *341*, 1230444.
- (5) Horike, S.; Shimomura, S.; Kitagawa, S. Soft Porous Crystals. *Nat. Chem.* **2009**, *1*, 695–704.
- (6) Horcajada, P.; Surlé, S.; Serre, C.; Hong, D.-Y.; Seo, Y.-K.; Chang, J.-S.; Grenèche, J.-M.; Margiolaki, I.; Férey, G. Synthesis and Catalytic Properties of MIL-100(Fe), an Iron(III) Carboxylate with Large Pores. *Chem. Commun.* **2007**, *27*, 2820–2822.

- (7) Volkringer, C.; Popov, D.; Loiseau, T.; Férey, G.; Burghammer, M.; Riekel, C.; Haouas, M.; Taulelle, F. Synthesis, Single-Crystal X-Ray Microdiffraction, and NMR Characterizations of the Giant Pore Metal–Organic Framework Aluminum Trimesate MIL-100. *Chem. Mater.* **2009**, *21*, 5695–5697.

- (8) Agostoni, V.; Horcajada, P.; Rodriguez-Ruiz, V.; Willaime, H.; Couvreur, P.; Serre, C.; Gref, R. “Green” Fluorine-Free Mesoporous Iron(III) Trimesate Nanoparticles for Drug Delivery. *Green Mater.* **2013**, *1*, 209–217.

- (9) Kökçam-Demir, Ü.; Goldman, A.; Esrafilı, L.; Gharib, M.; Morsali, A.; Weingart, O.; Janiak, C. Coordinatively Unsaturated Metal Sites (Open Metal Sites) in Metal–Organic Frameworks: Design and Applications. *Chem. Soc. Rev.* **2020**, *49*, 2751–2798.

- (10) Vitillo, J. G.; Gagliardi, L. Thermal Treatment Effect on CO and NO Adsorption on Fe(II) and Fe(III) Species in Fe₃O₄-Based MIL-Type Metal–Organic Frameworks: A Density Functional Theory Study. *Inorg. Chem.* **2021**, *60*, 11813–11824.

- (11) Christodoulou, I.; Bourguignon, T.; Li, X.; Patriarche, G.; Serre, C.; Marlière, C.; Gref, R. Degradation Mechanism of Porous Metal–Organic Frameworks by In Situ Atomic Force Microscopy. *Nanomaterials* **2021**, *11*, 722.

- (12) Horcajada, P.; Gref, R.; Baati, T.; Allan, P. K.; Maurin, G.; Couvreur, P.; Férey, G.; Morris, R. E.; Serre, C. Metal–Organic Frameworks in Biomedicine. *Chem. Rev.* **2012**, *112*, 1232–1268.

- (13) Quijia, C. R.; Lima, C.; Silva, C.; Alves, R. C.; Frem, R.; Chorilli, M. Application of MIL-100(Fe) in Drug Delivery and Biomedicine. *J. Drug Delivery Sci. Technol.* **2021**, *61*, No. 102217.

- (14) Rodriguez-Ruiz, V.; Maksimenko, A.; Anand, R.; Monti, S.; Agostoni, V.; Couvreur, P.; Lampropoulou, M.; Yannakopoulou, K.; Gref, R. Efficient “Green” Encapsulation of a Highly Hydrophilic Anticancer Drug in Metal–Organic Framework Nanoparticles. *J. Drug Targeting* **2015**, *23*, 759–767.

- (15) Li, X.; Salzano, G.; Qiu, J.; Menard, M.; Berg, K.; Theodossiou, T.; Ladavière, C.; Gref, R. Drug-Loaded Lipid-Coated Hybrid Organic-Inorganic “Stealth” Nanoparticles for Cancer Therapy. *Front. Biotechnol.* **2020**, *8*, 1027.

- (16) Unamuno, X.; Imbuluzqueta, E.; Salles, F.; Horcajada, P.; Blanco-Prieto, M. J. Biocompatible Porous Metal–Organic Framework Nanoparticles Based on Fe or Zr for Gentamicin Vectorization. *Eur. J. Pharm. Biopharm.* **2018**, *132*, 11–18.

- (17) Li, X.; Semiramo, N.; Hall, S.; Tafani, V.; Josse, J.; Laurent, F.; Salzano, G.; Foulkes, D.; Brodin, P.; Majlessi, L.; et al. Compartmentalized Encapsulation of Two Antibiotics in Porous Nanoparticles: An Efficient Strategy to Treat Intracellular Infections. *Part. Part. Syst. Charact.* **2019**, *36*, 1800360.

- (18) Agostoni, V.; Chalati, T.; Horcajada, P.; Willaime, H.; Anand, R.; Semiramo, N.; Baati, T.; Hall, S.; Maurin, G.; Chacun, H.; et al. Towards an Improved Anti-HIV Activity of NRTI via Metal–Organic Frameworks Nanoparticles. *Adv. Healthcare Mater.* **2013**, *2*, 1630–1637.

- (19) Taherzade, S. D.; Rojas, S.; Soleimannejad, J.; Horcajada, P. Combined Cutaneous Therapy Using Biocompatible Metal–Organic Frameworks. *Nanomaterials* **2020**, *10*, 2296.

- (20) Chalati, T.; Horcajada, P.; Couvreur, P.; Serre, C.; Ben Yahia, M.; Maurin, G.; Gref, R. Porous Metal Organic Framework Nanoparticles to Address the Challenges Related to Busulfan Encapsulation. *Nanomedicine* **2011**, *6*, 1683–1695.

- (21) Simon-Yarza, M. T.; Baati, T.; Paci, A.; Lesueur, L. L.; Seck, A.; Chiper, M.; Gref, R.; Serre, C.; Couvreur, P.; Horcajada, P. Antineoplastic Busulfan Encapsulated in a Metal Organic Framework Nanocarrier: First in Vivo Results. *J. Mater. Chem. B* **2016**, *4*, 585–588.

- (22) Feng, Y.; Wang, C.; Ke, F.; Zang, J.; Zhu, J. MIL-100(Al) Gels as an Excellent Platform Loaded with Doxorubicin Hydrochloride for PH-Triggered Drug Release and Anticancer Effect. *Nanomaterials* **2018**, *8*, 446.

- (23) Li, X.; Porcino, M.; Qiu, J.; Constantin, D.; Martineau-Corcoss, C.; Gref, R. Doxorubicin-Loaded Metal–Organic Frameworks Nanoparticles with Engineered Cyclodextrin Coatings: Insights on Drug

- Location by Solid State NMR Spectroscopy. *Nanomaterials* **2021**, *11*, 945.
- (24) Porcino, M.; Christodoulou, I.; Vuong, M. D. L.; Gref, R.; Martineau-Corcoss, C. New Insights on the Supramolecular Structure of Highly Porous Core–Shell Drug Nanocarriers Using Solid-State NMR Spectroscopy. *RSC Adv.* **2019**, *9*, 32472–32475.
- (25) Giménez-Marqués, M.; Bellido, E.; Berthelot, T.; Simón-Yarza, T.; Hidalgo, T.; Simón-Vázquez, R.; González-Fernández, Á.; Avila, J.; Asensio, M. C.; Gref, R.; et al. GraftFast Surface Engineering to Improve MOF Nanoparticles Furtiveness. *Small* **2018**, *14*, 1801900.
- (26) Agostoni, V.; Horcajada, P.; Noiray, M.; Malanga, M.; Aykaç, A.; Jicsinszky, L.; Vargas-Berenguel, A.; Semiramoth, N.; Daoud-Mahammed, S.; Nicolas, V.; et al. A “Green” Strategy to Construct Non-Covalent, Stable and Bioactive Coatings on Porous MOF Nanoparticles. *Sci. Rep.* **2015**, *5*, 1–7.
- (27) Cutrone, G.; Qiu, J.; Menendez-Miranda, M.; Casas-Solvas, J. M.; Aykaç, A.; Li, X.; Foulkes, D.; Moreira-Alvarez, B.; Encinar, J. R.; Ladavière, C.; et al. Comb-like Dextran Copolymers: A Versatile Strategy to Coat Highly Porous MOF Nanoparticles with a PEG Shell. *Carbohydr. Polym.* **2019**, *223*, No. 115085.
- (28) Hidalgo, T.; Giménez-Marqués, M.; Bellido, E.; Avila, J.; Asensio, M. C.; Salles, F.; Lozano, M. V.; Guillevic, M.; Simón-Vázquez, R.; González-Fernández, A.; et al. Chitosan-Coated Mesoporous MIL-100(Fe) Nanoparticles as Improved Bio-Compatible Oral Nanocarriers. *Sci. Rep.* **2017**, *7*, 43099.
- (29) Bellido, E.; Hidalgo, T.; Lozano, M. V.; Guillevic, M.; Simón-Vázquez, R.; Santander-Ortega, M. J.; González-Fernández, A.; Serre, C.; Alonso, M. J.; Horcajada, P. Heparin-Engineered Mesoporous Iron Metal-Organic Framework Nanoparticles: Toward Stealth Drug Nanocarriers. *Adv. Healthcare Mater.* **2015**, *4*, 1246–1257.
- (30) Aykaç, A.; Noiray, M.; Malanga, M.; Agostoni, V.; Casas-Solvas, J. M.; Fenyvesi, É.; Gref, R.; Vargas-Berenguel, A. A Non-Covalent “Click Chemistry” Strategy to Efficiently Coat Highly Porous MOF Nanoparticles with a Stable Polymeric Shell. *Biochim. Biophys. Acta, Gen. Subj.* **2017**, *1861*, 1606–1616.
- (31) Qiu, J.; Li, X.; Rezaei, M.; Patriarche, G.; Casas-Solvas, J. M.; Moreira-Alvarez, B.; Costa Fernandez, J. M.; Encinar, J. R.; Savina, F.; Picton, L.; et al. Porous Nanoparticles with Engineered Shells Release Their Drug Cargo in Cancer Cells. *Int. J. Pharm.* **2021**, *610*, No. 121230.
- (32) Ruyra, Á.; Yazdi, A.; Espín, J.; Carné-Sánchez, A.; Roher, N.; Lorenzo, J.; Imaz, I.; Maspoch, D. Synthesis, Culture Medium Stability, and In Vitro and In Vivo Zebrafish Embryo Toxicity of Metal-Organic Framework Nanoparticles. *Chem. – Eur. J.* **2015**, *21*, 2508–2518.
- (33) Grall, R.; Hidalgo, T.; Delic, J.; Garcia-Marquez, A.; Chevillard, S.; Horcajada, P. In Vitro Biocompatibility of Mesoporous Metal (III; Fe, Al, Cr) Trimesate MOF Nanocarriers. *J. Mater. Chem. B* **2015**, *3*, 8279–8292.
- (34) Baati, T.; Njim, L.; Neffati, F.; Kerkeni, A.; Bouttemi, M.; Gref, R.; Najjar, M. F.; Zakhama, A.; Couvreur, P.; Serre, C.; et al. In Depth Analysis of the In Vivo Toxicity of Nanoparticles of Porous Iron(III) Metal–Organic Frameworks. *Chem. Sci.* **2013**, *4*, 1597–1607.
- (35) Simon-Yarza, T.; Baati, T.; Neffati, F.; Njim, L.; Couvreur, P.; Serre, C.; Gref, R.; Najjar, M. F.; Zakhama, A.; Horcajada, P. In Vivo Behavior of MIL-100 Nanoparticles at Early Times after Intravenous Administration. *Int. J. Pharm.* **2016**, *511*, 1042–1047.
- (36) Bellido, E.; Guillevic, M.; Hidalgo, T.; Santander-Ortega, M. J.; Serre, C.; Horcajada, P. Understanding the Colloidal Stability of the Mesoporous MIL-100(Fe) Nanoparticles in Physiological Media. *Langmuir* **2014**, *30*, 5911–5920.
- (37) Li, X.; Lachmanski, L.; Safi, S.; Sene, S.; Serre, C.; Grenèche, J. M.; Zhang, J.; Gref, R. New Insights into the Degradation Mechanism of Metal-Organic Frameworks Drug Carriers. *Sci. Rep.* **2017**, *7*, 13142.
- (38) Bryce, D. L. NMR Crystallography: Structure and Properties of Materials from Solid-State Nuclear Magnetic Resonance Observables. *IUCr* **2017**, *4*, 350–359.
- (39) Lucier, B. E. G.; Chen, S.; Huang, Y. Characterization of Metal–Organic Frameworks: Unlocking the Potential of Solid-State NMR. *Acc. Chem. Res.* **2018**, *51*, 319–330.
- (40) Brunner, E.; Rauche, M. Solid-State NMR Spectroscopy: An Advancing Tool to Analyse the Structure and Properties of Metal–Organic Frameworks. *Chem. Sci.* **2020**, *11*, 4297–4304.
- (41) Xu, J.; Terskikh, V.; Huang, Y. Resolving Multiple Non-Equivalent Metal Sites in Magnesium-Containing Metal-Organic Frameworks by Natural Abundance ²⁵Mg Solid-State NMR Spectroscopy. *Chem. – Eur. J.* **2013**, *19*, 4432–4436.
- (42) Cooper, L.; Guillou, N.; Martineau, C.; Elkaim, E.; Taulelle, F.; Serre, C.; Devic, T. ZrIV Coordination Polymers Based on a Naturally Occurring Phenolic Derivative. *Eur. J. Inorg. Chem.* **2014**, *2014*, 6281–6289.
- (43) Sin, M.; Kavooosi, N.; Rauche, M.; Pallmann, J.; Paasch, S.; Senkowska, I.; Kaskel, S.; Brunner, E. In Situ ¹³C NMR Spectroscopy Study of CO₂/CH₄ Mixture Adsorption by Metal–Organic Frameworks: Does Flexibility Influence Selectivity? *Langmuir* **2019**, *35*, 3162–3170.
- (44) Cadiau, A.; Lee, J. S.; Borges, D. D.; Fabry, P.; Devic, T.; Wharmby, M. T.; Martineau, C.; Foucher, D.; Taulelle, F.; Jun, C.-H.; et al. Design of Hydrophilic Metal Organic Framework Water Adsorbents for Heat Reallocation. *Adv. Mater.* **2015**, *27*, 4775–4780.
- (45) Skorupska, E.; Jeziorna, A.; Paluch, P.; Potrzebowski, M. J. Ibuprofen in Mesopores of Mobil Crystalline Material 41 (MCM-41): A Deeper Understanding. *Mol. Pharmaceutics* **2014**, *11*, 1512–1519.
- (46) Azais, T.; Laurent, G.; Panesar, K.; Nossov, A.; Guenneau, F.; Sanfeliu Cano, C.; Tourné-Péteilh, C.; Devoisselle, J.-M.; Babonneau, F. Implication of Water Molecules at the Silica–Ibuprofen Interface in Silica-Based Drug Delivery Systems Obtained through Incipient Wetness Impregnation. *J. Phys. Chem. C* **2017**, *121*, 26833–26839.
- (47) Azais, T.; Tourné-Péteilh, C.; Aussenac, F.; Baccile, N.; Coelho, C.; Devoisselle, J.-M.; Babonneau, F. Solid-State NMR Study of Ibuprofen Confined in MCM-41 Material. *Chem. Mater.* **2006**, *18*, 6382–6390.
- (48) Porcino, M.; Li, X.; Gref, R.; Martineau-Corcoss, C. Solid-State NMR Spectroscopy: A Key Tool to Unravel the Supramolecular Structure of Drug Delivery Systems. *Molecules* **2021**, *26*, 4142.
- (49) Cendak, T.; Zunkovič, E.; Godec, T. U.; Mazaj, M.; Logar, N. Z.; Mali, G. Indomethacin Embedded into MIL-101 Frameworks: A Solid-State NMR Study. *J. Phys. Chem. C* **2014**, *118*, 6140–6150.
- (50) Sciortino, L.; Alessi, A.; Messina, F.; Buscarino, G.; Gelardi, F. M. Structure of the FeBTC Metal–Organic Framework: A Model Based on the Local Environment Study. *J. Phys. Chem. C* **2015**, *119*, 7826–7830.
- (51) Du, M.; Li, L.; Li, M.; Si, R. Adsorption Mechanism on Metal Organic Frameworks of Cu-BTC, Fe-BTC and ZIF-8 for CO₂ Capture Investigated by X-Ray Absorption Fine Structure. *RSC Adv.* **2016**, *6*, 62705–62716.
- (52) Márquez, A. G.; Demessence, A.; Platero-Prats, A. E.; Heurtaux, D.; Horcajada, P.; Serre, C.; Chang, J.-S.; Férey, G.; de la Peña-O’Shea, V. A.; Boissière, C.; et al. Green Microwave Synthesis of MIL-100(Al, Cr, Fe) Nanoparticles for Thin-Film Elaboration. *Eur. J. Inorg. Chem.* **2012**, *2012*, 5165–5174.
- (53) Menegollo, M.; Tessari, I.; Bubacco, L.; Szabadkai, G. Determination of ATP, ADP, and AMP Levels by Reversed-Phase High-Performance Liquid Chromatography in Cultured Cells. In *Calcium Signalling; Methods in Molecular Biology*; Vol. 1925, Springer: Humana, New York, NY, 2019; pp. 223–232. DOI: 10.1007/978-1-4939-9018-4_19.
- (54) Malvern Panalytical. *An Introduction to Dynamic Light Scattering (DLS)*; Malvern Panalytical, 2010.
- (55) Haouas, M.; Volklinger, C.; Loiseau, T.; Férey, G.; Taulelle, F. Monitoring the Activation Process of the Giant Pore MIL-100(Al) by Solid State NMR. *J. Phys. Chem. C* **2011**, *115*, 17934–17944.
- (56) Haouas, M.; Taulelle, F.; Martineau, C. Recent Advances in Application of ²⁷Al NMR Spectroscopy to Materials Science. *Prog. Nucl. Magn. Reson. Spectrosc.* **2016**, *94-95*, 11–36.
- (57) Mortlock, R. F.; Bell, A. T.; Radke, C. J. Phosphorus-31 and Aluminum-27 NMR Investigations of the Effects of pH on Aqueous Solutions Containing Aluminum and Phosphorus. *J. Phys. Chem.* **1993**, *97*, 775–782.

(58) Mooney, R. C. L. The Crystal Structure of Aluminium Phosphate and Gallium Phosphate, Low-Cristobalite Type. *Acta Crystallogr.* **1956**, *9*, 728–734.

(59) Müller, D.; Jahn, E.; Ladwig, G.; Haubenreisser, U. High-Resolution Solid-State ^{27}Al and ^{31}P NMR: Correlation between Chemical Shift and Mean Al-O-P Angle in AlPO_4 Polymorphs. *Chem. Phys. Lett.* **1984**, *109*, 332–336.

(60) Atkári, K.; Kiss, T.; Bertani, R.; Martin, R. B. Interactions of Aluminum(III) with Phosphates. *Inorg. Chem.* **1996**, *35*, 7089–7094.

(61) Karlik, S. J.; Elgavish, G. A.; Eichhorn, G. L. Multinuclear NMR Studies on Aluminum(III) Complexes of ATP and Related Compounds. *J. Am. Chem. Soc.* **1983**, *105*, 602–609.

(62) Khan, M. M. T.; Martell, A. E. Metal Chelates of Adenosine Triphosphate. *J. Phys. Chem.* **1962**, *66*, 10–15.

(63) Song, Y.; Zavalij, P. Y.; Suzuki, M.; Whittingham, M. S. New Iron(III) Phosphate Phases: Crystal Structure and Electrochemical and Magnetic Properties. *Inorg. Chem.* **2002**, *41*, 5778–5786.

Recommended by ACS

Comprehensive Review on the Degradation Chemistry and Toxicity Studies of Functional Materials

Roshani R. Pagar, Prabhanjan S. Giram, *et al.*

MAY 06, 2022
ACS BIOMATERIALS SCIENCE & ENGINEERING

READ 

Review of Natural Phytochemical-Based Self-Assembled Nanostructures for Applications in Medicine

Jiaxin Zhu, Wei Qu, *et al.*

FEBRUARY 21, 2022
ACS APPLIED NANO MATERIALS

READ 

Chemically Designed Nanoscale Materials for Controlling Cellular Processes

Koushik Debnath, Nikhil R. Jana, *et al.*

JULY 07, 2021
ACCOUNTS OF CHEMICAL RESEARCH

READ 

Electronic Band-Engineered Nanomaterials for Biosafety and Biomedical Application

Yan Cheng, Xiaogang Qu, *et al.*

AUGUST 09, 2021
ACCOUNTS OF MATERIALS RESEARCH

READ 

Get More Suggestions >